Insights into the Solvation and Selectivity of Chiral Stationary Phases Using Molecular Dynamics Simulations and Chemical Force Microscopy

by

Sorin Nita

A thesis submitted to the Department of Chemistry

in conformity with the requirements for

the degree of Doctor of Philosophy

Queen's University

Kingston, Ontario, Canada

August, 2008

Abstract

The mechanism by which chiral selectivity takes place is complicated by the surface morphology, the possible involvement of the solvent, and the characteristics of the chiral molecules at the surface. My goal is to model and understand the factors which lead to significant discrimination in the case of three closely related chiral stationary phases: *N*-(1-phenylethyl)-*N'*-[3-(triethoxysilyl)propyl]-urea (PEPU), [(3,5-dinitrobenzoyl)-amino]-*N*-[3-(triethoxysilyl)propyl]-2-phenylacetamide (DNB-phenyglycine), and [(3,5-dinitrobenzoyl)amino]-*N*-[3-(triethoxysilyl)propyl]--4-methylpentanamide (DNB-leucine).

Ab initio calculations are used to develop molecular models of these chiral selectors. These models are employed in molecular dynamics (MD) simulations, which provide the theoretical framework for modelling chiral interfaces in different solvent mixtures. The MD simulations of PEPU interfaces show that, in alcohol/water mixtures, the alcohols form domains at the interface with the hydrophobic portions of the molecule tending to orient towards the surface. This disrupts the water hydrogen bonding networks at the interface and leads to the exclusion of water from the surface region relative to the bulk. The MD simulations of DNB-phenylglycine and DNB-leucine selectors in hexane/2-propanol mixtures demonstrate that the interfaces are distinct both in terms of the selector orientations at the surface and in the number of hydrogen bonds formed with 2-propanol. This occurs despite the structural similarity between these two selectors.

The interfaces are also prepared experimentally by attaching the chiral selectors onto oxidized Si(111) samples and AFM tips. In particular, for DNB-phenylglycine and DNB-leucine samples, two synthetic routes have been explored. Using AFM, the morphologies of the resulting chiral interfaces are obtained. X-ray photoelectron spectroscopy and refraction-absorption infrared spectroscopy provide information regarding the relative distribution of the compounds on the surface. Using chemical force microscopy (CFM) measurements, chiral self-selectivity is examined in various solvent mixtures. For PEPU interfaces, the extent of hydrogen bonding at the surface is the dominant contributor to the measured forces. In the case of DNB-phenylglycine and DNB-leucine, CFM measurements of the chiral self-selectivity in 2-propanol demonstrate that chiral discrimination is present in both systems, but larger forces are observed for DNB-phenylglycine, consistent with the molecular dynamics study that shows much weaker solvent interactions with this species.

Acknowledgements

I am grateful to many people for help, both direct and indirect, for the work described in this thesis. First, I would like to thank my supervisors, Drs. Natalie Cann and Hugh Horton, for their constant support during my graduate studies, as well as for providing the opportunity for me to work on a project of an interdisciplinary nature. I have grown a lot in the last few years and they are directly responsible for this. They taught me how to approach a research problem and the best way to get it solved. This thesis is the result of many discussions that I had with them regarding my challenging project. Besides my supervisors, I would also like to thank Drs. Donal Macartney and Gang Wu for their insightful suggestions provided at my supervisory committee meetings.

I am also greatly indebted to Dr. Gelu Bourceanu from Al. I. Cuza University, for getting me so passionately involved into physical chemistry. He encouraged me to pursue a Ph.D. at Queen's University, knowing that this would fit very well with my career plans. I want to acknowledge the entire Queen's community for an extraordinary environment that is set to creating great scientific results. I would like to thank Dr. Hartmut Schmider for spending many hours on telephone with me trying to get some programs to run on HPCVL Sun Cluster. Special thanks to Drs. Carmen Lazar, Gheorghe Roman, David Edwards, and Jeffrey Roberts for their help regarding organic synthesis.

I am fortunate to have some great friends in my research groups, with whom I had many discussions and I shared experiences: Jenel Vatamanu, Irina Paci, Chunfeng Zhao, Shihao Wang, Rodica Pecheanu, and Vishya Goel. The great atmosphere in the

Department of Chemistry allowed me to develope many friendships that made the graduate experience very pleasant. Special thanks to Stephen Lee, Adrian Andriescu, Constantin Romanescu, Andrew Munro, and Serban Iliuta. Also, I am deeply grateful to the Hulls (Lorraine, Ian, Alison, Blair, and Keisha) for their affection and support shown in the last year.

Last, but not least, I thank my parents, Adrian and Aneta, and my sister, Ramona, for all the love they offered me during the years. I am so fortunate to have you near me, knowing that you support me in everything I do.

Financial support from Queen's University in the form of Graduate Awards, William Neish Fellowships, and conference travel allowances is also gratefully acknowledged.

Statement of Originality

I hereby certify that all of the work described within this thesis is the original work of the author. Any published (or unpublished) ideas and/or techniques from the work of others are fully acknowledged in accordance with the standard referencing practices.

Sorin Nita

July, 2008

Table of Contents

List of Tables

List of Figures

List of abbreviations

AES	Auger Electron Spectroscopy
AFM	Atomic Force Microscopy
AMBER	Assisted Model Building with Energy Refinement
APTES	3-aminopropyltriethoxysilane
CE	Capillary Electrophoresis
CEC	Capillary Electrochromatography
CFM	Chemical Force Microscopy
CGTO	Contracted Gaussian-Type Orbital
CHARMM	Chemistry at Harvard Molecular Modeling
CMPA	Chiral Mobile Phase Additive
CSP	Chiral Stationary Phase
DFT	Density-Functional Theory
DMF	dimethylformamide
DNB	dinitrobenzoyl
DNB-leucine	[(3,5-dinitrobenzoyl)amino]-*N*-[3-(triethoxysilyl)propyl]-4-methylpentanamide
DNB-phenylglycine	[(3,5-dinitrobenzoyl)-amino]-*N*-[3-(triethoxysilyl)propyl]-2-phenylacetamide
DNP	dinitrophenyl

EEDQ	1-ethoxycarbonyl-1,2-dihydroquinoline
ESCA	Electron Spectroscopy for Chemical Analysis
FTIR	Fourier Transform Infrared
GC	Gas Chromatography
GTO	Gaussian-Type Orbital
HF	Hartree-Fock
HPLC	High-Performance Liquid Chromatography
IR	Infrared
LC	Liquid Chromatography
LCAO	Linear Combination of Atomic Orbitals
LDA	Local-Density Approximation
LEC	Ligand-Exchange Chromatography
LJ	Lennard-Jones
LSDA	Local-Spin-Density Approximation
MC	Monte Carlo
MD	Molecular Dynamics
MM	Molecular Mechanics
MP	Møller-Plesset
NMR	Nuclear Magnetic Resonance

OPLS	Optimized Potential for Liquid Simulation
PEPU	*N*-(1-phenylethyl)-*N'*-[3-(triethoxysilyl)propyl]-urea
PES	Potential Energy Surface
RAIRS	Refraction-Absorption Infrared Spectroscopy
RU	Rigid Unit
SAM	Self-Assembled Monolayer
SCF	Sub- & Super-Critical Fluid Chromatography
SMB	Simulated Moving Bed Chromatography
SPM	Scanning Probe Microscopy
STM	Scanning Tunnelling Microscopy
STO	Slater-Type Orbital
THF	tetrahydrofuran
TLC	Thin Layer Chromatography
TraPPE-UA	Transferable Potential for Phase Equilibria-United Atoms
UV	Ultraviolet
VDZ	Valence Double Zeta
VTZ	Valence Triple Zeta
WHELK-O1	1-(3,5-dinitrobenzamido)-1,2,3,4-tetrahydrophenanthrene
XPS	X-ray Photoelectron Spectroscopy

Chapter 1

Introduction

The separation of enantiomers in chiral chromatography results from the formation of diastereomeric complexes between a chiral substrate and a chiral selector.[1] Understanding the physical nature of these interactions is central for the *systematic* development of new and improved chiral selectors and has an important impact on the ability to separate mixtures of enantiomers. Although in the last few years there has been an increase in available new chiral selectors, there has not been a proportionate advance on elucidating the mechanisms by which these chiral separations occur.[2] In my thesis, I address this need for fundamental knowledge by using a combination of chemical force microscopy, X-ray photoelectron spectroscopy, molecular dynamics simulations, and *ab initio* calculations, among other methods.

The selector in chiral chromatography can be introduced through chiral additives in the mobile phase, but it is more common to use a chiral stationary phase (CSP) where the selective molecule is immobilized on a surface. Brush-type[3] CSPs have a chiral end group attached, via an amide or ether linker, to the siloxane "tether". The tether is then covalently bonded to the surface of a colloidal silicate particle *via* a siloxane linkage. W.H. Pirkle developed a number of brush-type CSPs and two are of particular interest here. The first-generation CSPs prepared by Pirkle were based on 1-(9-anthryl)-2,2,2-trifluoroethanol and they were found to separate 3,5-dinitrobenzoyl derivatives of aryl

alcohols, amines, and thiols.[4,5] The reciprocal situation provided a clear continuation of the study and 3,5-dinitrobenzoyl derivatives were introduced in the CSP. These CSPs are the second generation of CSPs containing a few of the most widely used CSPs.[4] Two of the CSPs of interest in my study are based on *N*-(3,5-dinitrobenzoyl)-phenylglycine and *N*-(3,5-dinitrobenzoyl)-leucine that are prepared by a reaction of the dinitrobenzoyl-modified amino acid with a γ-aminopropylsilanized silica.[4,5,6] Alternatively, they can be synthesized by a reaction of the dinitrobenzoyl-modified amino acid with γ-aminopropyl(triethoxy)silane to form *R*- or *S*- versions of [(3,5-dinitrobenzoyl)amino]-*N*-[3-(triethoxysilyl)propyl]-2-phenylacetamide and [(3,5-dinitrobenzoyl)amino]-*N*-[3-(triethoxysilyl)propyl]-4-methylpentanamide[7] which are then coupled to the silica surface. These CSPs were found to be good at separating a wide range of π-donor and π-dipole-containing analytes: α-naphthamides of primary and secondary amines[6], alcohols, diols, sulfoxides, heterocyclic compounds, binaphtols,[8,9] among others. Because of their versatility, they were among the first commercially available HPLC CSPs, having been introduced by the Regis Chemical Company in the early 1980s. I will refer to these two CSPs as DNB-phenylglycine and DNB-leucine, to emphasize that their structure contains an amino acid and a dinitrobenzoyl group. I also consider in my study a brush-type CSP with a much simpler structure, *N*-(1-phenylethyl)-*N'*-[3-(triethoxysilyl)propyl]-urea, or PEPU. Although it is not as successful as other CSPs, it may be used to chromatographically separate the isocyanate and isothiocyanate derivatives of *S/R*-propranolol.[10,11]

These three CSPs (see Figure 1.1) are representative brush-type CSPs because they have aromatic groups which may undergo π-stacking interactions (present here are π-basic phenyl rings with a tendency to donate π-electrons and π-acidic dinitrophenyl rings with a tendency to accept π-electrons), and sites which may undergo hydrogen bonding in solution (in this case the amide groups and the urea residue). On a practical level, I chose to examine these CSPs for several important reasons. First, they are either commercially available or easily obtainable by organic synthesis. Second, they contain a triethoxysilane group that allows the molecules to be assembled on flat silanol (-SiOH) terminated surfaces, like etched Si(111), so that I can investigate the selector interfaces by means of X-ray electron spectroscopy, and scanning probe microscopy techniques. Third, the molecules have relatively simple and well-defined structures, so that appropriate models can be obtained and molecular dynamics simulations can be performed.

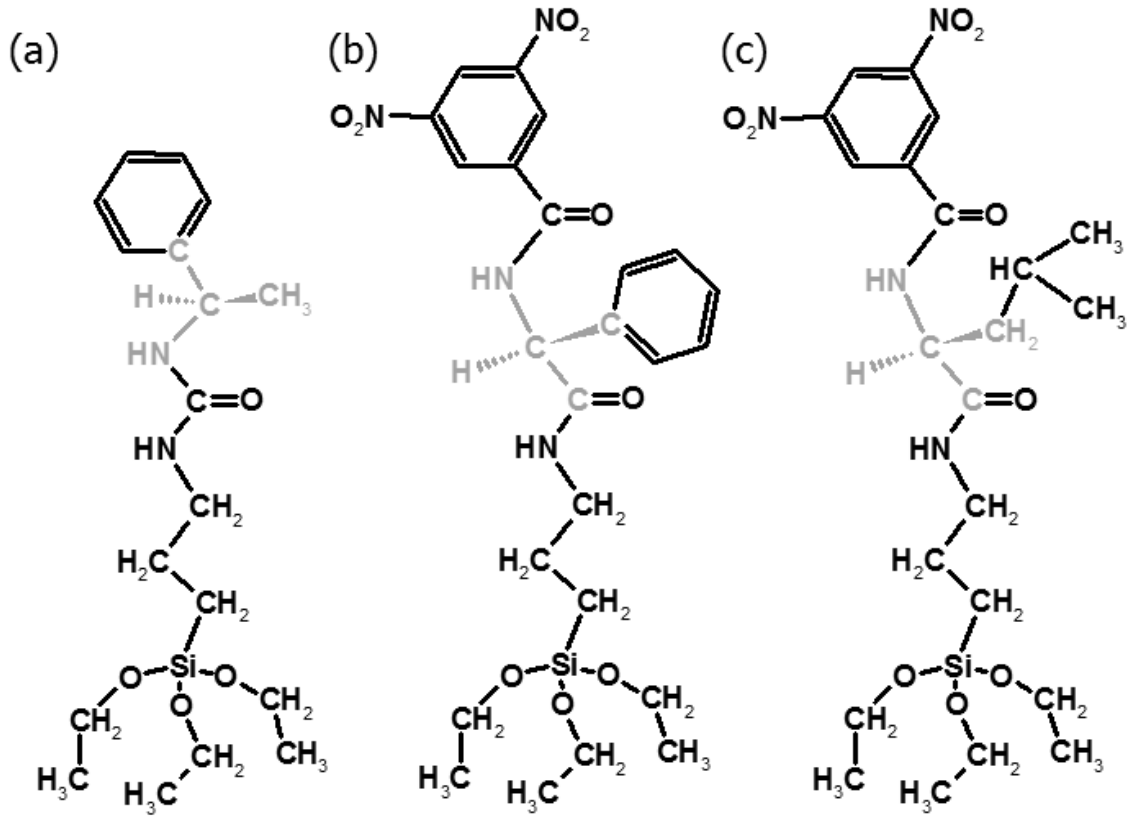

Figure 1.1 Diagram of the CSPs considered in this study:
(a) *N*-(1-phenylethyl)-*N'*-[3-(triethoxysilyl)propyl]-urea (PEPU),
(b) [(3,5-dinitrobenzoyl)amino]-*N*-[3-(triethoxysilyl)propyl]-2-phenylacetamide (DNB-phenyglycine), and (c) [(3,5-dinitrobenzoyl)amino]-*N*-[3-(triethoxysilyl)propyl]--4-methylpentanamide (DNB-leucine). The stereogenic region is noted in grey.

1.2 Literature review

From unicellular organisms to living plants and animals, chirality is found at the origin of life's building blocks, such as amino acids and sugars that form larger chiral structures in proteins and polysaccharides. As an important consequence, all biological processes are sensitive to stereochemical interactions and different reactions may be observed when comparing the activities of a pair of enantiomers.[12] From an economical point of view, the correct understanding of chiral interactions is driven mainly by the progress in the preparation of chiral drugs, food additives, and agrochemicals that have a high financial value and scientific potential.[13]

Enantiomers have identical properties except for the rotation of the plane of polarized light. However, in contact with a chiral environment like living systems they might exhibit very different biological responses. For example, *S*-carvone smells like caraway, while *R*-carvone smells like spearmint. Often, one enantiomer represents the active compound (called eutomer), while the other (distomer) might be inactive, or even contribute to unwanted side-effects showing toxicity or acting as an antagonist. For different behaviour of a pair of enantiomers, the literature usually quotes the tragic case of the drug thaliodomide that was introduced in the late 1960s as a sedative and a sleeping drug in a racemic form. The drug caused serious malformations in newborns of women who took the drug during pregnancy. Later it was shown that only *S*-enantiomer presented the teratogenic action.[14,15] However, even the nontoxic *R*-enantiomer exhibited negative side-effects because of *in vivo* interconversion into the harmful *S*-enantiomer.[12]

The demand for chiral chemicals has increased constantly in the last decade, driven primarily by the pharmaceutical industry and is fuelled by regulations governing chiral active pharmaceutical ingredients and the recognition that enantiomers of a chiral chemical can have very different biological activities. Pharmaceuticals account for about 80% of the total of chiral chemicals. The rest is divided by such uses as agricultural chemicals, electronics chemicals, flavours, and fragrances.[16] In 2006 about 80% of the drugs approved by the U.S. Food & Drug Administration were chiral and 75% of these were single-enantiomer drugs.[18] In terms of sales figures, a study from IMS Health shows that in the top ten drugs sold worldwide, nine have a chiral active ingredient. Their biologic activity is very diverse; examples include lipid-lowering agents (Lipitor, Zocor), inhibitors of gastric acid secretions (Prevacit, Nexium, Plavix), serotonin reuptake inhibitors (Zoloft), and anti-inflammatory agents (Advair). One of the top chiral drugs in terms of global sales, Lipitor (Pfizer), reached US $13 billion in 2006, in an industry that achieved more than US $160 billion annual revenue in the last few years and that is growing by 11.4% every year.[17,18] Furthermore, the pharmaceutical industry is employing a new approach to creating single-enantiomer drugs called the *racemic switch* that is a marketing strategy of patenting the single-enantiomer form of a drug that was already approved as a racemate. Although in some cases this separation is not showing a genuine therapeutic advantage, the number of single-enantiomer drugs created in the last few years is increasing.[13] This booming industry also created an increase of research activity regarding chiral methodologies. In the journals surveyed by the Chemical Abstracts Service, the number of papers per year that are associated to chiral technologies tripled in

the last decade, from about 1,300 in 1994 to more than 4,400 in 2003, and even more in the last few years.[17]

When chemical reactions are performed in an achiral environment, the result of the synthesis is a mixture consisting of equal amounts of enantiomers, a *racemate*. In order to prepare a single enantiomer, an asymmetric synthesis route must be employed. However, this is very challenging because much of it relies on catalysis and the design and optimization of a catalytic process takes a lot of time. Recent advances in chiral separation techniques are making large-scale separations of enantiomers from a racemate (resolutions) more cost-effective than asymmetric synthesis.[18]

A large number of enantioseparation techniques have been developed since the famous first separation of racemic sodium ammonium tartrate by hand by Louis Pasteur in 1848.[19] The choice of the enantioseparation method is mostly determined by the amount of sample present and the purpose of the experiment (preparative or analytical). Figure 1.2 describes the most important techniques employed for chiral separations.

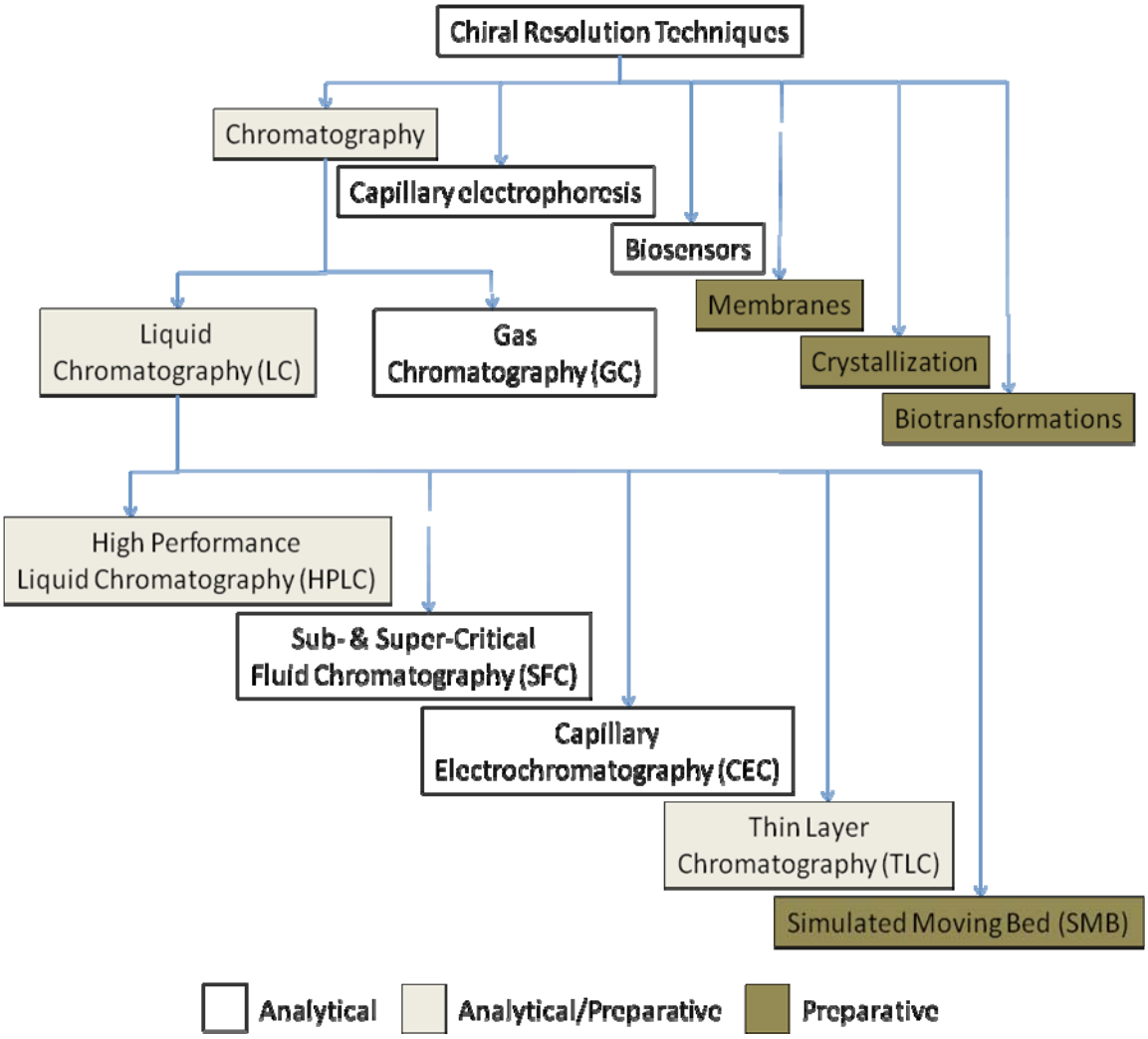

Figure 1.2 Techniques used for the preparation of enantiomers.[12,13]

For *analytical methods*, the primary purpose is to control the enantiomeric purity of the starting materials and final products. At this level the run time, sensitivity and selectivity are enhanced in order to improve the detection limits and the overall analysis time.[13] These aspects are very important for the pharmaceutical industry, which has very restrictive regulations regarding the purity and safety of chiral drugs. Taking into account these conditions, several techniques are used generally for analytical purposes: chromatographic methodologies (HPLC, GC, SFC, CEC, TLC), capillary electrophoresis (CE), and biosensors. While in chiral chromatography the mobile phase and the analytes are driven through the separating column by means of an applied hydraulic pressure, in capillary electrophoresis (CE) an external electric field is employed as the driving force. Chiral resolutions in CE involve the preparation of a chiral environment by adding chiral reagents (usually highly sulphated cyclodextrins) into the mobile phase. The main disadvantage of CE over chromatographic techniques are that it cannot be used in preparative separations. However, CE's high detection limit makes it a good alternative for the analytical separations of enantiomers. Recently, other analytical techniques have been adapted to enantioseparation, like the use of various organic molecules with chiral recognition capabilities for *chiral sensors* and enantiomeric resolution. These methods are promising alternatives to traditional enantioseparation techniques, but further improvements are needed in order to make them useful at the preparative scale.

For *preparative methods*, other than having an appropriate enantioselectivity, the techniques are required to have a high loading capacity and the employed chiral stationary phases should be easy to prepare, chemically inert, thermally stable, and very

robust. Chromatographic techniques in any of their different approaches are the most used at preparative level, but other methods are also employed with very good results. Crystallization is still used extensively for the separation of many compounds. Until the development of chiral chromatography, crystallization was one of the few existing ways to resolve enantiomers. However, direct crystallization is not generally applicable because only those compounds that have different crystals for both enantiomers can be resolved from racemates, either by using a chiral environment to achieve the crystallization, or by seeding the solution with the crystals of one enantiomer (preferential crystallization).[20] The use of polymeric *membranes* is an emerging technique for preparative enantioseparations that has important advantages for large-scale applications: continuous operation mode, easy adaptation to different production-important process configurations, and the use at ambient temperatures.[13] However, the use of enantioselective membranes has a few technical limitations: low flow rates, saturation of the chiral selectors, and the loss of enantioselectivity with usage time. Another technique already employed for industrial-scale separations involves the *biotransformation* of the chiral mixture. Usually these processes use the enantioselective properties of lipases, acylases, and hydrolases.[21] Although all these techniques have a great potential, at the moment the standard for enantioseparations is given by chromatographic methods. A detailed discussion of chromatographic enantioseparations is provided in the next section.

1.2.1 Chiral chromatography techniques

Depending on the mobile phase, there are gas chromatography (GC) techniques and liquid chromatography (LC) techniques. However, GC is not widely used for chiral separations because it requires that the chiral analyte be converted into a volatile species. Besides, it cannot be used at preparative scale, since the separated enantiomers cannot be collected for further analysis. In contrast, LC offers many advantages for the enantioseparation of racemates. Most importantly, it has the ability to separate enantiomers in both biological and environmental samples. There are many LC techniques developed for both analytical and preparative level separations that are among the best methods for the resolution of enantiomers.[12] Widely used LC techniques are summarized in the list below.

- *High Performance Liquid Chromatography* (HPLC). It is the most used technique for the separation of enantiomers, being estimated that about 90% of the chromatographic enantioseparations are done by means of HPLC.[12] In this technique, the mobile phase is forced into the chromatographic column at high pressures (up to 400 atm) ensuring a small retention time. Depending on the relative polarity of the mobile phase and the racemate, there are two methods: *normal phase HPLC*, when the mobile phase is a nonpolar organic solvent (hexane, heptane, cyclohexane), and *reverse phase HPLC*, when the mobile phase is a mixture of polar solvents (usually water/alcohols). This is the method of

choice for preparative scale separations because of its many advantages: sensitivity, reproducibility, high speed.

- *Sub- and supercritical Fluid Chromatography* (SFC). In this method, supercritical fluids are employed as mobile phases. The use of a supercritical fluid as a mobile phase in chiral chromatography is advantageous because the solute diffusion coefficients are usually of a higher order of magnitude. Commonly used supercritical fluids are carbon dioxide, nitrous oxide, and trifluoromethane. Using carbon dioxide as a mobile phase has many advantages, like low critical temperature and pressure, low toxicity and cost; however, because it is nonpolar, it lacks the ability to separate more polar compounds. To improve the elution ability usually some organic modifiers are added into the mobile phase.[12]

- *Capillary Electrochromatography* (CEC). This technique combines the chromatographic separation principles with the use of the electroosmotic flow in a capillary as driving force for the mobile phase. The main advantages are the high efficiency, speed, sensitivity, reproducibility, and lower detection limit. However, this method is not fully developed, and hence it is not very popular.

- *Thin-Layer Chromatography* (TLC). Despite the advances in the other chromatographic techniques, TLC is still used for the resolution of enantiomers because of its low running cost, simplicity, and coelution of the racemate and pure enantiomers. For enantiomer separations, it usually operates in the indirect mode,

requiring derivatization of the racemic mixture. The main disadvantages are the high limit of detection and the low resolution.

- *Simulated Moving Bed Chromatography* (SMB). This technique has the potential of becoming the method of choice for chiral separations. In this method, six to twelve chiral columns are joined in a circle and four to five pumps keep the liquid phase circulating through the entire system. Fractions are collected in separate evaporators in this system that works in a continuous mode with solvent recycling. Depending on the size of the columns, the products of enantiomeric separations can be from a few grams to tonnes. The biggest advantage of SMB is the high productivity, and despite the high cost of acquiring the technology, it is one of the most important chromatographic methods for preparative separations.[17]

1.2.2 Mechanistic characteristics of chromatographic enantioseparation

It is very important to obtain a clear description of how chiral recognition takes place because this can provide information about the qualitative magnitude of enantioseparation, types of analytes separated by a specific selector, predictability of the elution order, and correct chromatographic conditions. A systematic understanding can lead to the construction of quantitative structure-enantioselectivity retention relationships that combine quantitatively comparable retention data for analytes and those for molecular descriptors that reflect the structural features of these analytes.[13]

In chromatographic systems there are a multitude of interactions that are fundamental for considering how the chiral recognition occurs. These are usually attractive interactions such as hydrogen bonding, π-π stacking, dipole-dipole interactions, or repulsive steric constrains. It is generally accepted that chiral recognition requires a minimum of three simultaneous interactions between the selector and at least one of the enantiomers, with at least one of these interactions being stereochemically dependent.[22] This is known in the literature as the *three-point rule* and it was first introduced by Dalgleish.[23] To obtain a separation of enantiomers at least one of the enantiomers must form a diasteromeric complex with the chiral selector, and the binding constants of the enantiomers must be different. For two enantiomers A and B that interact with the CSP there are two equilibria:

$$A + CSP \overset{K_A}{\rightleftharpoons} A\text{-}CSP \tag{1.1}$$

$$B + CSP \overset{K_B}{\rightleftharpoons} B\text{-}CSP \tag{1.2}$$

The effectiveness of the chromatographic discrimination is described by the thermodynamic enantioselectivity factor α that is defined as the ratio of equilibrium constants for the two binding processes:

$$\alpha = \frac{K_A}{K_B} \tag{1.3}$$

Considering the equilibrium constant expression in terms of the molecular free energy of adsorption (ΔG) of the A and B enantiomers, the equation (1.3) becomes:

$$\alpha = \frac{\exp(-\Delta G_A/kT)}{\exp(-\Delta G_B/kT)} \qquad (1.4)$$

Rearrangement of (1.4) gives that the thermodynamic enantioselectivity is connected to the differential free energy of the two enantiomers:

$$\Delta(\Delta G) = \Delta G_A - \Delta G_B = -RT \ln \alpha \qquad (1.5)$$

In order to attain a chromatographic separation, the differences in the binding energies for the two enantiomers and the $\Delta(\Delta G)$ do not need to be very large, a modest difference in free energy of $\Delta(\Delta G) = 0.24$ kcal/mol is sufficient to achieve a separation factor of $\alpha = 1.5$.[26] This is reasonable for an analytical-scale enantioseparation that only requires narrow chromatographic peaks that are easily separated. However, a high level enantioselectivity is required for preparative-scale resolutions. This is done by enhancing the $\Delta(\Delta G)$, therefore a thorough understanding of the enantioseparation mechanism is essential.[22]

For practical chromatographic calculations, it is more common to express α in terms of the retention factors k_A and k_B. The kinetic expression for the enantioselectivity factor is:

$$\alpha = k_A / k_B \qquad (1.6)$$

where the retention factors are defined in terms of their retention times t_r relative to the retention time for an unretained compound t_0:

$$k = (t_r - t_0) / t_0 \quad (1.7)$$

The CSPs are the most important element in the enantioselectivity process because they have the most important impact on the retention factors for a particular chiral mixture. In the next section the important types of chiral selectors are discussed in detail.

1.2.3 Selectors in chiral chromatography

There are two approaches that can be used for chiral separations: direct and indirect. *Indirect* separations are based on the use of chiral derivatization reagents to form diastereomeric derivatives with different chemical and physical properties and which therefore can be separated on achiral stationary phases. Commonly used chiral derivatization reagents are 1-(9-fluorenyl)ethylchloroformate and *o*-phthaldialdehyde in combination with chiral thiols.[24,25] The main advantage in this case is the use of relatively cheap and readily available achiral stationary phases, but there are many disadvantages: the derivatization is an additional step that can produce undesired results (racemization, formation of decomposition products) and finding the appropriate derivatizing agent in pure chiral form might be very difficult. For preparative enantioseparations, the indirect approach requires an additional synthetic step because after the separated diastereoisomers have been resolved on the achiral column, the derivatizing agent must be cleaved off.[12]

The *direct* approach involves the use of the chiral selector either in the mobile phase (chiral mobile phase additive (CMPA)) or in the stationary phase (chiral stationary phase (CSP)). When chiral selectors are used as CMPAs the approach can be expensive because of the large quantities of chiral selector required for the preparation of the mobile phase, and the large amount of selector that is wasted in the separation process. Another disadvantage is that this approach is not suitable for preparative separations, since the eluate fractions contain the CMPAs and makes potential recovery of the analyte complicated. The method of choice in chromatography is using CSPs that are chemically bonded, coated or absorbed on a suitable solid support (usually silica particles). The enantioseparation is due to differences in free energy between temporary diastereomeric complexes formed by the solute enantiomers and the CSP. The larger the difference, the greater the separation.[15] A large number of CSPs are commercially available and sometimes it is difficult to determine which is most suitable for a particular resolution. This difficulty is minimized by grouping the CSPs in classes according to their common characteristics.

1.2.3.1 Chiral stationary phases

According to the mode of formation of the solute-CSP complex the CSPs are divided into seven important categories:[24,26]

1. *Proteins*. The CSP is a protein and the analyte-CSP complexes are based in combinations of hydrophobic, polar interactions and hydrogen bonds that act as dispersive forces on the most retained enantiomer. Several proteins show good

enantioselectivity and are commercially available for use as CSPs: bovine serum albumin (BSA),[27] human serum albumin (HSA),[28] chicken egg albumin,[29] and enzymes like cellobiohydrolases (CBH I, CBH II),[30] lysozyme,[31] and pepsin.[32] Although there is a modest loading capacity and a restricted stability (at high temperature and pH), they offer a wide applicability.

2. *Modified polysaccharides*. Useful polysaccharides CSPs for HPLC have been prepared since the 1980s by Okamoto as cellulose triacetate (CTA-II),[33] cellulose trisphenylcarbamate derivatives (CTPCs).[34] Other CSPs have been prepared by substituting the cellulose with amylose,[35] or by using other polysaccharides like chitosan,[36] chitin,[37] and amylopectin.[38] Of particular interest are the stationary phases cellulose-tris(3,5-dimethyl-phenylcarbamate) and amylose-tris(3,5-dimethyl-phenylcarbamate), known as Chiralcel OD and Chiralpak AD, respectively. They are among the most versatile CSPs, being used for compounds with aromatic, amide, carbamate, ester, and alkyl-amine groups, or multiple stereogenic sites. The proposed separation mechanism contains attractive interactions rather than an inclusive contact, being based on hydrogen bonds, steric, π-π and dipole-dipole interactions with the enantiomers to be resolved.[39] These are among the most frequently used CSPs for chromatographic separations in both analytical and preparative scales. Although the enantioselectivities are not very high, the fact that there is a broad range of chiral compounds that can be separated increases their use.

3. *Synthetic polymers*. Blaschke *et al.* prepared chiral synthetic polymers based on polyacrylamides and polymethacrylamides with chiral side chains and used them for low-pressure chromatographic resolutions of benzodiazepines, barbiturates and hydantoins.[40] Okamoto *et al.* synthesized triphenylmethyl methacrylate, a chiral polymer that showed enantioselectivity for more than 200 chiral compounds.[41] Although these examples illustrate the potential of chiral polymers as CSPs, their relative lack of chemical stability and high cost make them less suitable for large-scale applications.

4. *Macrocyclic antibiotics*. CSPs based on the cavity of macrocyclic glycopeptides bound to silica have been shown to be very effective chiral selectors in chiral HPLC and CE. There are a few glycopeptides that have been investigates widely: vancomycin,[42] teicoplanin,[43] ristocetin A,[44] avoparcin,[45] thiostrepton,[42] and ansamycin rifamycin B.[42] They contain an aglycin portion of fused macrocyclic rings that form a characteristic basket shape and a carbohydrate moiety. The separation mechanism involves the inclusion of the hydrophobic part of the chiral analyte into the hydrophobic basket and interactions by hydrogen bonds, π-π stacks, and steric repulsions with the suspended side-chains are responsible for the formation of inclusion complexes. Although these selectors work very well for a few classes of chiral compounds, only a limited number of such selectors are available and their cost is very high.

5. *Cyclic low molecular weight compounds*. *Crown ethers* are known to form host-guest complexes with a variety of analytes. They can be used as CSPs for the enantioseparation of amino acids.[46] Although these selectors are highly selective and stable, they only have a limited applicability. Totally different is the case of *cyclodextrins* (CD), because they have proven to be widely applicable chiral selectors in electrophoresis, liquid and gas chromatography. These cyclic oligosaccharides consist of six (α-CD), seven (β-CD), or eight (γ-CD) glucopyranose units. Their structure has a truncated cone with a hydrophobic cavity that can accommodate the enantiomers that need to be separated. Additionally, the lateral interactions at the hydroxyl sites create hydrogen bonds and dipole-dipole interactions with the analyte. Attached covalently to silica, they are relatively inexpensive to prepare and separate a wide range of chiral molecules, although they only have modest selectivities.[47]

6. *Metal ion complexes*. These CSPs have a central metal ion (usually Cu^{2+} or Ni^{2+}) complexed by two chelating chiral bifunctional molecules (like proline and hydroxyproline) with a steric rigidity that provides a high degree of enantioselectivity. The support is usually polystyrene-divinylbenzene polymers. The enantioseparation is based on the formation of ternary mixed metal complexes between the selector and the analyte ligand. The chromatographic technique based on this procedure is known in the literature as ligand-exchange chromatography (LEC). They only separate properly a limited number of racemates such as amino acids, amino alcohols, hydroxyacids, and Schiff bases.[48]

7. *Small chiral molecules*. These CSPs were introduced in the 1980s and are known as brush-type CSPs. They are particularly useful in chiral separations because of their broad applicability, chemical and thermal inertness, good kinetic performance, high loadability, and compatibility with many mobile phases. The structure of these CSPs usually contains a hydrogen bond donor/acceptor system (an amino acid, an amide, a urea group), an aromatic moiety (3,5-dinitrobenzoyl, phenyl, or naphthyl), and an achiral tether that is used to attach the chiral molecule to the silica beads.[12,49] Phenyl and naphthyl groups have the tendency to donate π-electrons (π-basic character) whereas the aromatic groups with electronegative atoms/groups are π-electron deficient and have a tendency to accept π-electrons (π-acidic character). The chiral separation mechanism is complicated and includes steric effects, dipole-dipole forces, as well as the formation of a π-π charge-transfer diastereomeric complex stabilized by hydrogen bonds with the rest of the selector. The understanding of these complex interactions is the focus of this thesis. Pirkle developed some very successful CSPs like DNB-phenylglycine, DNB-leucine, and WHELK-O1 that are commercialized by Regis Technologies and were shown to be applicable to a broad range of chiral compounds.[50] Most of these selectors have as their chiral center an amino acid residue, but in the last few years other CSPs were developed with the chiral centers based on 1,3,5-triazine,[51] tartaric acid,[52] cholic acid,[53] deoxycholic acid,[54] ergot alkaloid,[55] cinchona alkaloid quinine,[56] and many others. Many organic solvents are used as mobile phases. In normal-phase mode

HPLC nonpolar solvents like hexane, heptane, and cyclohexane are commonly used. Aliphatic alcohols like 2-propanol, methanol, and ethanol, are added in the mobile phase to improve the chiral resolution because they are hydrogen donors and acceptors and may interact with the amide groups of the CSPs generating hydrogen bonds.[12]

1.2.4 Studies of CSPs using Chemical Force Microscopy

Scanning probe methods have been used extensively to image chiral surfaces. In some studies the surfaces become chiral when the rotation of the adsorbed molecules is restricted in two-dimensions. An example is the identification of *R*,*R* and *S*,*S* isomers of trans-2-butene[57] that become chiral when adsorbed on Si(100). Other workers have described chiral molecules adsorbed on metal surfaces, such as cysteine on Au(111),[58,59] or tartaric acid on Cu(110).[60] With the advance of chemical force spectrometry – using the force-displacement curve to measure the adhesion force between atomic force microscopy (AFM) tips and samples – a different approach to scanning probe research on chiral molecules becomes available. As it is based on the measurement of interaction forces between two surfaces, this technique provides means of quantifying the surface chirality, with a direct application in understanding the separation mechanisms of CSPs. Nevertheless, chemical force spectrometric measurements with chiral components presents many challenges because adhesion interactions depend on a series of experimental factors such as surface roughness, solvent, and the nature of the support. Only a few such studies examining chiral discrimination have been published. The

interaction between AFM tips derivatized with DNB-phenylglycine and Au surfaces derivatized with mandelic acid in an ethanol solvent was studied by McKendry *et al*.[61,62] The adhesive force between the tip and sample was about 1 nN smaller when the two were of like stereochemistry (*R*/*R* or *S*/*S*) as opposed to unlike (*R*/*S* or *S*/*R*). In another study, the tips were modified with 2,2,2-trifluoro-1-(9-anthryl)ethanol and the samples were derivatized with DNB-phenylglycine, but the adhesive forces did not show a clear chiral discrimination.[63] My studies of the CSP *N*-(1-phenylethyl)-*N'*-[3-(triethoxysilyl)propyl]-urea (PEPU),[64,65] DNB-phenylglycine and DNB-leucine in different solvents and solvent mixtures are discussed in detail in this thesis.

1.2.5 Studies of CSPs using theoretical methods

The elucidation of chiral recognition from chiral chromatography means to understand the intermolecular forces that are stabilizing the enantiomers in their transient complexes established with the chiral selector. Theoretical methods are employed for modelling CSPs and provide a valuable basis to make predictions regarding the resolution of classes of chiral compounds, the elution order, and the magnitude of enantioselectivity.[13] Techniques for atomistic modeling of CSPs have been summarized in several recent reviews.[66,67,68] Statistical approaches that provide structure-selectivity relationships have been applied to chiral chromatography.[69,70,71] These methods have the important advantage that they provide a quick prediction of separation efficiency. However, their range of applicability is restricted to analytes that are closely related to those upon which the structure-selectivity relationship was originally designed. A

docking study typically examines single host-guest complexes that are either isolated or embedded within a dielectric continuum. Some time ago, Lipkowitz *et al.* [72,73,74,75] completed a number of molecular mechanics and energy minimization studies in order to determine conformations of DNB-phenylglycine and predict the mechanism by which the chiral separation occurs. Similar studies have been performed on DNB-leucine,[76] *N*-(1-naphthyl)leucine,[77] BOC-D-alanine-*N'*-*n*-propylamide,[78] and PEPU[79] CSPs. Together, these studies provide an important first step in understanding the behaviour of these CSPs, but the complexity of the analyte-CSP interaction meant that retention order was not always predicted successfully. As Lipkowitz noted in a review article,[72] "the best approach is to carry out full molecular simulations rather than simple energy minimizations." However, molecular dynamics (MD) simulations of chiral interfaces present many challenges. Stationary phase interfaces are particularly demanding because they require that the selector have a complete, atomic level description, together with a proper representation of its flexibility, and with an appropriate representation of the surface environment (surface coverage, end-caps, etc.).[80] Nonetheless, some simulations of achiral selectors for HPLC have been reported in the literature. Most notably, the entanglement and solvation of long chain alkanes tethered to silica has been examined in some detail.[81,82,83,84] Another study examined the binding of tryptophan enantiomers to α-cyclodextrin and both the enantioseparation factor and the elution order were in agreement with NMR experiments.[85] Also, of particular note are the results of this thesis on the solvation and selectivity of PEPU,[64,65] DNB-phenylglycine and DNB-leucine and Zhao's study on the Whelk-O1 CSP.[86,87]

1.3 Thesis organization

My thesis contains a comprehensive investigation of the solvation and self-selectivity of PEPU, DNB-phenylglycine, and DNB-leucine. Chapter 1 shows the importance of understanding the behaviour of CSPs in chiral enantioseparations. Chapter 2 presents the theoretical methods employed in this study, with a focus on molecular dynamics (MD) simulations and *ab initio* techniques. Chapter 3 describes the experimental techniques, with an emphasis on X-ray photoelectron spectroscopy (XPS) and chemical force microscopy (CFM). Chapter 4 contains the experimental and theoretical results obtained for PEPU in mixed solvents. Chapter 5 provides experimental and theoretical details for the DNB-phenylglycine and DNB-leucine CSPs. The thesis closes with brief conclusions.

Chapter 2

Theoretical methods

Understanding the behaviour of interfaces is not only important for explaining phenomena such as chiral chromatography, but is also important at the fundamental/theoretical level, as the system is characterized by a number of unique properties that are different from the properties of the bulk solvent. Therefore it is not surprising that theoretical studies of the structure, reaction dynamics, thermodynamics and solvation at interfaces date back to at least the beginning of the 20th century.[88] Recent theoretical studies of bulk liquid chemical reaction dynamics show that researchers can no longer be satisfied by a picture that portrays the solvent as a structureless medium, and that the effect of the liquid must be considered at the *microscopic level*.[89] This is particularly important for understanding processes at interfaces, as the interfacial region itself is only a few molecular diameters thick. Advances in statistical mechanics and computer simulations of liquids have contributed significantly in the recent years to a theoretical understanding of the microscopic structure and dynamics of the neat interface.[88,89]

Quantum mechanical methods are particularly useful to microscopic level studies because they provide accurate *ab initio* descriptions of the configuration and energy of chemical systems. These methods, with an emphasis on density-functional theory, are treated in the first part of this chapter. Another approach particularly useful for many-

body systems is the use of *classical mechanics* in the form of computer simulations to analyse the behaviour of systems from atomic level details to macroscopic properties. Advances in computational power in the last decades have made Monte Carlo and molecular dynamics simulations very important tools for the investigation of fluids and interfaces. These methods are discussed in the second part of this chapter.

2.1 Quantum mechanics methods

In quantum mechanics, the state of a system is completely defined by a *wave function* Ψ. In the time-independent formulation, this is a function of particle coordinates, containing all possible information about a system. The behaviour of a quantum-mechanical system is governed by the Schrödinger equation:

$$\hat{H}\Psi = E\Psi \tag{2.1}$$

where E is the total energy of the system and $\hat{H}$ is the molecular Hamiltonian operator given by:

$$\hat{H} \equiv -\frac{h^2}{8\pi^2}\sum_{\alpha}\frac{1}{m_\alpha}\nabla_\alpha^2 - \frac{h^2}{8\pi^2 m_e}\sum_i \nabla_i^2 + \sum_{\alpha<\beta}\frac{Z_\alpha Z_\beta e^2}{r_{\alpha\beta}} + \sum_{i<j}\frac{e^2}{r_{ij}} - \sum_{i,\alpha}\frac{Z_\alpha e^2}{r_{i\alpha}} \tag{2.2}$$

where *i* and *j* refer to electrons and α and β refer to nuclei. The first two terms are the operators for the kinetic energy of the nuclei and electrons, respectively. $\nabla^2 \equiv \frac{\partial^2}{\partial x^2} + \frac{\partial^2}{\partial y^2} + \frac{\partial^2}{\partial z^2}$ is the Laplacian operator, h is Planck's constant, m_α and m_e are

the nuclear and electronic masses. The third term is the potential energy from the repulsion between nuclei, where Z_α and Z_β are the atomic numbers for nuclei α and β, respectively, $r_{\alpha\beta}$ is the internuclear distance, and e is the electron charge. The fourth term is the potential energy from the repulsion between electrons, r_{ij} being the interelectronic distance. Finally, the last term is the potential energy of attraction between nuclei and electrons, $r_{i\alpha}$ being the distance between the nucleus α and the electron i.[90] However, the electrons move much faster than the nuclei, since the nuclei are much heavier ($m_\alpha >> m_e$), so that a good approximation is obtained by considering the nuclei as fixed while electrons perform their motion. This approximation of separating nuclear and electronic motions is known as the *Born-Oppenheimer approximation*. The purely electronic Hamiltonian has a much simpler expression:

$$\hat{H} \equiv -\frac{h^2}{8\pi^2 m_e}\sum_i \nabla_i^2 + \sum_{i<j}\frac{e^2}{r_{ij}} - \sum_{i,\alpha}\frac{Z_\alpha e^2}{r_{i\alpha}} \qquad (2.3)$$

The Hamiltonian expression from (2.3) shows that Schrödinger's equation is a multi-dimensional, multicenter, differential equation that is very difficult to solve. There are two main approaches to solving this equation: *ab initio* methods and semiempirical methods.

Ab initio (or *first principles*) methods use the correct Hamiltonian and generally do not employ any data in the calculation other than the values of fundamental physical constants. An example is the Hartree-Fock method for the calculation of the optimal antisymmetrized product Φ of spin-orbitals. This Hartree-Fock self-consistent field

calculation employes the minimization of the variational integral $\int \Phi^* \hat{H} \Phi d\tau$, where $\hat{H}$ is the Hamiltonian from (2.3). However, it is difficult to apply *ab initio* calculations to large molecules, and alternative *semiempirical methods* have been developed. These methods use a simpler form of the Hamiltonian than the true one, neglect some of the integrals that appear in the calculation and employ parameters whose values are fitted to experimental data. A typical example is the extended Hückel method, which uses a one-electron Hamiltonian and a simple parameterization procedure for the calculation of bond integrals. An important, and relatively recent, development in the application of quantum mechanics to molecular systems is *density-functional theory* (DFT). Unlike typical *ab initio* methods, DFT does not attempt to solve Schrödinger's equation for the molecular electronic wave function, but calculates the molecular electronic energy from the molecular electron probability density ρ_0. Because of recent advances,[90] this method gives good results even for large molecules and is therefore widely used in energetic and structural calculations. A detailed overview is given in the next section.

2.1.1 Density-Functional Theory

In traditional quantum mechanics one first finds the wave function, and then finds the other electronic properties by integration. In DFT the ground-state energy, the wave function, and all other electronic properties of a molecule are uniquely determined from the ground-state electron probability density ρ_0(x,y,z), a function of only three variables. This is the Hohenberg-Kohn theorem that was proved in 1964.[91] The exact formalism by

which the ground-state energy is found from the density ρ_0 is known as the Kohn-Sham method.[92]

In the Kohn-Sham method, ρ_0 is obtained in terms of the *Kohn-Sham spin-orbitals* θ_i^{KS} that belong to a fictitious system of noninteracting electrons defined to have the same electron density as that in the ground-state molecule:

$$\rho_0 = \rho_s = \sum_{i=1}^{n} \left| \theta_i^{KS} \right|^2 \tag{2.4}$$

These Kohn-Sham orbitals have no physical significance other than allowing the exact molecular ground-state ρ_0 to be calculated from equation (2.4). In these conditions, the ground-state energy E_0 of the fully-interacting real system is determined as a functional of the function ρ_0 as:

$$E_0 = E_v[\rho_0] = -\sum_{\alpha} Z_\alpha \int \frac{\rho_0(\mathbf{r}_1)}{r_{1\alpha}} d\mathbf{r}_1 - \frac{1}{2} \sum_{i=1}^{n} \left\langle \theta_i^{KS}(1) \left| \nabla_1^2 \right| \theta_i^{KS}(1) \right\rangle + \\ + \frac{1}{2} \iint \frac{\rho_0(\mathbf{r}_1)\rho_0(\mathbf{r}_2)}{r_{12}} d\mathbf{r}_1 d\mathbf{r}_2 + E_{xc}[\rho_0] \tag{2.5}$$

The first term gives the electron-nuclear attraction in terms of the density-function ρ_0, the electron-nucleus distance $r_{1\alpha}$, and the atomic number of the nucleus Z_α. The second term is the average ground-state kinetic energy of the noninteracting electrons with electron density equal to that in the molecule calculated in terms of Kohn-Sham spin-orbitals θ_i^{KS}. The third term is the classical expression for the electrostatic interelectronic repulsion energy for the electrons in a continuous distribution of charge ρ_0

at the distance r_{12}. The last term, $E_{xc}[\rho_0]$ is a small fraction of the total energy called the *Kohn-Sham exchange-correlation energy*. As the functional derivative of the exchange-correlation energy, one can calculate the *exchange-correlation potential* v_{xc}:

$$v_{xc}(\mathbf{r}) \equiv \frac{\delta E_{xc}[\rho_0(\mathbf{r})]}{\delta \rho_0(\mathbf{r})}. \tag{2.6}$$

A typical Kohn-Sham DFT calculation starts with an initial guess for ρ_0 that provides an estimate of a selected $E_{xc}[\rho_0]$, and v_{xc} is determined from equation (2.6). The v_{xc} function is then used in the one-electron equations $\hat{h}^{KS}\theta_i^{KS} = \varepsilon_i^{KS}\theta_i^{KS}$, where the *Kohn-Sham operator* $\hat{h}^{KS}$ depends on the exchange-correlation potential v_{xc}.[93] By solving these equations, initial estimates of the Kohn-Sham orbitals θ_i^{KS} are obtained, which are then used in equation (2.4) to find an improved density ρ_0. The iterations continue in a self-consistent manner until there is no further significant change in the density and the Kohn-Sham orbitals.[90]

However, this method has an important problem: the correct relationship between the exchange-correlation functional E_{xc} and the density ρ_0 is not known. E_{xc} is a very important term because it includes all the details of the two-electron exchange and dynamical correlation, and because the second term in equation (2.5) is not the kinetic energy of the real system: E_{xc} contains a kinetic-energy correction as well. Consequently, in order to get E_{xc}, appropriate approximations needed to be introduced. The most common are *local-density approximation* (LDA), *Xα method*, and *local-spin-density*

approximation (LSDA). LSDA in particular gives relatively good molecular geometries and vibrational frequencies. Nevertheless, this exchange functional has a *universal* trend to underestimate exchange energies by a few percent and to overestimate correlation energies by a factor of roughly two. Consequently, the predicted bond energies are much too large; on a set of 56 small molecules called the "old G2 set" the mean absolute error is ~40 kcal/mol, which makes this method useless in thermodynamic applications.[94] Considering the fact that LSDA *always* underestimates the absolute value of the exchange energy, Becke constructed a corrected exchange functional that depends on the density and the gradient of the density, and yields the correct asymptotic energy density.[95] This *gradient-corrected exchange functional* is named Becke's 1988 functional (Bx88, Becke88, B88, or B) and has the explicit form:

$$E_x^{B88} = E_x^{LSDA} - b \sum_{\sigma=\alpha,\beta} \int \frac{(\rho_0^\sigma)^{4/3} \chi_\sigma^2}{1 + 6b\chi_\sigma \sinh^{-1} \chi_\sigma} d\mathbf{r} \qquad (2.7)$$

where $\chi_\sigma \equiv \frac{\left|\nabla \rho_0^\sigma\right|}{(\rho_0^\sigma)^{4/3}}$ is a dimensionless gradient variable, $\sinh^{-1}x = \ln[x + (x^2 + 1)^{1/2}]$, and b has a value of 0.0042 atomic units, as determined by a least squares fit to the known Hartree-Fock exchange energies of the noble gas atoms He through Rn.[90,94,95]

Becke's exchange functional can be combined with a correlation functional, such as the gradient-corrected Lee-Yang-Parr (LYP) correlation functional E_c^{LYP} and Vosko-Wilk-Nusair (VWN) correlation functional E_c^{VWN}. Of particular importance is the exchange-correlation functional BLYP that is a combination of Becke's (B) exchange

functional E_x^{B88} and Lee-Yang-Parr (LYP) correlation functional E_c^{LYP}. This gradient-corrected functional provides very good estimates of geometries and energies for many molecules, with errors of only 4-6 kcal/mol.[96]

Even better agreement with the experimental energies was obtained by using hybrid exchange-correlation functionals. These hybrid functionals combine together the gradient-corrected exchange-energy functional E_x, gradient-corrected correlation-energy functional E_c and the exchange-energy functional calculated using Hartree-Fock method E_x^{exact}. A very popular example is the B3LYP (or Becke3LYP, indicating a three-parameter functional) hybrid functional defined by:

$$E_{xc}^{B3LYP} = (1 - a_0 - a_x)\, E_x^{LSDA} + a_0\, E_x^{exact} + a_x\, E_x^{B88} + (1 - a_c)\, E_c^{VWN} + a_c\, E_c^{LYP} \qquad (2.8)$$

where the empirical parameters a_0, a_x, and a_c are chosen from fits to experimental molecular atomization energies ($a_0 = 0.20$, $a_x = 0.72$, and $a_c = 0.81$).[97]

Hybrid functionals and gradient-corrected functionals give good vibrational frequencies, dipole moment, and molecular geometries, and they are also generally accurate for molecular atomization energies, with errors smaller than 2 kcal/mol.[94]

2.1.2. Basis functions

The most common way to represent molecular orbitals ϕ_i is via linear combination of the form $\phi_i = \sum_i c_{ri}\chi_r$, where χ_r are a set of atom-centered *basis functions* and c_{ri} are the linear expansion coefficients. This is termed a *Linear Combination of*

Atomic Orbitals (LCAO). Each atomic orbital can be represented as a linear combination of one or more basis functions that are centered on the given atom in the molecule. Widely used are Slater-type orbitals (STOs). An STO centered on atom *a* has the exponential form $Nr_a^{n-1}e^{-\zeta r_a}Y_l^m(\theta_a,\phi_a)$, similar to the form of the exact wave functions for the hydrogen atom, except that the polynomial has been replaced by r_α^{n-1}, and the exponential includes a parameter ζ called the *orbital exponent*. The angular dependence is given by the spherical harmonic $Y_l^m(\theta_a,\phi_a)$, *n*, *m*, and *l* are integers, and *N* is a normalization constant.

It has been observed that STOs are good for calculations on individual atoms and small linear molecules, but for bigger molecules this is very difficult. For a better integral evaluation, Boys suggested the use of Gaussian-type orbitals (GTOs) instead of STOs for the representation of atomic orbitals.[98] GTOs are smooth and continuous at the nucleus, and are much easier to calculate for big molecules, since the products of GTOs on multiple centers can be reduced to a GTO on a single center. A Cartesian GTO centered on atom *a* has the form $Nx_a^i y_a^j z_a^k e^{-\alpha r_a^2}$, where x_a, y_a, and z_a are the Cartesian coordinates with the origin at nucleus *a*, *N* is the normalization constant and α is a positive orbital exponent, and *i*, *j*, *k* are nonnegative integers.

Since actual atomic orbitals have a "cusp" at the nucleus just as the STOs, it is necessary to use a fixed linear combination of GTOs with different orbital exponents in the calculation. Figure 2.1 shows that the H 1*s* atomic orbital is reasonably well simulated by fitting four GTOs with different exponents. Such linear combinations of GTOs are

called *contracted Gaussian-type orbitals* (CGTOs) and the individual Gaussian functions contributing to these contractions are called *primitive Gaussians*. A *minimal basis set* of CGTOs consists of one contracted Gaussian function for each inner-shell and valence atomic orbital.

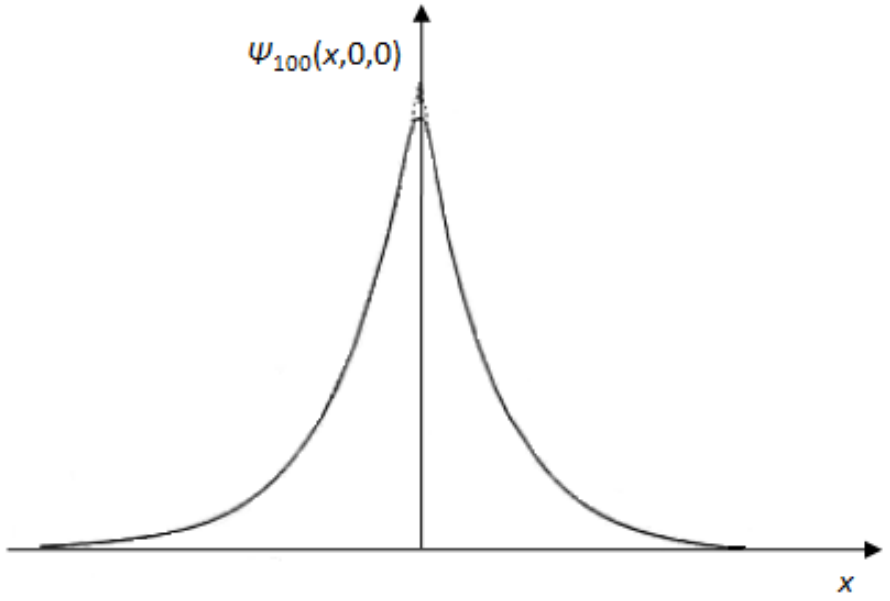

Figure 2.1 A comparison of a four-term GTO expansion and an STO for H 1*s*. The dashed line represents the STO and the solid line is the four-term Gaussian expansion.[98]

For quantitative quantum mechanics calculations, minimal basis sets are not sufficiently accurate. Consequently, the atomic orbitals need to be represented by additional contraction/expansion functions that do not appear in the minimal basis set. This radial flexibility for contraction/expansion is achieved by replacing each GTO from a minimal basis set with two or more Gaussian functions with different radial extents. A *double-zeta basis set* (DZ) is obtained by replacing each GTO by two Gaussian functions, and in a *triple-zeta basis set* (TZ) each GTO is replaced by three Gaussian functions. It is also conventional to split only the valence atomic orbitals; a minimal basis set is used for the inner-shell atomic orbitals and double-zeta, or triple-zeta for the valence atomic orbitals. These basis sets are named *valence double-zeta* (VDZ), *valence triple-zeta* (VTZ), based on the number of GTOs used for each valence atomic orbital.

In standard Pople-style basis set notation, a Gaussian basis set is termed x-xxxG, where the number before the hyphen describes the number of primitive Gaussian functions used for each inner-shell atomic orbital. If, after the hyphen, two numbers are specified, it means that the basis set is VDZ, and the numbers show how many Gaussian primitives are used in each split. For example 3-21G is a basis set that uses 3 Gaussian primitives for each of the core atomic orbitals, and it is VDZ, with a CGTO having 2 Gaussian primitives and 1 additional primitive for each split-valence atomic orbital. If after the hyphen three numbers are specified, a VTZ is used. For example 6-311G basis set has each valence atomic orbital split into three pieces composed of 3 Gaussian primitives, 1 Gaussian primitive, and 1 Gaussian primitive.

Along with this radial flexibility of the basis set, an extra angular flexibility is required to account for the distorted shape of the atomic orbitals caused by formation of molecules. This is achieved by addition of Gaussian functions with high angular momenta, called *polarization* functions. A common example is the *double-zeta plus polarization* (DZP) set that adds three *p* functions on each hydrogen atom and five *d* functions on nonhydrogen atoms to the DZ basis set. In Pople-style notation the polarization functions are shown after the G mark as * symbols. A single * denotes one polarization set added to nonhydrogen atoms only, while ** denote one polarization set added to nonhydrogen atoms, as well as a polarization set added to hydrogen atoms. For example, 6-31G* has *d*-type polarization functions added to nonhydrogen atoms, and because of this, it is also called 6-31G(d). The basis set 6-311G** has five *d*-type polarization functions added to nonhydrogen atoms, as well as three *p*-type polarization functions added to hydrogen atoms, so that it is also known as 6-311G(d,p). The notation with parentheses allows the specification of multiple polarization sets. For example, 6-311G(3df,2p) contains three sets of *d*-type polarization functions plus one set of *f*-type polarization functions added to nonhydrogen atoms, as well as two sets of *p*-type polarization functions added to hydrogen atoms.

For accurate descriptions of atomic orbitals in anions, compounds with lone pairs, and hydrogen-bonded dimers, that present significant electron density at large distances from the nuclei, additional diffuse functions with a very small orbital exponent (typically 0.01 to 0.1) and very large radial extent are required in the expression of the basis set. In Pople-style notation of basis sets, these are denoted as + signs added before the G letter

(for example, 6-311++G**). One + adds four diffuse functions (s, p_x, p_y, p_z) to nonhydrogen atoms only, while ++ adds four diffuse functions (s, p_x, p_y, p_z) to nonhydrogen atoms, as well as one diffuse function (s-type) to hydrogen atoms.

2.1.3 Geometry optimizations

By far the most widely used quantum mechanics program package is Gaussian.[99] This program was developed by Pople *et al*.[100] and has various versions labelled by their release year: Gaussian 94, Gaussian 98, Gaussian 03. Gaussian is a highly versatile electronic structure program. It contains all common *ab initio* methods (such as Hartree-Fock, Møller-Plesset, coupled cluster, density-functional theory etc.) and many semiempirical methods.

The procedure of finding an energetic local minimum in the neighbourhood of the initial assumed geometry is called *geometry optimization* or *energy minimization*. For a molecule with several stable conformations it is necessary to repeat the local minimum search procedure for each conformation in order to locate the *global minimum* that represents the equilibrium geometry of that molecule. Similarly, it is possible to obtain a representation of the *potential energy surface* (PES) for a molecule, which relates the molecular structure and the resultant energy. Often it is necesarry to "freeze" certain internal coordinates during a geometry optimization in order to examine how the PES depends on certain coordinate values. PES represents the potential energy in Schrödinger's equation (2.1) for nuclear positions and it is defined in the $3N$-6 multidimensional space, where N is the number of atoms in the molecule.

2.1.4 Development of force fields from *ab initio* data

Quantum mechanics methods are useful in the development of intramolecular potentials including explicit terms regarding the molecular flexibility, such as the bond stretching, bond angle bending, torsional movement, and out-of-plane bending. These are known as *force fields* because the derivatives of the potential energy function determine the forces on the individual atoms within the molecule. There are many force fields developed for various classes of molecules that are usually applied in *molecular mechanics* calculations. Among these, the most important have been developed for the study of alkanes, polypeptides, proteins, and nucleic acids and are named: AMBER (assisted model building with energy refinement) of Kollman *et al.*,[101] CHARMM (chemistry at Harvard molecular modeling) of Karplus *et al.*,[102] and OPLS (optimized potential for liquid simulation) of Jorgensen *et al*.[103] These force fields are considered *transferable* between molecules and can be employed for the study of a particular molecule of interest.

A more time consuming strategy is to explore the PES using constrained geometry optimizations and then fit the data to known potential forms to obtain the force field. The advantage in this case is that the force field is accurately describing the PES for the molecule of interest. This technique is preferred for the description of complicated molecules that have stretches, bond angles, improper-torsions and dihedrals that cannot be satisfactorily described by AMBER, CHARMM, or OPLS force fields. This is the approach that I used in this thesis for the description of DNB-phenylglycine and

DNB-leucine molecules. The intramolecular potential, U^{intra} is given by the sum of the energetic contributions from bond stretching, angle bending, torsions, and improper torsions:

$$U^{intra} = U^{stretch} + U^{bend} + U^{torsion} + U^{improper} \tag{2.9}$$

The potential energy $U^{stretch}$ of the bond stretching is usually taken in the harmonic-oscillator approximation as a quadratic function of the displacement:

$$U^{stretch} = k_{st}(r - r_e)^2 \tag{2.10}$$

where k_{st} is the stretching force constant, r is the distance between the two atoms, and r_e is the equilibrium bond length. Each k_{st} is determined from a least-squares fit of the configuration energies obtained in *ab initio* calculations for the stretch of a particular bond.

A similar treatment is applied to the bond bending potential U^{bend}. It is also taken as a quadratic function:

$$U^{bend} = k_\theta(\theta - \theta_e)^2 \tag{2.11}$$

where k_θ, θ, and θ_e are the force constant, the bond angle, and the equilibrium angle, respectively.

The out-of-plane bending potential energy terms are important for enforcing the planarity of some bends. For instance, a carbonyl group implies that the oxygen atom, the carbon atom and the other two atoms attached to the central carbon are in the same plane.

The same considerations apply for the planarity at the nitrogen atoms in amides. This out-of-plane correction is usually attained by including improper torsion terms fitted from the *ab initio* data as a quadratic function:

$$U^{improper} = k_{\omega}(\omega - \omega_e)^2 \tag{2.12}$$

where ω is the out-of-plane angle and ω_e is the corresponding equilibrium value. The out-of-plane angle, ω, for an atom D surrounded by three atoms A, B, and C, is defined as the angle between the vectors normal to the two planes DAB and ABC.

The treatment of the torsional movement is very important because an appropriate molecular model system should attain the same flexibility as that obtained in the *ab initio* configurations. In this thesis, a modified Ryckaert-Bellemans[104] potential is adopted for torsions:

$$U^{torsion} = \sum_{j=1}^{N^{torsions}} \sum_{i=0}^{6} c_{ij} \cos^i(\phi_j + \varphi_{ij}) \tag{2.13}$$

where, for the j^{th} torsion, c_{ij} is the coefficient of the i^{th} term, ϕ_j is the dihedral angle, and φ_{ij} is the corresponding phase-shift. If a phase-shift is not required, the simple Ryckaert-Bellemans[104] potential developed in terms of $\cos(\phi)$ can be used instead:

$$U^{torsion} = \sum_{l=0}^{5} c_l \cos^l(\phi) \tag{2.14}$$

where ϕ is the dihedral angle and c_l are constants found from least-squares fits to the *ab initio* energies. Figure 2.2 shows that with appropriate c_l values, the potential (2.14) is a realistic model of the flexible *n*-butane molecule since it emphasizes the global minimum found for the *trans* conformation and the local minima at the *gauche* conformations. However, other potentials can also be considered.

This approach of designing force fields for individual molecules is particularly important for obtaining proper molecular models that are employed in molecular dynamics simulations, completed with a description of the molecular flexibility from the bond stretching, bond angle bending, and torsional behaviour.

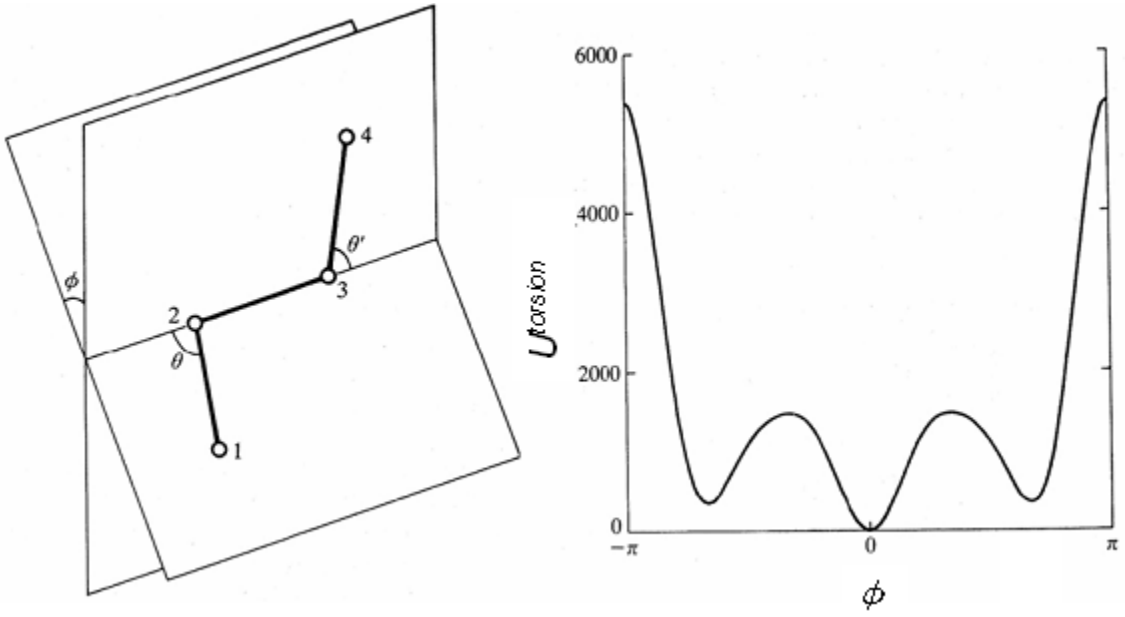

Figure 2.2 Torsional potential for *n*-butane proposed by Ryckaert and Bellemans.[104]

2.1.5 Details on *ab initio* calculations

Geometry optimizations have been performed for PEPU, DNB-phenylglycine, and DNB-leucine molecules using the Gaussian[100] program. Depending on the level of theory, each geometry optimization requires between 7-14 days on a Sun Fire 6800 using 8-12 processors in parallel.

2.1.5.1 *Ab initio* calculations on PEPU

B3LYP/6-31G* *ab initio* optimizations were performed for the identification of the global minimum and local minima configurations, followed by single point calculations at the B3LYP/6-311++G** level of theory to provide a better estimate of the relative energies for the minima. Explicit water molecules were added around the PEPU molecules to test the amount of hydrogen bonding around the urea group. In order to identify the important minimum configurations from the PES, each *ab initio* calculation is repeated 3-5 times starting from different initial configurations. These calculations were performed on slightly modified PEPU molecules. The representation of the triethoxysilyl group that covalently attaches the PEPU molecule to the surface, is somewhat problematic. First, the group is relatively large and "far" from the chiral center. Second, the attachment of the triethoxysilyl to the surface may involve intertether linkages, as well as direct bonds with the surface. In my approach, I replaced the triethoxysilyl group by a hydrogen, making the tether terminated by a methyl group.

These geometry optimizations have been performed for PEPU monomers, dimers, and dimers in the presence of water and ions. In the dimers, the distance between two hydrogens on the terminal methyl is constrained to correspond to a typical[105,106] Si-O-Si distance of 3 Å (Figure 2.3). By doing this the PEPU molecules correctly reproduce the physical constraints of the surface. In particular, greater flexibility in the representation of hydrogen is desirable because of the prevalence of hydrogen bonding in these complexes.

The impact of *implicit* water molecules around the PEPU monomer was explored using the SCI-PCM (self-consistent isodensity-polarized continuum model) method.[107] This is done by surrounding the PEPU by a dielectric continuum of $\varepsilon = 87.3$ Debyes, typical for water, followed by a geometry optimization. I found that the optimized configuration of the solvated molecule was quite similar to that of the isolated monomer. Conversely, it is better to explore the interaction of *explicit* water molecules with the PEPU interface for two reasons. First, only a segment of the PEPU molecule is exposed to solvent. Second, the exploration of the extent of hydrogen bonding between PEPU slabs and the solvent requires explicit solvent molecules. The solvated PEPU dimers were surrounded with 0-4 water molecules and geometry optimizations have been obtained. The results showed that the PEPU molecules like to form strong hydrogen bonds in the urea part of the molecule, in agreement with the molecular dynamics simulations results outlined in Section 4.2.3.

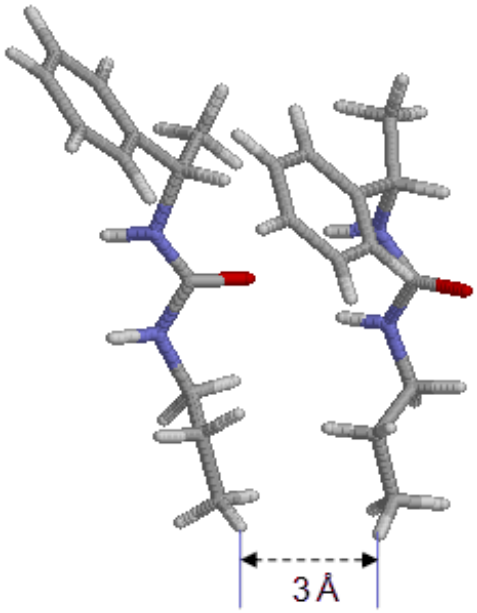

Figure 2.3 Structure of a PEPU dimer with distances between terminal hydrogens constrained to 3Å. The oxygen, nitrogen, carbon, and hydrogen atoms are shown in red, blue, gray, and white, respectively.

2.1.5.2 *Ab initio* calculations on DNB-phenylglycine and DNB-leucine

A comprehensive series of *ab initio* geometry optimizations was undertaken to examine the stable conformations and flexibility of the DNB-phenylglycine and DNB-leucine molecules. All calculations have been carried out using density-functional theory with the B3LYP functional,[97] and the 6-311G** basis set.[108] HF/6-311G**, MP2/6-311G** calculations were also employed to check for the validity of these conformers. My study starts with a full geometry optimization of an isolated selector. Since the tether is not expected to directly impact CSP solvation and chiral

discrimination, I simply replace the γ-propylsilyl group with a single methyl for the *ab initio* calculations (Figure 2.4). From the global minimum configuration, each dihedral torsion was explored in steps of 15-30 degrees over the entire 360 degree range, each bend and improper torsion was investigated in steps of 1 degree around $\pm$ 5 degrees of the global minimum value, and bond lengths were varied in steps of 0.02 Å. From this investigation, several stable conformers have been identified for the DNB-phenylglycine and DNB-leucine molecules, and stretching, bending, torsional, and improper torsional intramolecular potentials have been derived according to the procedure described in Section 2.1.4.

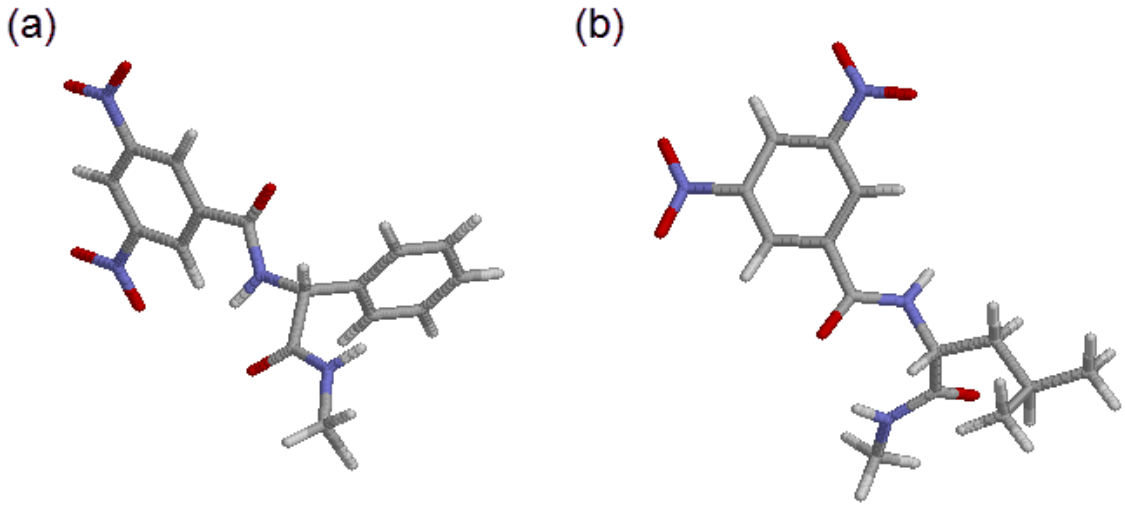

Figure 2.4 Global minimum configurations of DNB-phenylglycine (a) and DNB-leucine (b) molecules as considered in the DFT study. The oxygen, nitrogen, carbon, and hydrogen atoms are shown in red, blue, gray, and white, respectively.

2.2 Computer simulations

In the case of many-particle systems, quantum mechanics approaches are impractical. Instead *classical mechanics* can be applied to compute the equilibrium and transport properties of these systems. Computer simulations have evolved with the development of computers in the last 50 years. The simulations reported in this thesis are based on the *molecular dynamics* (MD) method.

MD is a technique that solves the classical Newtonian equations of motions for atoms and molecules in order to obtain the time evolution of the system. In many respects MD simulations are similar to real experiments. It starts with the selection of an appropriate model system consisting of N particles and then Newton's equations of motions are solved numerically for this system. After equilibration, the actual measurements are performed.

At the simplest level, a system is described by the classical Hamiltonian $H(\mathbf{q}_i, \mathbf{p}_i)$ that represents the total energy as the sum of the kinetic energy $T(\mathbf{q}_i, \mathbf{p}_i) = \sum_i \frac{\mathbf{p}_i^2}{2m_i}$ and the potential energy $V(\mathbf{q}_i)$:

$$H(\mathbf{q}_i, \mathbf{p}_i) = \sum_i \frac{\mathbf{p}_i^2}{2m_i} + H(\mathbf{q}_i) \tag{2.15}$$

where $\mathbf{p}_i$ are the momenta, and m_i are the masses. The Hamiltonian formulation for the equations of motion is symmetric with respect to coordinates and momenta:

$$\dot{\mathbf{q}}_i = \frac{\partial \mathrm{H}}{\partial \mathbf{p}_i}, \qquad \dot{\mathbf{p}}_i = -\frac{\partial \mathrm{H}}{\partial \mathbf{q}_i} \tag{2.16}$$

where $\dot{\mathbf{q}}_i \equiv \frac{d\mathbf{q}_i}{dt}$ are the coordinate derivatives (the velocities $\mathbf{v}_i$), and $\dot{\mathbf{p}}_i \equiv \frac{d\mathbf{p}_i}{dt}$ are the momenta derivatives (the forces $\mathbf{f}_i$). For Cartesian coordinates $\mathbf{r}_i$, Hamilton's equations become:

$$\dot{\mathbf{r}}_i = \frac{\mathbf{p}_i}{m_i}, \qquad \dot{\mathbf{p}}_i = -\nabla_{\mathbf{r}_i} \mathrm{V} = \mathbf{f}_i \tag{2.17}$$

These are 6N first-order differential equations and can also be written as 3N second-order differential equations:

$$m_i \ddot{\mathbf{r}}_i = \mathbf{f}_i \tag{2.18}$$

where $\ddot{\mathbf{r}}_i \equiv \frac{d^2\mathbf{r}_i}{dt^2}$ are the coordinate second derivatives (the accelerations $\mathbf{a}_i$). Equations (2.17) or the alternative (2.18) are solved in MD simulations to compute the center of mass trajectories of the particles in the system. During the simulation, the system is monitored by calculating the temperature and the total energy.

2.2.1 Molecular Dynamics (MD) simulations

A typical MD simulation of atomic particles has five important steps:[109]

1. *Read the simulation parameters*. In this step the important parameters that specify the conditions of the simulation are read: choice of simulation cell, initial temperature, number of particles, density, time step, etc.

2. *Initialization*. At the beginning of the simulation all the particles are assigned initial positions and velocities. In my simulations the initial positions are obtained by placing the particles randomly on a lattice within the simulation cell, and the initial velocities are assigned randomly but consistent with the selected temperature..

3. *Force calculation*. The MD formalism involves the calculation of the forces $\mathbf{f}_i$ acting on the molecules from the potential energy $\mathcal{V}$ using equation (2.18). In computer simulations, this potential energy is usually divided into terms involving the coordinates of individual atoms, pairs, triplets, etc.:

$$\mathcal{V} = \sum_i v_1(r_i) + \sum_i \sum_{j>i} v_2(r_i, r_j) + \sum_i \sum_{j>i} \sum_{k>j)i} v_3(r_i, r_j, r_k) + \ldots \qquad (2.19)$$

In equation (2.19) the first term represents the effect of an external field on the system, and the remaining terms represent the potential energy from the interactions between the particles in the system. The *pairwise approximation* where only the first two terms in equation (2.19) are considered is commonly made. This is done for practical reasons and because the effects of three-body and multi-body interactions

can be partially included by defining an *effective* pair potential.[110] The potential energy is then given by:

$$\mathcal{V} \approx \sum_i v_1(r_i) + \sum_i \sum_{j>i} v_2^{eff}(r_i, r_j) \tag{2.20}$$

A simple pair potential commonly used in computer simulations is the Lennard-Jones potential which can be written in two equivalent forms:

$$v^{LJ}(r_{ij}) = 4\varepsilon_{ij}\left(\left(\frac{\sigma_{ij}}{r_{ij}}\right)^{12} - \left(\frac{\sigma_{ij}}{r_{ij}}\right)^{6}\right) = \varepsilon_{ij}\left(\left(\frac{r_{ij}^*}{r_{ij}}\right)^{12} - 2\left(\frac{r_{ij}^*}{r_{ij}}\right)^{6}\right) \tag{2.21}$$

where r_{ij} is the distance between particles i and j, ε_{ij} is an energetic term representing the potential at the minimum in the interaction curve, σ_{ij} is a parameter that gives the distance at which the potential is zero, and the alternative parameter r_{ij}* gives the distance at the minimum value of the potential (see Figure 2.5). The Lennard-Jones potential has an attractive tail of the form $-1/r_{ij}^6$, an energetically negative well depth ε_{ij}, and a steeply rising repulsive part at distances smaller than the parameter σ_{ij}.

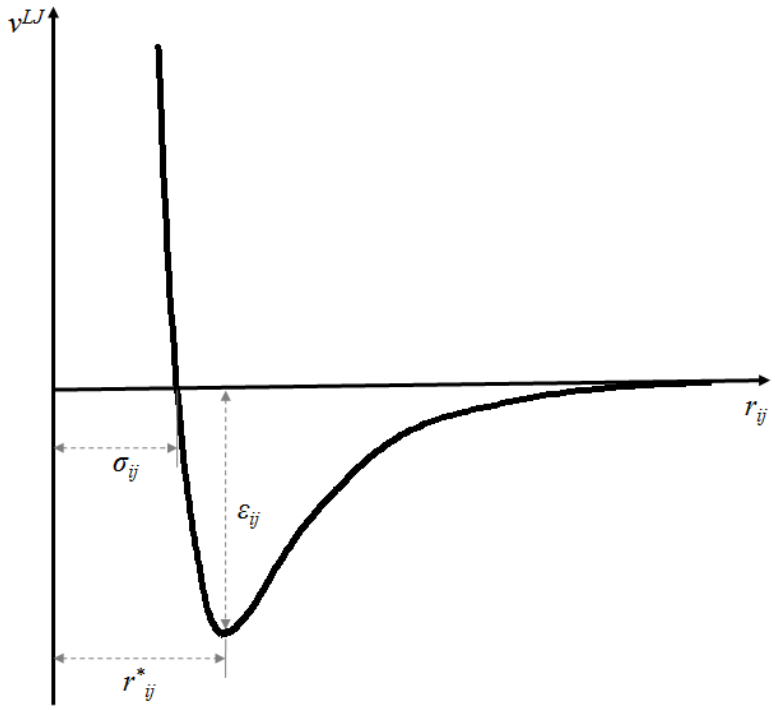

Figure 2.5 Typical Lennard-Jones pair potential as a function of interatomic distances.

4. *Integrate the equations of motion*. After all forces between particles have been evaluated, the next step is the integration of Newton's equation of motion (2.18). By writing a Taylor expansion around the coordinate of a particle, one gets:

$$\mathbf{r}(t + \Delta t) = \mathbf{r}(t) + \mathbf{v}(t)\Delta t + \tfrac{1}{2}\mathbf{a}(t)\,\Delta t^2 + \ldots, \text{ and}$$

$$\mathbf{r}(t - \Delta t) = \mathbf{r}(t) - \mathbf{v}(t)\Delta t + \tfrac{1}{2}\mathbf{a}(t)\,\Delta t^2 - \ldots \qquad (2.22)$$

where Δt is the time step, $\mathbf{r}(t)$, $\mathbf{v}(t)$, and $\mathbf{a}(t)$ are the positions, velocities, and accelerations at the time t, respectively. Summing equations (2.22) and neglecting the higher-order derivative terms establishes a relationship for advancing the positions:

$$\mathbf{r}(t + \Delta t) = 2\mathbf{r}(t) - \mathbf{r}(t - \Delta t) + \Delta t^2 \mathbf{a}(t) \tag{2.23}$$

This equation gives the *Verlet algorithm* of estimating the new positions $\mathbf{r}(t + \Delta t)$ from the positions at the previous steps, $\mathbf{r}(t)$ and $\mathbf{r}(t - \Delta t)$. The error in this algorithm is of the order Δt^4. It is important to note that the velocities are not required for the calculation of the new positions, but they are useful for the estimation of the kinetic energy. In the Verlet algorithm, the velocities are determined from the known positions, with an accuracy of the order Δt^2:

$$\mathbf{v}(t) = \frac{\mathbf{r}(t + \Delta t) - \mathbf{r}(t - \Delta t)}{2\Delta t} \tag{2.24}$$

Several Verlet-equivalent algorithms, such as the *Leap-frog algorithm* and the *Velocity-Verlet algorithm*, have been derived from the basic Verlet scheme and have the velocities appearing explicitly in the equation for advancing positions.

An important characteristic of the Verlet algorithm is that it is reversible in time, since Newton's equations of motion are time reversible. That is, future and past phase space coordinates play a symmetric role in the algorithm. Another characteristic is the energy conservation. It has been observed that all Verlet-style algorithms have only moderate short-time energy conservation, but very good long-time energy conservation.[109] If short-time energy conservation is essential, other more sophisticated integration schemes, such as the *predictor-corrector algorithms*, can be used. These tend to have better short-time energy conservation, but they often have overall energy drift for long times and they are not time-reversible.

5. *Evaluate the system properties*. In the last step of the MD simulation, the measurable quantities of the many-particle system are averaged and, when possible, compared with experimental data. There are many observable quantities that can be evaluated from MD simulations: thermodynamic properties (such as temperature, pressure, heat capacity), dynamic properties (such as diffusion, autocorrelation functions), and functions that describe the local structure of the fluid (such as radial distribution functions, density profiles).

The MD simulations are based on the formalism that was summarized in these five steps. However, there are other important features regarding the implementation of this formalism that must be discussed for a better understanding of molecular simulations. In the following sections of this chapter, considerations regarding the simulation cell, various ensembles, treatment of long-ranged forces, and surface flexibility will be addressed.

2.2.2 Periodic boundary conditions

Computer simulations are usually performed on a relatively small number of particles (less than 2000) because of limitations in data storage on the host computer and the speed of execution of the program. These particles are confined in a *simulation cell* that usually has a cubic shape because of its geometric simplicity. However, sometimes the simulation cell is chosen as a rectangular prism, rhombic dodecahedron, truncated octahedron, or another space-filling polyhedron shape.[110]

Because of the limited number of particles in the simulation cell, in order to obtain properties of the bulk phase, it is customary to choose *periodic boundary conditions* that reproduce the presence of an infinite bulk surrounding the N-particle system. This is done by replicating the simulation cell throughout the space to form an infinite lattice. During the simulation, if a molecule has a certain trajectory within the original cell, its periodic image from adjacent cells moves exactly in the same way, and if a molecule leaves a cell by crossing a boundary, one of its periodic images enters through the opposite face. This is shown schematically in Figure 2.6, a two-dimensional system consisting of six particles in each simulation box. By the use of periodic boundary conditions, all the particles from the simulation cell have the same surroundings and the particles close to the simulation cell boundary have a similar behaviour as the particles located in the middle of the simulation cell. Although it is an effective method to simulate homogeneous bulk systems, there are some limitations. Because of the periodicity determined by the side-length of the simulation cell L, only those long-ranged fluctuations are allowed that have a wavelength smaller than L. Therefore, it would be impractical to simulate a liquid close to the gas-liquid critical point for example, because the range of critical fluctuations is macroscopic.

In principle each particle should interact with all other particles in the simulation cell, and all particles from the other cells, including its own periodic image. In these conditions, there are an infinite number of terms to be evaluated in the potential energy calculation, and, obviously, this is impossible to accomplish in practice. For a short-range potential, one might restrict this summation to only the closest periodic images of the

other N-1 particles. This is known as the *minimum image convention* and is shown in Figure 2.6 as the square surrounding particle 1. This approximation is commonly used, including the first simulation by Metropolis *et al*. in 1953.[111] However, for a big system of molecules (N > 1000) it is still difficult to evaluate all the terms of the potential energy due to pairwise interactions, and a further approximation is required. Since in the short-ranged potentials the most important contribution comes from the particles that are close to the particle of interest, it is customary to apply a *spherical cutoff*. This means that the potential $v_2(r_{ij})$ is zero for all the particles with $r_{ij} > r_{cut}$ and it is evaluated only for the particles with $r_{ij} \leq r_{cut}$ where r_{cut} is the cutoff distance. In Figure 2.6 the dashed circle represents a cutoff, and in this case only particle 2 and the images of particles 3 and 5 are considered for the calculation of the pairwise potential energy. The cutoff distance must be smaller than ½ L, for consistency with the minimum image representation. [110]

However, the use of a spherical cutoff implies that at the cutoff radius a discontinuity appears in the evaluation of the intermolecular potential. To overcome this, it is customary to truncate and shift the potential, such that it is zero at the cutoff:

$$v^{truncated\text{-}shifted}(r_{ij}) = \begin{cases} v^{LJ}(r_{ij}) - v^{LJ}(r_{cut}) & r_{ij} \leq r_{cut} \\ 0 & r_{ij} > r_{cut} \end{cases} \qquad (2.25)$$

The main advantage of using a truncated-shifted potential is that the intermolecular forces are always finite and therefore easy to handle in the algorithms that integrate the equations of motion.[109]

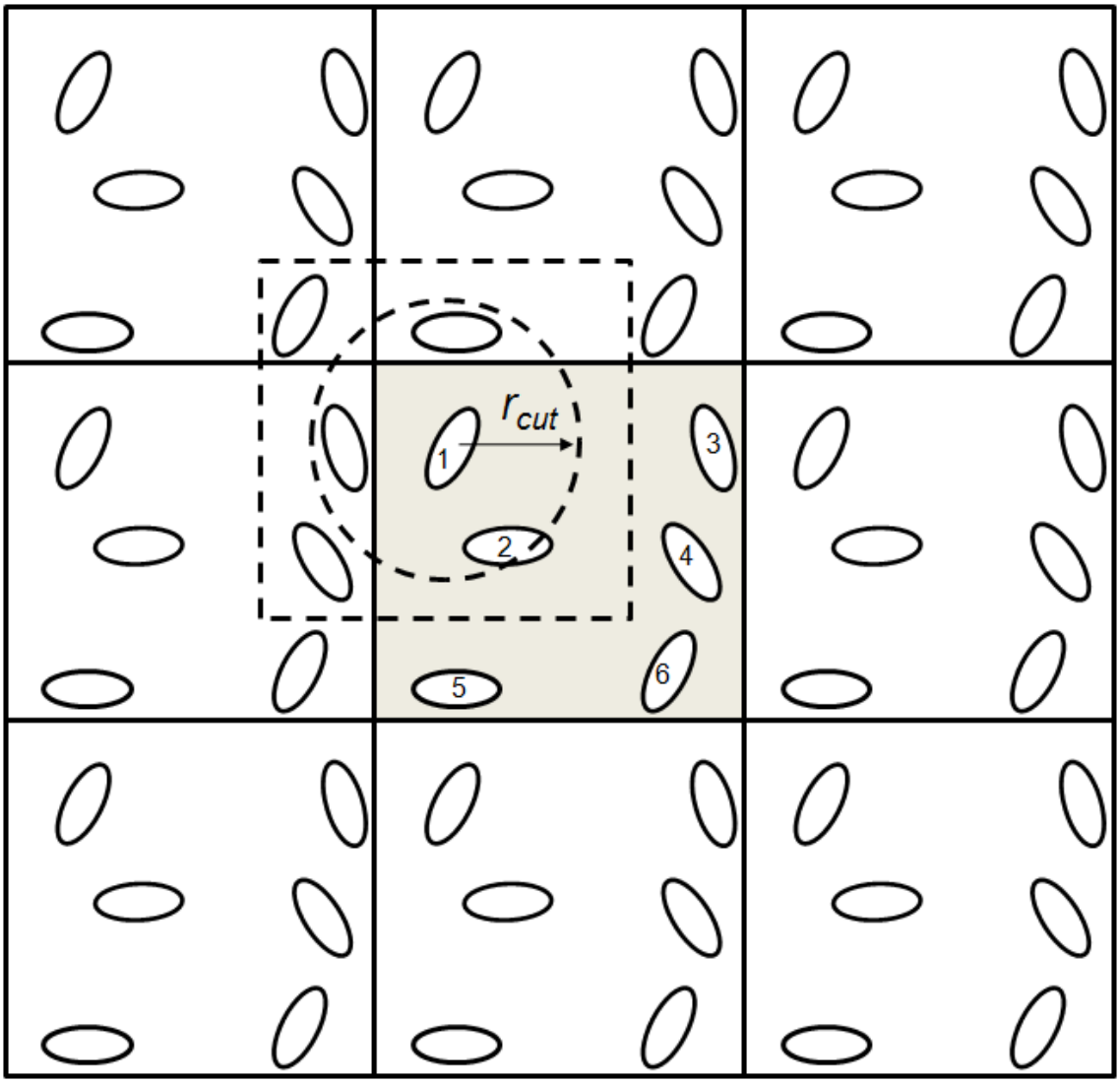

Figure 2.6 Schematic representation of periodic boundary conditions in a two-dimensional system. The dash square represents the minimum image representation and the dash circle shows a spherical cutoff.[110]

2.2.3 Molecular systems

Atomic particles can be easily handled in MD by using the formalism described in Section 2.2.1. However, when molecules need to be introduced in MD simulations, the situation is much more complicated. In a simple approximation, the molecules can be considered as rigid or semi-rigid units, with fixed bond lengths and, sometimes, fixed bond angles and dihedral angles. In this case, the equations of motion are applied to translation and rotation of the centre of mass. However, for larger molecules, it might be necessary to consider more flexibility, in particular the torsional movement about the bonds, which gives rise to conformational interconversion. For example in long-chain alkanes this flexibility cannot be neglected since the energetic requirement for a torsional movement is comparable to normal thermal energies. In the case of *n*-butane, Ryckaert and Bellemans derived a torsional potential given by equation (2.14) and illustrated in Figure 2.2. In this case, the potential $U^{torsion}(\phi)$ is added as an extra term in the total Hamiltonian of the system. For a better description of a system's flexibility, it is necessary to consider the stretching of the interatomic bonds, the bending of the angle between bonds, as well as the torsional movement and improper torsions. These can be expressed as extra intramolecular potential energy terms that can be derived from *ab initio* calculations, as shown in Section 2.1.4.

Often in MD simulations, there are some stretches, bends, and torsions considered to be flexible, and some considered to be rigid. In this case, it is required to introduce *constraint dynamics*, in which certain arbitrarily selected degrees of freedom (such as

bonds, angles, and torsions) are constrained, while others remain free to evolve under the influence of intermolecular and intramolecular forces. This must be considered in the Newtonian equations of motion (2.18) as an extra constraint force $\mathbf{g}_i$:

$$m_i \ddot{\mathbf{r}}_i = \mathbf{f}_i + \mathbf{g}_i \tag{2.26}$$

This constrained force is easily calculated by considering an undertermined multiplier λ_i that describes the constraint:

$$\mathbf{g}_i = -\lambda_i \mathbf{r}_i \tag{2.27}$$

Consequently, the equation for advancing the position in the Verlet algorithm (2.23) has an extra term:

$$\mathbf{r}_i^c(t+\Delta t) = 2\mathbf{r}_i^u(t) - \mathbf{r}_i^u(t-\Delta t) + \Delta t^2[\mathbf{f}_i^u(t)/m_i - \lambda_i \mathbf{r}_i(t)/m_i] = \mathbf{r}_i^u(t+\Delta t) - \Delta t^2 \lambda_i \mathbf{r}_i(t)/m_i \tag{2.28}$$

where $\mathbf{r}_i^c$ is the new position that includes the constraint and $\mathbf{r}_i^u$ is the old position without the constraint. The best approach is to go through the constraints one by one, adjusting the coordinates at each time step in order to satisfy each in turn within a certain tolerance value. This procedure is called the SHAKE algorithm[110] and has the advantage that it can be easily iterated for all the constraints. Thus, the coordinates are easily obtained for each time step in the Verlet integration scheme. Since the Verlet algorithm does not deal directly with the velocities, a separate algorithm is required to obtain the velocities at each time step in a constrained system. This algorithm is called RATTLE.[110]

Constraint dynamics as typified by SHAKE and RATTLE algorithms provide a simple approach, easily adapted to different molecular systems. They also allow many choices of where to apply constraints: it is generally considered that it is important to constrain bond lengths, but it is best to leave the molecule to have bending and torsional motions according to the appropriate potentials.[109]

2.2.4 Treatment of long-range forces: the Ewald summation

In MD simulations the particles have partial charges that cause long-ranged electrostatic forces. They represent a serious problem, since their range is larger than the cutoff distance r_{cut} for the evaluation of the intermolecular interactions, usually taken as the half-length of the simulation cell. Various mathematical techniques have been developed to handle the electrostatic long-range forces, such as the Ewald method,[114] the Particle-Particle/Particle Mesh (PPPM) method,[112] and the reaction field method.[113] Among these, the *Ewald method* is by far the most popular[110] and it is briefly described next.

In a cubic cell of length L containing N charged atoms, the Coulomb contribution to the potential energy of the system in the minimum image convention is:[109]

$$U_{Coul} = \frac{1}{2}\sum_{i=1}^{N} z_i \Phi(r_i) \tag{2.29}$$

where z_i is the charge on ion i and $\Phi(r_i)$ is the electrostatic potential at this position that is calculated as:

$$\Phi(r_i) = \sum_{j=1}^{N} \sum_{\mathbf{n}}{}' \frac{z_j}{|\mathbf{r}_{ij} + \mathbf{n}L|} \tag{2.30}$$

where z_j is the charge on ion j, $\mathbf{r}_{ij}$ is the position vector joining the ions i and j, and the sum over $\mathbf{n}$ is the sum over all simple periodic cells, $\mathbf{n}L = (n_xL, n_yL, n_zL)$ with n_x, n_y, n_z integers, except for the term $i = j$, when $\mathbf{n} = 0$ (indicated by the prime on the summation). Unfortunately, equation (2.30) cannot be employed for the calculation of the electrostatic energy because of convergence problems.

In the Ewald method[114] the solution to the above problem comes from considering that each charge z_i is surrounded by a diffuse charge distribution of opposite sign, such that the total charge of this electronic cloud exactly cancels z_i. In these conditions, the screened distributions are now short-ranged and once the electrostatic potential is determined for this charge distribution, the effect of the screening charge can be subtracted. This is shown schematically in Figure 2.7.

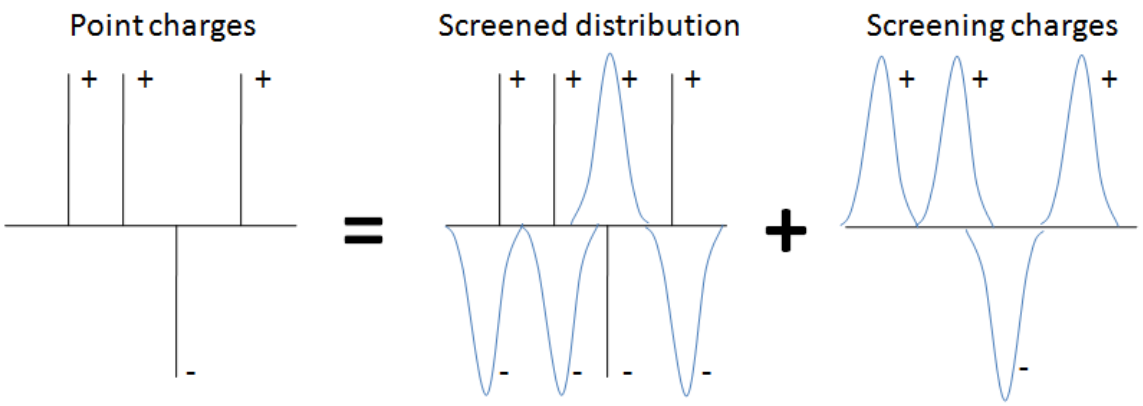

Figure 2.7 The charge distribution in the Ewald method.

Based on these considerations, the potential is obtained as a sum of three terms in the Ewald method. The first term represents the screening distribution potential. It is calculated as simply the sum of charges in the minimum image convention and it is known as the *complementary error function term* of the Ewald summation:

$$U_{sr} = \frac{1}{2}\sum_{i\neq j}^{N}\frac{z_i z_j}{\mathbf{r}_{ij}} erfc(\sqrt{\alpha}\mathbf{r}_{ij}) \tag{2.31}$$

where $erfc(x) \equiv 1 - \frac{2}{\sqrt{\pi}}\int_{x}^{\infty} e^{-u^2} du$ is the complementary error function, and the parameter α determines the width of the Gaussian screened distribution. The complementary error function has the property of going rapidly to zero for a large argument. For a suitable choice of the converge parameter α, this term can be restricted to the central simulation cell, as shown in equation (2.31).

The second term of the Ewald summation represents the contribution of the screening charge distribution of Gaussians that needs to be subtracted from the final potential energy. This is calculated considering the Fourier transform of the charge distribution in the reciprocal space defined by the vectors $\mathbf{k} = \left(\frac{2\pi n_x}{L_x}, \frac{2\pi n_y}{L_y}, \frac{2\pi n_z}{L_z} \right)$.

Thus, the screening charge distribution is calculated as the sum of these reciprocal vectors $\mathbf{k}$ and it is called *reciprocal space term* of the Ewald summation:

$$U_1 = \frac{1}{2\pi V} \sum_{\mathbf{k} \neq 0} \sum_{i,j=1}^{N} \frac{4\pi^2 z_i z_j}{\mathbf{k}^2} \cos(\mathbf{k} \cdot \mathbf{r}_{ij}) \exp\left(-\frac{\mathbf{k}^2}{4\alpha} \right) \tag{2.32}$$

where $V = L^3$ is the volume of the cubic cell. This is an important correction that needs to be subtracted from the final potential energy.

The third term is a small correction term that is introduced to account for the fact that an ion cannot interact with itself. This value is obtained from the equation (2.31) in the limit of $\mathbf{r}_{ii} = 0$ and it is called the *self-interaction term*:

$$U_{self} = \left(\frac{\alpha}{\pi} \right)^{1/2} \sum_{i=1}^{N} z_i^2 \tag{2.33}$$

Considering the equations (2.31), (2.32), and (2.33), in the Ewald method the potential energy of the system is calculated as $U = U_{sr} + U_1 - U_{self}$, or more explicitly:[115]

$$U = \frac{1}{2}\sum_{i \neq j}^{N} \frac{z_i z_j}{\mathbf{r}_{ij}} erfc(\sqrt{\alpha}\mathbf{r}_{ij}) + \frac{1}{2\pi V}\sum_{\mathbf{k}\neq 0}\sum_{i,j=1}^{N} \frac{4\pi^2 z_i z_j}{\mathbf{k}^2} \cos(\mathbf{k}\cdot\mathbf{r}_{ij}) \exp\left(-\frac{\mathbf{k}^2}{4\alpha}\right) - \left(\frac{\alpha}{\pi}\right)^{1/2} \sum_{i=1}^{N} z_i^2 \tag{2.34}$$

However, for a correct evaluation, a suitable value should be chosen for the convergence parameter α. This parameter is system-dependent and in practice it is common to choose a value for which the complementary error function term has the same effective range as the short range contributions. Figure 2.8 shows a plot of the potential energy as a function of the product αr_{cut} for a CO_2 system. The graph has three regions: an initial sharp increase in the potential energy, followed by a plateau, and a sharp decrease. For small values of α, the range of the real space contributions to the potential energy is the greatest and therefore the r_{cut} value is likely too small for an appropriate account in the potential energy. For large values of α, the sum in the reciprocal space is long ranged and gives a small contribution for the potential energy determining a slow convergence of the summation. The appropriate Coulomb energy is obtained for α values that give the energy at the plateau.[115]

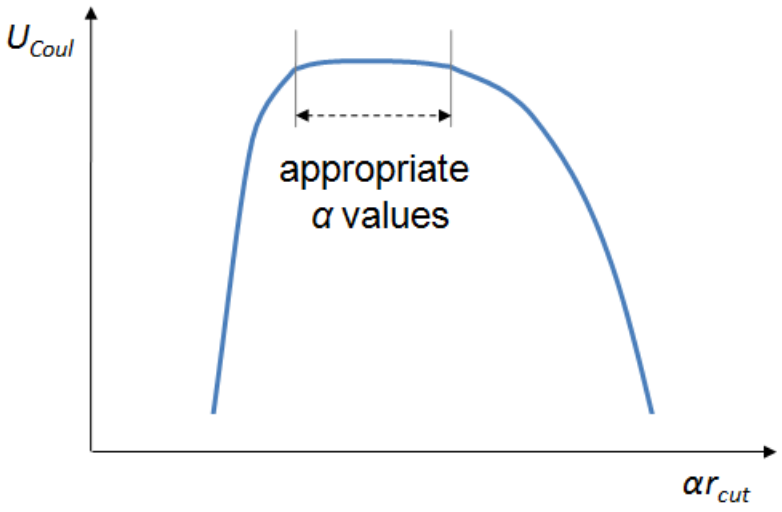

Figure 2.8 Plot of the potential energy determined in the Ewald method as a function of the convergence parameter α.

The equation (2.34) can be used to evaluate the electrostatic energy of the system in a cubic simulation cell. For a non-cubic cell, an extra shape-dependent term, $J(\mathbf{M},P)$ that depends on the summation geometry P, and on the total dipole moment of the unit simulation cell $\mathbf{M} = \sum_{i=1}^{N} z_i \mathbf{r}_i$ is required. Of particular importance is the rectangular prism cell elongated on the z axis; in this case the shape dependent correction to the Ewald sum is:[116]

$$J(\mathbf{M},P) = \frac{2\pi}{V} M_z^2 \tag{2.35}$$

where M_z is the z component of the total dipole moment of the simulation cell, and V is the volume of the simulation cell.

2.2.5 MD at constant temperature: the Nosé-Hoover thermostat

In the MD technique discussed in Section 2.2.1 the time evolution of a system of N particles in a volume V is done based on the conservation of the total energy E (the Hamiltonian $\mathcal{H}(q_i, p_i)$). This implies that the averages obtained in the conventional MD technique are equivalent to ensemble averages in the *microcanonical* (constant (N,V,E)) ensemble. However, if the MD calculation is required to simulate a real system, these typically do not take place with conservation of the total energy E, rather they are performed in constant-temperature T and, often, constant-pressure P, conditions. Since the number of molecules N from the simulation cell is much smaller than Avogadro's number N_A, constant (N,V,E) averages obtained do not imply that the temperature T is constant too. So that it becomes important to derive methods that give MD averages in other ensembles like the canonical ensemble (constant (N,V,T)) or the isothermal-isobaric ensemble (constant (N,P,T)). Of particular importance is the canonical ensemble, where the temperature T is chosen as a control parameter instead of the total energy E. The best way of obtaining constant temperature averages is based on the Hamiltonian introduced by Nosé[117] and the convenient real-time equations of motion proposed by Hoover, [118] which form the Nosé-Hoover thermostat. The implementation of this thermostat is discussed below.

The Nosé-Hoover thermostat is based on a reformulation of the equations of motion (2.17). Nosé introduced an additional degree of freedom *s* that allows the total energy to fluctuate. The basic equations of motion are:

$$\dot{\mathbf{r}}_i = \frac{\mathbf{p}_i}{m_i}, \quad \dot{\mathbf{p}}_i = -\frac{\partial \boldsymbol{\mathcal{V}}(\mathbf{r})}{\partial \mathbf{r}_i} - \xi \mathbf{p}_i, \quad \frac{d\xi}{dt} = \left(\sum_i \frac{\mathbf{p}_i^2}{m_i} - g k_B T \right) / Q, \quad \frac{\dot{s}}{s} = \frac{d \ln s}{dt} = \xi \tag{2.36}$$

where Q is a fictional mass parameter, $g = 3N$ is the number of degrees of freedom, k_B is Boltzmann's constant, and $\xi \equiv \frac{\dot{s}}{s}$ is a frictional coefficient.

The first two equations are Hamilton's equations of motion (2.17) with a frictional force. However, ξ is not a constant frictional parameter; it varies according to the third equation. The first three equations form a closed set and the time evolution in the phase space (r, p, ξ) is uniquely determined from these equations, the fourth being redundant. The last equation is only used as a diagnostic tool to check the conservation of the quantity $\boldsymbol{\mathcal{H}}_{Nose'}$ given by:

$$\boldsymbol{\mathcal{H}}_{Nose'} = \sum_{i=1}^{N} \frac{p_i^2}{2 m_i s^2} + \boldsymbol{\mathcal{V}}(r) + \frac{p_s^2}{2Q} + g k_B T \ln s \tag{2.37}$$

An important observation is that $\boldsymbol{\mathcal{H}}_{Nose'}$ is not a true Hamiltonian, since the equations of motion (2.36) cannot be derived from it. However, its conservation determines if the constant-temperature simulation is performed correctly.

It is relatively easy to show that the average of a quantity A that depends on the momenta and the coordinates reduces to the canonical average when the Nosé-Hoover thermostat is applied:[109]

$$\left\langle A(\mathsf{p}/s,\mathsf{r})\right\rangle_{Nose'-Hoover} = \left\langle A(\mathsf{p}/s,\mathsf{r})\right\rangle_{(N,V,T)} \tag{2.38}$$

2.2.6 Details on MD simulations

Lengthy MD simulations were performed for the PEPU, DNB-phenylglycine and DNB-leucine surfaces in the presence of several solvents and mixtures of solvents. Two Nosé-Hoover thermostats[117,118] are used to generate canonical (N,V,T) properties at 298 K. Independent translational and rotational thermostats are employed and the conserved quantity is written as:

$$\mathsf{H}_{NH} = E^{full} + \frac{Q_t}{2}\xi_t^{\,2} + g_t k_B T \ln s_t + \frac{Q_r}{2}\xi_r^{\,2} + g_r k_B T \ln s_r \tag{2.39}$$

where E^{full} is the total energy and the quantities marked with t and r are for translation and rotation, respectively. The two additional variables, s_t for translation and s_r for rotation, have masses of Q_t and Q_r,[109] respectively, and g_t and g_r are the corresponding degrees of freedom. The equations of motion are integrated following the algorithm of Martyna *et al*.[119] to preserve the RATTLED positions and velocities.

The important details of the MD simulations are emphasized below, separately for PEPU simulations and DNB-phenylglycine/DNB-leucine simulations. All simulations are performed with the MDMC program.[120]

2.2.6.1 MD simulations of PEPU

The solvation of the PEPU interface is examined for 36 binary solvent mixtures. These consist of methanol/water, 1-propanol/water, 2-propanol/water and methanol/ 1-propanol mixtures with the alcohol mole fraction ranging from 0 to 1.0. The comparison between these alcohols is interesting because they have virtually identical gas phase dipole moments but their dielectric constants vary from 32.6 for methanol to 18.3 for 2-propanol.[121]

Molecular dynamics simulations of the chiral interface require an atomic level description of the PEPU molecules. A realistic model was constructed based on a series of B3LYP/6-31G* optimization calculations using the Gaussian program as described in Section 2.1.5. Briefly, the calculations indicated that neighboring PEPU molecules align themselves to form energetically favorable hydrogen bonds between the urea groups. Based on these results and with the mesostructure of the silicon surface in mind, a model CSP consisting of a closely-packed, regular monolayer of PEPU molecules was constructed. (Figure 2.9) Each PEPU molecule is charge neutral although the constituent atoms bear partial charges and the dipole moment is 3.3 D. Since the PEPU molecules are closely spaced and interconnected with hydrogen bonds, the model surface is kept rigid throughout the simulations. The solvent accessible portion of the surface consists of a regular array of aromatic rings, each ring being the top-most segment of a PEPU molecule. The polar urea segment is directly below the aromatic group, rendering the nature of the full surface complex: hydrophobic groups directly exposed to solvent and

polar groups further away. The PEPU monolayer is placed above two layers of silicon with a silicon-silicon distance of 3 Å. Full details of the PEPU model, as employed in the simulations, are given in Section 4.2.

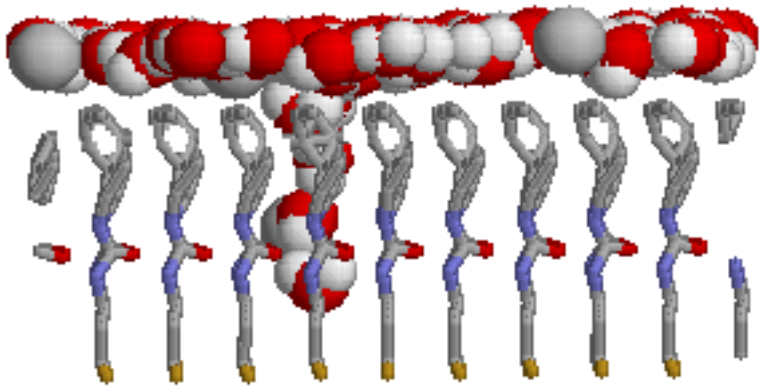

Figure 2.9 Sideview of the PEPU surface interacting with a 90:10 water/methanol solvent mixture. The interface has a cross-shaped imperfection in the middle where the water molecules like to form H-bonds with the urea groups. The oxygen, nitrogen, hydrogen, alkyl carbon, and silicon atoms are indicated in red, blue, white, grey, and gold, respectively.

Representations of water and three alcohols are required in the simulations. The three-point F3C model of water[122] was chosen. This non-polarizable flexible model has been used in recent years, notably for biomolecular simulations,[123,124] but it has also been employed to study methanol/water mixtures[125,126,127] and for investigation of Au-water interfaces.[128,129] The F3C model compares favorably with other models, as highlighted by

two recent and extensive comparisons between water models, for bulk properties[130] and for solvated biomolecules.[131] For the alcohols, it is important to use transferable models with functional forms paralleling the representation of water. The TraPPE-UA (transferable potential for phase equilibria-united atoms) alcohol models developed by Chen *et al*.[132] were chosen. The TraPPE-UA model has been extensively tested for phase-equilibria (vapor-liquid coexistence curves) and fluid structure.[132] In addition, this model has been used in recent simulations of alcohol/water mixtures.[133,134] In preliminary simulations of the PEPU interface, I allowed bending and torsional motion in the solvent. An analysis of the results showed that bending motion was limited but that torsional degrees of freedom are particularly important in understanding the molecular orientation of the alcohols at the PEPU surface. Consequently, bond lengths and angles were kept fixed in the subsequent simulations but torsional motion was allowed.

The full simulation cell is a rectangular prism and includes *two* well-separated surfaces, as is often done[135] for simulations of interfaces. The surfaces, including the underlying silicon atoms, are roughly 14.6 Å thick and are positioned perpendicular to the z-axis of the cell. The inter-surface distance depends on the fluid density and the number of solvent molecules included in the simulation. The simulation cell also includes empty space, above and below the surfaces, to eliminate any interactions between the surface-fluid-surface periodic images. The dimensions of the full rectangular prism cell are 30 Å x 30 Å x 360 Å for all water/alcohol simulations. A slightly more elongated cell is used for the methanol/1-propanol simulations: 30 Å x 30 Å x 400 Å. With these dimensions, the simulation cells are 12-13 times longer in the *z*

direction than along the x and y-axes. In contrast, the intersurface distance is 2-4 times the side-length of the cell. Ewald[114] summations, for a cell replicated in 3D, are used to treat the long-ranged Coulombic forces between charged sites. All PEPU results from Section 4.3 correspond to a position space cutoff of αL_x=7.175, and a momentum space cutoff of $k^2 = 27.0/L_x^2$.

The simulations are performed at 298 K and at the experimental densities[136] (see table 2.1 for details). Each MD simulation follows the evolution of the interface for 100000 time steps, with each step corresponding to 0.25 fs. Equilibration of the fluid occurs within the first 20000 time steps, and statistics are compiled for the remaining 80000 steps. For each of the four solvent mixtures, 9 compositions are considered, giving a total of 36 interfacial fluids. Between the surfaces, 1000 solvent molecules are included in the simulations. This relatively large number is required to ensure the accuracy of the surface distribution of molecules. I require that the distance between the center of the simulation cell and the topmost PEPU atom exceeds four solvent diameters. In this way, molecules at the center of the cell are "far" from either surface. The results presented for each fluid summarize five independent simulations, with two interfaces per simulation, for a total of 10 interfaces for water, methanol, and each binary solvent.

Table 2.1 Details of the PEPU simulations. The experimental densities,[136] the number distribution for each mixed solvent, and inter-surface distance of the simulation cell are given. Each interface is 900 $Å^2$ with 100 PEPU molecules. For methanol/1-propanol mixtures, methanol mass fractions and mole ratios are tabulated in the 3rd and 4th columns, respectively.

Simulation	Total density (g/cm^3)	Water mass fraction (%)	Water mole ratio	Distance between surfaces(Å)
Water/methanol mixtures				
1WM	0.97968	90	0.941	37.566
2WM	0.96352	80	0.877	39.892
3WM	0.94718	70	0.806	42.482
4WM	0.9291	60	0.727	45.454
5WM	0.90976	50	0.64	48.858
6WM	0.88818	40	0.543	52.84
7WM	0.86436	30	0.433	57.532
8WM	0.83974	20	0.308	63.002
9WM	0.81268	10	0.165	69.58
Water/1-propanol mixtures				
1W1P	0.98507	90	0.968	38.368
2W1P	0.96963	80	0.93	41.946
3W1P	0.9503	70	0.886	46.36
4W1P	0.9296	60	0.833	51.748
5W1P	0.90877	50	0.769	58.36
6W1P	0.88837	40	0.69	66.602
7W1P	0.86793	30	0.588	77.19
8W1P	0.84753	20	0.455	91.244
9W1P	0.8267	10	0.27	110.802
Water/2-propanol mixtures				
1W2P	0.9807	90	0.968	38.53
2W2P	0.96725	80	0.93	42.044
3W2P	0.9483	70	0.886	46.454
4W2P	0.9267	60	0.833	51.904
5W2P	0.90295	50	0.769	58.722
6W2P	0.87885	40	0.69	67.3
7W2P	0.85475	30	0.588	78.348
8W2P	0.83075	20	0.455	93.044
9W2P	0.80625	10	0.27	113.558
Methanol/1-propanol mixtures				
1M1P	0.80582	11.97	0.203	126.628
2M1P	0.80466	21.05	0.333	118.436
3M1P	0.80325	31.88	0.467	110.002
4M1P	0.80215	40.38	0.56	104.21
5M1P	0.80104	49.71	0.65	98.532
6M1P	0.80005	59.1	0.73	93.42
7M1P	0.79936	65.37	0.78	90.308
8M1P	0.79788	79.72	0.881	83.934
9M1P	0.79692	90.12	0.945	79.862

The procedure for generating an initial configuration consists of the following steps. First, an excess of solvent molecules (1372) are placed on a rectangular prism lattice, then molecules are removed at random, until 1000 remain at the mole fraction of interest. These remaining molecules are assigned random orientations. After that, the simulation cell is expanded (in 5% increments of the boxlength) until strong overlaps are removed (average potential energy is less than 1.0 in reduced units). The recompression of the simulation cell includes Monte Carlo cycles, where a cycle consists of 10000 attempted moves (translation and rotation) at an elevated temperature of 450 K. Specifically, Monte Carlo cycles are performed until two consecutive cycles predict potential energies within 8% of each other. The simulation cell is then compressed (boxlength is reduced by 5%) and the Monte Carlo cycles are repeated until two consecutive potential energies are again within 8%. The compression-plus-MC iterative cycle is completed when the desired density is recovered, provided a minimum of 25 MC cycles have been performed. Then the molecules are assigned random linear velocities and angular velocities, consistent with the temperature of interest (298K). This elaborate initialization procedure is time consuming, but the use of random numbers throughout ensures that initial configurations are highly distinct.

To explore the details of the solvent structure near the PEPU interface, molecules within 5 Å of the top-most PEPU atom, on either surface, were counted throughout the collection period of the simulation, at 20 iteration intervals. The atomic positions for each of these molecules were recorded to provide information on molecular orientation and hydrogen bonding at the surface. For comparison, atomic positions are also collected

for molecules located within 5 Å of the center of the simulation cell. From this data, density profiles, snapshots, molecular distributions and orientations, and hydrogen bonding at the surface are evaluated and reported in Section 4.3.

2.2.6.2 MD simulations of DNB-phenylglycine and DNB-leucine

Flexible representations of DNB-phenylglycine and DNB-leucine are employed in my simulations to accurately reflect the interfacial environment. The simulations are performed in 100% hexane, 90:10 hexane:2-propanol, 80:20 hexane:2-propanol, and 100% 2-propanol. In normal-phase chiral chromatography, the DNB-phenylglycine and DNB-leucine CSPs are used in conjunction with a hexane:2-propanol solvent mixture. The percentage of 2-propanol is varied between 0-20%, depending on the polarity of the compound that is separated.[9,137] I investigate the binary solvent mixtures, but also the 100% hexane and 100% 2-propanol solvents for comparison.

To be consistent with experiment, the model interface includes trimethylsilyl end-caps and silanol groups along with the selectors. The selectors have a surface coverage of 1.10 μmol/m^2 while the trimethylsilyl end-cap surface density is 3.29 μmol/m^2, consistent with experimental coverage for this type of CSP.[138,139] The typical coverage of silanol groups on a silica surface is around 4-8 μmol/m^2, and a surface density of 4.26 μmol/m^2 is chosen for the simulations. The trimethylsilyl end-caps correspond directly to a truncated selector tether and their intramolecular potential has the same form

as for the tethers: I have chosen OPLS[103] and CHARMM[102] parameters for the Lennard-Jones potential and published potentials[109] for bends and torsions. The OPLS force field[103,140,141] has been chosen for the silanol groups and the RATTLE algorithm[142] is employed to keep the bond lengths constant.

The selectors, end-caps, and silanol groups are covalently attached to a single underlying layer of Si that is stationary throughout the simulation. This layer is arranged perpendicular to the z-axis of the simulation cell, defines the boundary of the interfacial system, and is meant to provide a minimal representation of the underlying substrate. The closest side-by-side distance between two surface molecules (end-caps or selectors) is 6.150Å.

The simulation cell can be divided into several parts: two parallel surfaces that include selectors, end-caps, silanol groups and an underlying layer of Si; solvent between the surfaces; and empty space above the upper, and below the lower, surface (Figure 2.10). Considering the solvent, the TraPPE-UA models[132] for *n*-hexane and 2-propanol were chosen. These models were parameterized based on properties of alkane/alcohol mixtures. They provide an equivalent level of representation of molecular flexibility throughout the simulation cell. All solvent bond lengths are kept constant using RATTLE.[142]

Just like for the PEPU simulations, Ewald summations[114] are used to treat the long–ranged Coulombic forces that includes the correction for the elongated shape of the simulation cell introduced by Yeh and Berkowitz.[116] The Ewald convergence parameter

of $\alpha = 1.4783\ nm^{-1}$ was chosen for all simulations, with a reciprocal space cutoff of $k^{2*} \leq 27$. The full simulation cell has dimension of 49.92 Å x 49.92 Å x 150 Å, with 72.1-83.6% of this volume as empty space beyond the slabs (depending on the solvent). The distance between the two surfaces is determined by the solvent density. Densities of 0.660 g/cm^3, 0.664 g/cm^3, 0.676 g/cm^3, and 0.780 g/cm^3 are used for 100% hexane, 90:10 hexane:2-propanol, 80:20 hexane:2-propanol, and 100% 2-propanol, respectively.[143] However, in order to achieve the correct solvent density in the simulation cell, I account roughly for the volume of the selectors, end-caps, and silanol groups in setting the distance between the Si surfaces. Following this, the bulk density in the center of the simulation cell is examined during the simulation to ensure that it is within 5% of the experimental density. Thus, because of inexact estimates of surface volume, the solvent density in the simulation cell will differ from the experimental density.

For all four solvents, five 3,500,000 time step molecular dynamics simulations have been performed for both DNB-phenylglycine and DNB-leucine interfaces. The method of generating the starting configuration is similar to the one used for PEPU: solvent molecules are randomly placed between the chiral surfaces and strong overlaps are relaxed with Monte Carlo cycles. Once the starting configuration is obtained, the fluid equilibrates for the first 50000 time steps leaving a 3,450,000 step collection period. The equilibrium properties reported in Section 5.2 are averages over ten surfaces (2 surfaces/simulation and 5 simulations per solvent), reflecting a total collection period of 10.52 nanoseconds. The time step in each simulation is 0.3 fs, (0.25 for 100% 2-propanol

simulations) which is sufficient to limit the change in $H_{Nosé}$ (see equation (2.39)), to less than 1% during the collection period of the simulation.

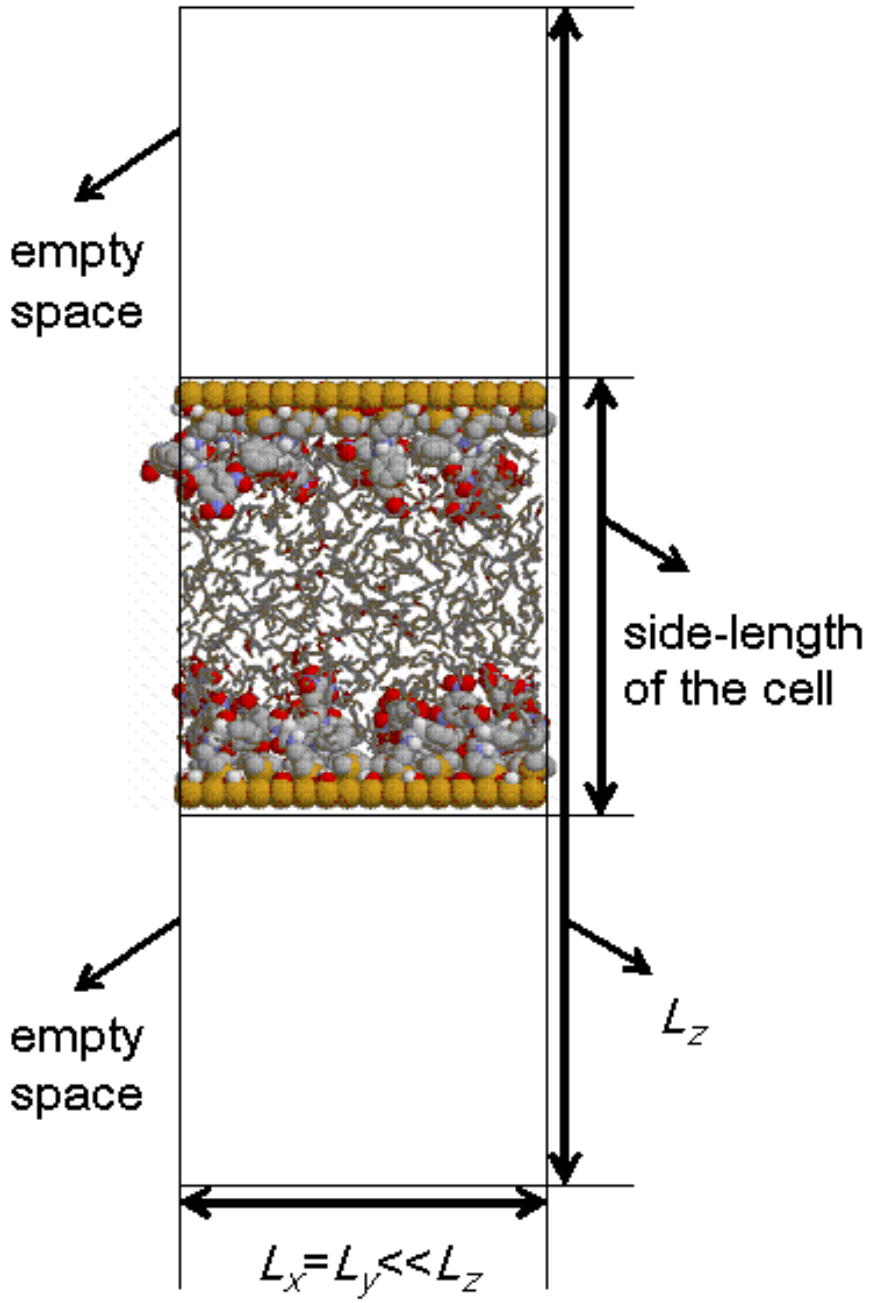

Figure 2.10 Sideview of the simulation cell employed in MD simulations of the DNB-phenylglycine interface. Similar simulation cells are used for PEPU and DNB-leucine simulations.

Chapter 3

Experimental methods

The physical chemistry of surfaces is an increasingly important area for the understanding of phenomena in heterogeneous catalysis, chromatography, corrosion, and adhesion, amongst others. Although classical thermodynamic methods can provide useful data regarding the average properties of the system, an accurate description is only obtained using surface-sensitive spectroscopic methods that are capable of offering information regarding the surface morphology, chemical composition, and electronic surface properties. In order to get a complete description of the system, modern surface science analysis relies on a multi-technique approach in which a combination of surface-sensitive probes is used to provide complementary information.

In this chapter, I first describe X-ray photoelectron spectroscopy (XPS), which is an important technique employed in the study of surface chemical composition. This will be followed by a brief description of a vibrational spectroscopy method that investigates the surface chemical bond formation and reactivity, reflection-absorption infrared spectroscopy (RAIRS). Finally, more direct surface techniques based on probe microscopy are described, with an emphasis on scanning tunnelling microscopy (STM), atomic force microscopy (AFM) and chemical force microscopy (CFM).

3.1 X-ray Photoelectron Spectroscopy (XPS)

The XPS technique is based on Einstein's explanation of the photoelectric effect, in which photons can induce electron emission from a solid if the photon energy $h\upsilon$ is greater than the work function ϕ of the solid. This work function is defined as the minimum energy required to remove an electron (known as the photoelectron) from the Fermi level into the vacuum. Although the photoelectric effect has been known since the work of Hertz in 1887, the development of the XPS technique took place much later. The basis of this advanced modern surface analysis method was set in the late 1960's by the Swedish scientist Kai Siegbahn, who received the Nobel Prize for Physics for his work.[144]

3.1.1 XPS instrumentation

In XPS the solid surface is probed by a monochromatic beam of X-rays that cause photoemission from both the core and valence levels of surface atoms into the vacuum. The ejected electrons are collected and analysed as a function of their kinetic energy using a photoelectron spectrometer.

A photoelectron spectrometer has three major components: an X-ray source, an energy analyser for the photoelectrons, and an electron detector. A schematic diagram is shown in Figure 3.1. The entire XPS experiment is performed in an ultra-high vacuum chamber that has the role of reducing the sample contamination and preventing the damage of the X-ray source that arcs at higher pressures.

The X-rays are generated by bombardment of a metal anode from electrons thermionically emitted by a cathode, which is usually a tungsten filament. The system is water-cooled to avoid overheating. The choice of the metal anode depends on the energy of the photons required, and, to a lesser extent, on the line width of the X-ray spectrum. The X-ray energy should be high enough to excite all atoms (with the exception of hydrogen) and the line width should be narrow, so that the peaks are easily identifiable. From a practical point of view, the metal anode should also be compatible with the high vacuum and high temperatures resulting from the electron bombardment. Usually the materials of choice are magnesium and aluminium. These are arranged in a twin anode configuration, which provides Kα radiation of 1253.6 eV and 1486.6 eV, respectively. The user is able to switch the energy of X-rays used in the experiment by simply changing from one anode to the other. This is the design used in the work described in this thesis. However, higher energy X-ray sources are also considered for gaining spectra from deeper core levels of the elements. The anodes in this case are made of silver (Ag Lα at 2984.4 eV), titanium (Ti Kα at 4510.9 eV) or chromium (Cr Kα at 5417.0 eV). The problem with these high energy X-ray sources is that they produce relatively broad peaks in XPS, with the peak width around 2.1 – 2.6 eV. This problem is usually addressed by using an X-ray monochromator that provides a useful way of generating a well defined source of photons.[145]

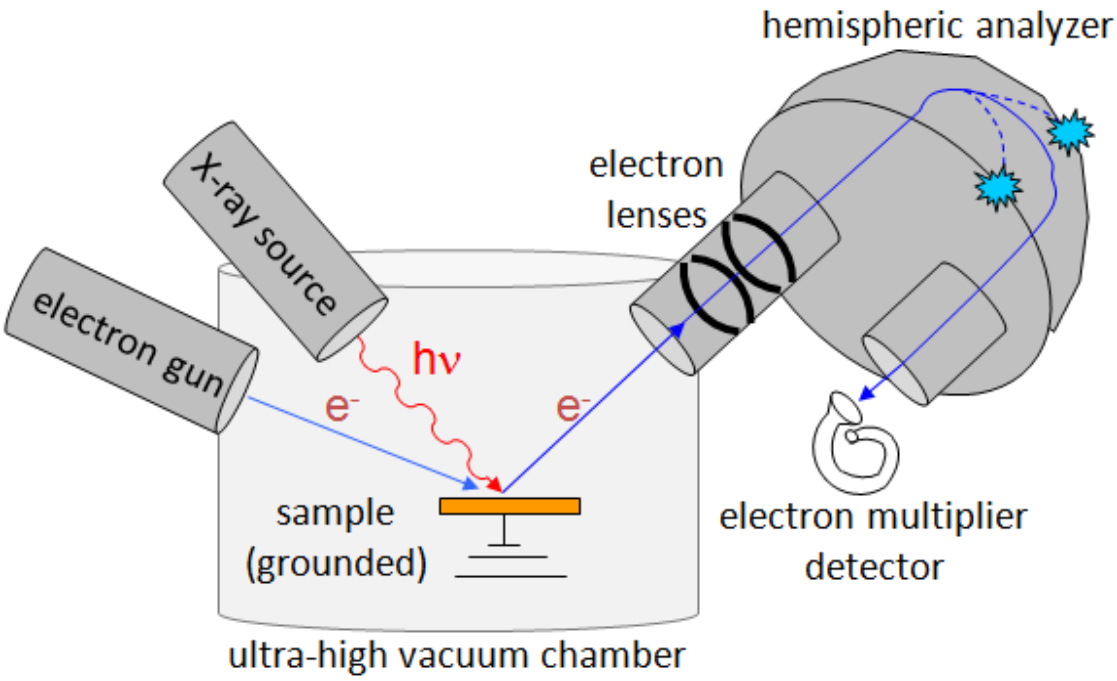

Figure 3.1 Schematic diagram of an XPS system.

The photoelectron energy analyser is the core of the XPS equipment and it is described schematically in Figure 3.2. The most common modern design is the concentric hemispherical analyser (CHA) that consists of two electrically isolated concentric hemispheres with a potential difference between them. This design allows the electrons of a chosen kinetic energy (named the *pass energy*) to go through the analyser to the detector. The electrons that have a lower or a higher energy than the pass energy hit the inner or the outer hemisphere, respectively, and are neutralized. The incoming photoelectrons of interest are retarded (accelerated) to the pass energy by changing the voltage on an electrostatic lens at the front of the analyser. By varying the lens voltage

and holding the pass energy constant, electrons with different kinetic energies are allowed through the analyser to the detector. This is known as *fixed analyser transmission* (FAT) mode and is normally employed in XPS since the resolution remains constant over all photoelectron energies. However, the system can also be run in a *fixed retard ratio* (FRR) mode in which both the retarding lens voltage and pass energy are varied such that the ratio of initial photoelectron energy to pass energy is kept constant. This mode has the advantage of giving high sensitivity to Auger electronic transitions at high kinetic energies, but has the drawback that the spectrometer resolution varies throughout the kinetic energy spectrum.

The detector is an electron multiplier tube that collects electrons of different energies. In order to accurately count the number of electrons passing through the spectrometer at each kinetic energy allowed by the retard plate, it is very important that the detector only captures the electrons that have been expulsed from the sample.

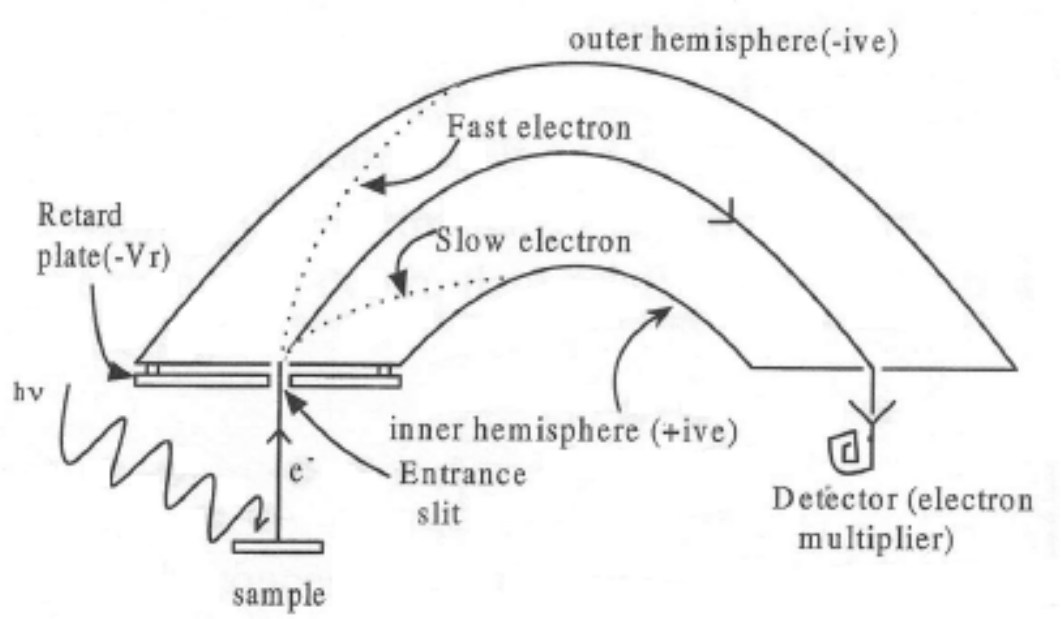

Figure 3.2 Electrostatic energy analyser used in XPS instrumentation.[146]

3.1.2 The basic principles of XPS

An XPS analysis can determine the amount of each element present in a sample and its oxidation state. This arises from the ability to probe the core orbitals which are generally narrow in their energy range, and valence orbitals, which are generally broad, creating a valence band (a broader set of energy levels). This is summarized briefly in Figure 3.3, which describes the energetics of an XPS experiment.[146]

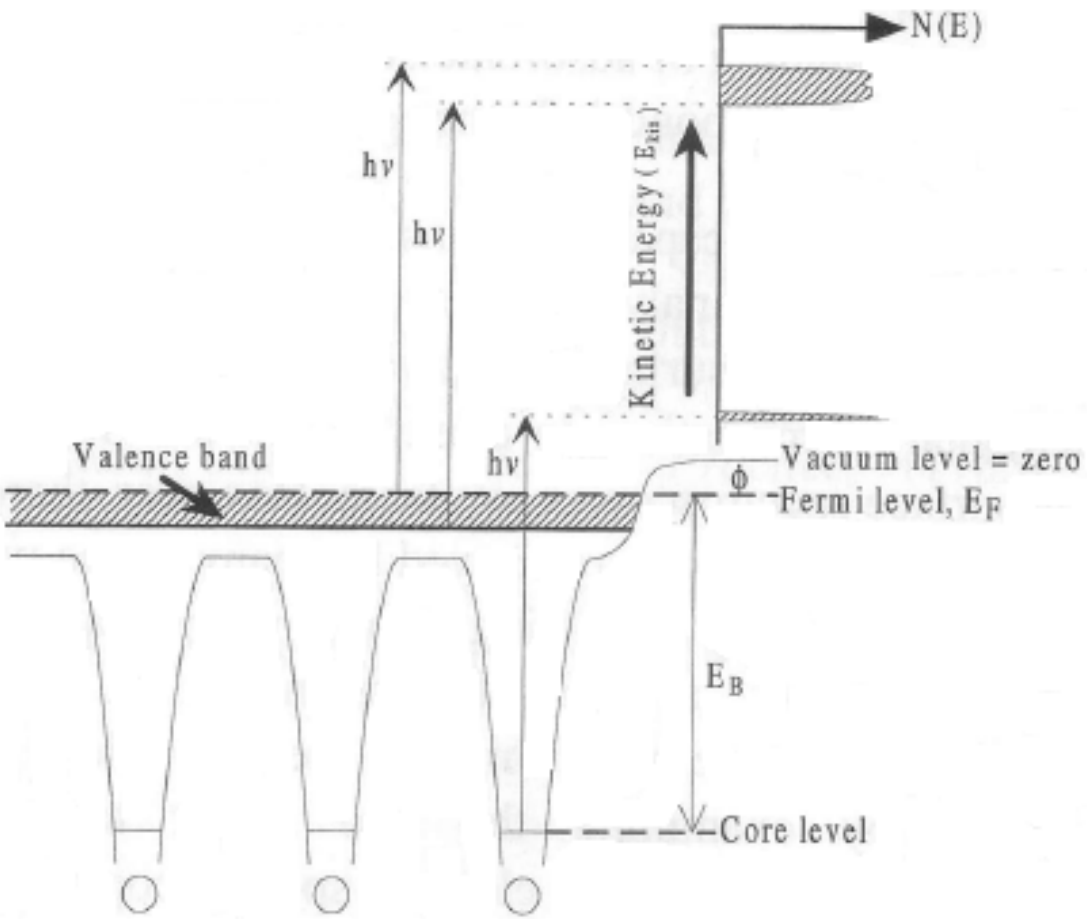

Figure 3.3 The energetics of the XPS experiment.[146]

Considering as an example a gold surface, the expected energy levels in XPS are given by the core and valence orbitals of Au. The core levels are defined as the inner shells that do not participate in chemical bonding, and for Au the highest energy core orbitals are 4s, 4p, 4d, and 4f. The valence levels are defined as the partially filled outer shells that have electrons more weakly bound because they are involved in chemical bonding; for Au the valence electron configuration is $5d^{10}$ $6s^1$. These are easily

observable in the XPS experiment, as is seen in Figure 3.4. This XPS example shows that the core levels give strong, narrow bands (Au 4s, Au 4p, Au 4d, and Au 4f), while the valence band presented in the insert from the high kinetic energy region is broad and has a weak signal. It is important to note that all core levels with orbital angular momentum quantum number higher than zero (p, d, f orbitals) are split into doublets by spin-orbit coupling, with the higher angular momentum state at higher kinetic energy.[146]

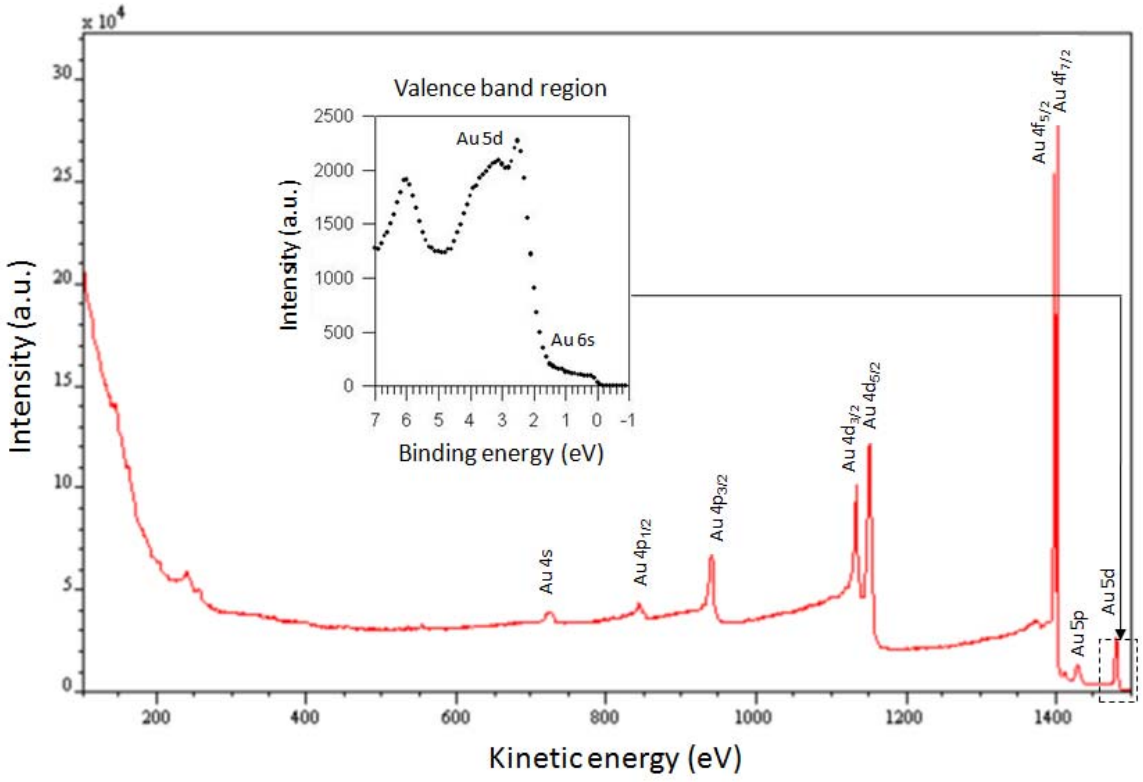

Figure 3.4 XPS experiment of a gold surface emphasizing the core energy levels Au 4s, Au 4p, Au 4d, and Au 4f. The valence band is presented in the insert.

By applying the principle of energy conservation, it is easy to obtain Einstein's photoelectric equation in which the kinetic energy E_{kin} of the outgoing electron is directly related to the binding energy E_B of the electron in the solid, the energy of the incoming photon $h\upsilon$ and the work function, ϕ (see Figure 3.3):

$$E_{kin} = h\upsilon - E_B - \phi \tag{3.1}$$

As discussed above, the photons used in XPS experiments are usually X-ray emissions from either Mg or Al anodes, with $h\upsilon$ energies of 1253.6 eV and 1486.6 eV, respectively. In equation (3.1), the binding energy E_B is given with respect to the Fermi level, as shown in Figure 3.3. The work function ϕ is a small correction (1-4 eV) that needs to be determined experimentally for the spectrometer used in the XPS analysis. Because the sample and the spectrometer are in electrical contact with each other, the work function observed is that of the spectrometer and is expected to be constant for all samples that are run in a specific XPS spectrometer. For conducting solid samples, the work function ϕ is usually measured by looking at the valence region of the XPS spectrum, finding the Fermi level (the point where the energy drops off) and setting this as the zero energy level. However, this method is not applicable to semiconductors or insulators because the density of states at the Fermi level is zero and there is no signal at this point. In this case, the work function is determined by a relative measurement of a peak position of a known standard (such as the C1s line from contaminants on the sample).

Following equation (3.1) and knowing the fixed photon energy *hν*, photoemission from an atom with well-defined core levels will produce well-defined kinetic energies varying methodically from element to element. From the value of the kinetic energy of the outgoing electrons, one can easily calculate the binding energy by rearranging equation (3.1)

3.1.3 Chemical shift in X-ray photoelectron spectra

The binding energy of the core orbitals depends critically upon the chemical environment in which the atom is found. Hence, XPS explores the local chemistry of the surface atoms or molecules. Because of these chemical effects, in the 1960's Siegbahn *et al.* used the term Electron Spectroscopy for Chemical Analysis (ESCA) for their XPS technique. Although the term ESCA is occasionally used today (for example in the names of commercially available spectrometers), it is largely been outdated by the more spectroscopically exact term of XPS.[145]

Charge transfer processes may leave the atom with partial positive or negative charges that determine a slight shift in core levels to higher or lower energies, respectively. This leads to a change in the Coulombic attraction between the atomic nucleus and the electrons. The consequence of this effect is that an atom in a higher oxidation state will have its XPS peak shifted to higher binding energy relative to the same atom in a lower oxidation state. This is called the *chemical shift* in the XPS spectrum and in some cases is as large as 10 eV. An example is the spectrum of the Si 2p line from a bulk silicon sample and an oxidized silicon sample presented in Figure 3.5. In

SiO_2, silicon has a higher oxidation state (Si^{IV}) compared to the bulk silicon (Si^0) determining an increase in binding energy for the core orbitals. This is observable in the XPS spectrum as a shift of about 4 eV at higher binding energy.[146]

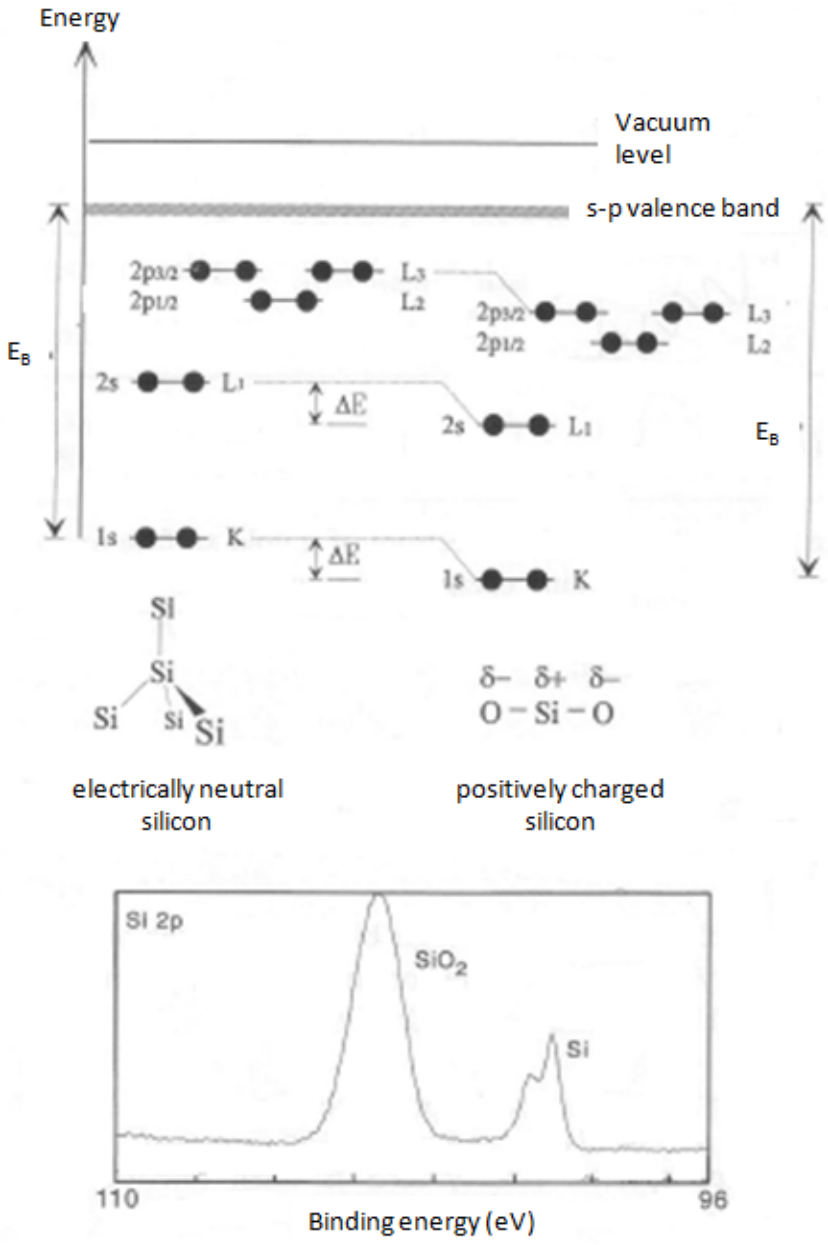

Figure 3.5 Chemical shifts of silicon core levels in XPS.[146]

3.1.4 Quantitative analysis of XPS spectra

In principle, one should observe a separate narrow XPS peak for each chemically distinct atom. These usually have a Gaussian shape, but more complicated peaks can appear because often on a sample there are more than one chemical species of the same element. Often this leads to small chemical shifts between the two peaks, which make them poorly resolved. One way of improving the resolution is by using an X-ray monochromator and a low energy X-ray radiation (like Mg Kα at 1253.6 eV) that creates relatively narrow XPS peaks, as shown in Figure 3.5.

Another important characteristic of the XPS peaks is the background. The excited photoelectrons may become *secondary electrons* if they undergo inelastic collisions with phonons or electrons while travelling through the solid. This results in a rise in the secondary electron background to higher binding energy for each transition in the XPS spectrum. This background can be effectively accounted for by a proper peak fitting technique. Practically, there are four approaches to this problem and they are illustrated in Figure 3.6.[145]

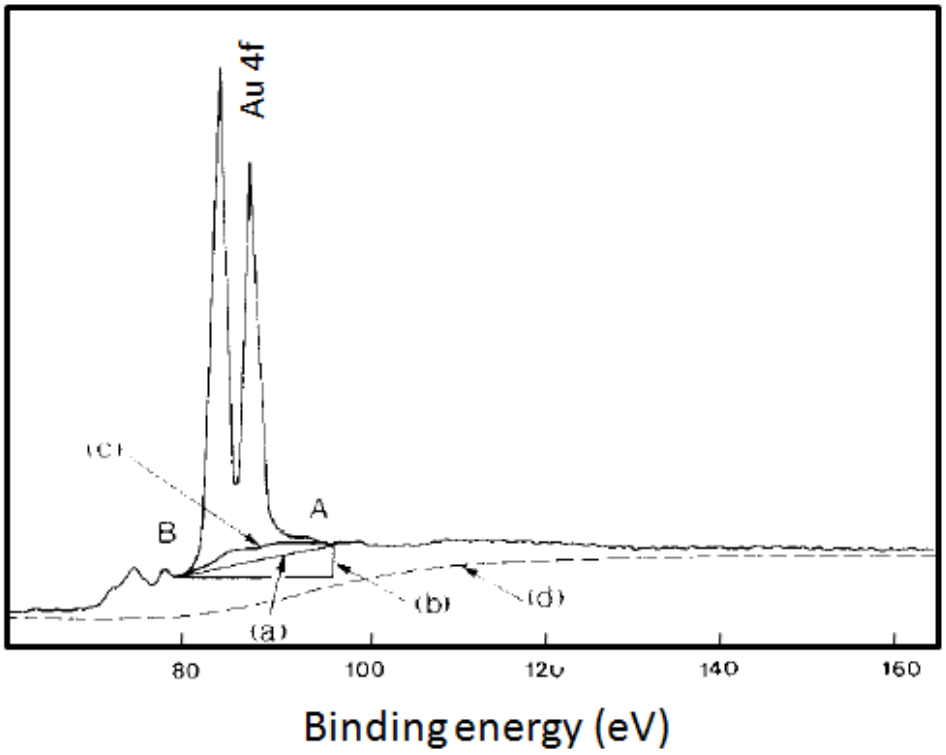

Figure 3.6 Choices of background subtraction fits for the doublet of Au 4f peak: (a) linear, (b) horizontal, (c) Shirley, and (d) Tougaard.[145]

The simplest approach is to use the linear background (denoted as case (a) in Figure 3.6). This is easy from a data processing point of view, but, unfortunately, it is very sensitive to the positions of start and end points. The horizontal approach ((b) in Figure 3.6) has very large errors and therefore it is not considered in practice for quantitative XPS analysis. The most common background subtraction employed in XPS spectra analysis is the Shirley method (situation (c)). In this method the background is fitted to an *S* shape curve that is proportional in intensity to the magnitude of the peak above it at any particular energy. The rationale behind this background fit is that the

number of secondary electrons that represent this background *S* curve should be proportional to the change in the number of photoelectrons that are produced. Other more sophisticated methods have been developed (like the Tougaard background subtraction method that extends many tens of electron volts to the lower kinetic energy side of the peak – see case (d) in Figure 3.6), but XPS researchers prefer the uncomplicated Shirley background fitting because it is simple and generally produces good results.[145]

After the background is properly determined, the XPS peak is fitted to a Gaussian (or sometimes a Lorentzian) shape with three varying parameters: peak height, peak center position (value of the binding energy), and peak width. By integration of this peak, it is easy to find the intensity of the XPS peak that is an important quantitative characteristic of the spectrum.

3.1.5 The escape depth

XPS can also be employed for a quantitative film thickness analysis. It has been shown that the area of an XPS peak is proportional to a quantity called escape depth that is a measure of the effective sampling depth. As the electrons move through the solid they may interact with other electrons or the ion cores and get scattered, losing energy. Thus, only the electrons that do not have these collisions reach the detector and appear in the XPS spectra. The XPS intensity *I* from a layer "buried" at the distance *d* below the surface is calculated with the formula:

$$I = I_0 e^{-d/\lambda} \qquad (3.2)$$

where I_0 is the signal that is acquired from an infinitely thick surface layer, d is the depth in the solid at which the photoelectron is being ejected, and λ is the escape depth. Thus, the escape depth is defined as the distance for which $1/e$ of the electrons have not been inelastically scattered.

Escape depths may be calculated from intensity ratios obtained for films of known thicknesses on a substrate when photoelectron lines from the film and substrate arise from the same atomic level. Once determined, they can be employed for an accurate determination of film thicknesses, by rearranging equation (3.2) and determining the value d.[147]

3.1.6 Auger electrons

In addition to producing photoelectrons, the excitation of electrons in a solid leaves a core hole that must be filled in order to stabilize the atom. This can be done by an autoionization process within the atom as shown schematically in Figure 3.7. The X-ray photon causes the emission of a photoelectron (electron 1) from, for example, the K energy level of the atom and it is detected in XPS. The created core hole may be neutralized by an electron transition from an electron level of lower binding energy. This is called the down electron and in the example from Figure 3.7 it belongs to the L_1 energetic level (electron 2). Thus, the energy difference $\Delta E = E_K - E_{L_1}$ can be removed from the atom as a photon (X-ray fluorescence phenomenon) or it can be transferred to a third electron that can escape into the vacuum. This is called the Auger electron, from the

name of the scientist that first described this autoionization process in 1923, Pierre Auger.[148] In Figure 3.7 the Auger electron belongs to the $L_{2,3}$ energetic level and has a kinetic energy calculated as:

$$E_{kin} = \Delta E - E_{L_{2,3}} - \phi = E_K - E_{L_1} - E_{L_{2,3}} - \phi \tag{3.3}$$

where ϕ is the work function of the spectrometer. It is very important to notice that the kinetic energy of the Auger electron solely depends on the binding energies of electrons within the atom and it is independent of the exciting radiation. This makes it a useful tool for routine analysis of surface composition and elemental identification. The Auger electrons are usually denoted by three letters which specify the levels from which the core hole, the down electron, and the Auger electron come from. The example in Figure 3.7 has an Auger electron termed as $KL_1L_{2,3}$.[146]

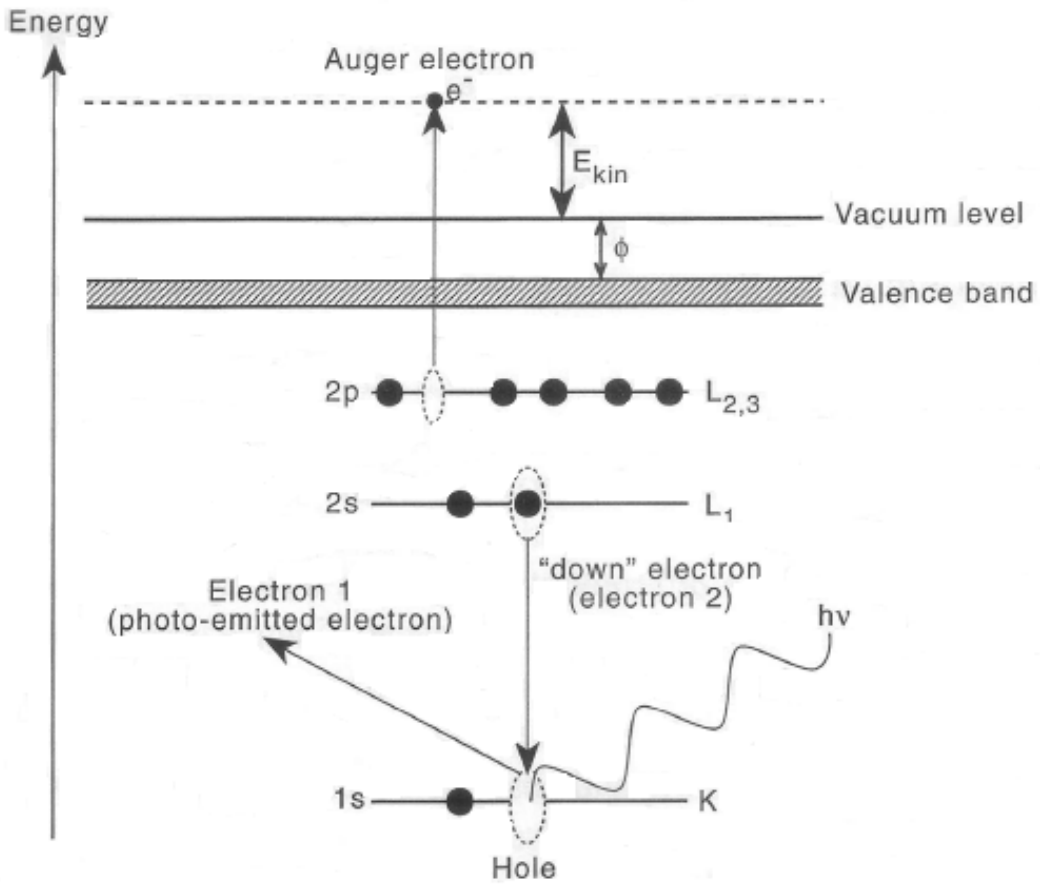

Figure 3.7 The energetics of the Auger process.[146]

Thus, in XPS spectra the secondary electrons will always induce the Auger process and concomitant with the photoelectron peaks one can observe Auger electron peaks. These peaks might interfere with a correct identification of XPS signals. However, the Auger electron peaks are easily distinguished by changing the excitation source energy. In this case the XPS peaks will shift in kinetic energy, but the Auger peaks will appear in the same place.

Auger electrons only depend on the discrete core energy levels on the atoms and do not depend on the excitation energy, and hence they are very useful for elemental identification. For each atom the Auger electrons create a very useful spectral fingerprint. This led to the development of a separate surface analysis technique named Auger Electron Spectroscopy (AES). For AES the energy of the primary electrons does not need to be monochromatic as in XPS. An energy spread of 0.2 – 0.6 eV is acceptable and is easily attainable from a flux of electrons. Electron beams are easy to control under high-vacuum conditions, they can be focused on a very small spot size, and have high energies that can ionize atomic inner shells. Because of this, in AES the primary excitation is usually done with electrons, rather than X-ray photons. Therefore, electron guns are present in the XPS/AES instrumentation as shown in Figure 3.1.[149] The electrons are thermionically emitted from a heated tungsten filament. They are accelerated to higher energies using an extractor and then are focused using a set of lenses.

3.1.7 Details on XPS measurements

In this thesis, the XPS measurements were performed using a Thermo Instruments Microlab 310F surface analysis system (Hastings, UK) under ultrahigh vacuum conditions and using an Mg Kα X-ray source (1253.6 eV) at 15 kV anode potential and 20 mA emission current. Scans were acquired at fixed analyzer transmission (FAT) mode at a pass energy of 20 eV and a surface/detector take off angle of 75^{o}. Spectra were background-subtracted using a Shirley fit algorithm and the peaks were fitted according to the Powell algorithm.

3.2 Reflection-Absorption Infrared Spectroscopy

Fourier-transform Infrared (FT-IR) spectroscopy is a very useful, non-destructive technique applied for the investigation of chemical bonds present in a molecule. However it cannot be easily employed for the study of surfaces because these are usually opaque to infrared radiation so that transmission experiments are not possible. As a consequence a reflection mode has been developed. This technique is known as reflection-absorption infrared spectroscopy (RAIRS) and it has only been regularly employed in surface analysis in the last twenty years, with the advance of proper spectrometers.[150]

The RAIRS instrumentation is reproduced schematically in Figure 3.8. The infrared radiation is shone through an IR-transparent alkali halide window on the solid sample at grazing incidence. The sample reflects the IR beam out into a vacuum-sealed window that is further transmitted to a photoconductive semiconductor detector.

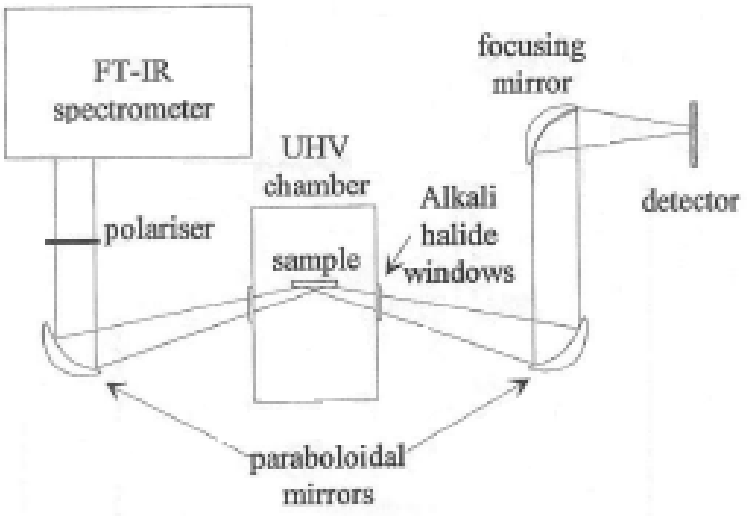

Figure 3.8 Schematic diagram of the experimental configuration of the RAIRS instrument.[146]

The amplitude and phase of the radiation are changed upon reflection by a mechanism that is not completely understood. However, this determines a surface selection rule that states that only molecular vibrations giving rise to a dynamic dipole moment perpendicular to the surface will yield IR absorption in RAIRS. As a consequence, if the surface contains bonds with active dipole moments, they won't appear in the RAIRS spectrum.[146]

In this thesis the RAIRS measurements have been obtained via a grazing angle specular reflectance accessory (Pike Technologies) using a Bruker Equinox 55 FTIR with a liquid nitrogen cooled MCT detector. Typically, 100 co-added sample scans were ratioed against scans from a gold mirror background to generate the log reflection spectra presented here.

3.3 Scanning probe microscopy techniques

Scanning probe microscopies (SPMs) are a group of methods developed in the last two decades for the microscopic investigation of the morphology and properties of surfaces. These methods have two important characteristics. First, the signal results from the interaction of the surface with a very sharp tip specially designed to probe sample surfaces. Second, unlike classical microscopy that uses either light or electrons to obtain magnified images of objects, in SPM the sharp tip is scanned across the surface, permitting a microscopic image of the sample to be obtained. In SPM the resulting image resolution is at least three orders of magnitude higher than in standard optical microscopy.

The development of SPM methods started with the invention of the Scanning Tunneling Microscopy (STM) by Gert Binning and Heinrich Röhrer, at IBM, Switzerland, in 1982,[151] for which they received the Nobel Prize for Physics in 1986. The working principle is very simple: an atomically sharp, conducting tip is approached within a few nanometres of a conducting surface, and a potential is applied between the tip and the sample. The electrons from the sample begin to tunnel through the gap into the tip and vice versa, depending on the sign of the bias voltage. By measuring the magnitude of the tunnelling current as the tip scans the sample surface, a topographic image of the surface is obtained. Very high image resolutions can be obtained in STM, up to atomic resolution. However, this technique has a major limitation, that comes from the fact that its operation requires a flow of electrons from the tip to the sample (or vice versa), so that both the tip and the sample must be electrically conductive (metals or semiconductors). For insulating surfaces, including such important classes of materials as minerals, polymer and biological samples, this method cannot be applied. To enable the detection of atomic-scale features on insulating surfaces, another SPM method has been developed, atomic force microscopy. This method is described in the next section.[146]

3.3.1 Atomic Force Microscopy

Atomic force microscopy (AFM) was invented in 1986 by Binning, Quate, and Gerber.[152] In this method, instead of measuring a tunnelling current between the tip and the sample like in STM, the force between the sample and a tip that is located at the end of a cantilever is determined based on the cantilever deflection.

There are four major components of an AFM instrument: a cantilever-mounted tip, a piezoelectric micropositioner, a cantilever deflection sensor, and an electrical feedback mechanism for the micropositioner.[153] A schematic diagram is shown in Figure 3.9 (a). The most important component is the cantilever-mounted tip that is made of silicon or silicon nitride. The tip is microscopically sharp and can be either conical or pyramidal. Scanning electron micrographs of commercially available silicon nitride V-shaped cantilevers having pyramidal tips are shown in Figure 3.9 (b) and (c).

The operating principle is very simple. The tip is approached to the surface and experiences a very small force (on the order of nanoNewtons) as a consequence of the interaction. The deflection of the cantilever is monitored with an optical technique in which a laser is reflected from the back of the cantilever onto a four-quadrant photodiode detector. As the tip is scanned across the sample, the cantilever is deflected up and down, shifting the position of the laser beam on the four-quadrant detector. The voltage difference signal between any pair of quadrants on the detector is proportional to the deflection of the cantilever. By employing a feedback loop which moves the piezoelectric micropositioner up or down such as to maintain a constant cantilever deflection, the surface morphology may be mapped as a function of the position of the tip on the surface.

Using Hooke's law it is very easy to calculate the force from the cantilever deflection relative to its equilibrium position Δz:

$$F = k\,\Delta z \tag{3.4}$$

where the proportionality constant k is the force constant of the cantilever.

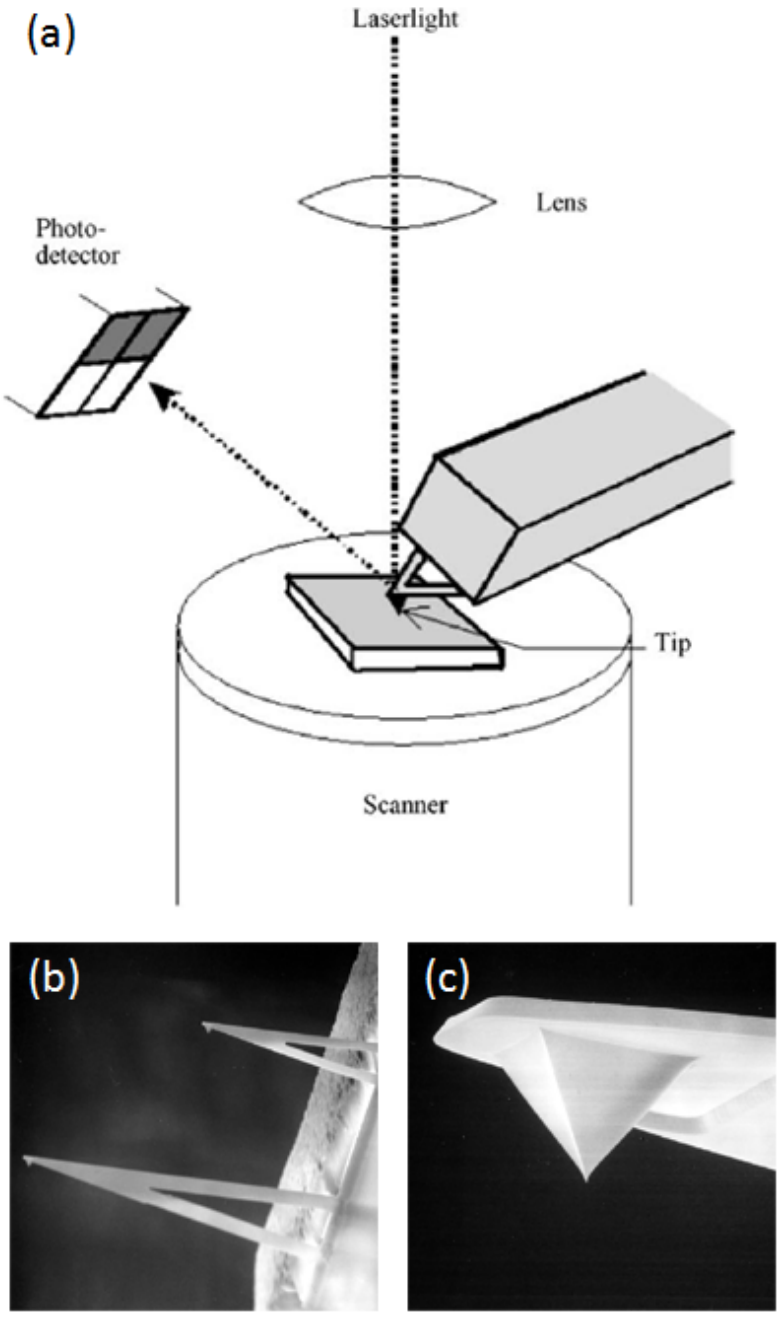

Figure 3.9 A schematic representation of an AFM instrument (a)[154] and SEM images of an AFM cantilever and tip (b), with a zoom on the tip (c).[155]

The AFM sensitivity depends on the value of the force constant. Commercially available cantilevers have a force constant of about 0.001 - 100 Nm^{-1}, and the instrumental sensitivities for normal deflection are about 0.01 nm. This leads to a limit in force detection of $10^{-13} – 10^{-8}$ N.[153]

3.3.1.1 The AFM as an imaging tool

AFM can operate in a number of measurement modes. The most common mode developed for AFM is the *contact mode*, characterized by a soft physical contact between the tip and the sample surface. As the tip is scanned and passes over the topographical features of the surface, the positive or negative vertical displacements of the tip are recorded and used to create an image of the sample. This is called force imaging (or constant height mode) because the force between the tip and the sample is in effect monitored by a vertical deflection sensor while the tip scans the surface. The more common option is to have the cantilever deflection kept constant using a feedback loop to keep the force at a preset value, as described above. This is called constant force topography and it is based on recording the vertical displacement of the tip that is required to maintain the preset force.

While contact mode AFM has proven to be a very useful tool in surface analysis, it cannot be successfully employed for imaging delicate samples, such as biological or polymeric surfaces. In these cases the imaging resolution is very poor and the lateral forces exerted on the surface by the tip may be sufficient to irreversibly damage the surface. For soft samples, a series of dynamic AFM techniques have been developed:

non-contact techniques (to employ attractive forces for imaging) and intermittent-contact techniques (commonly known as tapping mode imaging).

In *tapping mode* (registered trademark of Veeco Instruments Inc.) AFM the cantilever is externally driven to oscillate close to its resonance frequency by a piezoelectrical crystal or a magnetic field. This resonance frequency is generally on the order of 100 kHz. When the sample approaches the vibrating tip, they come into intermittent contact (the tip taps the surface) and the vibrational amplitude drops. The changes in vibrational amplitude are monitored by a lock-in amplifier and the differences in amplitude are used to map surface morphology. Other than the ability to image softer samples, tapping-mode AFM has two important advantages over conventional contact mode:

- the tip-sample forces act on a shorter time scale;
- the lateral force is greatly reduced and the short tip-sample contact prevents inelastic surface modifications. [156]

The standard type of image reflects the height at which the piezo tube is moved by means of an external feedback loop in order to maintain a constant oscillation amplitude as the tip scans the surface. It is therefore known as a height image (a constant amplitude mode). The cantilever's deflection amplitude can also be monitored and create deflection images. The deflection image is in effect a first derivative of the height image and it is particularly useful for observing fine detail of surfaces that have large variations in topography. Phase shift images are obtained by monitoring the phase lag between the

tip and the externally applied oscillation. These images are usually prepared to investigate surface regions with different composition and are also useful for the analysis of the adhesive and frictional properties of the sample.[157]

3.3.1.2 Contact AFM force curves

AFM is not only an impressive nanoscale imaging tool, but it can also be employed for the investigation of the tip-sample interaction, and thus being a powerful analytical tool. This is done by acquiring force curves. That is, plots of the forces that act on the tip at a single point on the sample as the vertical separation between the tip and the surface is varied in an oscillatory manner through cycles of approach and retraction of the tip relative to the sample.[153] These provide important information on local material properties, such as elasticity, hardness, Hamaker constant, adhesion, and surface charge densities. The measurement of force curves has become an increasingly important determination in different fields of research, such as surface science, materials engineering, and biology. New areas of research, in which force curves have a major role, are the determination of the stretch in polymer chains, the rupture of single chemical bonds in single molecules, and the determination of the properties of confined liquid films. [154]

The attractive/repulsive forces that can induce a deflection of the cantilever are summarized in Table 3.1. These forces include long-ranged electrostatic interactions that are the result of the electrical double layer formed in aqueous electrolytes, and hydrophobic van der Waals interactions.

Table 3.1 Types of interaction forces and interaction distances in AFM.[153]

Type	Distance (nm)
Long range	
Electrostatic force in air	100
Double layer force in electrolyte solution	100
van der Waals force	10
Short range	
Surface-induced solvent ordering	5
Hydrogen-bonding force	0.2
Contact	0.1

A force curve is determined by moving the sample up and down by applying a voltage to the piezoelectric translator, onto which the sample is mounted (see Figure 3.9 (a)), while measuring the cantilever deflection.[154] The cycle of a force curve can be divided into several regions that show the hypothetical attractive tip-sample interaction. For clarity, the force curve is separated into the approach and retraction portions, illustrated in Figure 3.10 (a) and Figure 3.10 (b), respectively. Schematically, the regions on the curve are described below:[153]

(1) At the start of the force curve cycle, the tip and the sample are sufficiently separated that they do not interact with each other. The force acting on the tip is negligible and the cantilever remains in its equilibrium position.

(2) As the tip approaches the surface, long-ranged and short-ranged forces act on it and can induce a deflection on the cantilever. If there is an attractive force, the

cantilever bends toward the sample (as illustrated in Figure 3.10 (a)) or if there is a repulsive force, the cantilever moves away from the surface.

(3) As the separation distance decreases, at a certain point the gradient of interaction force exceeds the force constant of the cantilever and the tip jumps into contact with the sample. This event is called snap-to-contact or jump-to-contact point.

(4) A repulsive force and positive deflection are induced as the tip moves further, and the tip and surface, which are now in contact, are pressed against each other. This is known as the contact regime. It is in this regime that the elastic properties of the substrate can be investigated. This region is also the beginning of the retraction curve, in which the forward motion is reversed and it is retracted from the sample.

(5) A negative deflection of the cantilever is detected until the adhesive force is overcome by the restoring force of the cantilever, at which point the contact is ruptured. The point where the tip loses contact with the sample is known as the jump-out point. The peak magnitude of the force curve at this point is related to the adhesion force of the tip-sample contact, also referred to as adhesive, rupture, or pull-out force.

(6) As the distance between the separated tip and sample increases, the force becomes negligible and the tip returns to its non-interacting equilibrium position.

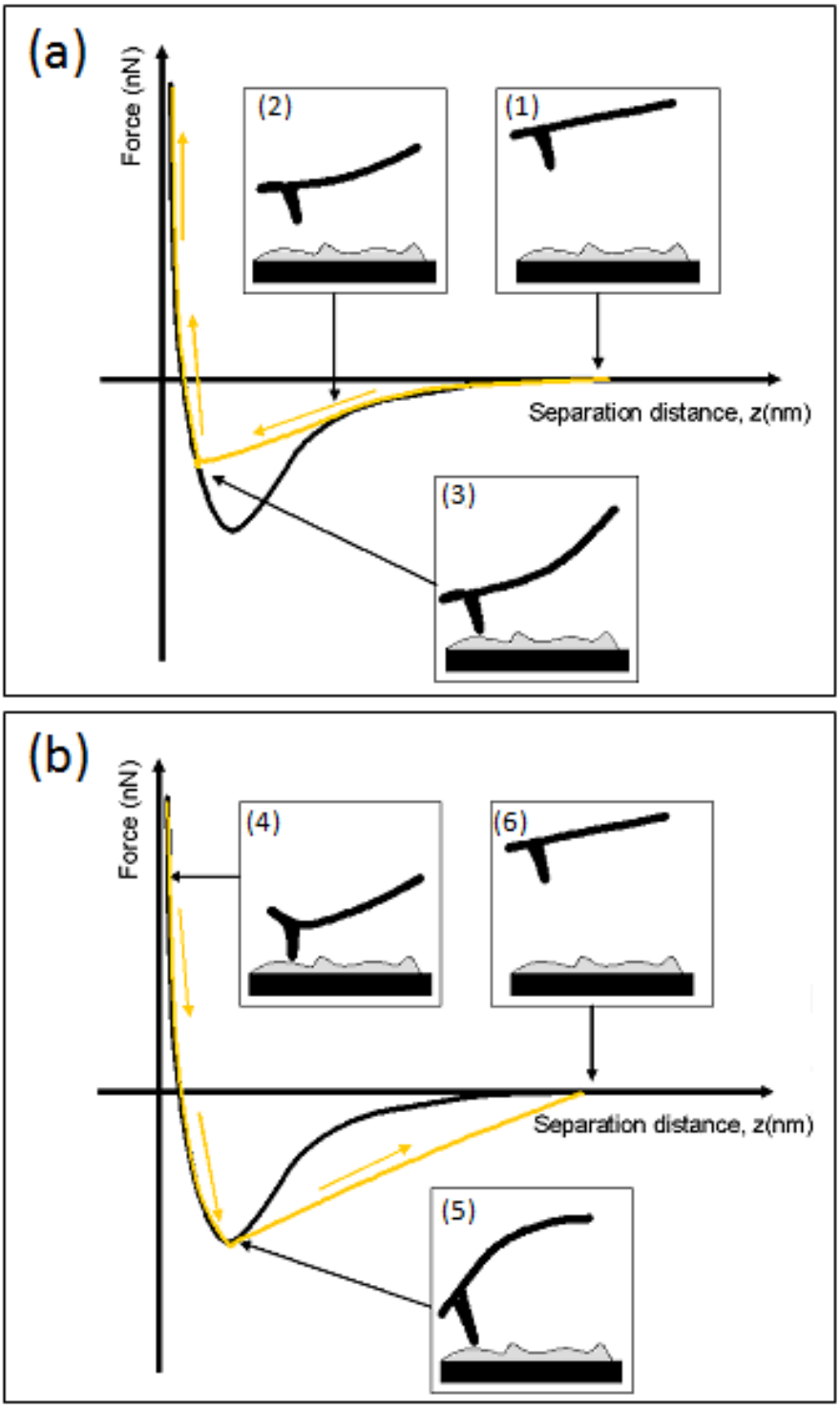

Figure 3.10 Illustration of the approach (a) and the retraction (b) portions of an AFM curve for an attractive tip-sample interaction.[153]

3.3.2 Chemical Force Microscopy (CFM)

Standard AFM tips have reasonably consistent shape, size, and mechanical properties, but they are poorly controlled in terms of their surface chemical composition. This may lead to a series of unwanted consequences. First, silicon and silicon nitride tips are usually oxide sharpened and have a large number of silanol groups (Si-OH) on the surface that (through hydrogen bonding) may create some undesired adsorption of contaminants. These contaminants can lead to tips that have varied surface composition. Second, uncoated tips are prone to mechanical wear that interferes negatively with image resolution and force measurement because they depend on the shape of the tip. Third, uncoated tips present hydrophilic surfaces that can lead to strong adhesive interactions with biological samples, which complicates the manipulation and maintenance of the applied load on the tip.[153]

Since the nature of the interactions between the tip and a substrate is critically determined by the physical and chemical nature of the small portion of the tip that comes in contact with the surface, several methods have been derived that allow a specific modification of the tip surface through covalent attachment of molecules in order to make them sensitive to specific molecular interactions. The technique that is able to directly probe the specific chemical groups at the molecular level is known as chemical force microscopy (CFM). By using chemically modified tips, CFM can be used to provide a multitude of information:[158]

- Measure forces between different chemical functional groups;
- Measure surface energetics at the nanoscale level;
- Determine pK_a values of the surface groups locally;
- Obtain the surface distribution of specific functional groups and their ionization state.

In CFM experiments, the magnitude of the adhesion force that corresponds to the jump-out from the force minimum when the tip-surface force gradient exceeds the cantilever spring constant (situation (5) in Figure 3.10) is accurately measured. Ideally, it is better to map the entire potential. That is only possible when the effective spring constant can be varied continuously, by applying a variable external force to the cantilever.[159] Such experiments are beyond the scope of this thesis.

In principle, there are many methods by which the AFM tips and samples can be functionalized, but two are more common. The first is based on the immobilization of alkanethiol self-assembled monolayers (SAMs) on gold-coated tips. In this method, the tip and samples are first coated with a vacuum-deposited thin adhesive layer of chromium (< 5 nm), followed by a deposition of a thicker layer of gold (usually 40 – 100 nm). The gold-coated tips and samples are then immersed in a dilute (10^{-4}-10^{-3} M) solution of organic thiols. The alkanethiols have thiol (S-H) groups at one end and are terminated with specific functional groups at the other end. As the gold coated tips and samples are brought in contact with the alkanethiols, a compact SAM layer is formed on the Au

surface via covalent bonds between the sulphur atoms and the gold atoms. Schematically this is shown in Figure 3.11 (a). The tips modified with alkanethiols are highly reproducible, easy to handle, chemically stable, and mechanically robust, with lower susceptibility to wear than uncoated silicon nitride probes.[160] Another advantage is that alkanethiols terminated with various functional groups are either commercially available or easily obtainable. However, because of the chromium and gold deposition, the radius of the tip can increase significantly, that may lead to a reduction in lateral resolution and can cause irreversible bending of the cantilever at higher termperatures.[161]

The second most common tip-sample modification method is based on organosilane adlayers or organotrichlorosilane, which couple directly to the surface silanol groups (Si-OH) of Si or Si_3N_4 surfaces. The deposition is usually preceded by a step in which the Si or Si_3N_4 surfaces are cleaned (e.g. ozone plasma) or etched (e.g. HF or H_2SO_4 chemical etching). In the deposition, the organosilane precursors form a two-dimensional network comprising a lateral network of cross linking Si-O-Si bonds that are covalently bound to the surface (see Figure 3.11 (b)). However, this surface modification technique presents a few problems, including the sensitivity of chlorosilanes to moisture, as well as the difficulty to control the polymerization process and film thickness.[162] Under appropriate preparative conditions, however, adlayers with the necessary degree of ordering are easily attainable, without a prior metallization step. This latter method is used to prepare the chemically modified tips and samples used in the experiments described in this thesis.

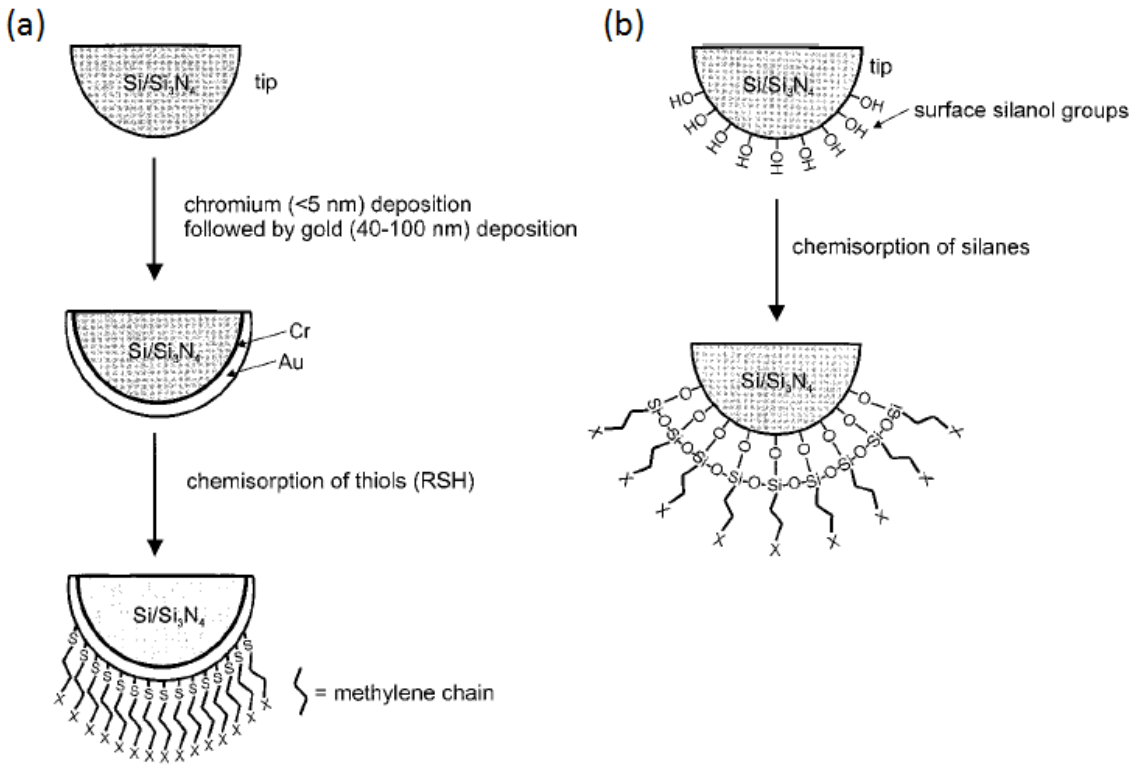

Figure 3.11 General schemes for chemical modification of tips and sample substrates using thiol-based monolayers chemisorbed on gold (a), or organosilanes-based self-assembled films (b). X represents different terminal functional groups.[153]

3.3.2.1 Adhesion forces measurement

The chemical environment in which the CFM experiment is performed has an important role in determining the observed forces. Force measurements performed in ambient air are more difficult to interpret because the capillary forces that appear between the tip and the sample are usually an order of magnitude higher than the specific chemical interactions, and thus obscure them. This capillary effect can be eliminated by performing the CFM experiment in liquid instead of air, since the adhesion force

measurements with the tip and the surface immersed in the liquid will reflect the interaction between surface free energies of solvated functional groups.[158]

CFM in aqueous solutions is particularly important because it leads to the understanding of complex systems, such as colloids, polyelectrolytes, micelles, and biological macromolecules. The adhesion force measured in water depends on a number of parameters, such as pH, ionic strength, and dielectric constant. In aqueous systems, a plot of the adhesive force determined in a series of force curves as a function of pH, called a force titration curve, may be considered for analysis. The shape of the force titration curve can give important information regarding the nature of functional groups active on the surface. A variation in sign and magnitude of the forces indicates a change in the surface charge, and an abrupt transition implies a transition that occurs at $pH \approx pK_a$ of the functional group.

Very important are CFM measurements performed in organic solvents because they provide information regarding the van der Waals and hydrogen bonding interactions. In an often-cited experiment,[163] force curves were obtained in ethanol for gold-coated tips and samples functionalized with SAMs terminated in CH_3 or COOH. The CFM experiments showed a trend in terms of an increase in adhesive interaction at the tip-sample contact: COOH/COOH > CH_3/CH_3 > COOH/CH_3 (see Figure 3.12 (a)). The COOH/COOH combination produced the biggest adhesive force because of strong hydrogen-bonding interactions that are greater than the weaker van der Waals interactions found in CH_3/CH_3 combinations. The smallest force in COOH/CH_3 is due to

the immiscibility of the COOH- and CH_3- terminated surfaces. However, these are only qualitative observations. In order to properly quantify the differences and uncertainties in the adhesive interactions between different functional groups, it is necessary to perform a large number of measurements and statistically analyse the results. This is done by generating histograms that emphasize the Gaussian distribution of the adhesive force measurements (Figure 3.12 (b)) that allow the calculation of mean adhesive force and the experimental uncertainty. For the COOH/COOH, CH_3/CH_3, and $COOH/CH_3$ combinations described above, the quantitative values were 2.3 ± 0.8, 1.0 ± 0.4, and 0.3 ± 0.2 nN, respectively. These are statistically different, showing that CFM is able to correctly identify the surface functional groups.[158,163]

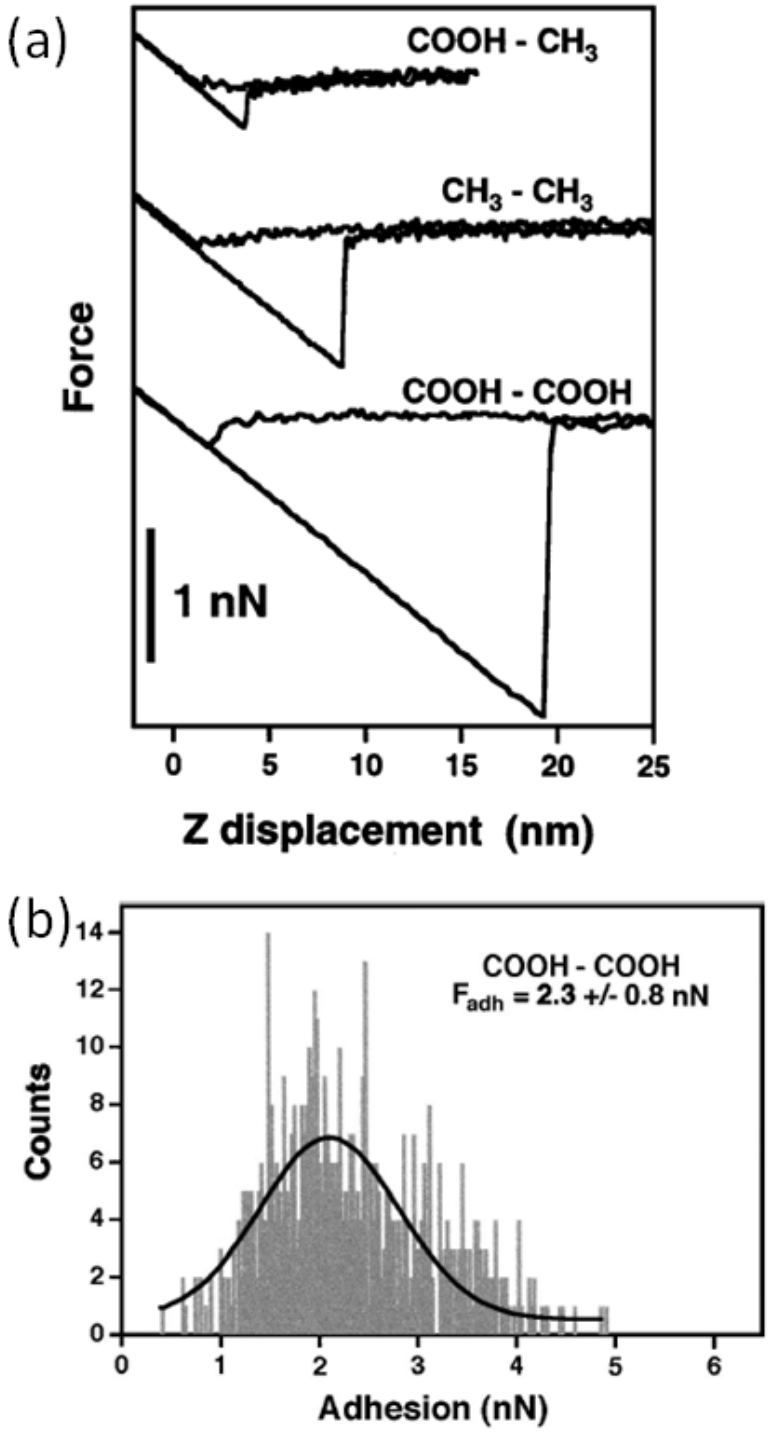

Figure 3.12 Representative force distance curves recorded in ethanol for COOH/COOH, CH_3/CH_3, and COOH/CH_3 tip-sample functionalization (a) and the histogram of adhesive force observed in COOH/COOH experiment (b).[163]

3.3.2.2 Tip calibration

In CFM and AFM, the local force is calculated from the value of the cantilever displacement (Δz) from equation (3.4). Therefore, in order to ensure that the forces in CFM and AFM are recorded accurately, the spring constant of the cantilever must be carefully determined. AFM and CFM experiments employ commercially available microfabricated silicon and silicon nitride cantilevers, and the manufacturer estimates the spring constants based on the geometry and elastic properties of the cantilever. However, these are only simple estimates of the force constants, since accurate values must include the thickness and mechanical properties of the coatings, such as those employed in CFM experiments. It was shown that gold-coated cantilevers used to prepare SAMs have larger spring constants than uncoated cantilevers.[158] Even in standard AFM, the force constant must be determined experimentally since it depends on the cube of the thickness level. This means that relatively small variations in the thickness can produce large variations among the force constants of identical tips. In addition, since the size and shape of the tip are very important in this calculation, experimentally used tips might exhibit smaller spring constants because they might have experienced a crush into a surface that changed their physical properties.

There are many methods that have been developed for the calibration of the cantilever spring constant. Two methods have been used in this thesis and both provided similar results that agreed with manufacturer's specifications.

The first method was developed by J.L. Hutter and J. Bechhoefer and it is a non-destructive way of calibrating the AFM tips.[164] This method is based on the idea that if a tip is far from a sample, its motion is due only to thermal fluctuation, and measurements of this motion at frequencies near the resonant frequency of the spring allow determination of the force constant based on the formula:

$$k = k_B T / P \tag{3.5}$$

where k_B is Boltzmann's constant, T is the absolute temperature and P is the area of the power spectrum of the thermal fluctuations alone. In this method, the power spectral density of the fluctuations in the spring displacement can be integrated as a Lorentzian to calculate the area P. This calculation is followed by the force constant determination, according to (3.5).

The second method used in this thesis was developed by Sader *et al.*[165,166,167,168] and calculates the spring constant considering the geometry of the cantilever, the resonance frequency ω_f and the quality factor Q_f. In this method the force constant is calculated using the formula:

$$k = 0.1906 \rho_f b^2 L Q_f \Gamma_i(\omega_f) \omega_f^2 \tag{3.6}$$

where b and L are the width and the length of a rectangular cantilever, ρ_f is the density of the fluid surrounding the cantilever (usually air), and Γ_i is the imaginary part of the so-called hydrodynamic function that can be easily plotted and calculated as a function of the Reynolds number $\mathrm{Re} = \rho_f \omega_f b^2 / (4\eta)$, where η is the viscosity of the surrounding fluid

(usually air). The expression of the hydrodynamic function is independent of the tip thickness and density. [167] In order to obtain the resonant frequency ω_f and the quality factor Q_f, the thermal noise spectrum of the cantilever is fitted to the response of a simple harmonic oscillator, using a nonlinear least squares fitting procedure. The geometrical characteristics b and L are determined by inspection of the cantilever with an optical microscope. Thus, all the variables in equation (3.6) are easily determined, and the method is an elegant way of calculating the cantilever spring constant. Although the method was initially developed for rectangular cantilevers, it is easily extendable to V-shaped cantilevers that can be considered equivalent to constructed rectangular cantilevers.[165]

3.3.3 Details on AFM measurements

AFM data were obtained using a PicoSPM (Molecular Imaging, Tempe, Arizona), using a Nanoscope IIE controller (Digital Instruments, Santa Barbara, CA). Images were acquired under ambient conditions, using the magnetic AC mode (intermittent contact). Height and phase shift data were recorded simultaneously. Images were recorded at scan rates of 1 – 2 Hz using a 30 μm x 30 μm scanner. A first order flattening is applied to the AFM images shown in this thesis. The non-contact probes used for image acquisition had a frequency of 100 – 300 kHz. For the acquisition of force-displacement curves, a chemically modified tip and corresponding sample were immersed in the organic solvents of interest and a series of 450 – 1000 force curves was obtained for each tip-sample combination. In this thesis, I report the average values of the adhesive interaction and the

errors that reflect the standard deviation of the data. The force constants of the chemically modified tips used in CFM experiments were calibrated using the methods of Hutter and Bechhoefer,[164] and Sader *et al.*[165,166,167,168] that are described in Section 3.3.2.2. The obtained force constant values were of about 0.2 – 1.5 Nm^{-1}, within the manufacturer's specifications.

Chapter 4

Study of *N*-(1-phenylethyl)-*N'*-[3-(triethoxysilyl)propylurea] (PEPU)

Water, alcohols, hexane, hexane/alcohol, and water/alcohol mixtures are often used as solvents in chemical processes and have many industrial applications. In mixtures of low molecular weight alcohols and water, the two components are completely miscible. Many experimental and theoretical studies suggested a complex structural arrangement in these systems. A significant self-association of alcohols in water has been observed in NMR,[169] infrared absorption,[170] thermodynamic,[171] and neutron diffraction[172] studies. In water-alcohol mixtures, hydrogen bonds are formed between water and alcohol molecules,[173,174] the water-water hydrogen bonding networks are fully percolating at low alcohol concentrations,[175] while evidence suggests that water clusters appear at high alcohol concentrations.[176,177,178]

4.1 Purpose of this study

In typical chromatography, the mobile phase is a mixture of organic solvents that mediate the interaction of the solvated components and the stationary phase. Because of this, understanding the mechanism by which the mixture of solvents interacts with the solid stationary phase is of critical importance. The reagent of interest in this study is *S*/*R*-*N*-(1-phenylethyl)-*N'*-[3-(triethoxysilyl)propyl]-urea, or PEPU (see Figure 1.1). PEPU may be readily covalently bonded to silica particles through a hydrolysis reaction.

The resulting stationary phase is a typical Type I, or Pirkle,[3] chiral stationary phase (CSP), where a chiral end group is attached, via an amide or ether linker, to the siloxane "tether". The tether is then attached to the surface of a colloidal silicate particle *via* a siloxane linkage. The PEPU interface also contains other features common to Type I CSPs: the presence of phenyl groups which may undergo stacking interactions, and sites (in this case within the urea group) which may undergo hydrogen bonding in solution. A PEPU-based CSP has been used to chromatographically separate the isocyanate and isothiocyanate derivatives of S/R-propranolol[10,11] in a mixed solvent of *n*-hexane, 2-propanol and acetonitrile.

The role of the solvent is precisely the objective of this study: my research purpose is to obtain a clear understanding of solvent distribution, solvent density, hydrogen bonding, and solvent orientation at the fluid-CSP boundary. Several recent articles[3,67,179,72] summarize techniques available for atomistic modeling of chiral interfaces. Briefly, modeling is generally restricted to *ab initio* or molecular mechanics calculations for non-covalently bonded host-guest complexes in the absence of solvent. Unfortunately, most CSPs do not form inclusion complexes where, to a first approximation, the solvent can be ignored. Alternatively, structure-function relationships[180,181] use experimental results for a series of analytes expressed as a function of molecular descriptors. After sophisticated regression, one arrives at a compact set of descriptors that reproduce elution orders and enantioseparation factors and have predictive power for related analytes. A representation of the CSP *and* solvent is included in this approach but only at an implicit level. In this study, I focus specifically on the

solvent, and perform detailed molecular dynamics simulations of the interface between PEPU and binary water/alcohol and alcohol/alcohol solvents.

The choice of solvent has a strong effect on the interaction forces observed in a chemical force spectrometric measurement. In systems where the pull-off forces between two hydrophobic surfaces are measured in aqueous solution[182] the forces observed are often very large and highly dependent on the ionic strength of solution, suggesting that solvation effects play a key role in the tip-sample interaction. It has been noted that[183] the interfacial free energy between the probe and substrate must dominate that of either the probe/solvent or substrate/solvent in order to achieve discrete sensitivity to chemical bonds formed in the contact between tip and sample. In this study, the solvation of the PEPU interface is examined in water, pure alcohols and in 36 binary solvent mixtures. These consist of methanol/water, 1-propanol/water, 2-propanol/water and methanol/1-propanol mixtures with the alcohol mole fraction ranging from 0 to 1.0. The comparison between these alcohols is interesting because they have virtually identical gas phase dipole moments but their dielectric constants vary from 32.6 for methanol to 18.3 for 2-propanol.[121] The solvation of PEPU interfaces in the binary solvents is modeled by molecular dynamics simulations to provide a molecular level description of the solvent characteristics at the surface. I have correlated these results to chemical force spectrometric measurements of the overall adhesive interaction between PEPU molecules and compare the structure and solvation in the various solvent mixtures.

4.2 Theoretical study of PEPU interfaces

4.2.1 PEPU model used in MD simulations

Model chiral stationary phases for PEPU are constructed based on the *ab initio* results, and considering the mesostructure of silicon surfaces. The interface, which consists of 1700 atoms, has been constructed from the optimized PEPU monomer with the terminal hydrogens used in the *ab initio* calculations replaced by silicon atoms. The PEPU molecules interact with the solvent through Lennard-Jones and electrostatic potentials. CHARMM[184] parameters are employed for the former, but atomic charges extracted from Mulliken population analysis of the optimized monomer, are employed for the latter. The united-atom representation, where the hydrogens do not appear explicitly, is used throughout. Details of the PEPU model, as employed in the simulations, are given in Table 4.1.

Table 4.1 Details of the PEPU monomer model. CHARMM parameters have been adopted for short-ranged repulsion and dispersion (as described by ε and σ), the charges are given in units of e, the electron charge, and are obtained from Mulliken population analysis. The positions given in the last three columns are relative to a silicon atom at (0,0,0).

Atom	ε(kJ/mol)	σ(nm)	q(|e|)	x(nm)	y(nm)	z(nm)
CH_2(terminal)	0.47781	0.2235	0.005496	-0.176	0.789	0.672
CH_2	0.47781	0.2235	-0.012318	-0.139	0.404	2.098
CH_2	0.47781	0.2235	0.152826	-0.037	1.588	2.971
NH	0.99746	0.1600	-0.142602	-0.351	1.359	4.329
O	0.66567	0.1600	-0.505865	1.229	2.547	5.126
C	0.50208	0.2100	0.526152	0.250	1.977	5.333
NH	0.99746	0.1600	-0.154374	-0.228	1.956	6.573
CH_3	0.75772	0.2165	0.020026	0.092	4.056	7.840
CH (chiral)	0.20334	0.2365	0.137784	0.466	2.577	7.701
CH(phenyl)	0.50208	0.2100	0.075069	0.240	1.732	8.949
CH(phenyl)	0.50208	0.2100	-0.048216	-0.607	2.120	9.985
CH(phenyl)	0.50208	0.2100	-0.022550	0.899	0.503	9.057
CH(phenyl)	0.50208	0.2100	-0.018984	0.716	-0.313	10.164
CH(phenyl)	0.50208	0.2100	-0.023431	-0.795	1.303	11.098
CH(phenyl)	0.50208	0.2100	0.010987	-0.135	0.085	11.192

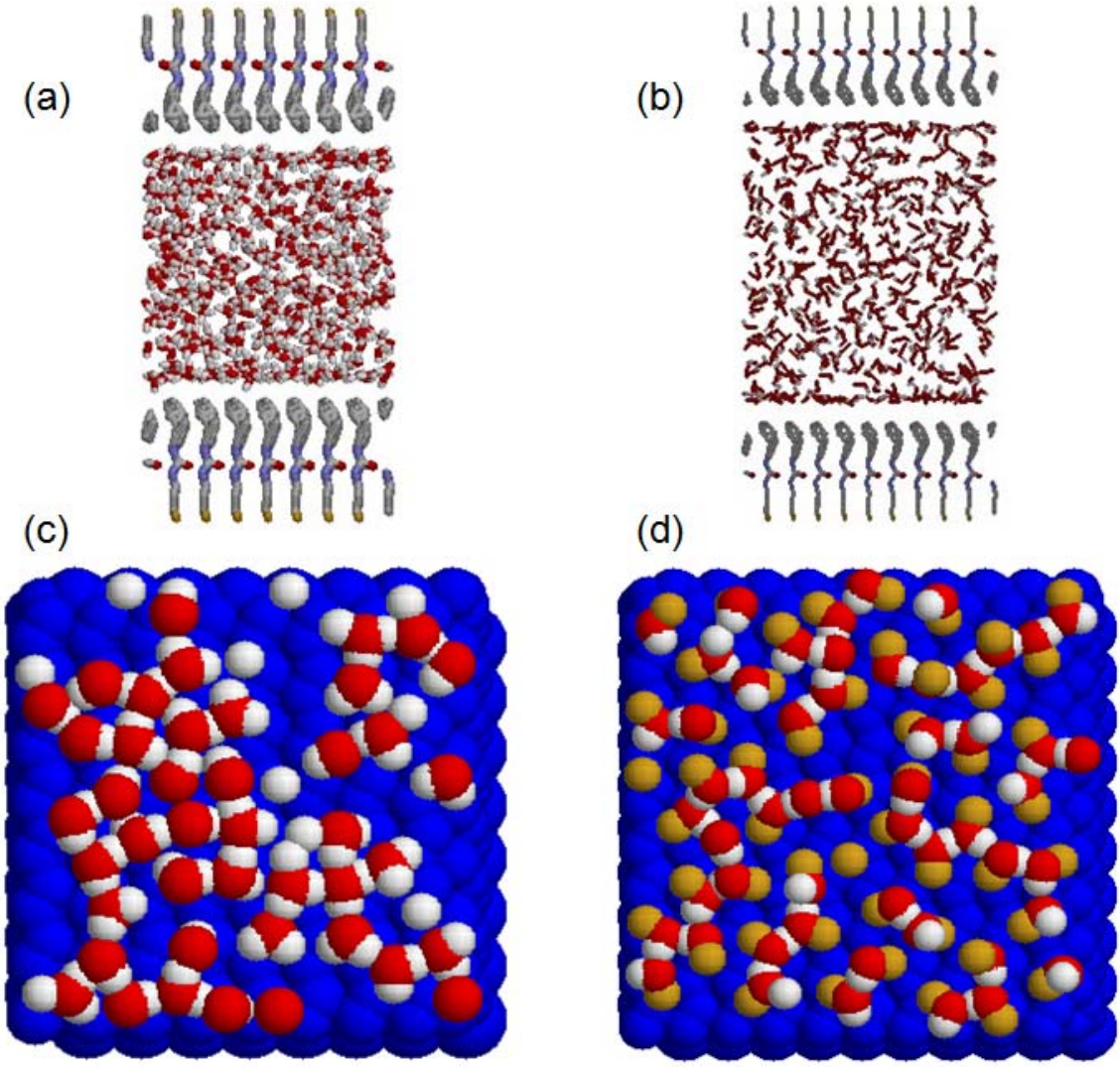

Figure 4.1 Snapshots from the simulations of water and methanol between two PEPU surfaces. For water simulations, each interface is 576 $Å^2$ with 64 PEPU molecules, snapshots of the sideview simulation cell and the contact layer (0-3 Å above the surface) are shown in (a) and (c), respectively. For methanol simulations, each interface is 900 $Å^2$ with 100 PEPU molecules, and snapshots of the sideview simulation cell and the contact layer (0-5Å above the surface) are shown in (b) and (d), respectively. The oxygen, nitrogen, carbon, hydrogen atoms, and methyl groups are indicated in red, blue, grey, white, and yellow, respectively. In (c) and (d), the atomic positions of the underlying surface are shown in blue.

4.2.2 Solvation of the PEPU interface

The interaction of the PEPU interface with pure-water or pure-methanol is complex. For instance, water is known to form a highly structured surface layer near uncharged surfaces with four and five membered rings evident.[36] For water, the poor interaction of the surface is offset by the energetic gains from an extensive hydrogen bonding network near the surface. For the PEPU interface, the presence of the urea group within the tether could potentially bring the water or methanol into closer proximity with the surface.

The distribution of water near the PEPU interface is shown in Figure 4.1. The side view of the simulation cell shows that the water is in contact with the surface and a higher solvent density is evident at the interface. Figure 4.1(a) also shows a well-defined second layer of water near the surface. A snapshot of the water layer nearest the surface is shown in Figures 4.1(c). Extensive hydrogen bonding networks, and four and five membered rings, are evident. These ring structures have been noted previously, but only with respect to highly idealized surfaces. Evidently, the morphology of the PEPU surface also allows formation of the ring structures. These simulations suggest that both the surface and the tip will be surrounded by two well organized layers of water in a CFM experiment with PEPU. These layers will be perturbed when the tip and surface come together and also when they are pulled apart.

The distribution of methanol near the PEPU surface is shown in Figures 4.1 (b) and (d). The sideview of the interface shows a dense layer of methanol near the surface but a second layer is only weakly present. A methanol monolayer is shown in Figure

4.1(d). Here it is clear that methanol adopts a dramatically different structure from water. First, since the methyl groups do not hydrogen bond, ring structures cannot form at the interface. Second, the methanol layer is less dense than for water even though hydrogen bonds are present within the layer. Similar results have been observed in pure-1-propanol and pure-2-propanol simulations.

In mixed water/alcohol systems, the interactions at the interface are even more complex. The extent of molecular motion at the PEPU interface in water/methanol is examined in Figure 4.2. Ideally, the duration of the simulation should be sufficient to allow molecules to arrive and leave the surfaces many times. Figure 4.2(a) illustrates the surface density fluctuations by showing the number of water and methanol molecules in a 5 Å layer above a PEPU surface during a typical simulation. From the figure, the solvent molecules exchange within the layer during the timeframe of the simulation, with the number of water molecules near the surface ranging from 90 to 110. Nevertheless, a closer inspection shows that many molecules remain in the interfacial region for the entire simulation (25 ps). Figure 4.2(b) summarizes the fraction of molecules that spend a given period of time within 5 Å of the PEPU surface for one water/methanol mixture. I find that 12% of the molecules spend the entire simulation time within 5 Å of the PEPU surface, 5% of the molecules spend only a very short time near the surface, and 7% of the molecules spend intermediate amounts of time at the surface. Most of the molecules never come within 5 Å of a surface. Examining the trajectories for individual surface molecules shows that molecules initially at the surface often move between 2 and 5 Å above the surface several times during the simulation (Figure 4.2(c)).

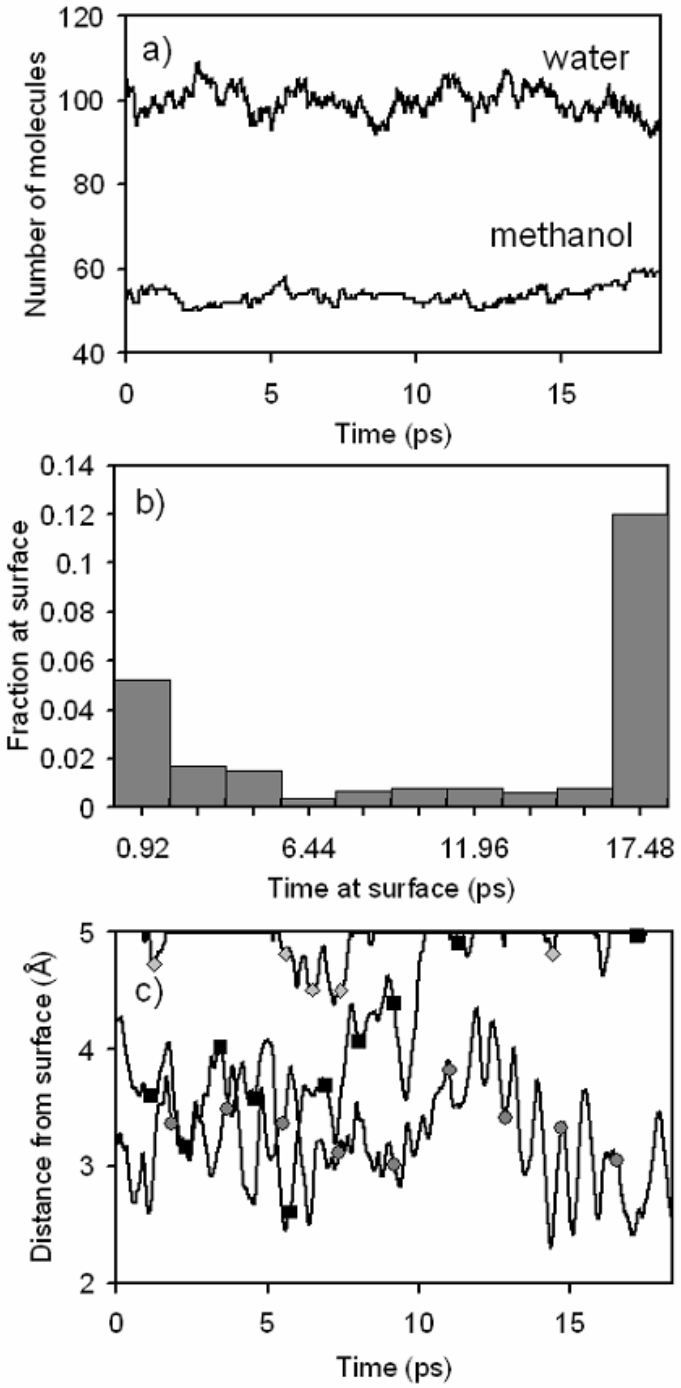

Figure 4.2 (a) Variation of the number of water and methanol molecules within 5 Å of the top-most carbon atom of the PEPU surface during the simulation. Data are presented for the mixture having a methanol mole fraction, X_{meth}, of 0.36. (b) Plots the distribution of residence times for solution molecules within a 5 Å layer next to the surface. (c) Trajectories of three molecules during the simulation.

As the fraction of methanol in the mixture increases, the overall number of molecules at the surface drops, but many remain near a surface for the entire simulation. Similar results were observed for the 1-propanol/water and 2-propanol/water mixtures. In order to provide a good description of the solvated PEPU interface, the results presented in this section are averages over 10 interfaces (five independent simulations, with 2 interfaces per simulation).

Figure 4.3 shows snapshots and density profiles for several water/methanol mixtures near the PEPU interface. Density profiles are collected by comparing the number of atoms found a distance z above the surface, relative to the number expected from the bulk density (ideal solvent). From the density profiles shown in Figure 4.3, a methyl group has a high probability of being within 2.5-3.0 Å of the topmost carbon atom of PEPU. In contrast, the alcohol oxygen distribution is broad, with a peak evident at roughly 2.8 Å above the surface, and a second peak at roughly 3.7 Å. The first peak corresponds to oxygen atoms in contact with the surface and, from Figure 4.3(b), the probability for contact decreases somewhat as the solvent becomes methanol-rich. Relative to methanol, the oxygen atom from water is more localized (within 2.5-3.0 Å) of the surface. The snapshot in Figure 4.3(d) shows all atoms within 3.0 Å of the surface for a predominantly water solvent. The water molecules prefer to form 4- and 5-membered hydrogen bonded rings that lie flat on the surface. When methanol accounts for a larger fraction of the solvent (Figures 4.3(e) and 4.3(f)), these ring structures are less evident at the surface but the water molecules still prefer to aggregate, forming at least one hydrogen bond parallel to the surface. The methanol molecules also participate in

hydrogen bonding, and some molecules lie flat on the surface (Figure 4.3(e)), but they typically orient the OH group towards the bulk. This may be seen by comparing the snapshots from Figures 4.3(e) and 4.3(f) that show the atoms 3 Å and 4 Å above the surface, respectively. For most of the molecules only the methyl group is usually found within 3 Å of the surface.

The behaviour of water and methanol near the PEPU surface can be understood by comparing their surface mole fraction with the mole fraction in the bulk liquid (Figure 4.4). For the purposes of defining a surface mole fraction, a molecule is counted if any atom belonging to that molecule is found within 3 Å of the top-most PEPU atom. Figure 4.4(a) shows the surface mole fraction of methanol and water, as a function of the bulk composition. Water prefers to reside in the bulk while the surface concentration of methanol is enhanced relative to the bulk. These results suggest that the networked water structure can be disrupted even by a small number of methanol molecules. Once this disruption occurs, the hydrogen bonding between waters on the surface is less favourable and the water prefers the bulk. The presence of methanol-rich surface domains, and partially formed networks of water, are evident in the snapshots (Figures 4.3(e) and 4.3(f)) and clearly show this disruption. Figure 4.4(b) shows the fraction of surface methanol molecules with an oxygen or a methyl group within 3 Å of the surface. Note that the fractions do not add up to unity since molecules in which both oxygen and methyl groups lie within 3 Å of the surface (i.e. lying parallel to the surface) are counted twice. From the figure, virtually all of the methanol molecules prefer to place the methyl group near the surface, and most point the hydroxyl group toward the bulk.

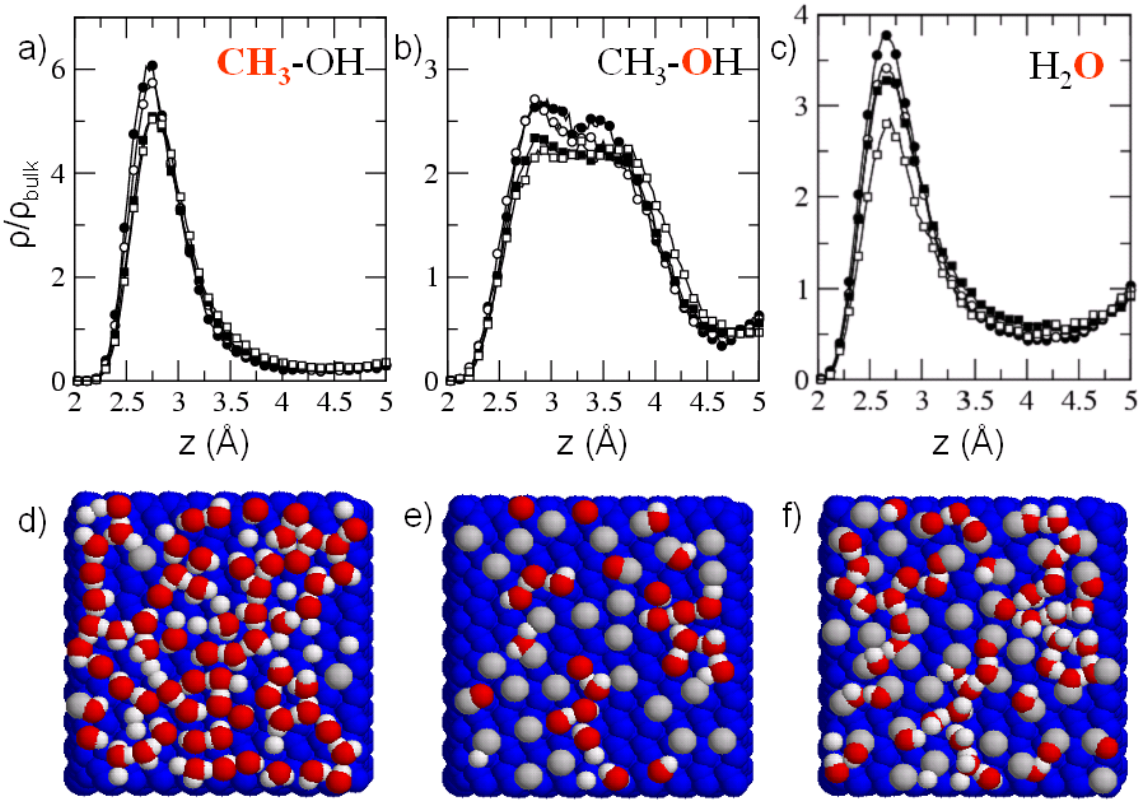

Figure 4.3 Density profiles and snapshots from water/methanol simulations. Distances are measured relative to the position of the top-most PEPU atom (z=0). Density profiles for the methyl group, the alcohol oxygen, and the water oxygen, are shown in (a), (b), and (c), respectively. The full circles, empty circles, full squares, and empty squares correspond to the mixtures with methanol mole fractions 0.123, 0.273, 0.457, and 0.692, respectively. Snapshots of the molecules found within 3 Å (d, e), and 4 Å (f) above the top-most PEPU are also shown. In (d) the methanol mole fraction is 0.059; for (e), and (f) the methanol mole fraction is 0.567. The oxygen, hydrogen, and alkyl carbon are indicated in red, white, and grey, respectively. The atomic positions of the underlying PEPU are shown in blue.

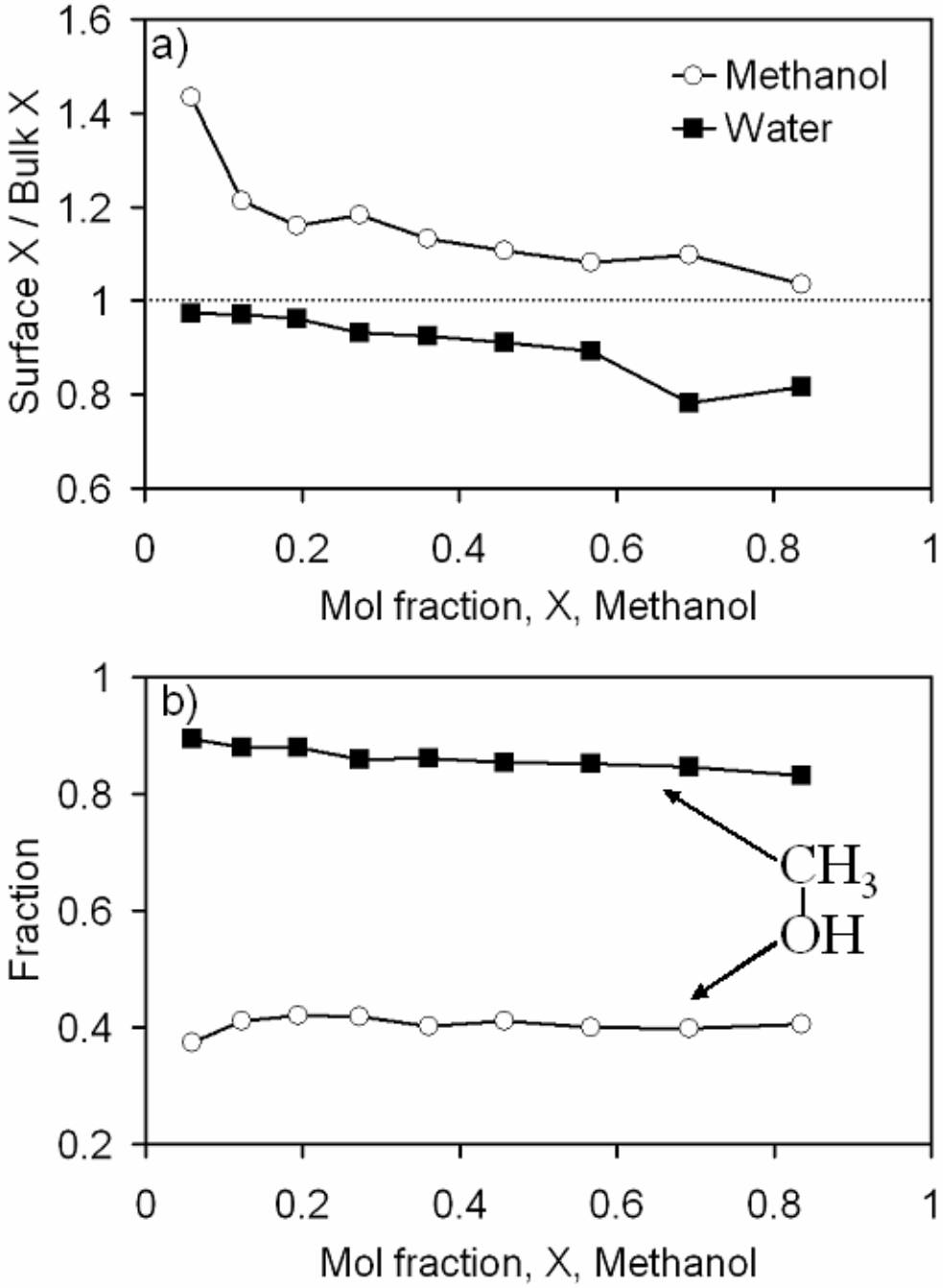

Figure 4.4 Relative distributions of water and methanol molecules at the PEPU interface. In (a) is plotted the ratio between the water and methanol mole fractions at the contact layer (0 – 3 Å above the surface) and their mole fractions from the bulk for all the water/methanol mixtures. The relative orientation of methanol molecules in the layer is shown in (b).

Density profiles and snapshots for 1-propanol/water mixtures are presented in Figure 4.5. The profiles are similar to the methanol/water profiles (Figure 4.3) except that the oxygen from 1-propanol has a broader distribution near the surface and the double-peak structure present for methanol (Figure 4.3(b)) is less evident. The peak in the density profile for the water oxygen also tends to be slightly higher for 1-propanol/water mixtures. Snapshots of molecules within 3 Å of the surface (Figures 4.5(d) and 4.5(e)) show that the hydrogen bonded water network is easily disrupted by the alcohol. 1-propanol tends to form domains with the apolar portion of the molecule at the surface. Since 1-propanol is large relative to water, the intermolecular spacing is larger than for water, and the water hydrogen bond network is disrupted more easily than for methanol/water mixtures. A comparison of Figures 4.5(d) and 4.5(e) shows that the alcohols form hydrogen bonds near the surface but they prefer to have their alkyl groups at the surface and form their hydrogen bonds 3-5 Å above the surface. A similar disruption of the water hydrogen bonding at the surface, and segregation, is observed for 2-propanol/water mixtures (Figure 4.7). Both 1- and 2-propanol displace water at the PEPU surface, as shown by the surface mole fractions (Figures 4.6(a) and 4.8(a)). The orientation of 1-propanol and 2-propanol at the PEPU surface are shown in Figures 4.6(b) and 4.8(b), respectively. At all concentrations, the molecules tend to place the terminal methyl groups within 3 Å of the surface. The other groups are less frequently found near the surface and, relative to methanol, fewer molecules have their oxygen atoms within 3 Å of the surface. A preference for the trans molecular configuration means that the

central carbon is often more than 3 Å away from the surface for 2-propanol (Figure 4.8(b)) and the surface fractions alternate for 1-propanol (Figure 4.6(b)).

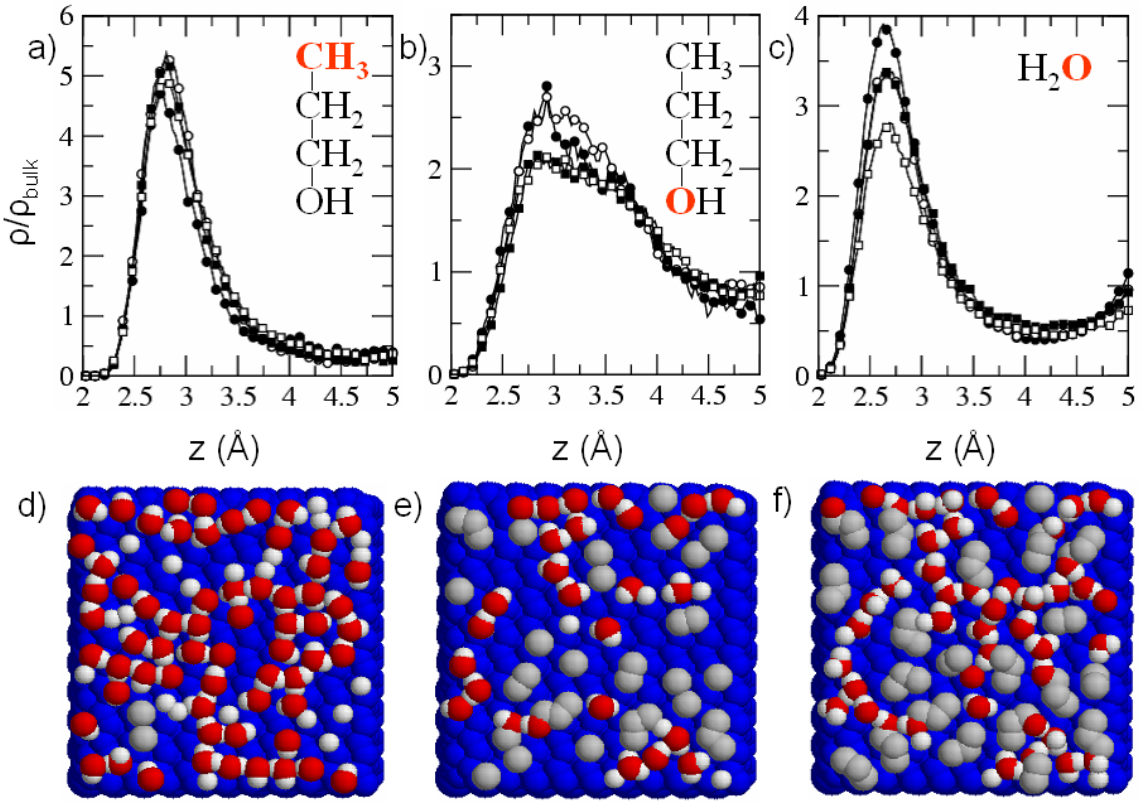

Figure 4.5 Density profiles and snapshots from water/1-propanol simulations. Distances are measured relative to the position of the top-most PEPU atom (z=0). Density profiles for the methyl group, the alcohol oxygen, and the water oxygen, are shown in (a), (b), and (c), respectively. The full circles, empty circles, full squares, and empty squares correspond to the mixtures with 1-propanol mole fractions 0.07, 0.167, 0.31, and 0.545, respectively. Snapshots of the molecules found within 3 Å (d, e), and 4 Å (f) above the top most PEPU atom are also shown. For (d) the 1-propanol mole fraction is 0.032; for (e), and (f) the 1-propanol mole fraction is 0.412. The oxygen, hydrogen, and alkyl carbon are indicated in red, white, and grey, respectively. The atomic positions of the underlying PEPU are shown in blue.

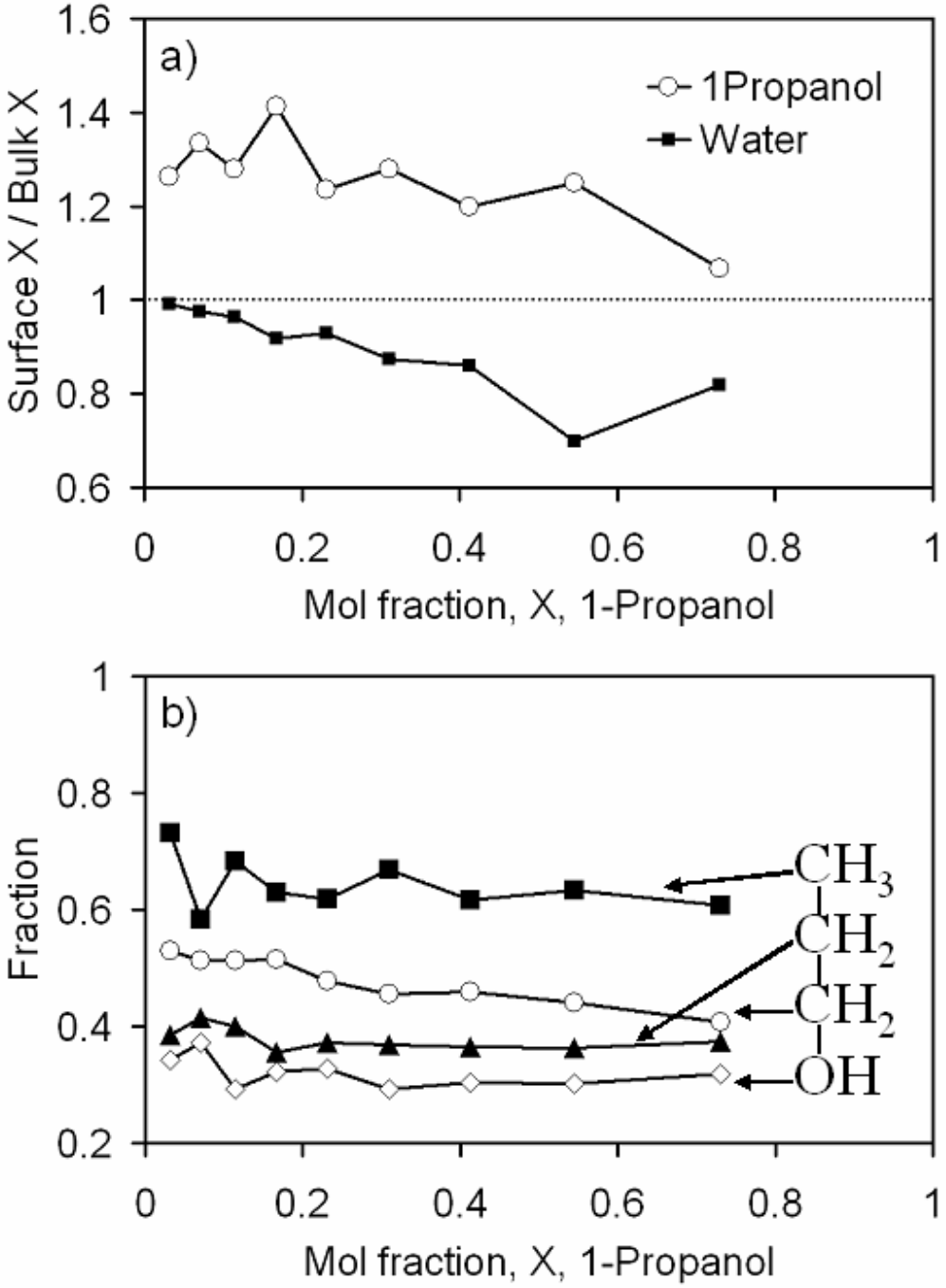

Figure 4.6 Relative distributions of water and 1-propanol molecules at the PEPU interface. In (a) is plotted the ratio between the water and 1-propanol mole fractions at the contact layer (0 – 3 Å above the surface) and their mole fractions from the bulk for all the water/1-propanol mixtures. The relative orientation of 1-propanol molecules in the layer is shown in (b).

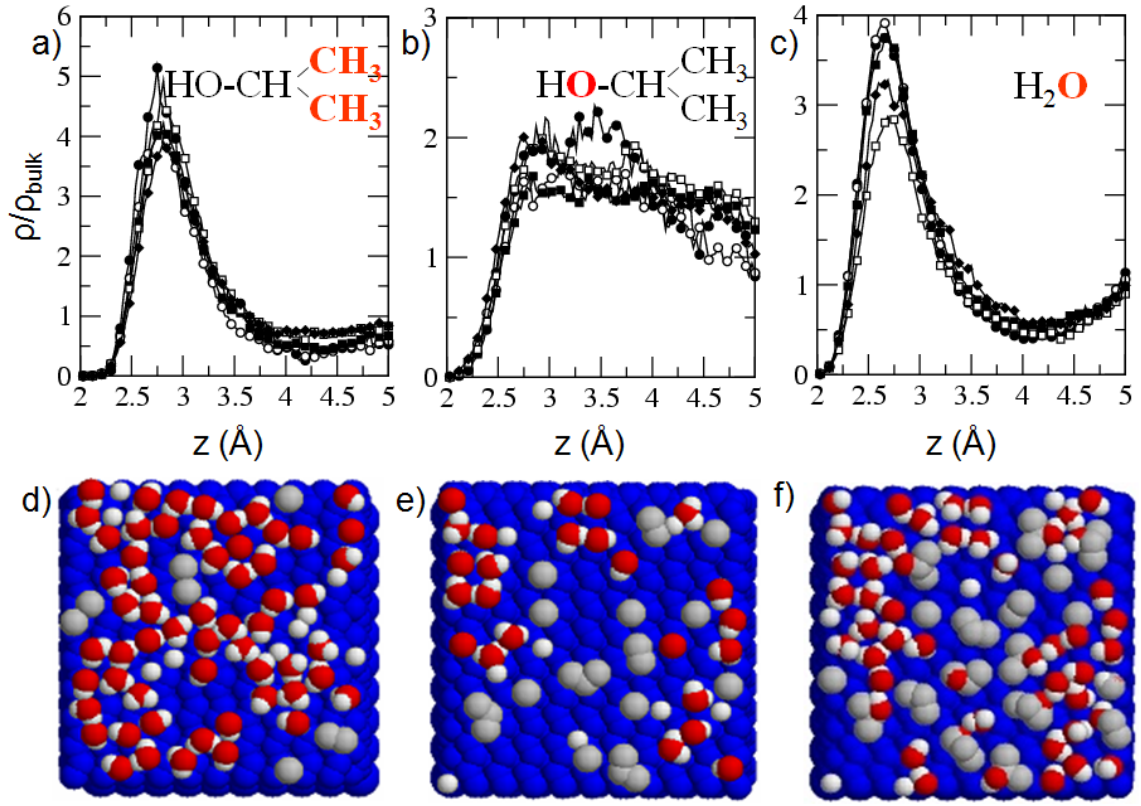

Figure 4.7 Density profiles and snapshots from water/2-propanol simulations. Distances are measured relative to the position of the top-most PEPU atom (z=0). Density profiles for the methyl group, the alcohol oxygen, and the water oxygen, are shown in (a), (b), and (c), respectively. The full circles, empty circles, full squares, and empty squares correspond to the mixtures with 1-propanol mole fractions 0.07, 0.167, 0.31, and 0.545, respectively. Snapshots of the molecules found within 3 Å (d, e), and 4 Å (f) above the top most PEPU atom are also shown. For (d) the 1-propanol mole fraction is 0.032; for (e), and (f) the 1-propanol mole fraction is 0.231. The oxygen, hydrogen, and alkyl carbon are indicated in red, white, and grey, respectively. The atomic positions of the underlying PEPU are shown in blue.

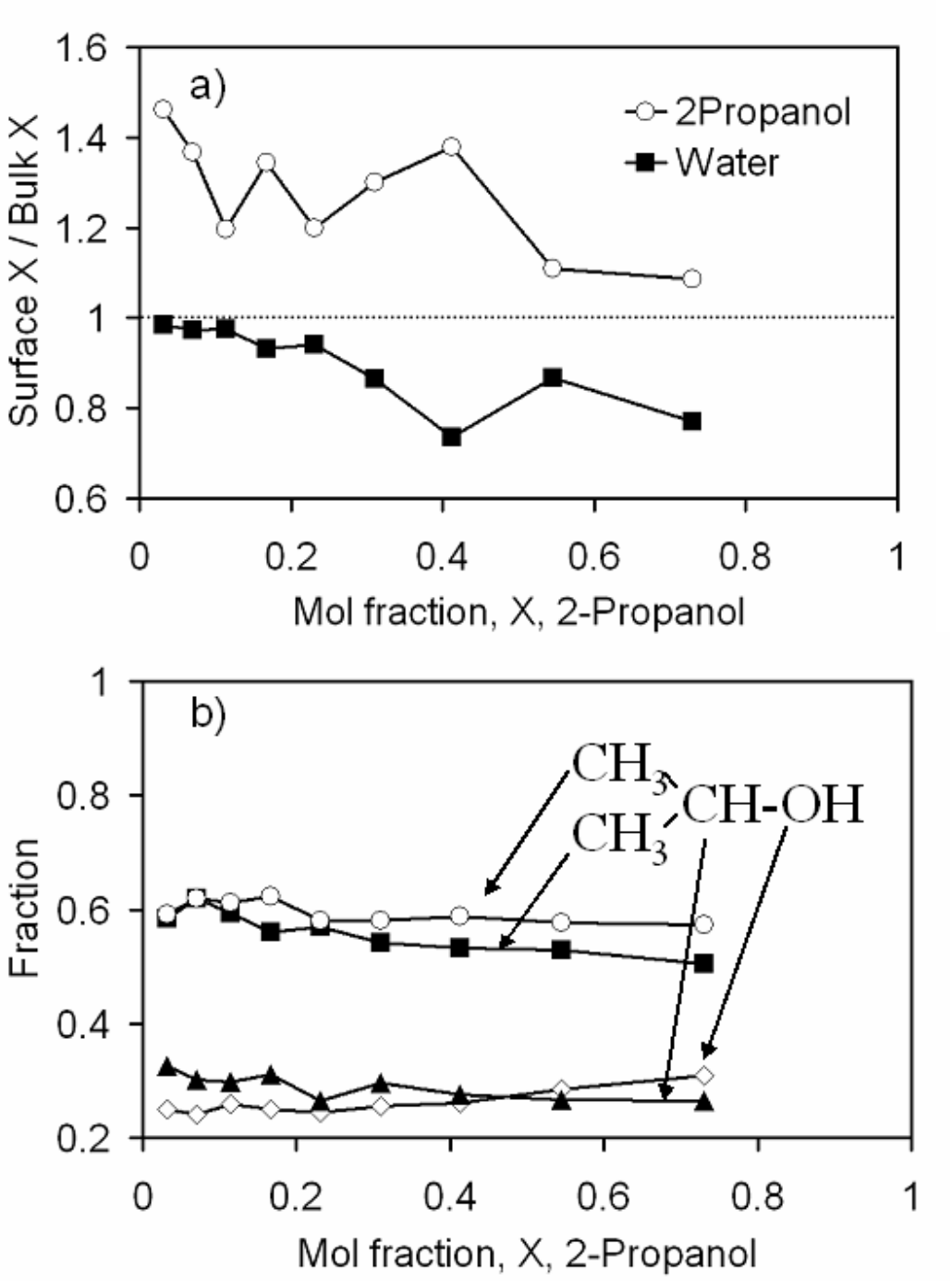

Figure 4.8 Relative distributions of water and 2-propanol molecules at the PEPU interface. In (a) is plotted the ratio between the water and 2-propanol mole fractions at the contact layer (0 – 3 Å above the surface) and their mole fractions from the bulk for all the water/2-propanol mixtures. The relative orientation of 2-propanol molecules in the layer is shown in (b).

The distinction between water and alcohol hydrogen bonding has been explored by Noskov *et al*.[175] for water/ethanol mixtures. They performed molecular dynamics simulations of mixtures of varying compositions and quantified the water/ethanol partitioning within the fluid. Their results indicate that the waters form hydrogen bonded clusters that have a large range of sizes. In particular, when the water mol ratio is 0.5, the probability distribution for cluster sizes is very broad: water clusters contain between 1 and 100 molecules. Overall, Noskov *et al*.[175] found that the fluid was more segregated into alcohol-rich and water-rich domains than one might expect for ethanol/water. I find a similar segregation at the PEPU surfaces. Even at very low alcohol concentrations, only methanol is able to integrate into the water structure (Figure 4.3(d)). 1- and 2-propanol, by virtue of their size and conformational preferences do not "fit" into the water structure at any concentration (Figures 4.5(d) and 4.5(e)). As a result, the PEPU surface can be roughly divided into water-rich regions and alcohol-rich regions. Figure 4.9 shows snapshots of the entire simulation cell, highlighting the water molecules. Water clusters are clearly present in the snapshots. Similar segregation was proposed by Dixit *et al*.[176] in a recent neutron diffraction study.

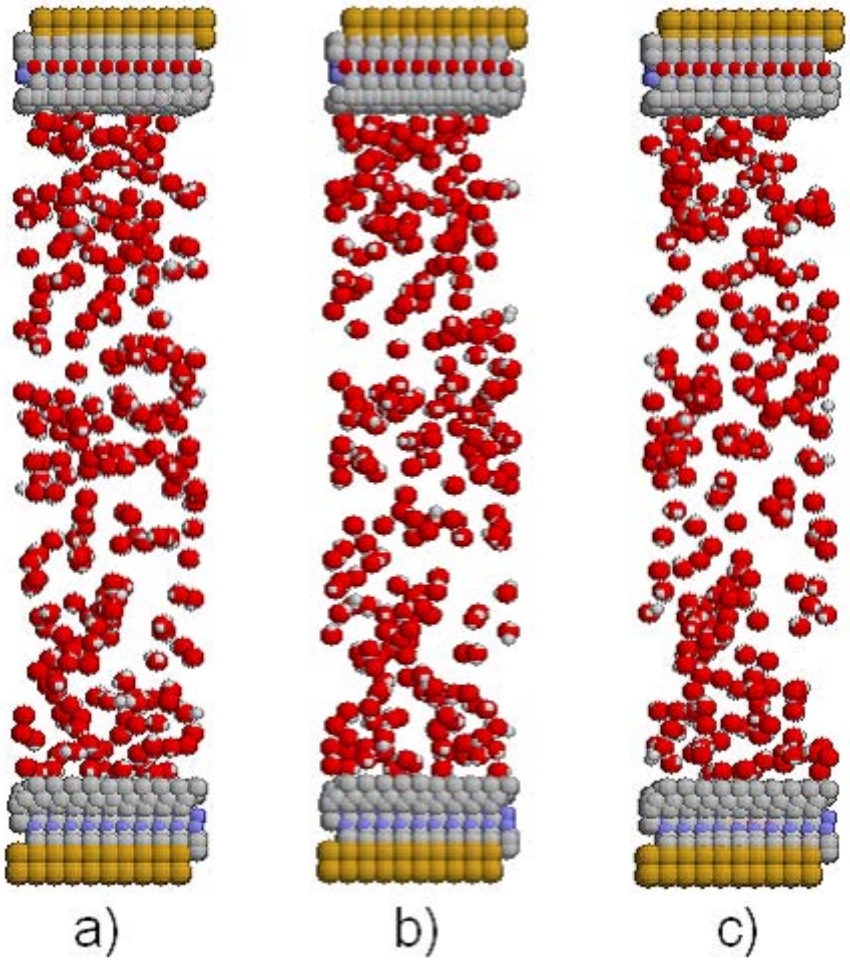

Figure 4.9 Sideview of the simulation cell for the 2-propanol/water mixture where the 2-propanol mole fraction is 0.73 at different simulation times:10.12 ps (a), 15.64 ps (b), and 21.16 ps (c). For clarity, only the water molecules are shown. The oxygen, nitrogen, carbon, and hydrogen are indicated in red, blue, grey, and white, respectively.

To further explore the relationship between hydrogen bonding preferences and segregation, methanol/1-propanol simulations were performed. The density profiles (Figures 4.10 (a),(b),(d),(e)) show that both alcohols prefer to have a contact layer at about 2.8 Å above the surface formed mainly from their alkyl component. The oxygen location is less well defined, but for methanol the oxygen distribution shows a double peak structure that is not present for 1-propanol. Snapshots of the contact layers show no clear indication of methanol or 1-propanol domains near the surface even at high concentrations of one of the alcohols (Figure 4.10(c)). In the absence of the water hydrogen bond network, the alcohols are more uniformly arranged. Figure 4.11(a) shows that the molecular distribution at the surface is equivalent (within statistics) to the bulk distribution. Note that the statistical error is highest for X_{meth}=0.945 since the solvent only contains 55 1-propanol molecules and only a few are near a surface during each simulation. The relative orientation of the molecules in the contact layer is shown in Figures 4.11(b) and (c). Methanol and 1-propanol adopt similar orientations at the surface in alcohol/alcohol and alcohol/water mixtures.

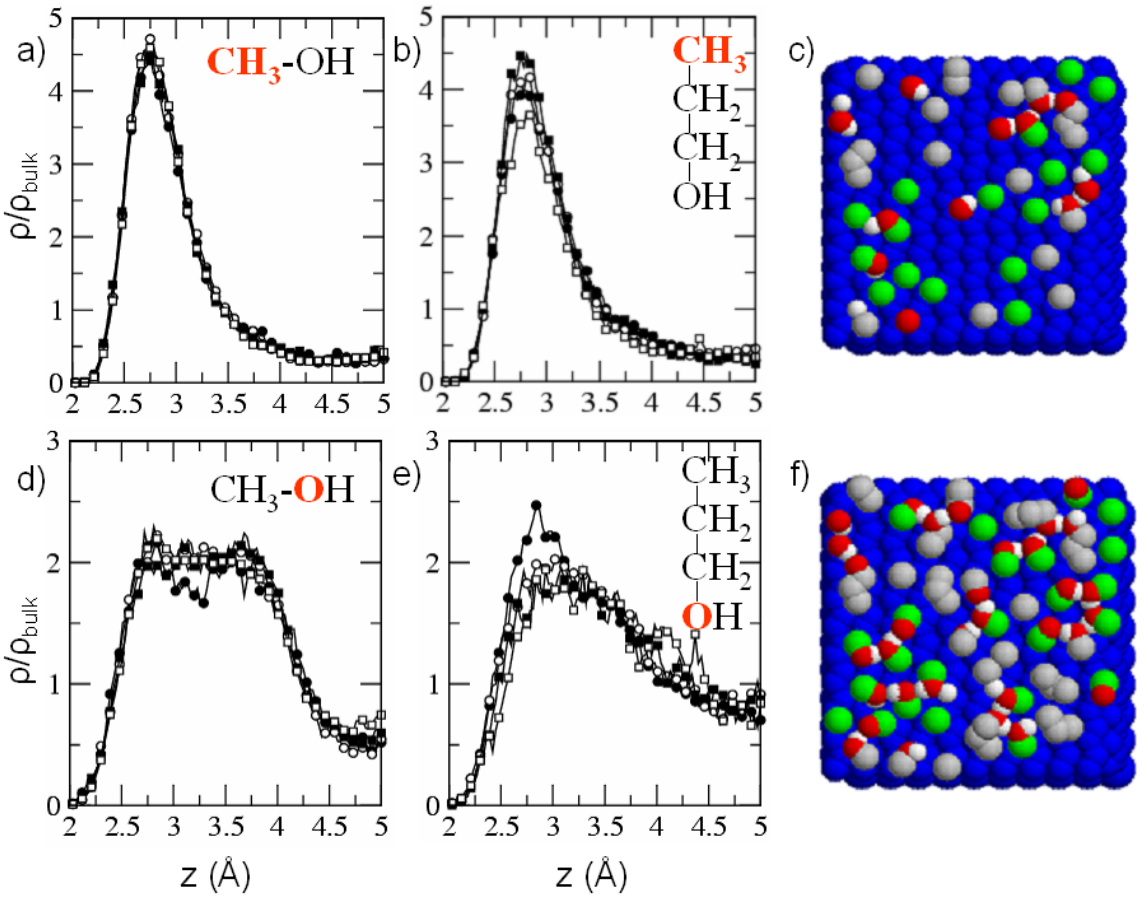

Figure 4.10 Density profiles and snapshots from methanol/1-propanol simulations. Distances are measured relative to the position of the top-most PEPU atom (z=0). Density profiles of methyl group from 1-propanol, methyl group from methanol, oxygen from 1-propanol, and oxygen from methanol, are shown in (a), (b), (d), and (e), respectively. The full circles, empty circles, full squares, and empty squares correspond to the mixtures with methanol mole fractions 0.333, 0.56, 0.73, and 0.881, respectively. Snapshots of the molecules found within 3 Å and 4 Å above the top most PEPU atom are shown in (c) and (f) for the methanol/1-propanol mixture with a methanol mole fraction 0.65. The oxygen, hydrogen, 1-propanol alkyl carbon, and methanol carbon are indicated in red, white, grey, and green, respectively. The atomic positions of the underlying PEPU are shown in blue.

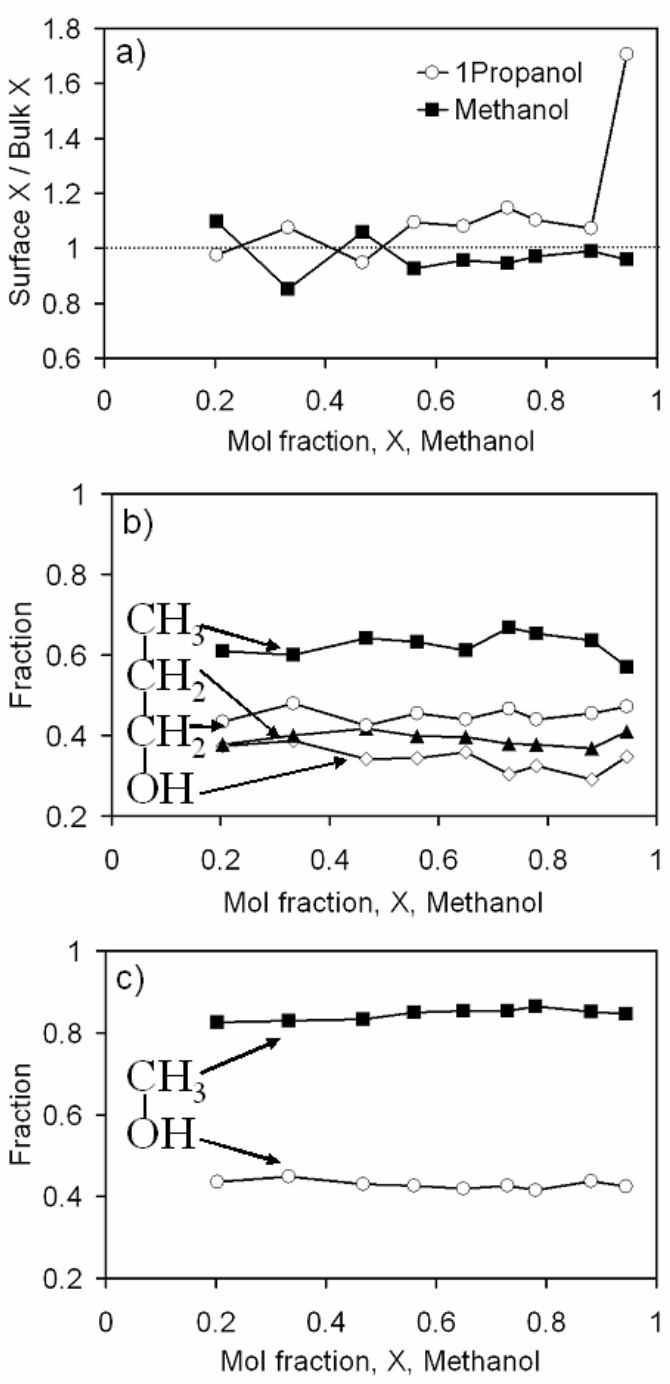

Figure 4.11 Relative distributions of methanol and 1-propanol molecules at the PEPU interface. In (a) is plotted the ratio between the methanol and 1-propanol mole fractions at the contact layer (0 – 3 Å above the surface) and their mole fractions from the bulk for all the methanol/1-propanol mixtures. The relative orientation of 1-propanol and methanol molecules in the layer is shown in (b) and (c).

By counting the number of hydrogen bonds in the 5 Å layer near the PEPU interface I can quantify the solvation effects at the surface. Following others, [175,185,186] I use a structural definition for hydrogen bonds: two molecules are considered to be hydrogen bonded if the H···O distance is less than 2.4 Å and the O–H···O angle is larger than 150º. In Figure 4.12 it can be observed that the total number of hydrogen bonds in methanol/water mixtures is larger than in either of the propanol/water mixtures at the same mole fraction. This is due to the larger number of hydrogen bonds formed by the alcohol in the methanol solutions. For example, at a methanol mole fraction of 0.36 in water, only 40% of the total hydrogen bonds are water-water hydrogen bonds. In the propanol mixtures of similar concentration, this value has increased to 60%. In methanol/1-propanol mixtures the preference for hydrogen bonding increases with the mole fraction of methanol, presumably as the smaller molecule may more readily form hydrogen bonding networks. A hydrogen bond analysis was also performed in the center of the simulation cell. The same overall trends with alcohol composition and concentration were observed, but a quantitative comparison between the number of hydrogen bonds at the surface and in the bulk is not possible since an accurate estimate of the solvent volume excluded by the structured PEPU surface is required.

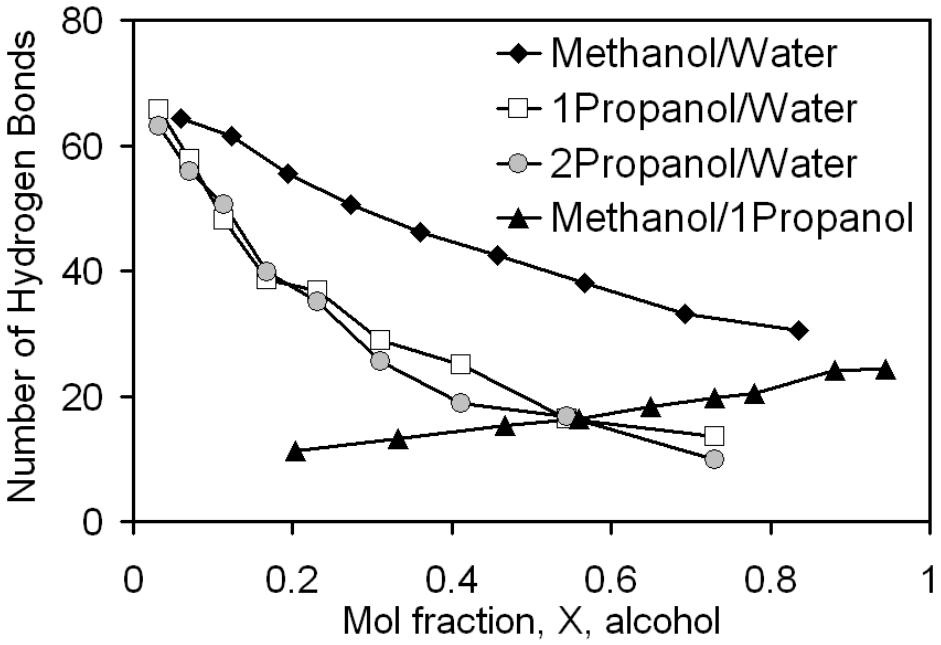

Figure 4.12 Number of hydrogen bonds in the 5 Å layer near the PEPU interface in methanol/water, 1-propanol/water, 2-propanol/water, and methanol/1-propanol mixtures as a function of the alcohol mole fraction (the methanol mole fraction is used for methanol/1-propanol mixtures).

4.3 Experimental study of PEPU interfaces

4.3.1 Morphology of the PEPU interface

All glassware used in chemical modification of either the substrate or AFM tips was passivated towards adsorption of alkoxysilanes. This was carried out by exposing the glassware to a 10^{-3} $molL^{-1}$ solution of octadecyltrichlorosilane in toluene. Silicon samples that were employed in this study were etched based on the method described by Hines.[187] Prior to etching, the glassware was cleaned using a basic peroxide solution composed of 1:1:4 volumes of $28\%NH_{3(aq)}$:$30\%H_2O_{2(aq)}$:H_2O at 80^oC for 10 minutes and then rinsed with doubly deionised distilled water. The Si samples were cleaned in the

basic peroxide solution described above for 10 minutes, and after this the oxide layer was stripped by immersion in an aqueous $HF_{(aq)}/NH_4F_{(aq)}$ solution for 2 minutes. After thorough rinsing, the samples were cleaned once again using 1:1:4 volumes of $30\%HCl_{(aq)}$:$30\%H_2O_{2(aq)}$:H_2O at 80°C for 10 minutes and then rinsed with doubly deionised distilled water. Both oxidized Si(111) surfaces and oxide sharpened silicon nitride cantilevers (Veeco Metrology LLC., Santa Barbara, CA) were functionalized with a chirally terminated surface by solution deposition from 1.0×10^{-3} $molL^{-1}$ in toluene of either (*R*) or (*S*) *N*-(1-phenylethyl)-*N'*-[3-(triethoxysilyl)propyl]-urea (95%, Gelest Inc., Tullytown, PA).

Previous XPS work[188] has shown that the surface becomes terminated with SiOH sites upon oxidation. These sites on the surface can be subsequently reacted with the ethoxy groups of PEPU to form a covalent link to the surface:

$$\text{-Si-OH} + (C_2H_5O)_3\text{Si-PEPU} \rightarrow \text{-Si-O-}(C_2H_5O)_2\text{Si-PEPU} + C_2H_5OH \qquad (4.1)$$

leaving two more ethoxy groups which might undergo further links to the surface or, more likely, react with ethoxy groups on neighboring PEPU molecules and those in solution to form a cross-linked structure. Similar depositions on oxidized Si(111) surfaces have been performed for alkoxylsilanes and chlorosilanes[189] and showed consistent results. AFM images of the PEPU-terminated Si surface are shown in Figures 4.13. Several pits, probably a result of the Si etch process, as well as some agglomerates, presumably of highly cross-linked PEPU are present on the surface, but generally, the resulting surfaces are very smooth and uniform.

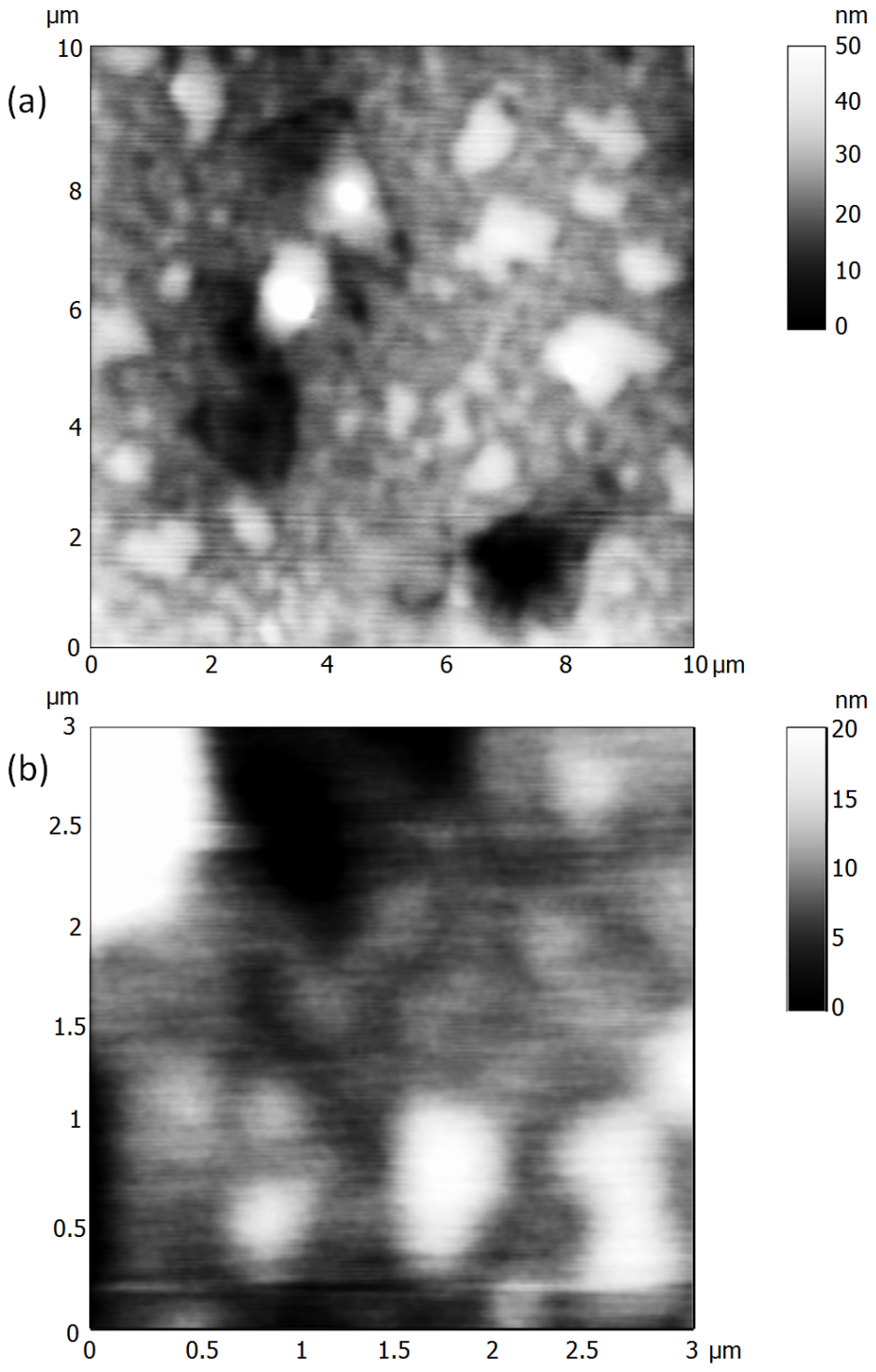

Figure 4.13 Tapping mode height images of the Si(111) surface after exposure to *S*-PEPU. Scale is 10 µm in (a) and 3 µm in (b). Similar topographies were obtained for *R*-PEPU and *racemic*-PEPU.

4.3.2 Chemical force spectrometric measurements

Force profiles for *R*-PEPU terminated tips on *S*-PEPU-terminated samples in a series of water/alcohol mixtures are shown in Figure 4.14(a). The solvent mixtures experimentally used had the same compositions as those modeled using molecular dynamics simulations and discussed in Section 4.3. Force profiles for the other chiral combinations (*R*/*R*, *S*/*S*, *S*/*R*) were also acquired giving similar results, but without highlighting a clear chiral discrimination. The well depth obtained from the force-displacement curve as the tip was retracted from the surface was used to obtain the adhesive force between tip and sample. For any given solvent composition, the adhesive force reported was the average of between 150 – 250 such measurements. At high water concentrations, the adhesive forces between tip and sample were not highly reproducible.

Despite the poor reproducibility at high water concentrations, some general trends may be observed in the data. In all cases, the magnitude of the adhesion force decreases with increasing alcohol concentration. With pure water as the solvent, the adhesive forces observed are on the order of 25 – 50 nN. This is reduced by an order of magnitude with pure alcohol as a solvent. In the mixtures where water is predominant, there is a high force interaction between the tip and the substrate as the hydrogen bonding network is disrupted at the interfacial region. In the alcohol rich mixtures, the force is significantly lowered as the hydrogen bonding network is less pronounced. This is consistent with the molecular dynamics results which showed a decline in the number of hydrogen bonds as

the fraction of alcohol increases (Figure 4.12). The modeling showed that water forms domains at the interface and also cage-like regions inside the bulk.

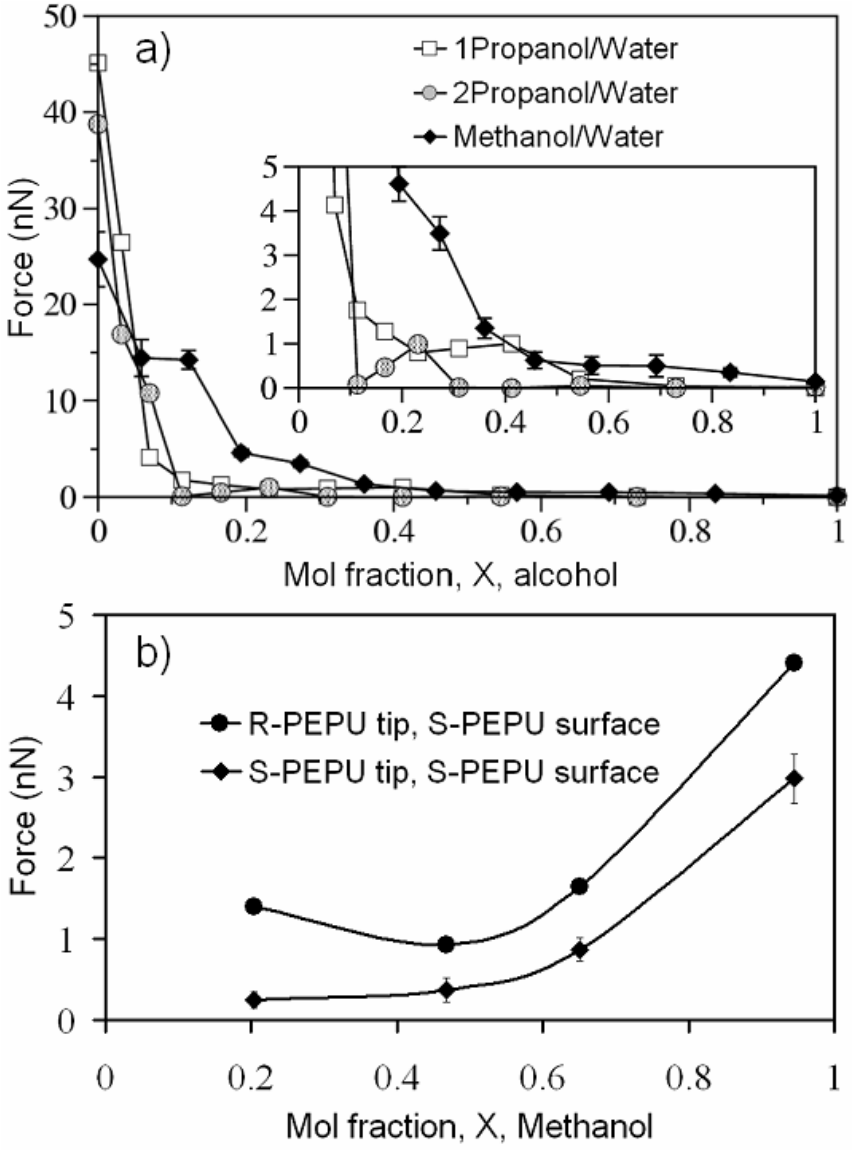

Figure 4.14 (a) Force curves obtained in water/alcohol mixtures between an R-PEPU tip and S-PEPU surface. (b) Force curves obtained in methanol/1-propanol mixtures for two combinations of R and S isomers of PEPU deposited on an AFM tip and an oxidized Si(111) surface. Typical error bars are shown on one curve. The errors reflect the standard deviation of the data acquired from 150-200 force curves for each mixture. Error bars on the remaining data are similar in magnitude, but are omitted for clarity.

There is also a significant difference between the 1-propanol/water or 2-propanol/water force profile as compared with the methanol/water profile. The forces from 1- or 2-propanol/water mixtures decrease sharply at an alcohol mole fraction of about 0.1 and are very low (0 – 2 nN) for the higher alcohol fractions. Such a sharp decrease is not apparent for the methanol/water mixtures. The curves in Figure 4.14(a) decrease much more smoothly as the methanol fraction is increased. These results can be understood by considering the distribution of hydrogen bonding networks at the surface (compare the profiles of the curves in Figure 4.14(a) with those in Figure 4.12). 1-propanol and 2-propanol are large molecules that prefer to have their hydrophobic alkyl groups near the surface. Thus, even at relatively low alcohol concentrations, the hydrogen bonding network is strongly disrupted. As the tip/sample interaction appears to be strongly controlled by the extent of the hydrogen bonding network at the interface, this leads to the lower adhesive forces observed. For example, from Figure 4.12 one may note that a 1-propanol mole fraction of just 0.2 in water is sufficient to nearly halve the number of hydrogen bonds at the surface. In Figure 4.14(a), it can be observed that at the same concentration of 1-propanol, the adhesive interaction has dropped to < 5% of its value in pure water. As a smaller molecule, methanol is more predisposed to form hydrogen bonds to other methanol molecules, or to water molecules. Indeed, I see that for methanol/water mixtures in Figure 4.12, methanol mole fractions in excess of 0.6 are required to halve the number of hydrogen bonds at the interface, as compared to pure water. This may be compared to Figure 4.14, which shows that the adhesive interactions drop off relatively slowly. Thus, the hydrogen bonding network remains intact over a

much wider range of methanol/water compositions, leading to a much more gradual decrease in adhesive interaction as the methanol concentration is increased.

In methanol/1-propanol mixtures, the forces observed between a PEPU-terminated tip and a PEPU-terminated surface are much smaller that those found in the water/alcohol mixtures. These forces range from 0 to 5 nN (Figure 4.14(b)), and are comparable to the adhesive forces observed in the pure alcohols. The forces also increase with the content of methanol in the mixture, mirroring the increase in hydrogen bonding with methanol concentration, as seen in Figure 4.12. While the MD simulations show that the alcohols are less densely packed than water at the interface, so that the forces required to disrupt the hydrogen bond network are smaller, there nonetheless appears to be a strong correlation between the adhesive forces observed and the degree of hydrogen bonding taking place at the interface. This correlation is present regardless of the handedness of the enantiomer coating the tip.

Force spectrometric measurements were performed in pure solvents as well. Force titration profiles were obtained in water with varying pHs. For each CFM experiment, 300-500 force curves were acquired at 10 different points on the surface at a given pH. The average standard deviation within a data set was found to be 6%, and the standard deviation between data sets was determined as 4%. Since the surface is homogeneous (Figure 4.13), it does not affect the force interactions. I have found a small variation in the magnitude of the adhesive interaction as a function of pH, but chiral selectivity was not observed in this system. The average of all PEPU experiments in water is presented in Table 4.2.

Table 4.2 Adhesive chemical force interactions observed between *R*- and *S*-PEPU terminated tips and samples in water.

tip terminal group	adhesive interaction (nN) on sample	
	R-PEPU	*S*-PEPU
R-PEPU	27.8±10.9	38.6±10.5
S-PEPU	35.9±16.3	35.5±6.7

These data indicate that chiral selectivity might be more than just a function of the type of chiral centre present: morphology may also play an important role, with a surface containing many configurations of the chiral site presumably being less selective. The magnitude of the forces observed between the PEPU-modified tip/sample combinations can provide important information. These range between about 30 and 50 nN, which is of a similar magnitude to that observed for the interaction of a tip and sample coated with SAM's of 16-thiohexadecane (60 nN) or 1-thiododecane (12.5 nN).[158,190] This demonstrates that the force interactions observed are dominated by what are commonly referred to as hydrophobic interactions between the PEPU chains. As shown by the molecular dynamics simulations, these large forces arise because in order to pull apart the tip and sample, the hydrogen bonding water network must be disrupted at the interfacial region.

The experiment on the PEPU-terminated Si(111) surface was also performed in pure methanol. As seen in Table 4.3, in this case discrimination was indeed observed on the surface, with the like-like (*R*-*R* or *S*-*S*) combination having an interaction about 2 nN

greater than the non-like (*S*-*R* or *R*-*S*) combinations. The same tip was used in both pairs of experiments, with 300 data points being collected at four different locations on the surface. The errors reported are the standard deviation from all 1200 data points, although the adhesive wells observed did not vary, within experimental error between points on the surface in this case. Using tips coated with a racemic mixture of PEPU resulted in no variation in force interaction on *R*- and *S*-PEPU-terminated surfaces.

Table 4.3 Adhesive chemical force interactions observed between *R*- and *S*-PEPU terminated tips and samples in methanol.

tip terminal group	adhesive interaction (nN) on sample		
	R-PEPU	*S*-PEPU	*racemic*-PEPU
R-PEPU	6.7±1.7	1.8±0.5	6.2±3.0
S-PEPU	2.7±0.7	6.7±2.0	6.7±3.0
racemic-PEPU	7.4±2.5	6.6±3.0	6.3±3.0

The difference in adhesive interaction between like-like and unlike pairs can be attributed to two effects. First, for the data acquired in water as a solvent, hydrophobic forces are much more important than in a less polar solvent such as methanol. In methanol, the solvent no longer forms strong hydrogen bonding networks in the interfacial region. Second, methanol still shows little tendency to interact with the PEPU layer, as seen from the MD simulations. This leaves the chiral centers at the end of the molecules free to interact with one another at the interface and give rise to chiral discrimination. However, when water is added in a binary mixture with methanol (or other alcohols such as1-propanol and 2-propanol), the system behaves closer to the pure-water case, rather than the pure-alcohol case, because the number of hydrogen bonds increases significantly. Consequently, there is no chiral discrimination observable in water/alcohol binary mixtures (Figure 4.14).

Chapter 5

Study of phenylglycine- and leucine-derived chiral stationary phases

The presence of chirality at an interface enables a surface to distinguish between enantiomers. The mechanism by which this selectivity occurs is complicated by the surface morphology, the possible involvement of the solvent, and the characteristics of the chiral molecules at the surface. The separation is usually performed with a chiral interface, or chiral stationary phase (CSP) that acts as a selector for the enantiomers from the mobile phase. In this section I examine the detailed atomic structure and dynamics at "brush"-type chiral interfaces using molecular dynamics simulations, *ab initio* methods, X-ray photoelectron spectroscopy, and techniques in scanning probe microscopy, particularly chemical force methods.

5.1 Purpose of this study

In this study, I focussed my attention on developing a better understanding of the interfacial structure and the solvent interaction with the DNB-phenylglycine and DNB-leucine CSPs. It is well known that solvent composition has an effect on the absolute retention times because of competitive hydrogen bonding with the substrate.[137] Typically there is a decrease in retention time as the alcohol percentage is increased in the mobile phase.[191] DNB-phenylglycine and DNB-leucine have common selectivity for some classes of compounds.[6] However, DNB-leucine has an enhanced selectivity for compounds like benzodiazepines, whereas DNB-phenylglycine is usually used for

separating aryl-substituted sulfoxides and derivatives of β-naphthol, α-indanol, α-tetratol, and aryl-substituted hydantoins.[192] The chiral separation mechanism for these two CSPs has been extensively investigated and debated in the literature:[9,193,194,195,196] A minimum of three points of interaction are required between the solute and the CSP and these are: the dinitrophenyl ring can form face-to-face ring interactions with a π-donor group in the analyte; the dinitrobenzamide NH (N(23)-H(24) in Figure 5.1(a) and N(21)-H(22) in Figure 5.1(b)) can hydrogen bond with the analyte; and the oxygen from the other amide carbonyl (O(14) in Figures 5.1(a) and 5.1(b)) can act as a hydrogen bonding site. The access to these three interaction sites is governed by the steric bulk of the phenyl or isobutyl groups located on the C(15) atom of the selectors.[193]

By means of molecular dynamics simulations I examined the DNB-phenylglycine and DNB-leucine conformations at the interface and related these to H-bonding abilities of the selectors. Simulations of interfaces present many challenges. Stationary phase interfaces are particularly demanding because they require that the selector have a complete, atomic level description, together with a proper representation of its flexibility, and with an appropriate representation of the surface environment (surface coverage, end-caps, etc.).[80] Nonetheless, some simulations of achiral selectors for HPLC have been published.[81,82,83,84] Most notably, the entanglement and solvation of long chain alkanes tethered to silica has been examined in some detail.[81,82,83,84] To date, only a few simulations of chiral interfaces have been published. Notable are Zhao's studies of Whelk-O1 CSP.[86,87] In this section I present the MD results for interfaces that include the selectors (DNB-phenylglycine or DNB-leucine), trimethylsilyl end-caps, and silanol

groups and these are covalently attached to a single underlying layer of Si that is stationary throughout the simulation. The selectors, end-caps, and silanol groups have surface coverages of 1.10 μmol/m^2, 3.29 μmol/m^2, and 4.26 μmol/m^2, respectively, consistent with experimental coverage for this type of CSP.[2,138,139] To fully understand the impact of solvent composition, these interfaces are examined for four solvents: 100% hexane, 90:10 hexane/2-propanol, 80:20 hexane/2-propanol, and 100% 2-propanol. The MD simulations reveal the solvent distribution in the vicinity of the DNB-phenylglycine and DNB-leucine interfaces, and emphasis is placed on identifying and characterizing hydrogen bonding interactions between the solvent and selectors.

I also examined the chiral interactions in the DNB-phenylglycine and DNB-leucine CSPs using chemical force spectrometry, X-ray photoelectron spectroscopy (XPS), and surface infrared spectroscopy. Both CSPs show an enhanced self-selectivity,[196,197] that allows performing chemical force spectrometric measurements in which I probed the interactions between an atomic force microscope (AFM) tip and sample both modified with the CSP and looked for self-discrimination between different diastereomeric pairs (*R,R* or *S,S* vs. *R,S* or *S,R*) formed between tip and sample.

5.2 Theoretical study of DNB-phenylglycine and DNB-leucine interfaces

5.2.1 Representation of the chiral selectors

The DNB-phenylglycine and DNB-leucine selectors are shown in Figure 5.1. Throughout this section, the term "selector" will be used to refer to a single chiral molecule of a CSP. The two selectors consist of a dinitrophenyl (DNP) group, a chiral carbon located between two amide linkages, a lateral group (a phenyl ring for DNB-phenylglycine and an isobutyl chain for DNB-leucine), and a tether that joins the selector to the surface. As shown in Figure 5.1, the model tether is trifunctionally bonded to the surface. Experimental surfaces may also include mono- and bi-functionally linked selectors,[22] but these are undesirable since they are less resistant to hydrolysis. There are multiple hydrogen bonding sites within each selector but the oxygen and hydrogen atoms in the amide groups are of particular interest. The nitro groups on the dinitrophenyl ring are also examined. Figure 5.1 shows the atom numbering which will be used throughout this study.

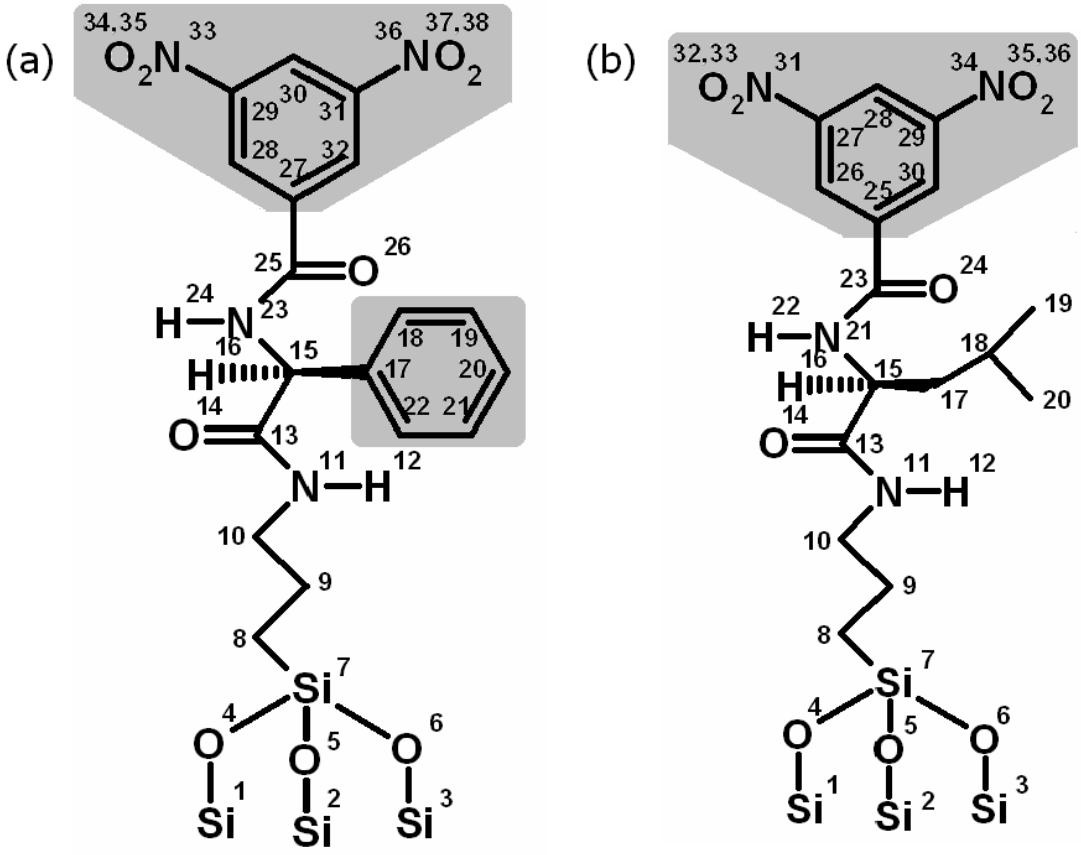

Figure 5.1 The semi-flexible representations of the DNB-phenylglycine (a) and DNB-leucine (b) selectors with the rigid units indicated by shaded areas. The silicon atoms numbered 1-3 form part of the underlying silicon layer representative of the surface. The atom numbering shown here will be used throughout this study.

Semi-rigid representations of both CSPs are employed in simulations. To be precise, the aromatic regions, including the dinitrophenyl rings in both selectors and the phenyl ring in DNB-phenylglycine, are rigid. All other portions of the selectors are flexible. These rigid regions are referred to as rigid units (RUs) and, in the simulations, a rigid unit translates and rotates consistent with the forces on the atoms within the unit. However, the *relative* atomic positions within the unit do not vary with time. In defining an interaction potential, I omit intramolecular potentials within the RU because these will be constant. It is important to note that the RU atoms still interact with atoms outside of the unit, including atoms within the same selector, from other selectors, from the end-caps, and so on. RUs are also involved in intramolecular potentials that include non-RU atoms. For example, in the DNB-phenylglycine selector the potential includes a bend for C(15)-C(17)-C(18) and a torsion for C(13)-C(15)-C(17)-C(18). The shaded regions in Figure 5.1 identify the RUs for DNB-phenylglycine and DNB-leucine.

The energy of the interfacial system is given by:

$$E^{full} = \frac{1}{2}\sum_i m_i \vec{v}_i^{\,2} + \frac{1}{2}\sum_{RU} m_{RU} \vec{v}_{RU}^{\,2} + \frac{1}{2}\sum_{RU} I_{RU} \vec{\omega}_{RU}^{\,2} + \sum U^{LJ} + \sum U^{electro} + \sum U^{intra} \tag{5.1}$$

The first term is the translational kinetic energy of all the atoms, except those involved in RUs. The second and third terms are the translational and rotational kinetic energies, respectively, of the rigid units. m_{RU}, I_{RU} and $\vec{\omega}_{RU}$ are the total mass, moment of inertia and angular velocity of the rigid unit, respectively. The last three terms in equation (5.1) are the Lennard-Jones potential $\left(U^{LJ}\right)$, the electrostatic potential $\left(U^{electro}\right)$,

and the intramolecular potential $\left(U^{intra}\right)$. Simulations of the chiral interfaces require appropriate definitions of these three potential terms for the selectors, the end-caps, the silanol groups, the solvents, and the underlying Si layer.

5.2.2 *Ab initio* investigation

The electrostatic and intramolecular potentials are obtained based on a comprehensive series of *ab initio* calculations. Specifically, density-functional theory calculations, with the B3LYP functional[97] and the 6-311G** basis set,[108] have been carried out using the Gaussian 03[100] electronic structure program. For comparison, the major conformers of DNB-phenylglycine and DNB-leucine were also obtained from geometry optimizations at the MP2/6-311G** and HF/6-311G** levels of theory. All *ab initio* calculations are based on the individual, isolated selector, and since the tether is not expected to directly impact CSP solvation and chiral discrimination, the propylsilyl group is replaced with a methyl group for the *ab initio* calculations. A similar truncation has been adopted by others.[74,76,198]

For DNB-phenylglycine, all three *ab initio* methods identify the same global minimum, and two local minima within 20 kJ/mol of the global minimum. Additional minima, at higher energies, were also identified but these are less relevant for the simulations and will not be discussed further. It is worth noting that MM2 force field optimizations[198] identified similar structures for the global and lowest-energy local minimum, although the relative energy was considerably smaller than the *ab initio* values.

The three lowest-energy structures, obtained from the B3LYP calculation, are shown in Figure 5.2, along with the energies relative to the minimum. The MP2 and B3LYP methods lead to nearly identical structures, with all dihedral angles agreeing to within 10 degrees and an average difference in the dihedrals of only 5 degrees. The HF structures are also in close agreement except for the structure in Figure 5.2(b), where HF predicts that the lower amide group is twisted relative to the B3LYP and MP2 structures.

The global minimum (Figure 5.2(a)) is characterized by the C(13)-O(14) and N(23)-H(24) bonds pointing in the same direction and almost in the same plane (dihedral angle O(14)-C(13)-N(23)-H(24) is -2.9 degrees). However, the O(14)-H(24)-N(23) angle is only 111 degrees suggesting that there is poor intramolecular H-bonding. In the energetically-nearest local minimum, shown in Figure 5.2(b), the N(11)-H(12) and C(25)-O(26) bonds appear close, but the N(11)-H(12)-O(26) angle is only 139 degrees thereby suggesting, at best, a strained hydrogen-bond between these groups. Overall, the energetically nearest local minima result from backbone twists either above or below the chiral carbon.

For DNB-leucine, all three methods identify the same global minimum, and two local minima within 5 kJ/mol. This small energy difference is within the level of accuracy of all three methods[90] and highlights the important difference between DNB-phenylglycine and DNB-leucine. Specifically, the flexible isobutyl side-chain in the latter leads to additional minima very close in energy to the global minimum. In fact, eight local minima were identified with energies within 20 kJ/mol of the global minimum, and still more are expected based on torsions of the sec-butyl group. Not

surprisingly, Gallagher *et al.*[199] identified two different backbone conformations present in crystals of DNB-leucine. Lipkowitz *et al.*[200] also noted the multitude of minima in their force field (MM2D) study of a DNB-leucine analog. The global minimum, and the two nearly isoenergetic local minima, are shown in Figure 5.2. The figure shows the B3LYP structures, but all three methods yield nearly identical structures: the average difference between the dihedrals predicted from B3LYP and MP2 is only 5.4 degrees.

Consider the global and local minima for DNB-leucine. The global energy structure for DNB-leucine (Figure 5.2(d)) closely resembles the local minimum of DNB-phenylglycine shown in Figure 5.2(b). The converse is also true and the DNB-leucine local minimum in Figure 5.2(e) has a backbone structure that is very close to the global energy structure of DNB-phenylglycine (Figure 5.2(a)). Several points are worth noting with respect to this exchange. First, B3LYP calculations predict that the two backbone structures differ by 10.86 kJ/mol for DNB-phenylglycine but only by 1.88 kJ/mol for DNB-leucine. Second, for DNB-leucine, torsions within the lateral group will lead to several more energetically accessible structures, for a given backbone structure, but this will not occur for DNB-phenylglycine. Finally, the simple replacement of a phenyl ring with an isobutyl group has altered the energy landscape such that a local minimum for DNB-phenylglycine becomes the global minimum for DNB-leucine, and vice-versa. IR studies of gas phase dipeptides offer an instructive analog.[201] When the residue is small (a methyl group for alanine, for example), the C_7 conformer is favoured, followed by a C_5. The former is comparable to the backbone structures in Figures 5.2(b) and 5.2(d) while the latter is analogous to Figures 5.2(a) and 5.2(e). In contrast, an

aromatic residue interchanges this order such that C_5 is favoured. Thus, the interchange observed for the lowest-energy backbone conformations of DNB-leucine and DNB-phenylglycine is directly analogous to the experimental trend observed for dipeptides.

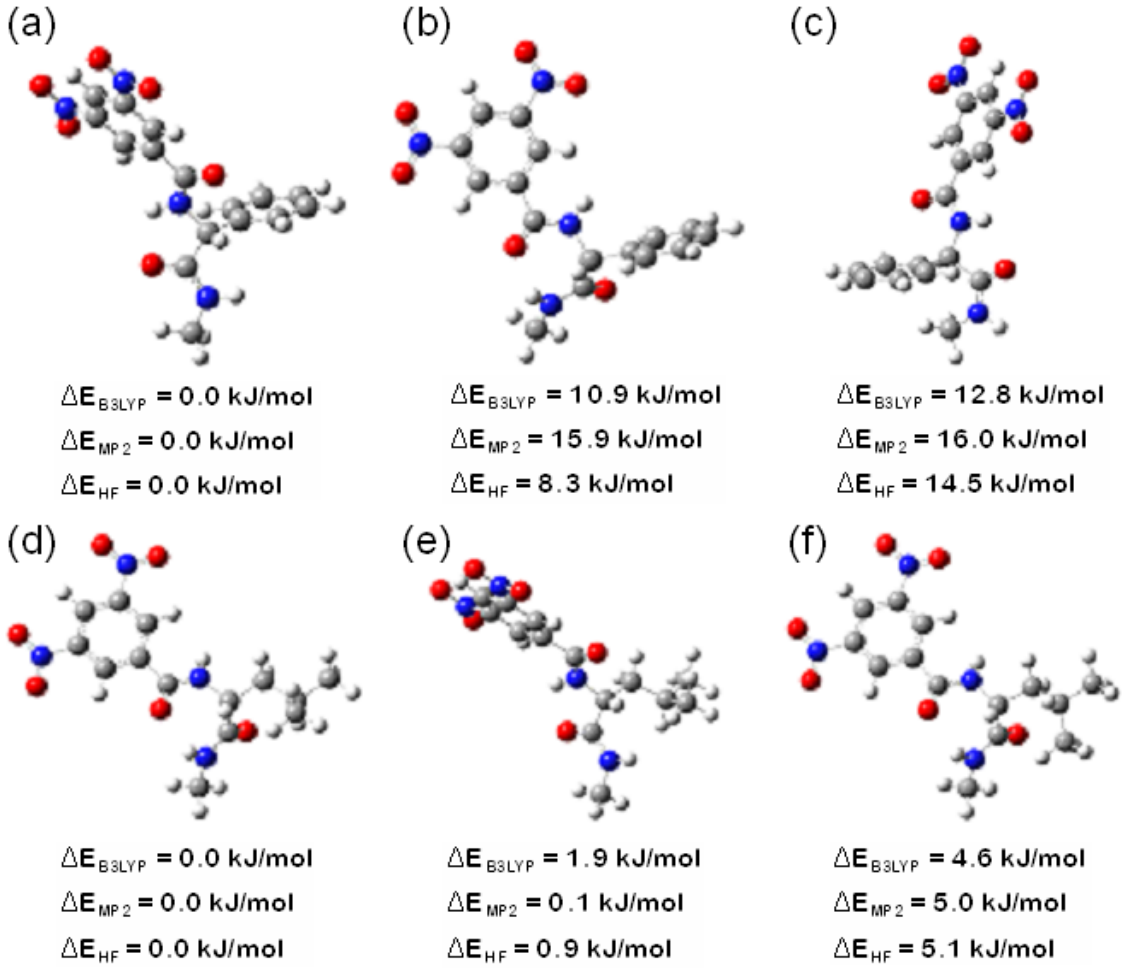

Figure 5.2. Stable conformers of the DNB-phenylglycine and DNB-leucine selectors identified from B3LYP/6-311G** calculations: (a) is DNB-phenylglycine global minimum, (b) and (c) are DNB-phenylglycine lowest energy local minima, (d) is DNB-leucine global minimum, (e) and (f) are DNB-leucine lowest energy local minima. Energy differences are reported relative to the appropriate global minimum from B3LYP/6-311G**, MP2/6-311G**, and HF/6-311G** calculations. Oxygen, nitrogen, carbon, hydrogen atoms are shown in red, blue, grey, and white respectively.

5.2.3 Characteristics of the intramolecular potentials

The intramolecular potential, U^{intra} is given by equation (2.9), and contains energetic contributions from bond stretching, angle bending, torsions, and improper torsions.

The bond stretching potential is described by equation (2.10). Within the simulations, bonds are generally kept fixed using the RATTLE algorithm,[142] except for bonds joining RUs to the flexible portions of the molecule. For these bonds, a series of *ab initio* calculations is performed as the bond length is varied and the force constant is obtained from a linear least-squares fit of the *ab initio* energies versus $(r - r_e)^2$. The force constants are 1.355×10^5 kJ·mol^{-1}·nm^{-2}, 1.106×10^5 kJ·mol^{-1}·nm^{-2}, and 1.123×10^5 kJ·mol^{-1}·nm^{-2} for the C(15)-C(17) and C(25)-C(27) bonds of DNB-phenylglycine, and the C(23)-C(25) bond of DNB-leucine, respectively. The relevant equilibrium bond lengths can be obtained from Table 5.1.

The bending potential is given by equation (2.11) and the full set of bending parameters is given in Table 5.2. The equilibrium angles are obtained from the global energy minimum and the corresponding force constants are obtained from a least squares fit to energy calculations for angles within $\theta_e \pm 5^0$, or from a known force field[140,141], as indicated in the table.

Improper torsion potentials with the expression (2.12) have been employed to restrict out-of-plane bending motions at amide nitrogens, amide carbons, and the ring

carbons joining an RU to the rest of the molecule. Least-squares fits yield the set of parameters shown in Table 5.4.

A modified Ryckaert-Bellemans[202] potential is adopted for torsions. The expression is shown in equation (2.13) and the full set of torsion parameters is given in Table 5.3. Literature potentials for hydrocarbon chains[203,204,173] were employed for torsions within the tether. In all other cases, selector-specific torsion potentials were derived as follows. For each dihedral, eleven-to-eighteen restricted geometry optimizations were performed with the chosen angle given a fixed value between 0 and 360 degrees, while the other parameters are fully optimized. Prior to data analysis, the energies are corrected for intramolecular Lennard-Jones, electrostatic, bend and improper torsion contributions[87] to yield corrected energies that reflect the torsional contributions to the total energy. Both selectors have long chains of single bonds, and the molecules reorganize to a great extent for each restricted geometry optimization, so that the torsions are strongly coupled. As a result, the energies are viewed as a function of all the dihedral angles. That is, the parameters of equation (5.5) were obtained from a single least squares fit[205] to 94 and 110 energies, for DNB-phenylglycine and DNB-leucine, respectively.

Table 5.1 Details of the DNB-phenylglycine and DNB-leucine models. Atomic positions are extracted from the B3LYP/6-311G** geometry optimization. Values marked with *a* are obtained from geometry optimization of $Si(OH)_3CH_2CH_2CH_2NHCH(O)$.

Atom no.	DNB-phenylglycine		DNB-leucine	
	Atom/ group	Atomic positions x(Å), y(Å), z(Å)	Atom/ group	Atomic positions x(Å), y(Å), z(Å)
1	Si	0.000[a], 0.000[a], 0.000[a]	Si	0.000[a], 0.000[a], 0.000[a]
2	Si	0.000[a], 3.120[a], 0.000[a]	Si	0.000[a], 3.120[a], 0.000[a]
3	Si	3.120[a], 0.000[a], 0.000[a]	Si	3.120[a], 0.000[a], 0.000[a]
4	O	0.295[a], 0.303[a], 1.490[a]	O	0.295[a], 0.303[a], 1.490[a]
5	O	0.928[a], 2.834[a], 1.490[a]	O	0.928[a], 2.834[a], 1.490[a]
6	O	2.924[a], 0.929[a], 1.489[a]	O	2.924[a], 0.929[a], 1.489[a]
7	Si	1.433[a], 1.357[a], 2.059[a]	Si	1.433[a], 1.357[a], 2.059[a]
8	CH_2	1.577[a], 1.303[a], 3.918[a]	CH_2	1.577[a], 1.303[a], 3.918[a]
9	CH_2	2.686[a], 2.189[a], 4.511[a]	CH_2	2.686[a], 2.189[a], 4.511[a]
10	CH_2	2.755, 2.084, 6.040	CH_2	2.755, 2.084, 6.040
11	N	3.813, 2.898, 6.635	N	1.951, 1.000, 6.584
12	H	4.755, 2.535, 6.647	H	1.093, 1.220, 7.075
13	C	3.631, 4.197, 6.957	C	2.423, -0.267, 6.701
14	O	2.565, 4.787, 6.834	O	3.517, -0.637, 6.306
15	C	4.874, 4.912, 7.543	C	1.441, -1.236, 7.411
16	H	5.149, 4.411, 8.477	H	0.418, -0.957, 7.153
17	C	6.073, 4.851, 6.605	CH_2	1.718, -2.697, 7.054
18	CH	7.250, 4.217, 7.004	CH	1.464, -3.074, 5.581
19	CH	8.343, 4.145, 6.141	CH_3	-0.004, -2.889, 5.168
20	CH	8.268, 4.715, 4.874	CH_3	1.916, -4.520, 5.334
21	CH	7.098, 5.360, 4.472	N	1.547, -1.054, 8.867
22	CH	6.007, 5.428, 5.332	H	2.282, -1.557, 9.339
23	N	4.456, 6.270, 7.849	C	0.866, -0.082, 9.524
24	H	3.498, 6.465, 7.574	O	0.135, 0.724, 8.956
25	C	5.069, 6.975, 8.837	C	1.035, -0.028, 11.022
26	O	6.039, 6.562, 9.453	CH	0.671, 1.163, 11.657
27	C	4.490, 8.338, 9.138	C	0.793, 1.262, 13.034
28	CH	4.877, 8.939, 10.338	CH	1.250, 0.214, 13.821
29	C	4.387, 10.196, 10.657	C	1.586, -0.960, 13.167
30	CH	3.534, 10.900, 9.818	CH	1.485, -1.104, 11.788
31	C	3.180, 10.287, 8.627	N	0.417, 2.537, 13.701
32	CH	3.640, 9.024, 8.270	O	0.525, 2.583, 14.917
33	N	4.793, 10.826, 11.941	O	0.027, 3.446, 12.987
34	O	4.354, 11.940, 12.180	N	2.062, -2.115, 13.972
35	O	5.535, 10.185, 12.668	O	2.144, -1.960, 15.179
36	N	2.285, 11.013, 7.691	O	2.339, -3.140, 13.367
37	O	1.876, 12.108, 8.043		
38	O	2.018, 10.464, 6.632		

Table 5.2 Details of the bending potentials for the DNB-phenylglycine and DNB-leucine models. The relevant angles are identified by three atoms, following the numbering in Figure 5.1.

DNB-phenylglycine			DNB-leucine			Source
Angle	θ_e (rad)	k_θ ($kJmol^{-1}rad^{-2}$)	Angle	θ_e (rad)	k_θ ($kJmol^{-1}rad^{-2}$)	
7, 4, 1	2.20	142.26	7, 4, 1	2.20	142.26	Ref. 140
7, 5, 2	2.20	142.26	7, 5, 2	2.20	142.26	Ref. 140
7, 6, 3	2.13	142.26	7, 6, 3	2.13	142.26	Ref. 140
8, 7, 4	1.96	209.10	8, 7, 4	1.96	209.10	Ref. 141
8, 7, 5	1.97	209.10	8, 7, 5	1.97	209.10	Ref. 141
8, 7, 6	1.84	209.10	8, 7, 6	1.84	209.10	Ref. 141
9, 8, 7	2.01	259.81	9, 8, 7	2.01	259.81	Ref. 141
10, 9, 8	1.96	259.81	10, 9, 8	1.96	259.81	Ref. 141
11, 10, 9	1.98	259.81	11, 10, 9	1.98	259.81	Ref. 141
12, 11, 10	2.07	349.31	13, 11, 10	2.14	481.48	This work
13, 11, 10	2.14	484.32	12, 11, 10	2.08	502.70	This work
13, 11, 12	2.06	347.98	13, 11, 12	2.04	385.04	This work
14, 13, 11	2.17	884.04	14, 13, 11	2.17	790.30	This work
15, 13, 11	2.00	762.56	15, 13, 14	2.12	796.65	This work
15, 13, 14	2.11	884.20	15, 13, 11	1.98	820.43	This work
16, 15, 13	1.89	295.79	16, 15, 13	1.90	349.99	This work
23, 15, 16	1.89	354.74	21, 15, 16	1.84	375.50	This work
17, 15, 16	1.89	352.90	21, 15, 17	1.91	500.45	This work
23, 15, 13	1.86	720.08	17, 15, 13	1.96	544.44	This work
17, 15, 23	1.97	566.03	21, 15, 13	1.91	545.62	This work
17, 15, 13	1.96	532.70	17, 15, 16	1.94	331.83	This work
18, 17, 15	2.10	545.96	22, 21, 15	2.04	357.37	This work
22, 17, 15	2.10	545.89	23, 21, 22	2.09	346.67	This work
24, 23, 15	1.98	330.89	23, 21, 15	2.13	567.11	This work
25, 23, 24	2.12	324.13	25, 23, 21	2.04	736.92	This work
25, 23, 15	2.10	453.23	24, 23, 21	2.15	841.78	This work
26, 25, 23	2.15	792.59	25, 23, 24	2.10	845.15	This work
27, 25, 26	2.10	792.53	26, 25, 23	2.04	634.27	This work
27, 25, 23	2.03	735.36	30, 25, 23	2.16	635.98	This work
28, 27, 25	2.04	639.69	18, 17, 15	2.01	440.86	This work
32, 27, 25	2.16	638.52	20, 18, 17	1.91	512.33	This work
			20, 18, 19	1.93	494.41	This work
			19, 18, 17	1.97	543.65	This work

Table 5.3 Details on the torsional potentials for DNB-phenylglycine and DNB-leucine used in the simulations. The first column identifies the 4 atoms involved in the torsion. The following 8 columns show the parameters used in Eq. (2.13), either least-square optimized or converted from OPLS force field.

Torsion	c_0	c_1	c_2	c_3	c_4	c_5	c_6	φ^0 (rad)	Source
DNB-phenylglycine									
8, 7, 4, 1	7.94	7.89	2.72	-18.56					Ref. 204
8, 7, 5, 2	7.94	7.89	2.72	-18.56					Ref. 204
8, 7, 6, 3	7.94	7.89	2.72	-18.56					Ref. 204
9, 8, 7, 4	6.98	17.73	0.88	-25.60					Ref. 173
10, 9, 8, 7	8.23	16.95	1.13	-26.31					Ref. 203
11, 10, 9, 8	8.23	16.95	1.13	-26.31					Ref. 203
13, 11, 10, 9	0.89	-0.19	-0.82	7.51	10.68	-5.91	-5.22	0.11	This work
15, 13, 11, 10	12.62	7.80	18.92	-48.10	14.58	50.86	1.94	1.48	This work
23, 15, 13, 11	12.62	14.63	-42.18	-70.64	47.52	51.83	-18.63	0.57	This work
25, 23, 15, 13	12.62	-8.76	-7.18	81.30	-57.45	-56.00	46.15	3.18	This work
27, 25, 23, 15	12.62	-59.26	-35.16	138.50	6.51	-87.66	-11.76	6.07	This work
28, 27, 25, 23	12.62	2.50	-17.94	-6.18	104.85	3.69	-59.12	1.71	This work
18, 17, 15, 13	12.62	8.01	-2.88	-18.61	-2.97	10.27	-6.69	2.75	This work
DNB-leucine									
8, 7, 4, 1	7.94	7.89	2.72	-18.56					Ref. 204
8, 7, 5, 2	7.94	7.89	2.72	-18.56					Ref. 204
8, 7, 6, 3	7.94	7.89	2.72	-18.56					Ref. 204
9, 8, 7, 4	6.98	17.73	0.88	-25.60					Ref. 173
10, 9, 8, 7	8.23	16.95	1.13	-26.31					Ref. 203
11, 10, 9, 8	8.23	16.95	1.13	-26.31					Ref. 203
13, 11, 10, 9	0.89	-0.19	-0.82	7.51	10.68	-5.91	-5.22	0.11	This work
15, 13, 11, 10	5.80	12.44	34.66	-44.21	-6.10	39.62	6.26	4.84	This work
21, 15, 13, 11	5.80	4.28	56.19	-21.16	-103.84	6.63	50.45	3.86	This work
23, 21, 15, 13	5.80	-19.30	-11.58	8.15	83.89	5.45	-61.47	1.33	This work
25, 23, 21, 15	5.80	-41.80	-26.99	113.90	32.08	-68.50	-34.17	0.00	This work
26, 25, 23, 21	5.80	0.40	2.63	-2.33	-124.10	2.42	101.07	3.34	This work
18, 17, 15, 13	5.80	-26.12	-27.79	64.71	127.15	-42.90	-108.29	4.61	This work
19, 18, 17, 15	5.80	18.58	33.24	-64.04	-20.80	40.13	-0.67	5.19	This work

Table 5.4 Improper torsional potentials for the DNB-phenylglycine and DNB-leucine models. The first column identifies the four atoms defining the improper torsional angle. The second and third columns define the equilibrium angle and the corresponding force constant.

Improper torsion	ω_e (rad)	k_ω ($kJmol^{-1}rad^{-2}$)
DNB-phenylglycine		
27, 28, 32, 25	-0.02	459.17
25, 26, 27, 23	0.00	435.00
23, 24, 15, 25	0.24	223. 38
17, 18, 22, 15	0.00	531.25
13, 14, 11, 15	0.01	453.56
11, 12, 13, 10	-0.10	208.09
DNB-leucine		
25, 26, 30, 23	-0.02	440.15
23, 24, 25, 21	0.00	427.64
21, 22, 15, 23	0.12	290.31
13, 14, 15, 11	-0.01	457.75
11, 12, 10, 13	-0.14	117.55

5.2.4 Determination of the intramolecular and intermolecular potentials

DNB-phenylglycine and DNB-leucine differ only in the identity of the lateral group. Based on this, one might expect that the potential parameters in equations (2.10)-(2.13) would be very similar for both. In particular, one might expect identical, or near identical, backbone parameters. However the differences in their experimentally observed selectivities[22,8,9] suggests otherwise. According to the three point binding

model, the lateral groups do not participate directly in the selectivity,[74,200] and thus the conformations of the two selectors at the interface differ such that selector-analyte interactions are impacted. Experimental studies of related compounds also indicate important conformational differences. Chin *et al*.[201] summarized the results of infrared (IR) spectroscopy studies on the impact of lateral groups based on gas phase isolated dipeptides. These dipeptides share a common backbone with the selectors of interest here. Interestingly, Chin observed a change in the optimal backbone structure when the lateral group is aromatic. Gung *et al*.[206] also noted, based on the results of NMR and IR studies, that bulkier alkyl substituents lead to a change in conformational probabilities, such that new backbone configurations appear.

With these considerations in mind, I have proceeded by carefully evaluating the intramolecular parameters for both selectors rather than adopting published transferable parameters. Figure 5.3 outlines the iterative, eight step process used to obtain the interaction potential for the truncated DNB-phenylglycine selector. Since the B3LYP and MP2 calculations are in good agreement for the conformer structures and relative energies, all further calculations employ the more efficient B3LYP functional with the 6-311G** basis set. The same procedure is used for DNB-leucine, except that a few more bends and torsions are required to represent the motion of the isobutyl chain.

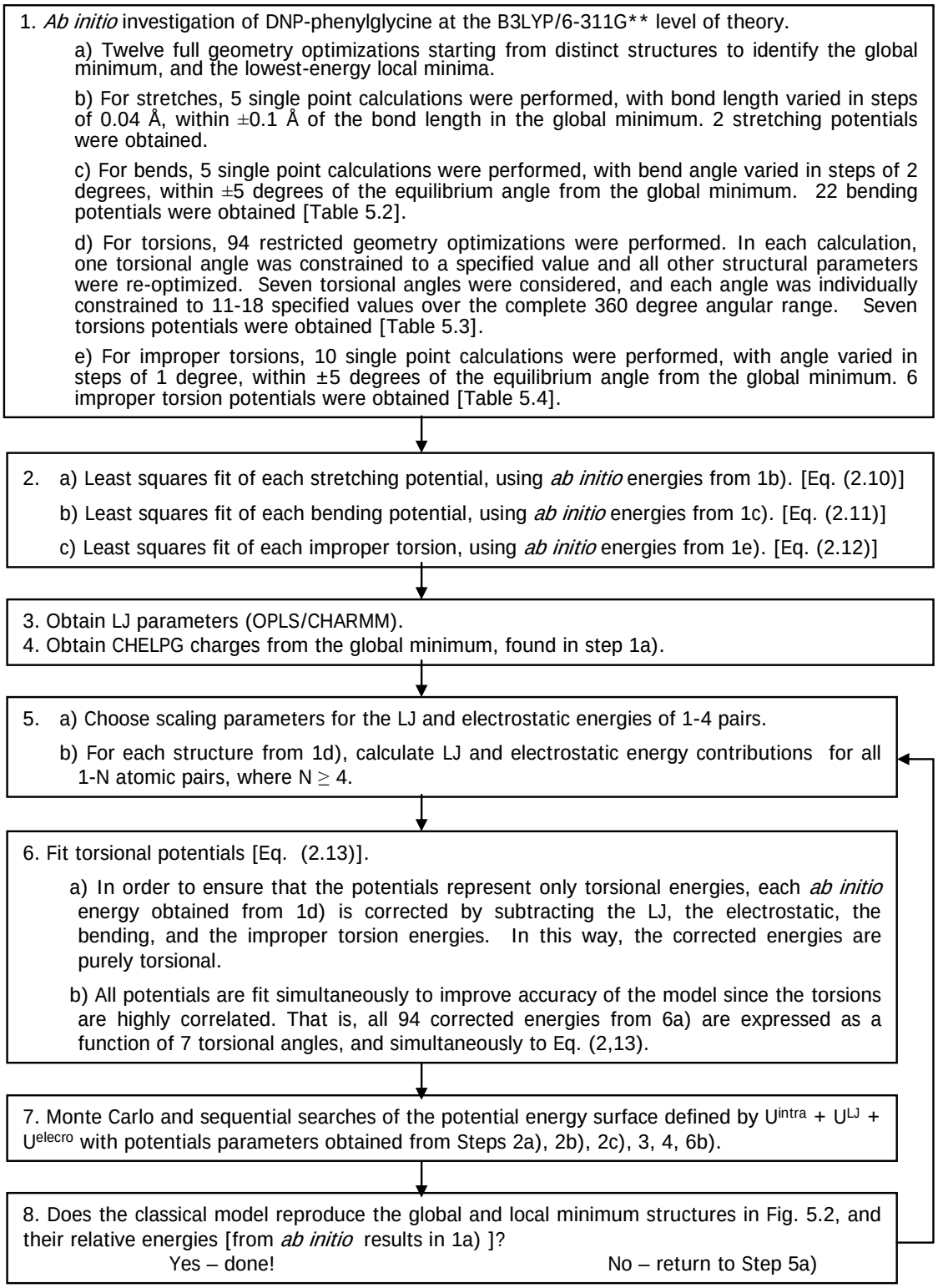

Figure 5.3 Detailed explanation of the parameterization procedure for the DNB-phenylglycine model.

Consider first the DNB-phenylglycine molecule. The interaction potential should reproduce, as best as possible, the energetically accessible conformers of the selector along with the energetic costs of conformational changes. In Step 1, single point calculations around the equilibrium values are performed. The resulting energies are fitted to obtain the intramolecular potential parameters in Step 2 as outlined in Section 5.4.3.

Steps 3 and 4 are, respectively, the assignment of Lennard-Jones parameters and the evaluation of atomic charges for the electrostatic potential (see Table 5.5). The OPLS force field[103,207,208] is used for the LJ parameters of all atoms, except for silicon where OPLS parameters are not available and CHARMM[140] values have been used instead. Lorentz-Berthelot rules[209,210] are used for all pairs of distinct atoms. CHELPG[211] atomic charges have been evaluated from the B3LYP/6-311G** global minimum. The resulting charges were compared to OPLS[103,207,208] values and, overall, the differences are small. Of course, the CHELPG charges are correctly non-zero for the DNP carbons but transferable OPLS parameters cannot capture this. This is noteworthy since π-π interactions with the DNP ring are expected in the three point binding model[193] of DNB-phenylglycine. CHELPG atomic charges were also evaluated for the local minima and compared to the selected set. Again, the differences are small.

Table 5.5 Details of the DNB-phenylglycine and DNB-leucine models. Atomic charges are obtained using the CHELPG algorithm applied to the B3LYP/6-311G** global energy minimum. Lennard-Jones energy and length parameters are taken form the OPLS[103,207,208] and CHARMM[140] force fields.

Atom no.	DNB-phenylglycine				DNB-leucine			
	Atom/ group	ε (kJ/mol)	σ (nm)	q (|e|)	Atom/ group	ε (kJ/mol)	σ (nm)	q (|e|)
1	Si	2.510	0.392	0.00	Si	2.510	0.392	0.00
2	Si	2.510	0.392	0.00	Si	2.510	0.392	0.00
3	Si	2.510	0.392	0.00	Si	2.510	0.392	0.00
4	O	0.636	0.315	0.00	O	0.636	0.315	0.00
5	O	0.636	0.315	0.00	O	0.636	0.315	0.00
6	O	0.636	0.315	0.00	O	0.636	0.315	0.00
7	Si	2.510	0.392	0.00	Si	2.510	0.392	0.00
8	CH_2	0.494	0.391	0.00	CH_2	0.494	0.391	0.00
9	CH_2	0.494	0.391	0.00	CH_2	0.494	0.391	0.00
10	CH_2	0.494	0.391	0.25	CH_2	0.494	0.391	0.22
11	N	0.711	0.325	-0.48	N	0.711	0.325	-0.52
12	H	0.193	0.040	0.21	H	0.193	0.040	0.31
13	C	0.439	0.375	0.49	C	0.439	0.375	0.53
14	O	0.879	0.296	-0.48	O	0.879	0.296	-0.51
15	C	0.276	0.350	0.17	C	0.276	0.350	0.14
16	H	0.126	0.250	0.04	H	0.126	0.250	0.05
17	C	0.293	0.355	0.23	CH_2	0.494	0.391	-0.01
18	CH	0.460	0.375	-0.10	CH	0.335	0.385	0.23
19	CH	0.460	0.375	0.06	CH_3	0.670	0.391	-0.10
20	CH	0.460	0.375	-0.04	CH_3	0.670	0.391	-0.08
21	CH	0.460	0.375	0.08	N	0.711	0.325	-0.54
22	CH	0.460	0.375	-0.15	H	0.193	0.040	0.30
23	N	0.711	0.325	-0.54	C	0.439	0.375	0.57
24	H	0.193	0.040	0.27	O	0.879	0.296	-0.51
25	C	0.439	0.375	0.57	C	0.293	0.355	-0.03
26	O	0.879	0.296	-0.51	CH	0.460	0.375	0.07
27	C	0.293	0.355	-0.02	C	0.293	0.355	0.02
28	CH	0.460	0.375	0.06	CH	0.460	0.375	0.05
29	C	0.293	0.355	0.02	C	0.293	0.355	0.03
30	CH	0.460	0.375	0.02	CH	0.460	0.375	0.01
31	C	0.293	0.355	0.05	N	0.502	0.325	0.65
32	CH	0.460	0.375	0.01	O	0.711	0.296	-0.38
33	N	0.502	0.325	0.66	O	0.711	0.296	-0.38
34	O	0.711	0.296	-0.38	N	0.502	0.325	0.66
35	O	0.711	0.296	-0.38	O	0.711	0.296	-0.38
36	N	0.502	0.325	0.64	O	0.711	0.296	-0.38
37	O	0.711	0.296	-0.38				
38	O	0.711	0.296	-0.38				

The iterative portion of the model parameterization couples two factors. First, Lennard-Jones and electrostatic potentials are evaluated for all intermolecular and intramolecular atomic pairs, except for intramolecular atoms that are "close". To be precise, these potentials are evaluated for all intramolecular pairs of atoms separated by four or more bonds, and pairs of atoms separated by only 1 or 2 bonds are considered "close". For atoms separated by three bonds, so called 1-4 atomic pairs, a scaling factor is introduced[212,213] so that a fraction of these energetic contributions is included. For the selectors of interest here, 1-4 scaling is particularly critical due to the proximity of the amide groups. Specifically, the backbone conformation is sensitive to the strength of the interaction between the amides, and this interaction is impacted directly by the chosen scaling factors. For instance, with the 1-4 scaling factors set to zero, the lowest-energy structures are similar to Figures 5.2(a) and 5.2(e). On the other hand, when the scaling factor is closer to one, the lowest-energy structures are similar to Figures 5.2(b) and 5.2(d). Clearly, the 1-4 scaling parameters must be optimized[212,213] to yield the correct balance of backbone structures.

Second, torsional motion introduces significant changes in the molecular shape and selector-specific torsion potentials were derived as follows. For each dihedral, eleven-to-eighteen restricted geometry optimizations were performed with the chosen angle given a fixed value between 0 and 360 degrees, while the other parameters are fully optimized. This allows for structural relaxation, an essential step since the backbone consists of a series of single bonds, so that the torsions are strongly coupled. As a result, the energies obtained from restricted geometry optimizations are viewed as functions of

all the dihedral angles and the parameters of Eq. (2.13) are obtained from a simultaneous least squares fit[205] to 94 energies. Prior to data analysis, the energies are corrected[87,214] for Lennard-Jones, electrostatic, bend, and improper torsion contributions to yield corrected energies that reflect the torsional contributions to the total energy. In this way, the model will reproduce the correct relative energies when the various contributions are combined to yield the total potential energy. Importantly, this correction depends on the 1-4 scaling factors chosen for the electrostatic and LJ contributions.

An iterative cycle consists of selecting scaling factors for the 1-4 atomic pairs, correcting the torsional energies, simultaneous fitting of all torsional potentials, and model assessment. The latter is based on energy minimization following a combination of sequential and Monte Carlo conformational changes. Minimizations begin from a total of 33000 randomly generated starting structures. Following this, the optimized structures are compared to the B3LYP/6-311G** global energy minimum and the lowest energy local minimum (Figures 5.2(a) and 5.2(b)). A new cycle begins with the examination of different 1-4 scaling factors.

Since the *ab initio* model selector does not include the tether, literature potentials for hydrocarbon chains[215,204,203] were employed for torsions within the tether. However, the C(8)-C(9)-C(10)-N(11) torsion at the top of the tether is evaluated from B3LYP/6-311G** calculations of *N*-[3-(trihydroxysilyl)]propyl]formamide, a truncated analog of the lower portion of the selector. The full set of torsion parameters is given in Table 5.3. Scaling factors of 0.7 and 0.0 for the 1-4 Lennard-Jones and electrostatic potentials, respectively, yield the best agreement with *ab initio* results. Specifically, the

optimal parameters yield the correct global energy minimum structure, and a structure very similar to Figure 5.2(b) roughly 9 kJ/mol higher in energy. In between these two structures, a few additional minima are found. First, one structure having the global energy minimum backbone with a small twist in the DNP group has been identified. Second, a somewhat twisted backbone structure also appears as a minimum for the model. This structure is similar to the global energy minimum and, in *ab initio* calculations, this structure optimizes to the global minimum. With the addition of the tether, and in the presence of the silanol and end-caps at the surface, this minimum adopts surface conformations similar to those of the global minimum. As a result, I have not considered it further.

The development of a classical potential for the intramolecular motion of DNB-leucine proceeds analogously to Figure 5.3. However, a few more bends and torsions are required to represent the motion of the lateral isobutyl group. In particular, torsional potentials were obtained from a least squares fit to energies obtained from 110 restricted geometry optimizations. The optimal LJ and electrostatic scaling factors are both 0.6 for DNB-leucine. The electrostatic scaling factor is quite different from the optimal value for DNB-phenylglycine. However, keeping in mind the impact of the scaling factors on backbone structure, and the important differences between the optimized structures of both selectors (see Figure 5.2), the models should differ in significant ways. The Monte Carlo and sequential energy minimization, starting from 33000 random structures, correctly identified the DNB-leucine global minimum, and the lowest energy local minimum. The energy difference between these two structures is

predicted to be roughly 6 kJ/mol, a difference that is small but somewhat larger than predicted from *ab initio* calculations. Importantly, the classical model correctly predicts the presence of additional minima resulting from torsions in the lateral group. In fact, the minimum in Figure 5.2(f) results from a twist in the isobutyl group. The classical model correctly identifies this minimum, although it appears within 1 kJ/mol of the global. An additional twisted structure, analogous to the structure found for DNB-phenylglycine, is also predicted for DNB-leucine. With the addition of the tether, and the spatial constraints at the surface, the surface-distribution for this structure is expected to be very close to that of the global.

5.2.5 Distribution functions.

Surface distributions provide probabilities for finding atoms at a specified distance above the underlying silicon layer. Within the simulations, these distributions are evaluated from

$$g(z) = \frac{n^{act}(z)}{n^{ideal}} = \frac{n^{act}(z)L_z}{N\Delta z} \tag{5.2}$$

where $z=0$ corresponds to the underlying immoveable layer of Si atoms, N is the total number of atoms in the simulation cell, and L_z is the distance between the two surfaces. $n^{act}(z)$ is the number of atoms found between z and $z+dz$ above the underlying Si while n^{ideal} is the number expected for an unstructured fluid. Surface distributions are employed for the selectors to identify their major conformations at the interface. These distributions are also evaluated for the solvents where they identify preferred solvent

locations and solvent partitioning at the interface. Since the simulation cell includes two surfaces, the surface distributions reported below are averages over both surfaces.

Radial distributions, g(r), have been evaluated between potential selector-solvent hydrogen-bonding pairs. These distributions offer a first indication of the importance of hydrogen bonding at specific selector sites. I explore hydrogen bonding in two other ways. First, snapshot analysis coupled with the application of a geometric criterion[216,186] of a hydrogen bond provides H-bonding statistics. In regards to the criterion, a hydrogen bond is identified as follows: the distance between H and the hydrogen bond acceptor should be less than 2.6 Å and the angle formed between donor-H-acceptor should be larger than 150°. I report statistics based on an analysis of solvent near 112000 (5 simulations/solvent x 700 snapshots/simulation x 32 selectors/snapshot) selectors. Two-dimensional (2D) cylindrical distributions $g(r_c,z_c)$ are also used to study the relative positions of the solvent atoms around the selector atoms. In a 2D distribution the distance between two chosen atoms is divided into two components, r_c and z_c, according to $r = \sqrt{(x_c^2 + y_c^2) + z_c^2} = \sqrt{r_c^2 + z_c^2}$. The variable r_c defines the distance between the atoms in a direction parallel to the underlying Si layer while z_c provides the corresponding information perpendicular to the surface. Within the simulation, the 2D distribution is calculated from:

$$g(r_c, z_c) = \frac{n^{act}(r_c, z_c)}{n^{ideal}(r_c)} = \frac{n^{act}(r_c, z_c)}{2\pi\, r_c\, \Delta r_c\, \Delta z_c\, \rho} \tag{5.3}$$

where ρ is the number density of the solvent. These distributions are evaluated every 20 iterations for potential solvent-selector hydrogen-bonding pairs. A positive value for z_c

indicates that the solvent atom is further away from the Si layer than is the selector atom. In other words, the solvent atom is closer to the bulk fluid in the center of the simulation cell. This analysis is particularly instructive for hydrogen bonding as it provides direct information on the solvent position relative to the selector. I examine 2D distributions, and provide corresponding snapshots, to identify the most probable positions for hydrogen bond donors/acceptors about the selectors.

5.2.6 Surface structure

The DNB-phenylglycine and DNB-leucine chiral selectors are flexible. As shown in Figure 5.2, for each selector the global energy minimum and the lowest-energy local minimum are close in energy. This is particularly true for DNB-leucine where the energy difference is within the error of the B3LYP functional used to find the optimized structures.

Each simulation begins with all selectors at the interface given the structure corresponding to the global energy minimum. However, the selectors quickly adopt a range of conformations, which is evident from Figures 5.4(a), 5.4(b), 5.5(a), and 5.5(b). These snapshots show the chiral surface, after 1.05 ns, including the trimethylsilyl end-caps and the silanol groups. It is worth noting that the end-caps and silanol groups are found within 5 Å of the underlying silicon layer. Similarly, the tether atoms are very well localized and found within 7 Å of the Si layer. The solvent is omitted from the snapshot to highlight the selector conformations.

The snapshots in Figures 5.4 and 5.5 correspond to a 90:10 *n*-hexane:2-propanol solvent mixture. Figure 5.5(a) shows that the DNB-phenylglycine prefers to place the

dinitrophenyl ring roughly parallel to the surface for this solvent composition. This is a bent configuration, similar to the global energy minimum in Figure 5.2(a) when the alkyl tether is included.

The DNB-leucine interface in Figure 5.5(b) is distinct from the DNB-phenylglycine interface. In particular, the dinitrophenyl rings are often perpendicular to the surface. The lateral groups shown in Fig. 4 also adopt preferred positions relative to the underlying surface. Figure 5.4(a) shows that the phenyl rings are roughly perpendicular to the surface. The isobutyl group of DNB-leucine prefers to tip towards the surface (Figure 5.4(b)).

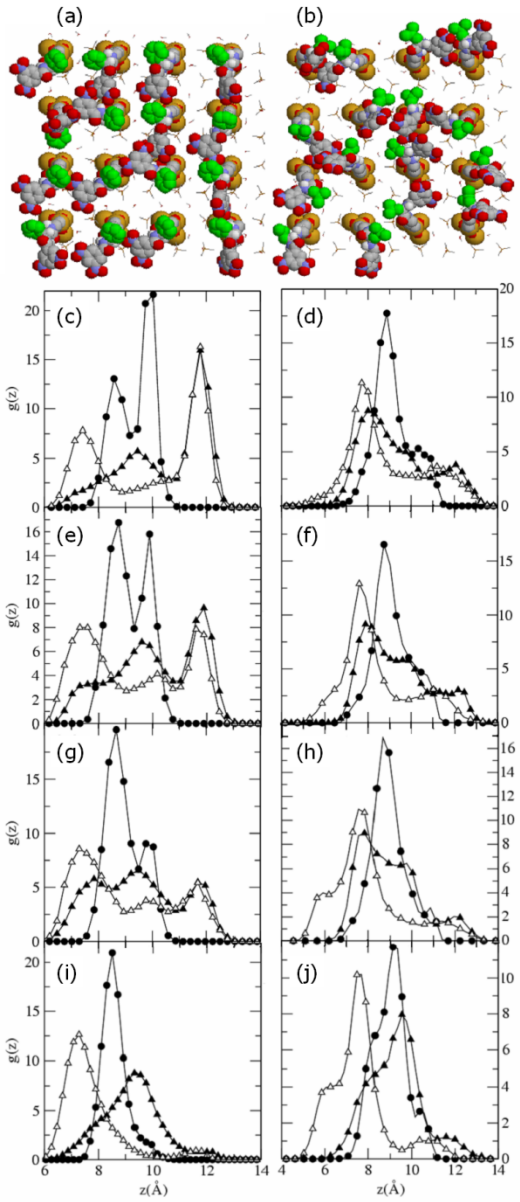

Figure 5.4 Surface distribution of the lateral groups. Snapshots illustrate the range of conformers for DNB-phenylglycine (a) and DNB-leucine (b) in 90:10 *n*-hexane: 2-propanol. Silicon, oxygen, nitrogen, carbon, and hydrogen are shown in gold, red, blue, grey, and white respectively. The phenyl ring and isobutyl chain are emphasized in green. The phenyl ring distribution in DNB-phenylglycine is shown with C(17), C(19), and C(21) distributions (filled circles, filled triangles and open triangles, respectively) in 100% hexane (c), 90:10 *n*-hexane:2-propanol (e), 80:20 *n*-hexane:2-propanol (g), and 100% 2-propanol (i). Similarly, the distribution of the isobutyl chain in DNB-leucine is shown with C(17), C(19), and C(20) distributions (filled circles, filled triangles and open triangles, respectively) in 100% hexane (d), 90:10 *n*-hexane:2-propanol (f), 80:20 *n*-hexane:2-propanol (h), and 100% 2-propanol (j).

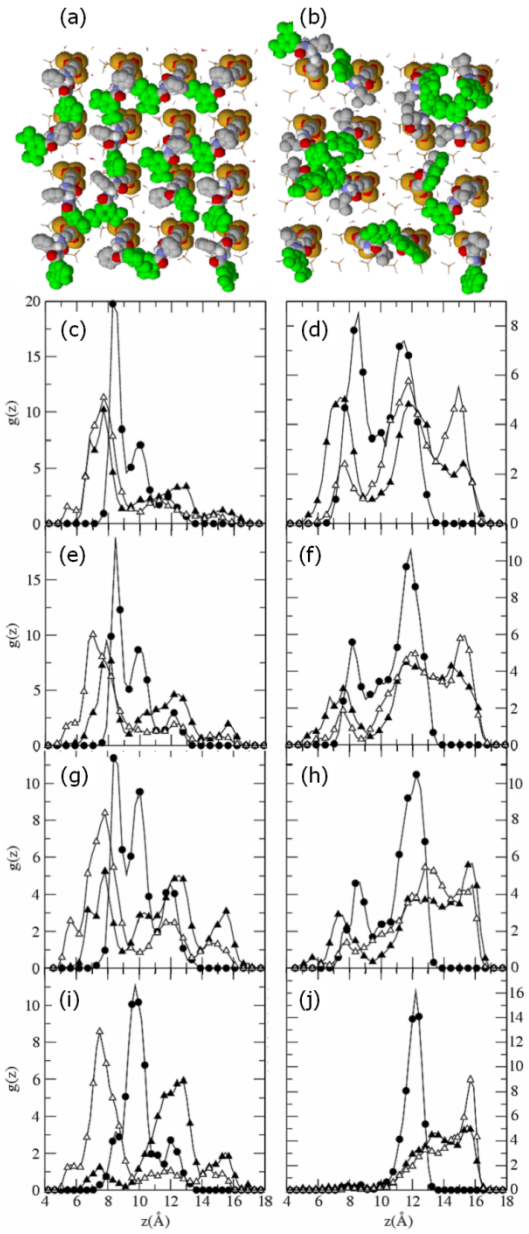

Figure 5.5 Surface distribution of the DNP rings. Snapshots show the range of conformers explored for DNB-phenylglycine (a) and DNB-leucine (b) in 90:10 *n*-hexane:2-propanol. Silicon, oxygen, nitrogen, carbon, and hydrogen are shown in gold, red, blue, grey, and white respectively. The DNP rings are emphasized in green. The DNP distribution in DNB-phenylglycine is shown with C(27), N(33), and N(36) atoms (filled circles, filled triangles and open triangles, respectively) in 100% hexane (c), 90:10 *n*-hexane:2-propanol (e), 80:20 *n*-hexane:2-propanol (g), and 100% 2-propanol (i). Similarly, the DNP distribution in DNB-leucine is shown with C(25), N(31), and N(34) atoms (filled circles, filled triangles and open triangles, respectively) in 100% hexane (d), 90:10 *n*-hexane:2-propanol (f), 80:20 *n*-hexane:2-propanol (h), and 100% 2-propanol (j).

The impact of solvent composition on the surface distributions of the lateral groups and the DNP rings are shown in Figures 5.4 and 5.5, respectively. Consider DNB-phenylglycine first. In pure hexane, the solvent does not interact strongly with the selectors and the dinitrophenyl groups are often parallel to the surface. This is evident from Figure 5.5(c) where the distributions show that C(27) and the nitrogens are all most-likely to be found at roughly 8 Å above the surface. The lateral phenyl rings, in this solvent, prefer to point towards the bulk, as shown in Figure 5.4(c) where C(19) and C(21) tend to be further away from the surface than C(17). With the addition of 2-propanol, the dinitrophenyl groups are more likely to be found perpendicular to the surface. Specifically, some selectors place their dinitrophenyl group such that one nitro points towards the surface while the other is directed into the bulk. In a 100% 2-propanol solvent, the latter becomes the dominant conformation for DNB-phenylglycine selectors at the interface. This is evident from Figure 5.5(i) where one nitrogen is closest to the surface, followed by C(27), then the other nitrogen. The lateral group adopts a similar arrangement relative to the surface: Figure 5.4(i) shows that C(21) is closer to the surface than C(17) or C(19).

The solvent dependence is equally striking, but quite different, for DNB-leucine. This selector, in pure *n*-hexane, displays a variety of conformations. The broad range of distances over which the DNP atoms may be found above the surface (Figure 5.5(d)) reflects this. The lateral isobutyl group also displays a range of conformations, but Figure 5.4(d) indicates that the end carbons (C(19) and C(20) in Figure 5.1(b)) tend to be slightly closer to the surface than C(17). The low energy of the local minima found for

this selector (see Figure 5.2) is consistent with these observations: many conformations are energetically accessible. The addition of small quantities of 2-propanol quickly shifts the conformations towards an extended structure where the dinitrophenyl groups point into the bulk. In fact, dinitrophenyl groups are virtually never parallel to the surface for the DNB-leucine interface if the solvent is pure 2-propanol. This is clear from Figure 5.5(f), where both nitrogens of the DNP ring are found further from the surface than C(25). The lateral group also adopts a different configuration with the most probable isobutyl arrangement corresponding to one end carbon closer to the surface than the other (Figure 5.4(j)).

Inter-selector interactions at the interface are rare, despite the potential for hydrogen-bonding and ring-ring interactions. This was verified by an analysis of all snapshots. Virtually all interactions occur with negligible probability except perhaps for hydrogen-bonding interactions between amide H and nitro Os of neighboring selectors. In pure *n*-hexane, roughly 1% of the selectors participate in these hydrogen bonds. However, with the addition of 2-propanol, hydrogen bonds to the solvent replace inter-selector hydrogen bonding and the probability for these interactions drops below 1%. Ring-ring stacking between neighboring selectors occurred for less than 0.4% of the selectors: a rare occurrence. *Intra*-selector hydrogen bonding was also examined in the snapshots. From the snapshots, intramolecular amide-amide H-bonds were not found.

Panels (e) and (f) in Figures 5.6 and 5.8 show the distribution of amide groups above the underlying silicon layer, for DNB-phenylglycine and DNB-leucine, respectively. The amide group nearest the surface, atoms 11-14 in Figure 5.1, is referred

to as the “lower” amide group, the other amide linkage is termed the “upper” amide group. The amide atom distributions above the surface are similar for DNB-phenylglycine and DNB-leucine although the upper group explores a broader range of separations for the latter. For instance, the upper amide oxygen can be found between 6.0 and 12.5 Å above the underlying silicon for DNB-leucine but this atom is only found between 8.0 and 12.5 Å for the DNB-phenylglycine CSP. The peak heights are consistently lower for DNB-leucine, which also indicates a greater flexibility and delocalization for this selector.

Despite the evident structural similarity between DNB-phenylglycine and DNB-leucine, the replacement of a lateral phenyl ring by an isobutyl group leads to important structural changes. First, *ab initio* results identify an interchange between global and lowest-energy local minima. Furthermore, the flexible isobutyl group introduces additional energetically accessible local minima. Within the simulations, both selectors exhibit unique conformational preferences at the interface and the atoms of DNB-phenylglycine are more localized relative to the underlying surface. As discussed above, these solvents respond differently to increasing concentrations of hydrogen-bonding solvent: the alcohol encourages DNB-phenylglycine to orient the dinitrophenyl ring perpendicular to the surface, with one nitro group pointing towards the bulk and the other towards the surface, while the DNB-leucine ring points towards the bulk in 100% 2-propanol.

5.2.7 Solvation of DNB-phenylglycine CSP

Figure 5.6(a) shows a sideview snapshot from the simulation of the DNB-phenylglycine interface with 90:10 *n*-hexane:2-propanol. The alcohol clearly prefers the interface over the bulk. However, when the alcohol is in the bulk it typically clusters with other alcohols, with hydrogen bonds between them. The alcohols do not descend below the end-caps and this is evident from the snapshot. However, the selectors are well surrounded by 2-propanol. The distribution of alcohol at the interface is more evident from the surface distribution in Figure 5.6(d). The figure shows two peaks beginning at roughly 5 Å, which is directly above the end-caps, and ending at roughly 15 Å, above the amide groups and generally above the dinitrophenyl groups. A region of decreased probability occurs between 9-10 Å above the underlying surface. The snapshot in Figure 5.6(a) identifies the reason for this: Most of the selector atoms are found at, or near, these separations. There is consequently little space available for solvent, and the surface distribution of 2-propanol reflects this crowding. Figure 5.6(c) presents the distribution of *n*-hexane above the DNB-phenylglycine interface. Hexane molecules prefer the bulk; however, there is a region of enhanced probability around 7 Å from the underlying silicon. The topmost atom of the tether is found at this separation, and the upper amide (Figure 5.6(f)), the lateral phenyl ring (Figure 5.4(e)), and the dinitrophenyl ring (Figure 5.5(e)) are usually found at larger distances from the surface. Thus, between the top of the end-caps and the crowded region around 9-10 Å, there is room for solvent. Both 2-propanol and *n*-hexane are found in this region.

The presence of alcohol at the interface strongly suggests that solvent-selector hydrogen bonding is significant for DNB-phenylglycine. Radial distributions between potential hydrogen-bonding pairs are shown in Figure 5.6(b). The distribution between an amide oxygen (O(14) or O(26)) and the hydrogen of 2-propanol shows a significant region of enhanced probability. Specifically, the probability of finding the alcohol hydrogen within 2 Å of the upper amide oxygen, O(26), is forty times higher than expected based on the bulk density. The lower amide oxygen, O(14), also has a significant probability of having a hydrogen from 2-propanol nearby. The alcohol can also accept hydrogen bonds from the selector. For the hydrogen in the upper amide, H(24), the probability of finding the alcohol oxygen roughly 2.5 Å away is seven times higher than expected based on the bulk density. These radial distributions strongly suggest important solvent-selector hydrogen bonding interactions, especially for the amide oxygens (O(14) and O(26)) of DNB-phenylglycine.

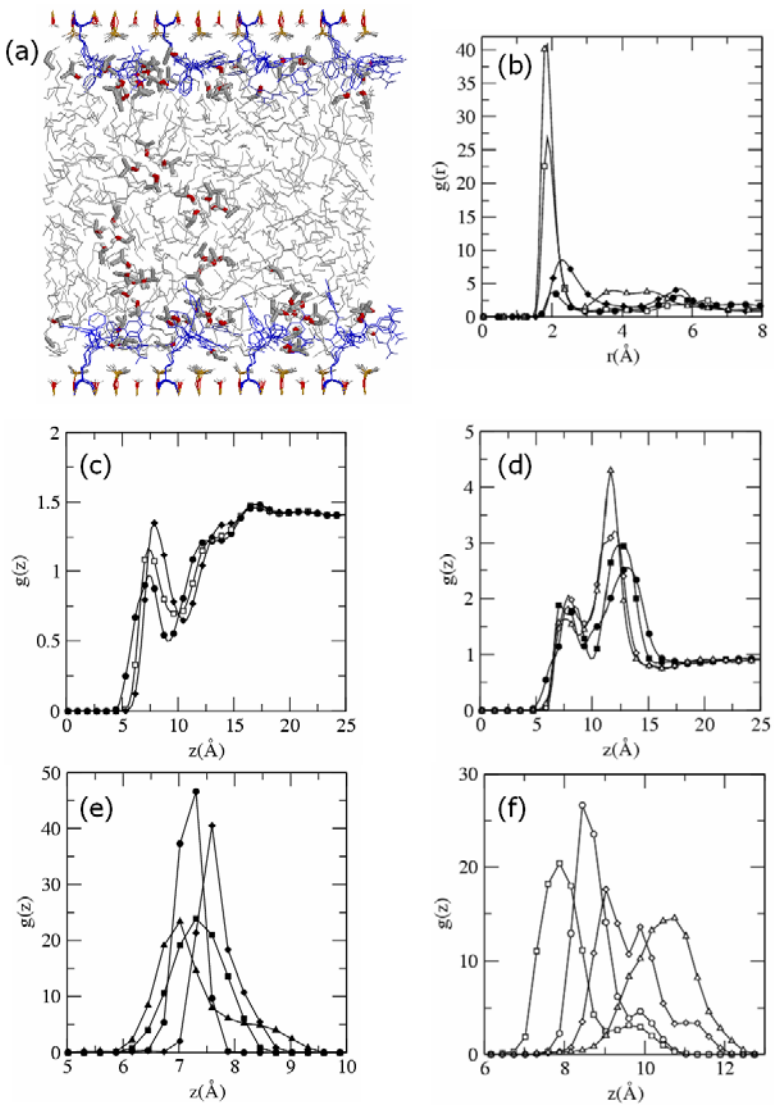

Figure 5.6 Simulation results for DNB-phenylglycine in 90:10 *n*-hexane:2-propanol. A sideview of the simulation cell is presented in (a). Silicon, oxygen, carbon, hydrogen atoms are shown in gold, red, grey, and white respectively. Selector molecules are shown in blue and 2-propanol molecules are bolded. (b) Radial distributions between potential selector-solvent H-bonding pairs: H(12)-O(2-propanol), O(14)-H(2-propanol), H(24)-O(2-propanol), and O(26)-H(2-propanol) are represented by filled circles, open squares, filled diamonds, and open triangles respectively. (c) The *n*-hexane distribution above the surface: CH_3, 2-CH_2, and 3-CH_2 are represented by filled circles, open squares, and filled diamonds respectively. (d) The distribution of 2-propanol above the surface: CH_3, CH, O and H are identified by filled circles, filled squares, open diamonds, and open triangles respectively. The surface distribution of the upper amide atoms is shown in (e). Circles, squares, diamonds, and triangles correspond to N(23), H(24), C(25), O(26), respectively. The surface distribution of the lower amide atoms is shown in (f). Circles, squares, diamonds, and triangles correspond to N(11), H(12), C(13), and O(14), respectively.

Further evidence of hydrogen bonding is obtained from the snapshots. Specifically, all 3500 snapshots are examined for the presence of hydrogen bonds between 2-propanol and the DNB-phenylglycine selectors. The results of this analysis are summarized in Table 5.6. Focusing on the results for 90:10 *n*-hexane:2-propanol, on average 19.6% of the upper amide oxygen, O(26), are hydrogen bonded while 11.6% of the lower amide oxygens, O(14), have hydrogen bonds. In contrast, 2.6-3.6% of the amide hydrogens have H-bonds on average. The nitro oxygens could hydrogen-bond in principle but snapshot analysis reveals that fewer than 1% of the selectors have H-bonds of this type, on average. This is consistent with the proposed recognition models[137,22] for these selectors where the nitro groups do not have a major role in H-bonding, but their role is to make the dinitrophenyl ring a good π-acceptor.

Table 5.6 Hydrogen-bonding statistics for DNB-phenylglycine and DNB-leucine interfaces. A structural definition of hydrogen-bonding has been applied and results are presented for three solvent compositions. The first two columns identify the selector and solvent atoms involved in the hydrogen-bonding, and the following columns identify the percentage of the selectors with the specified hydrogen-bond.

Selector component	2-propanol component	Percentage occurrence in 90:10 hexane: 2-propanol	Percentage occurrence in 80:20 hexane: 2-propanol	Percentage occurrence in 0:100 hexane: 2-propanol
DNB-phenylglycine				
O(14)	H	11.6	11.8	18.1
O(26)	H	19.6	32.7	50.5
H(12)	O	2.6	5.1	4.7
H(24)	O	3.6	4.3	3.7
O(14) and H(24)	H and O	1.0	1.1	0.9
O(34) or O(35) or O(37) or O(38)	H	0.7	1.5	3.6
DNB-leucine				
O(14)	H	21.0	29.6	54.6
O(24)	H	24.6	35.6	71.8
H(12)	O	27.4	38.6	73.9
H(22)	O	33.3	43.6	49.7
O(14) and H(22)	H and O	3.4	4.5	2.5
O(24) and H(12)	H and O	3.7	3.8	1.4
O(32) or O(33) or O(35) or O(36)	H	1.4	2.2	5.9

Both snapshot analysis and radial distributions indicate significant H-bonds to the amide oxygens (O(14) and O(26)), but relatively few H-bonds to the amide hydrogens (H(12) and H(24)). This means that, for a chromatographic separation, the amide hydrogens may be available to the analyte for hydrogen bonding, although steric factors may interfere with this conclusion. The 2D distributions in Figure 5.7 provide information on the location of the solvent about the hydrogen-bonding groups in the selectors. Consider the 2D distribution of the alcohol oxygen about H(12), the lower amide hydrogen of the selector, shown in Figure 5.7(a). Four distinct regions are apparent: a ridge beginning at $z_c = 2$ Å and $r_c = 0$ Å and ending at $z_c = 0$ Å and $r_c = 2$ Å; a broad ridge beginning at $z_c = 4$ Å and $r_c = 0$ Å; a peak at $z_c = 0$ Å and $r_c = 5.5$ Å; and a ridge appearing above $r_c = 6$ Å. The snapshot in Figure 5.7(e) shows solvents distributed around H(12) with z_c and r_c values given. A 2-propanol directly hydrogen bonding to H(12) is evident in the snapshot and is separated by a distance that corresponds to the ridge beginning at $z_c = 2$ Å and $r_c = 0$ Å. Thus, this particular ridge corresponds to direct hydrogen bonding to H(12) and indicates that the H-bonding alcohol is either parallel ($z_c = 0$ Å) or above (0 Å < z_c < 2 Å) the hydrogen, but typically not below. In the snapshot, a second 2-propanol, located at $z_c = 4.1$ Å and $r_c = 1.7$ Å, is hydrogen bonding to the upper carbonyl oxygen, O(26). This alcohol contributes to the ridge beginning at $z_c = 4$ Å and $r_c = 0$ Å, and from the 2D distribution, it is further from the underlying surface than H(12). A third 2-propanol is shown in the snapshot. This alcohol is hydrogen bonding to the lower carbonyl oxygen, O(14), and its position relative to H(12) indicates that it is the source of the peak at around $z_c = 0$ Å and $r_c = 5.5$ Å.

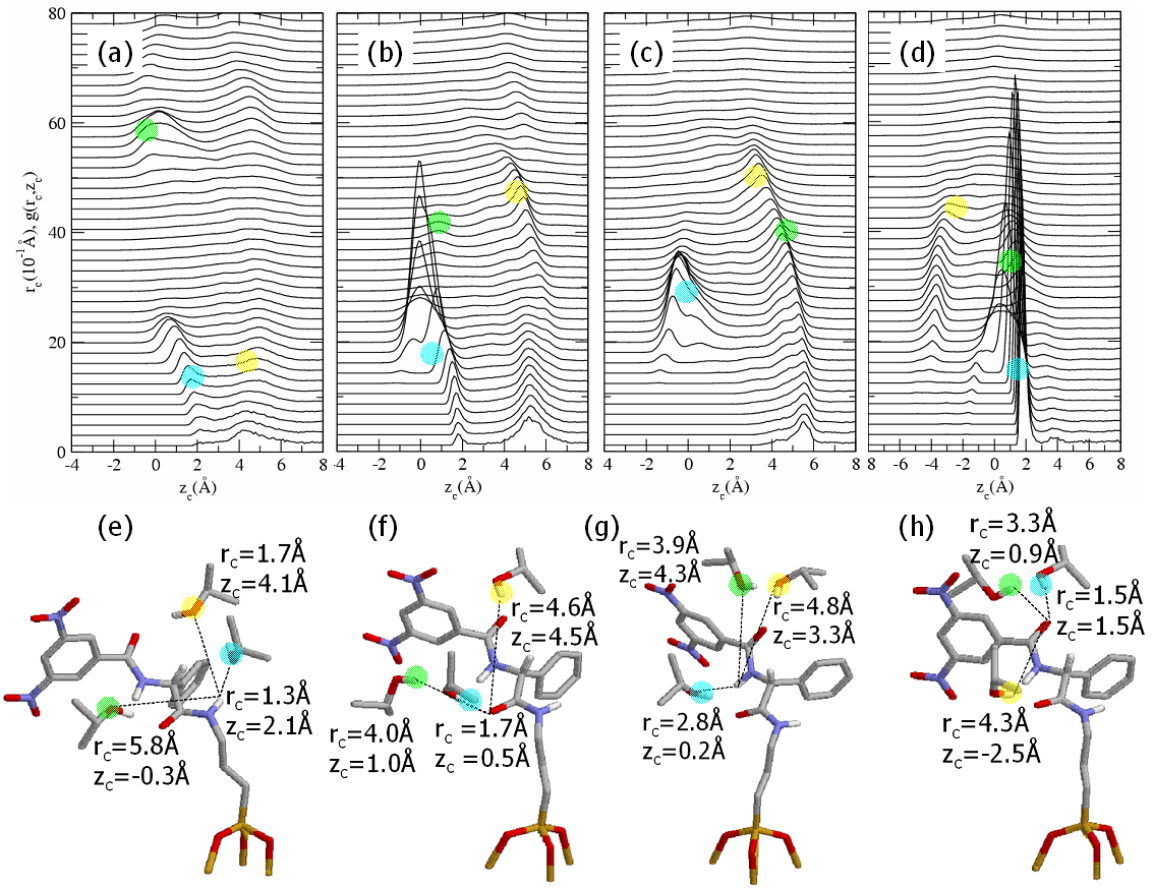

Figure 5.7 An analysis of hydrogen-bonding for the DNB-phenylglycine interface in 90:10 *n*-hexane:2-propanol. 2D distribution functions, $g(r_c,z_c)$, and representative snapshots are shown. The distribution of O(2-propanol) about H(12), H(2-propanol) about O(14), O(2-propanol) about H(24), and H(2-propanol) about O(26) are shown in (a), (b), (c), and (d), respectively. Illustrative snapshots, showing 2-propanol molecules around a single selector are shown in (e), (f), (g), and (h) with interatomic separations given in Å. Silicon, oxygen, nitrogen, carbon, hydrogen atoms are shown in gold, red, blue, grey, and white respectively. The 2-propanol molecules are emphasized in the snapshots and their corresponding positions are shown in panels (a)-(d).

The 2D distribution about the lower amide oxygen, O(14), is shown in Figure 5.7(b) and the associated snapshot is provided directly below, in Figure 5.5(f). The alcohol has a high probability to H-bond to O(14) and this is evident from the prominence of the ridge beginning at $z_c = 2$ Å and $r_c = 0$ Å in the 2D distribution. This solvent prefers to be further from the underlying surface than O(14), but it may also be slightly closer. The snapshot shows that it may also simultaneously hydrogen bond to another 2-propanol, and this second alcohol contributes to a weak peak in the 2D distribution that appears around $z_c = 1$ Å and $r_c = 4$ Å. Finally, an alcohol hydrogen bonded to the upper carbonyl oxygen is evident in the snapshot and contributes to the ridge at $z_c = 5$ Å. This latter ridge indicates that the alcohol hydrogen, for the 2-propanol hydrogen bonded to the upper carbonyl, is typically 5Å further from the surface than O(14), but it may be directly above or shifted parallel to the surface.

For hydrogen, H(24), a peak at $z_c = 0$ Å is evident in the 2D distribution of Figure 5.7(c). The presence of a peak, rather than a ridge, in the 2D distribution indicates that the alcohol is fairly localized. In particular, the location of the peak indicates that hydrogen-bonding to H(24) occurs when the solvent is on the side, as shown in the snapshot in Figure 5.7(g). It is also possible for a solvent to simultaneously hydrogen bond to H(24) and O(14), and this is evident in the snapshot shown in Figure 5.7(g). A closer inspection of the peak in the 2D distribution reveals that there are, in fact, two peaks contributing in this region. Returning to Table 5.6, 1% of the selectors have simultaneous H-bonds to a single 2-propanol, via O(14) and H(24). However, on average, only 3.6% of selectors have hydrogen bonds to H(24). Therefore, roughly one

third of every hydrogen bonding event at H(24) involves a solvent that simultaneously H-bonds to O(14). Both of these events contribute to the peak in the 2D distribution.

The 2D distribution of the upper amide oxygen, O(26), shown in Figure 5.7(d) has a significant ridge at 0 Å < z_c < 2 Å indicating a high probability for hydrogen bonding with the solvent preferring to be above O(26). The other ridge in the 2D distribution, at $z_c \approx$ -4 Å, reflects H-bonding to the lower amide group.

The relationship between solvent composition and selector conformations has been discussed previously. The extent and characteristics of solvent-solute hydrogen bonding will also depend on solvent composition. Snapshot analysis has been performed for all solvent compositions and the results are presented in Table 5.6. Compare the hydrogen bonding statistics for 90:10 and 80:20 *n*-hexane:2-propanol. The addition of more alcohol leads to significantly more hydrogen bonds to the upper amide oxygen, O(26). The frequency of hydrogen bonding events for other amide atoms also increases, but by a smaller amount, when the solvent includes more alcohol. In a 100% 2-propanol solvent, over 50% of the upper amide oxygens and roughly 18% of the lower amide oxygens have hydrogen bonds to solvent. The hydrogen bond probabilities to amide hydrogens are small by comparison and have increased by only a few percent relative to 90:10 *n*-hexane:2-propanol. Thus the impact of increasing alcohol content in the solvent is different for amide oxygens and amide hydrogens.

5.2.8 Solvation of DNB-leucine CSP

Figure 5.8 presents a sideview snapshot of the DNB-leucine interface with 90:10 *n*-hexane:2-propanol. The alcohol clearly prefers the interface, as it also did for

DNB-phenylglycine. The extended structure of the DNB-leucine selectors is evident in the snapshot and, relative to DNB-phenylglycine, there is less crowding of the selectors at the interface.

Figures 5.8(c) and 5.8(d) show the distribution of solvent as a function of separation from the underlying silicon layer. Both *n*-hexane and 2-propanol have an increased probability of being found directly above the end-caps. However, *n*-hexane shows a region of decreased probability at around 10 Å while the distribution of 2-propanol is more complex. In particular, the probability for the alcohol oxygen and hydrogen are still significant at this separation although the CH and CH_3 groups are less likely to be found at this distance from the underlying Si. This is in contrast to DNB-phenylglycine where selector crowding excluded the alcohol from this region.

Figure 5.8(b) provides radial distributions between potential solvent-selector hydrogen bonding pairs. As with DNB-phenylglycine, the amide oxygens have a significant probability of finding an alcohol hydrogen roughly 2 Å away. Unlike DNB-phenylglycine, both the upper and lower amide oxygens are comparable, with the respective radial distributions showing that approximately forty-five times more alcohol oxygen is found at this separation than expected based on the bulk density. Consider the amide hydrogens. For DNB-phenylglycine, solvent H-bonding to these hydrogens occurred infrequently. This is not the case for DNB-leucine where the radial distribution between these hydrogens and the alcohol oxygen are sharply peaked. Specifically, both the upper and lower hydrogens are 45-55 times more likely to have an alcohol at roughly 2 Å than expected based on the bulk density.

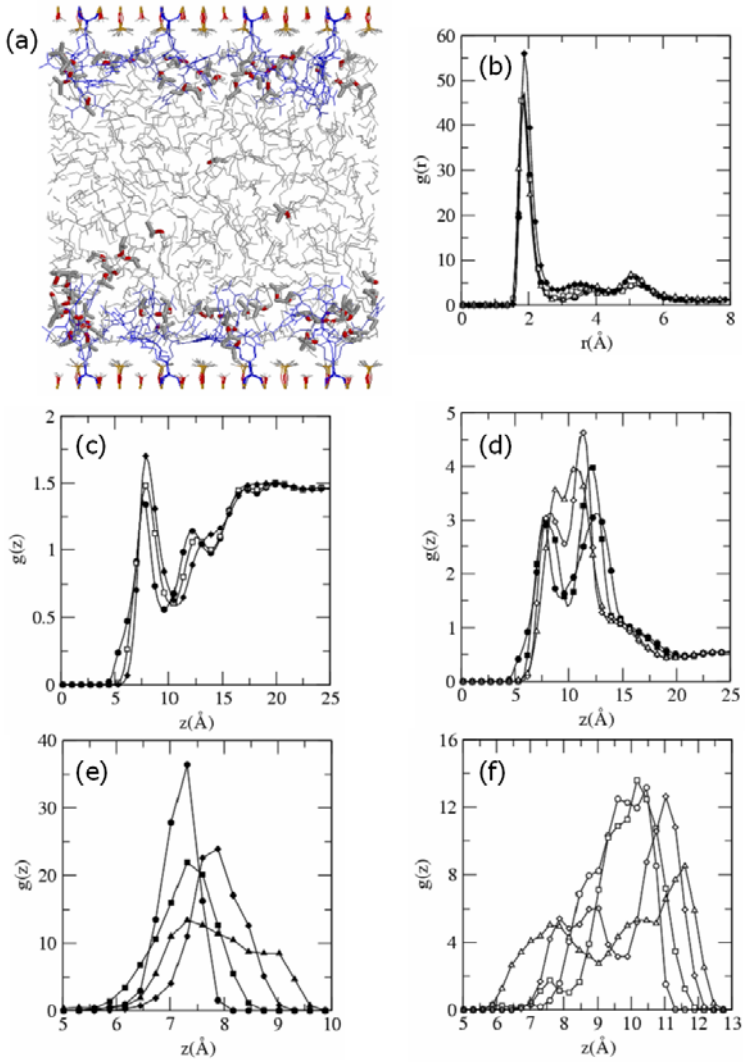

Figure 5.8 Simulation results for the DNB-leucine interface in 90:10 *n*-hexane: 2-propanol. A sideview of the simulation cell is presented in (a). Silicon, oxygen, carbon, hydrogen atoms are shown in gold, red, grey, and white respectively. Selector molecules are shown in blue and 2-propanol molecules are bolded. (b) Radial distributions between potential selector-solvent hydrogen bonding pairs: H(12)-O(2-propanol), O(14)-H(2-propanol), H(22)-O(2-propanol), and O(24)-H(2-propanol) are represented by filled circles, open squares, filled diamonds, and open triangles respectively. (c) The distribution of *n*-hexane above the surface: CH_3, 2-CH_2, and 3-CH_2 are represented by filled circles, open squares, and filled diamonds respectively. (d) The distribution of 2-propanol above the surface: CH_3, CH, O and H are identified by filled circles, filled squares, open diamonds, and open triangles respectively. The surface distribution of the upper amide atoms is shown in (e). Circles, squares, diamonds, and triangles correspond to N(21), H(22), C(23), O(24), respectively. The surface distribution of the lower amide atoms is shown in (f). Circles, squares, diamonds, and triangles correspond to N(11), H(12), C(13), and O(14), respectively.

Snapshot analysis for hydrogen bonding at the DNB-leucine interface is presented in Table 5.6. Even in 90:10 *n*-hexane:2-propanol, on average 27-33% of the selectors have a hydrogen bond to one of the amide hydrogens (H(12) and H(22)). In contrast, the amide oxygens (O(14) and O(24)) form hydrogen bonds in 21-25% of the selectors, on average. A comparison with the hydrogen bond statistics for DNB-phenylglycine shows that the leucine-based selector forms many more hydrogen bonds with 2-propanol. This increase occurs mostly at the amide hydrogens, but the hydrogen bonding probability is also higher for the amide oxygens.

Simultaneous hydrogen bonding between a single 2-propanol and multiple atoms in DNB-leucine occurs. The snapshot analysis results in Table 5.6 indicate that 3.4% of the selectors have simultaneous H-bonds to O(14) and H(22) while 3.7% of the selectors have H-bonds to O(24) and H(12). In both cases, a single solvent molecule forms simultaneous hydrogen bonds to the upper and lower amide groups.

Figure 5.9 shows 2D distributions for hydrogen bonding about DNB-leucine selectors. The distributions for H(12) (Figure 5.9(a)), O(14) (Figure 5.9(b)), H(22) (Figure 5.9(c)), and O(24) (Figure 5.9(d)) all show a prominent ridge beginning at $r_c = 0$ Å and $z_c = 2$ Å. This ridge indicates the probable location for solvent hydrogen bonding directly to the relevant selector atom. For the lower amide group, the ridge vanishes as z_c becomes negative, indicating that the solvent prefers to hydrogen bond from above or on the side. The upper amide groups have a ridge that persists to negative z_c and, for O(24), the hydrogen bonding solvent prefers to be closer to the surface. This is evident in the snapshot in Figure 5.9(h) where the solvent hydrogen bonding to O(24)

is closer to the surface. Secondary ridges in the 2D distributions of Figure 5.9 are also evident. These correspond either to contributions from hydrogen bonding to other groups in the selector, or to solvent-solvent hydrogen bonding where one of the solvents also bonds to a selector atom.

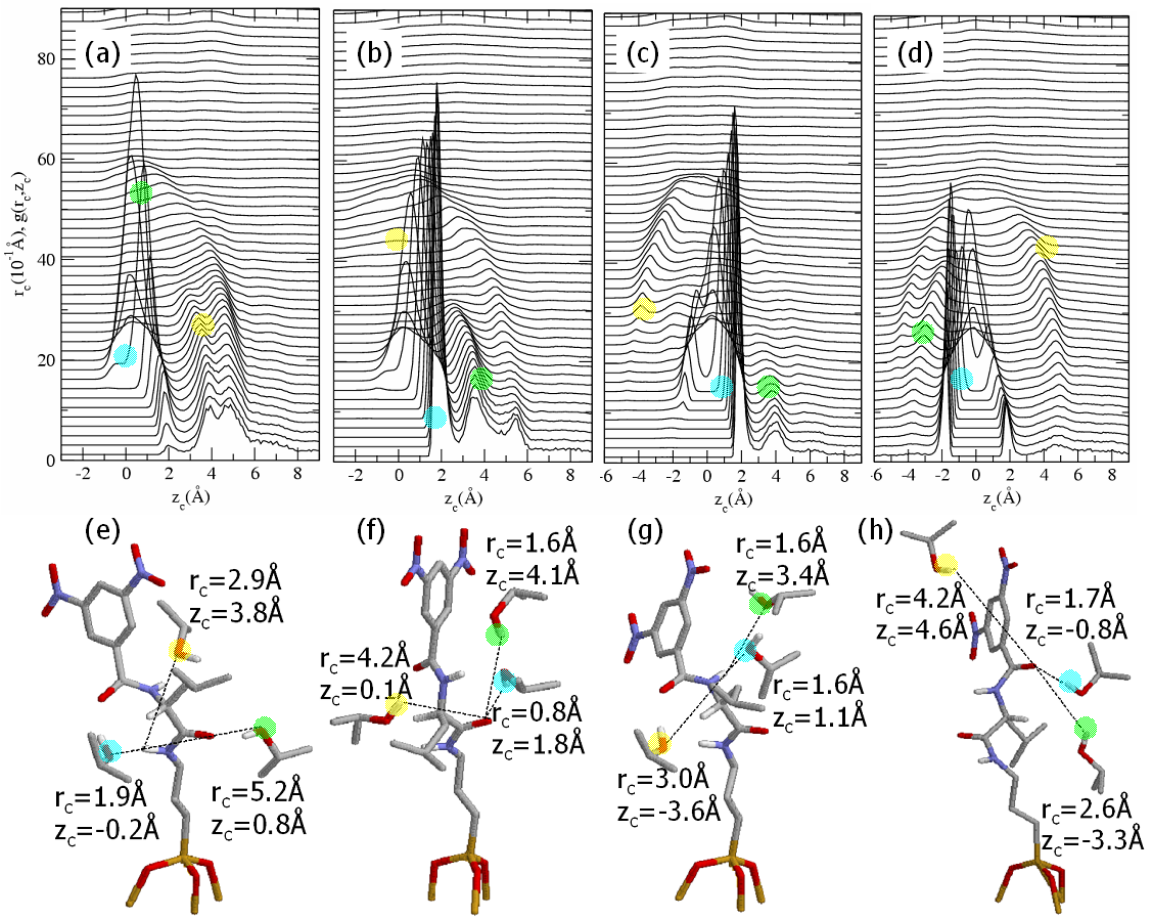

Figure 5.9 An analysis of hydrogen-bonding for the DNB-leucine interface in 90:10 *n*-hexane:2-propanol. 2D distribution functions, $g(r_c,z_c)$, and representative snapshots are shown. The distribution of O(2-propanol) about H(12), H(2-propanol) about O(14), O(2-propanol) about H(22), and H(2-propanol) about O(24) are shown in (a), (b), (c), and (d), respectively. Illustrative snapshots, showing 2-propanol molecules around a single selector are shown in (e), (f), (g), and (h) with interatomic separations given in Å. Silicon, oxygen, nitrogen, carbon, hydrogen atoms are shown in gold, red, blue, grey, and white respectively. The 2-propanol molecules are emphasized in the snapshots and their corresponding positions are shown in panels (a)-(d).

Consider the impact of solvent composition on hydrogen bonding at the DNB-leucine interface. The lower half of Table 5.6 provides the relevant H-bond statistics. As the alcohol content of the solvent increases from 90:10 to 80:20 *n*-hexane:2-propanol, all the non-simultaneous hydrogen bonding probabilities to amide atoms increase by 9-11%. This is in contrast to DNB-phenylglycine where an increase in hydrogen bonds was observed primarily for the "upper" amide oxygen. When the solvent is 100% 2-propanol, the probability for hydrogen bonding is between 50-74% for the amide groups. Thus solvent-selector hydrogen bonding is extensive. Compare the hydrogen bonding of the lower amide hydrogen, H(12), in 100% 2-propanol for DNB-phenylglycine and DNB-leucine. For the former, 4.7% of these hydrogens have H-bonds whereas 73.9% have H-bonds for DNB-leucine.

Table 5.7 summarizes the number of solvent-selector H-bonds observed, on average, for individual selectors. Consider 90:10 *n*-hexane:2-propanol. For the DNB-phenylglycine interface, most selectors do not have any H-bonds although 27% will have one H-bond, on average, and this bond will typically involve an amide oxygen. For DNB-leucine, 33.7% of the selectors have one H-bond, 22.6% have two H-bonds, and 6.8% have three H-bonds. So a much more significant fraction of the selectors have H-bonds for DNB-leucine and all four amide atoms (H(12),O(14),H(22),O(24)) participate in H-bonding. Clearly, these two selectors have very different hydrogen bonding characteristics at the interface.

Table 5.7 Number of hydrogen bonds per selector in 90:10, 80:20, and 0:100 *n*-hexane: 2-propanol solvents.

Number of H-bonds per selector molecule	Percentage occurrence in 90:10 hexane: 2-propanol	Percentage occurrence in 80:20 hexane: 2-propanol	Percentage occurrence in 0:100 hexane: 2-propanol
DNB-phenylglycine			
0	68.0	55.8	38.1
1	27.0	35.9	48.5
2	4.5	7.8	11.9
3	0.4	0.5	1.4
4	0.0	0.0	0.1
DNB-leucine			
0	35.2	19.8	2.4
1	33.7	34.1	14.7
2	22.6	29.2	31.9
3	6.8	12.8	33.3
4	1.7	4.1	17.1

5.3 Experimental study of DNB-phenylglycine and DNB-leucine interfaces

The MD results obtained for DNB-phenylglycine and DNB-leucine chiral interfaces are correlated with an experimental characterization described in this section. The samples are obtained using two different preparation methods. They are methodically analysed with XPS, RAIRS, and AFM. Chemical force spectrometric measurements are employed for probing the chiral self-selectivity of these interfaces.

5.3.1 Sample preparation

Prior to functionalization, the Si(111) wafers were etched in a $HF_{(aq)}/NH_4F_{(aq)}$ solution using the method described in Section 4.3.1. In some experiments, etching with a solution of H_2SO_4-30% H_2O_2 (70:30 by volume) for two hours was used instead, with similar results. The resulting –Si-OH sites in the surface can be subsequently reacted to form a covalent link to the substrate. The AFM tips used in CFM experiments were oxide sharpened silicon nitride probes. Prior to functionalization they were cleaned in a plasma oxidizer for 4 minutes.

For the preparation of tethered DNB-phenylglycine and DNB-leucine samples, I used 3-aminopropyltriethoxysilane (APTES), *S*- or *R*-*N*-(3,5-dinitrobenzoyl)-phenylglycine, and 2-ethoxy-1-ethoxycarbonyl-1,2-dihydroquinoline (EEDQ) that are commercially available in high purity (Aldrich). Since *S*- or *R*-*N*-(3,5-dinitrobenzoyl)-leucine are not available commercially in pure chiral forms, they were synthesized from *R*- or *S*-leucine according to the literature protocols:[217] to 1.0 g (7.6 mmol) of *S*-leucine

(or *R*-leucine) suspended in 50 ml of dry THF was added 1.9 g (8.35 mmol) of 3,5-dinitrobenzoyl chloride and 0.5 g (8.6 mmol) of propylene oxide (dropwise, over 15 minutes). The mixture was stirred at room temperature under nitrogen. After 2 hours the solvent was removed and the crude *S*-*N*-(3,5-dinitrobenzoyl)-leucine (or *R*-*N*-(3,5-dinitrobenzoyl)-leucine) was recrystalized from acetone-CCl_4. 3.8 g white crystals of *S*-*N*-(3,5-dinitrobenzoyl)-leucine (76 %) were obtained. Similar values were obtained for *R*-*N*-(3,5-dinitrobenzoyl)-leucine.

^{1}H NMR (DMSO) of *S*-*N*-(3,5-dinitrobenzoyl)-leucine: δ 0.89 (d, 3H), 0.92 (d, 3H), 1.69 (m, 1H), 1.78 (m, 1H), 1.79 (m, 1H), 4.52 (m, 1H), 8.98 (t, 1H), 9.12 (d, 2H), 9.39 (d, broad, 1H).

Two methods of sample/tip preparations have been employed in this research. The first method is based on the Pirkle DNB-phenylglycine and DNB-leucine CSP preparation technique.[5,6] Amine-terminated Si(111) surfaces (and Si_3N_4 tips) are obtained by refluxing them in a solution of 100g (0.45 mol) APTES in 500 ml of dry toluene for 18-36 hours. Then, the γ-aminopropyl functionalized Si(111) surfaces (and Si_3N_4 tips) are reacted with one of *R*- or *S*-*N*-(3,5-dinitrobenzoyl)-phenylglycine or *R*- or *S*-*N*-(3,5-dinitrobenzoyl)-leucine, to form chirally-terminated surfaces. 0.05 g (0.14 mmol) *R*-*N*-(3,5-dinitrobenzoyl)-phenylglycine (or *S*-*N*-(3,5-dinitrobenzoyl)-phenylglycine), 0.038 g (0.15 mmol) EEDQ and γ-aminopropyl functionalized samples and tips were swirled for 8 hours in 1 ml of dry THF; 0.033 g (0.1 mmol) *S*-*N*-(3,5-dinitrobenzoyl)-leucine (or *R*-*N*-(3,5-dinitrobenzoyl)-leucine), 0.033 g (0.13 mmol) EEDQ and γ-aminopropyl functionalized samples and tips were swirled for

8 hours in 1 ml of dry CH_2Cl_2. At the end the samples and tips were washed gently with methanol. In the remainder of the thesis I will refer to this technique as the *two-step surface deposition method*. Schematically, this method is illustrated in Figure 5.10.

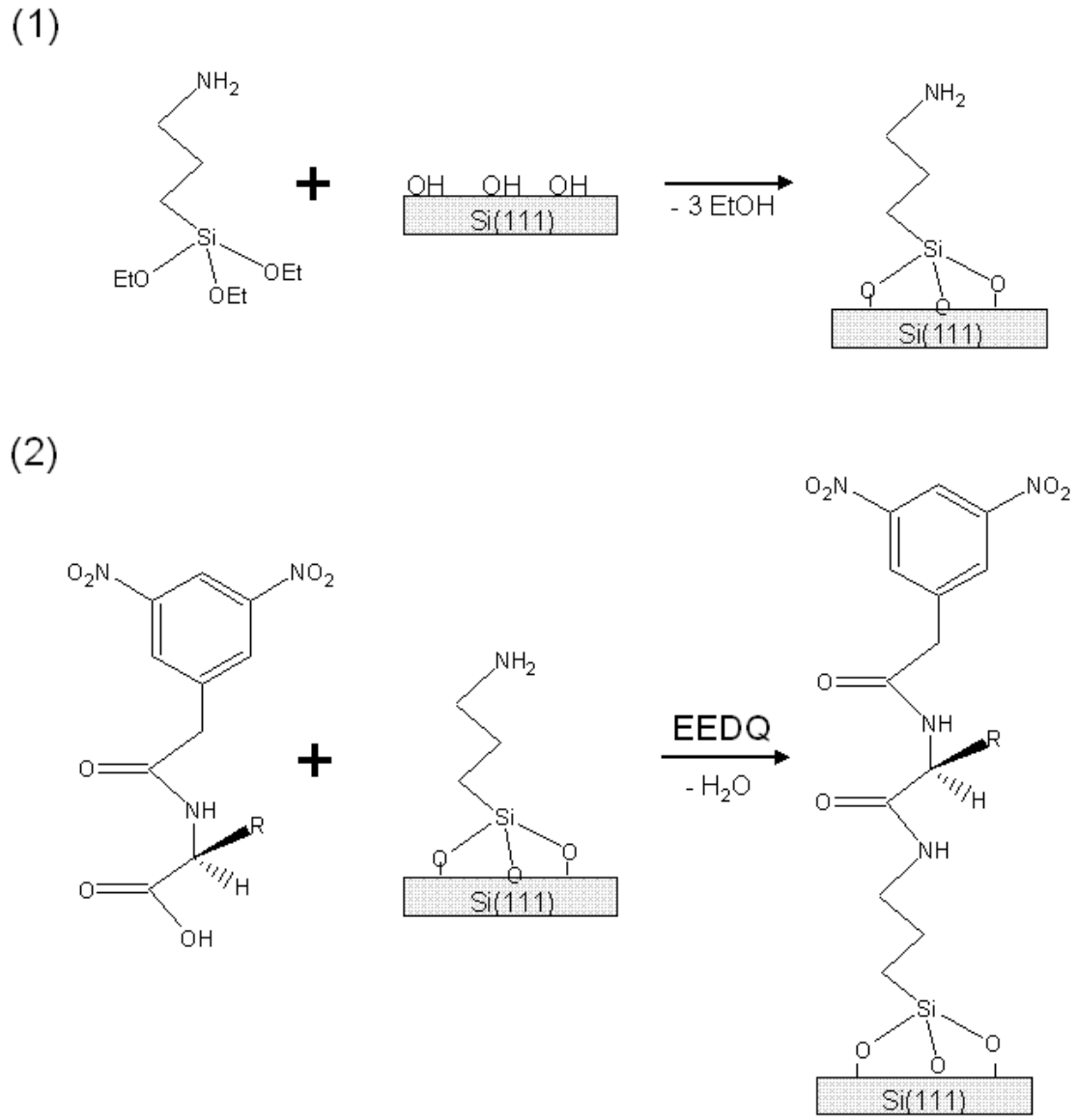

Figure 5.10 Chemical equations for the two-step surface deposition method. R is phenyl for DNB-phenylglycine and isobutyl for DNB-leucine. In step (1) APTES is deposited onto oxidized surfaces, and in step (2) the resulted surface is reacted with *N*-(3,5-dinitrobenzoyl)-phenylglycine and *N*-(3,5-dinitrobenzoyl)-leucine.

In the second method of preparation, the tethered DNB-phenylglycine and DNB-leucine compounds, properly named *R*- or *S*- [(3,5-dinitrobenzoyl)amino]-*N*-[3-(triethoxysilyl)propyl]-2-phenylacetamide and *R*- or *S*- [(3,5-dinitrobenzoyl)amino]-*N*-[3-(triethoxysilyl)propyl]-4-methylpentanamide, are synthesized prior to the deposition on the surface. These CSPs were synthesized based on previously reported methods.[7] 0.022 g (0.1 mmol) APTES was stirred for 2 hours with 0.069 g (0.2 mmol) *R*-*N*-(3,5-dinitrobenzoyl)-phenylglycine (or *S*-*N*-(3,5-dinitrobenzoyl)-phenylglycine) in the presence of 0.059 g (0.24 mmol) EEDQ in 1 ml dry THF. Similarly, 0.022 g (0.1 mmol) APTES was reacted for 2 hours with 0.065 g (0.2 mmol) *S*-*N*-(3,5-dinitrobenzoyl)-leucine (or *R*-*N*-(3,5-dinitrobenzoyl)-leucine) in the presence of 0.059 g (0.24 mmol) EEDQ in 1 ml DMF-CH_2Cl_2 (10:90 by volume). The etched Si(111) samples and oxidized Si_3N_4 tips were immersed in solutions of *R*- or *S*-[(3,5-dinitrobenzoyl)amino]-*N*-[3-(triethoxysilyl)propyl]-2-phenylacetamide and *R*- or *S*-[(3,5-dinitrobenzoyl)amino]-*N*-[3-(triethoxysilyl)propyl]-4-methylpentanamide for 24 hours at room temperature for the final tip/sample preparation step. In this thesis I will refer to this preparation technique as the *direct surface deposition method*. Schematically, the reactions involved in this method are shown in Figure 5.11.

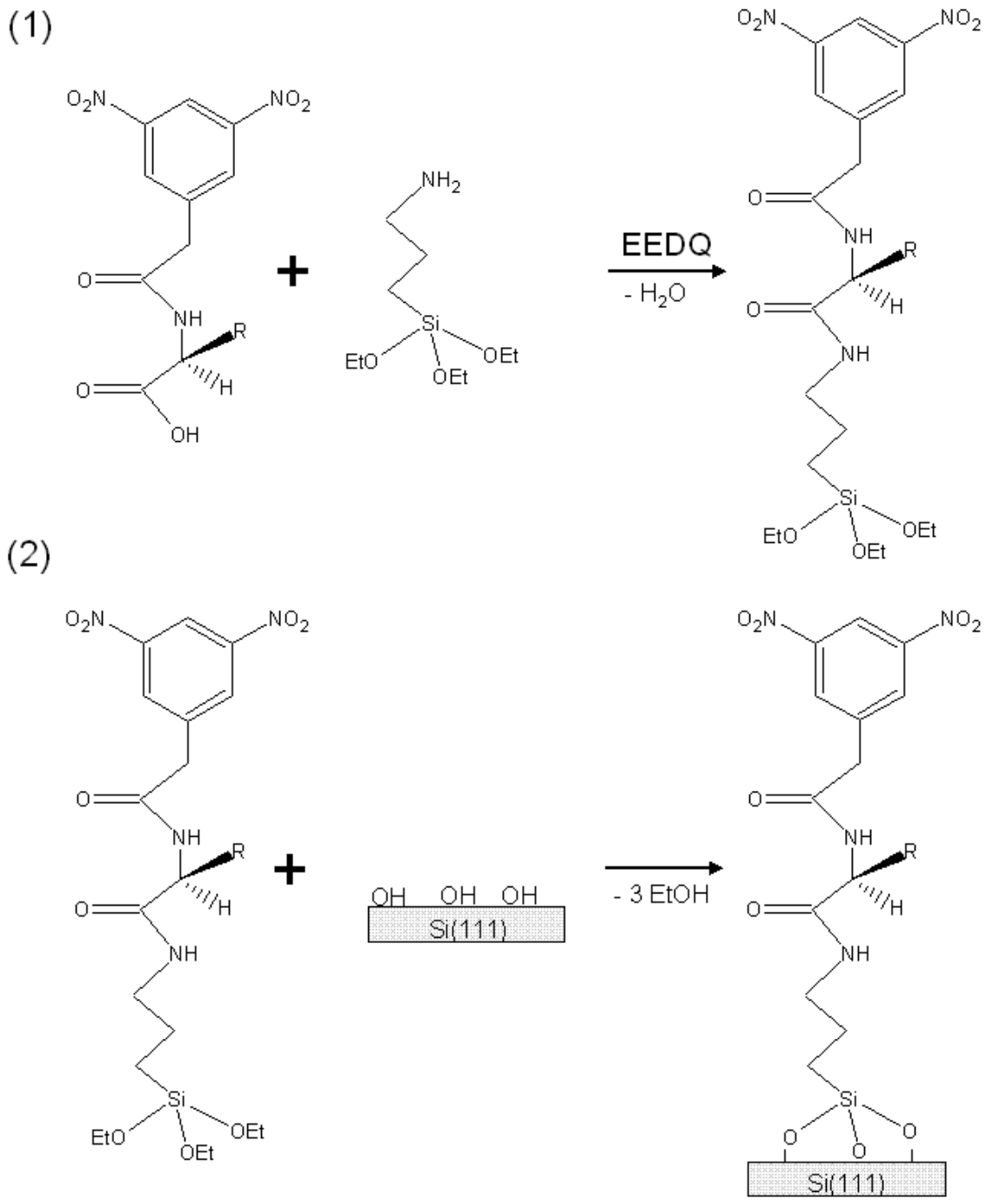

Figure 5.11 Chemical equations for the direct surface deposition method. R is phenyl for DNB-phenylglycine and isobutyl for DNB-leucine. In equation (1) DNB-phenylgycine and DNB-leucine are synthesized, and in equation (2) they are directly deposited on the oxidized surfaces.

5.3.2 Surface analysis

As outlined in the Section 5.3.1, chirally-terminated Si substrates were prepared using two different methods which I compare in this study. Although real CSPs are deposited on silica particles, here I wish to prepare samples that do not have a complex morphology that might become an impediment to chiral force spectrometric measurements. Therefore, I have deposited the compounds of interest on flat surfaces of etched Si(111), through a Si-O linkage. This type of deposition has been studied extensively, for example at the attachment of alkoxysilanes on Si(111).[189] AFM images displaying the morphology of the surfaces obtained in the two preparation methods are shown in Figure 5.12(a) (two-step surface deposition method) and 5.12(b) (direct surface deposition method). Similar results were obtained for *R* and *S* versions of both CSPs, so only two representative images are shown here. The surface prepared with the two-step surface deposition method (Figure 5.12(a)) displays pronounced roughness provided by the layer of APTES that is first deposited on the surface which acts as a template for the final surface morphology. Some agglomerates of highly cross-linked molecules are obvious from the image. These structures are as much as 180 nm in height and themselves contain some finer arrangement. However, using the direct surface deposition method (Figure 5.12(b)), the surface is much smoother, with structures that are only about 20 Å in height. The horizontal cross section provides a detailed look at the finer structure from the surface and confirms that the surface has a relatively smooth and uniform distribution.

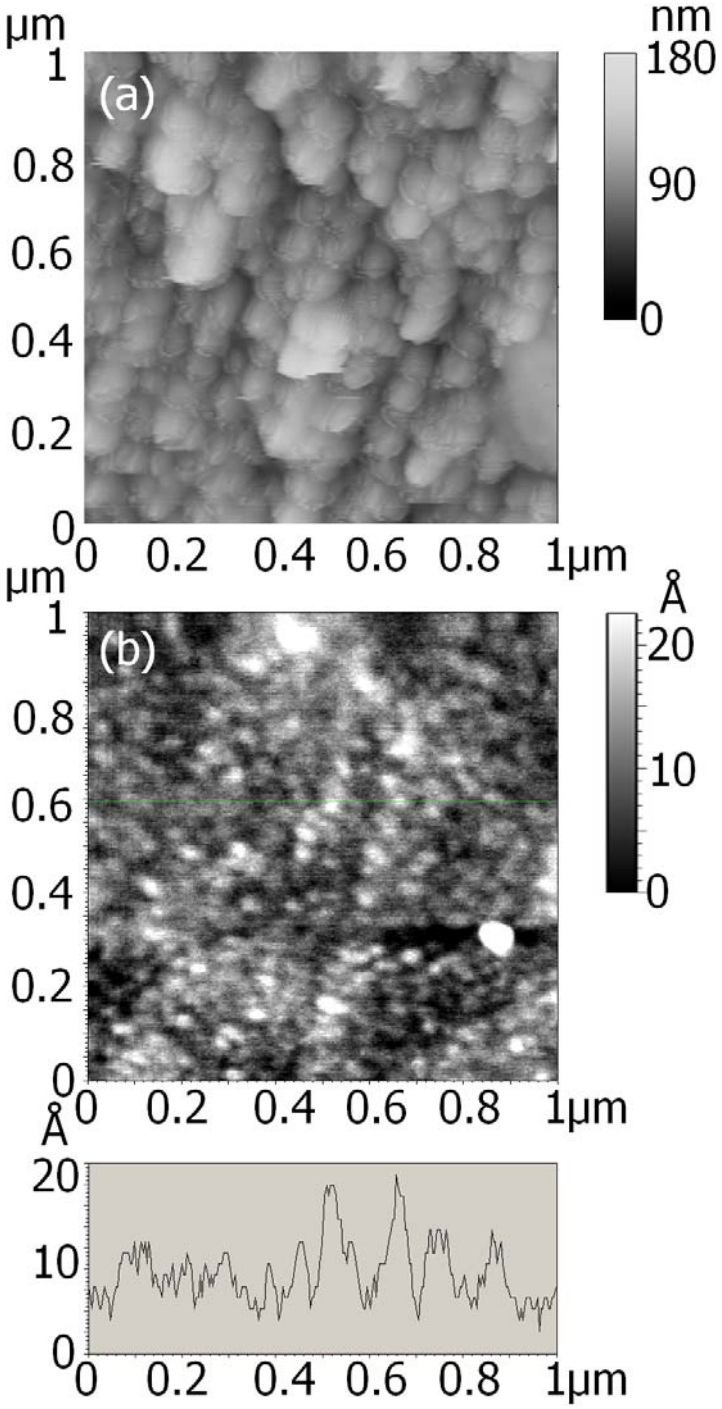

Figure 5.12 Tapping mode AFM images of (a) *R*-*N*-(3,5-dinitrobenzoyl)-phenylglycine reacted with an γ-aminopropyl functionalized surface in the two stage deposition process and (b) *R*-DNB-leucine directly deposited on Si(111). For the latter, the horizontal cross section at y = 0.59 μm is also provided.

A more precise analysis of the surface layer thickness was performed with XPS. The oxidized Si(111) surface gives rise to two lines in the Si 2p XPS: a strong peak at 99.6 eV associated with silicon and a smaller peak at higher binding energy, 103.4 eV, associated with silicon oxide (Figure 5.13(a)). As the CSP is deposited on the surface, the Si 2p oxide peak intensity increases, while the Si 2p substrate line intensity decreases. This was observed in the samples prepared with the two-step surface deposition method (Figure 5.13(b)) and the direct surface deposition method (Figure 5.13(c)). The layer thickness was estimated assuming attenuation of the underlying Si substrate signal by the overlying CSP using the relationship $I = I_o e^{-d/\lambda}$, where I is the signal from the modified surface layer, I_o is the signal from the unmodified Si(111), d is the depth in the solid at which the photoelectron is being ejected, and λ is the mean escape depth. For the attenuation of the Si 2p substrate line intensity, the previously determined value of 23 ± 2 Å was used for the mean escape depth,[147] and the intensity values were corrected based on the background signal beyond the valence band. The calculated layer thickness for the tethered DNB-leucine and DNB-phenylglycine surfaces prepared using the two-step surface deposition method is 137 ± 12 Å, in agreement with the rough surface observed by AFM (Figure 5.12(a)). For the chiral surfaces prepared using the direct surface deposition method, the layer thickness was significantly smaller, at 30 ± 4 Å. Considering the size of the tethered DNB-phenylglycine and DNB-leucine molecules, this means that I have one or two layers on the surface, confirming the features observed in AFM (Figure 5.12(b)).

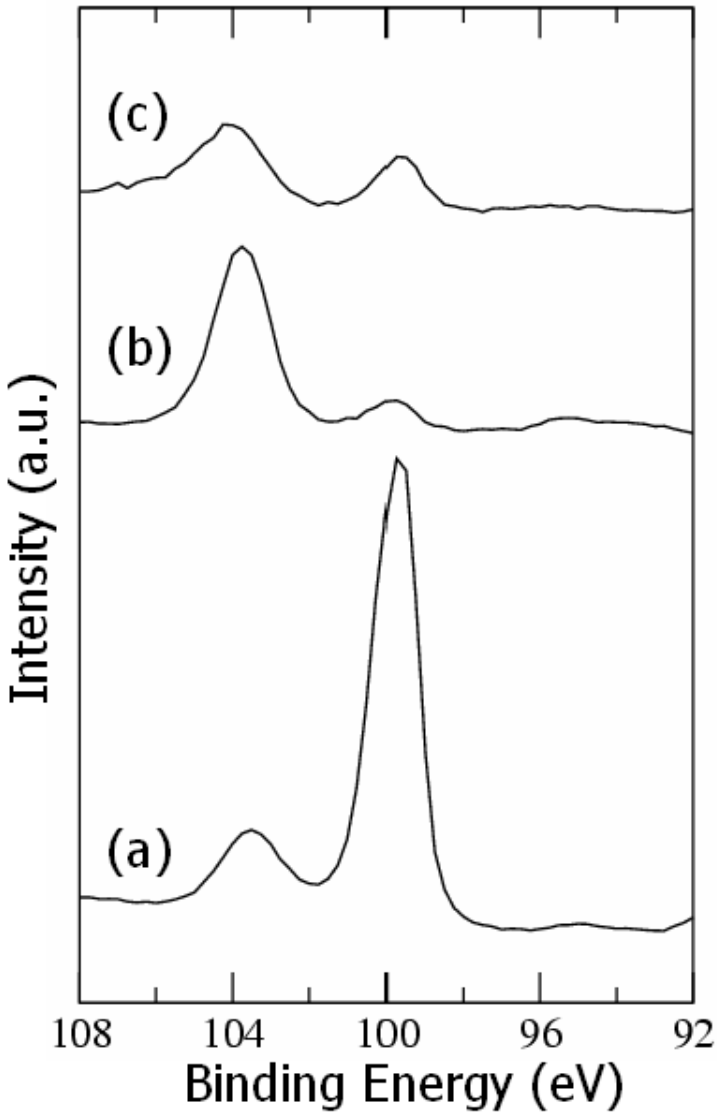

Figure 5.13 Si2p XPS spectra of an (a) oxidized Si(111) surface, (b) *R*-*N*-(3,5-dinitrobenzoyl)-leucine reacted with an γ-aminopropyl functionalized Si(111) surface in at two-stage deposition process and (c) *R*-[(3,5-dinitrobenzoyl)amino]-*N*-[3-(triethoxysilyl)propyl]-4-methylpentanamide directly deposited on a Si(111) surface.

Figure 5.14(a) shows the surface RAIRS spectrum of APTES-modified Si(111). The major peaks are assigned in Table 5.8. Peaks of particular note are those at 3439 cm^{-1} and 3348 cm^{-1}, typical for N-H stretches that appear in primary amines. Another characteristic peak is 1584 cm^{-1} due to the scissoring NH_2 bend. After the APTES-modified surface was reacted with the DNB-phenylglycine (two-step surface deposition method), the surface RAIRS spectrum changes significantly (Figure 5.14(b)). In particular, characteristic peaks for amide N-H stretches (asymmetric - 3264 cm^{-1}, symmetric – 3099 cm^{-1}), and those typical NO_2 groups (asymmetric – 1537 cm^{-1}, symmetric – 1340 cm^{-1}) are present suggesting that DNB-phenylglycine has been successfully linked to the surface. However, the continued presence of the peak at 1590 cm^{-1} indicates that unreacted APTES remains on the surface. The strong peak at 1784 cm^{-1} is typical of a C=O stretch in a carboxylic acid group. This suggests that some of the DNB-phenylglycine is physisorbed on the surface and remains unreacted with the APTES groups. To verify this, I observed that a transmission IR of a THF solution of DNB-phenylglycine exhibits the same peak at 1784 cm^{-1}. This peak did not appear in the surface RAIRS spectrum of tethered DNB-phenylglycine that was synthesized prior to the deposition (direct surface deposition method) on the Si(111) surface (Figure 5.14(c)). This spectrum lacks both the peak at 1784 cm^{-1} and the peak due to amine at 1584 cm^{-1}, demonstrating that the best interface for the CFM experiments is prepared by using the synthetic approach, because it provides only the compound of interest on the surface and there are no free amine groups present.

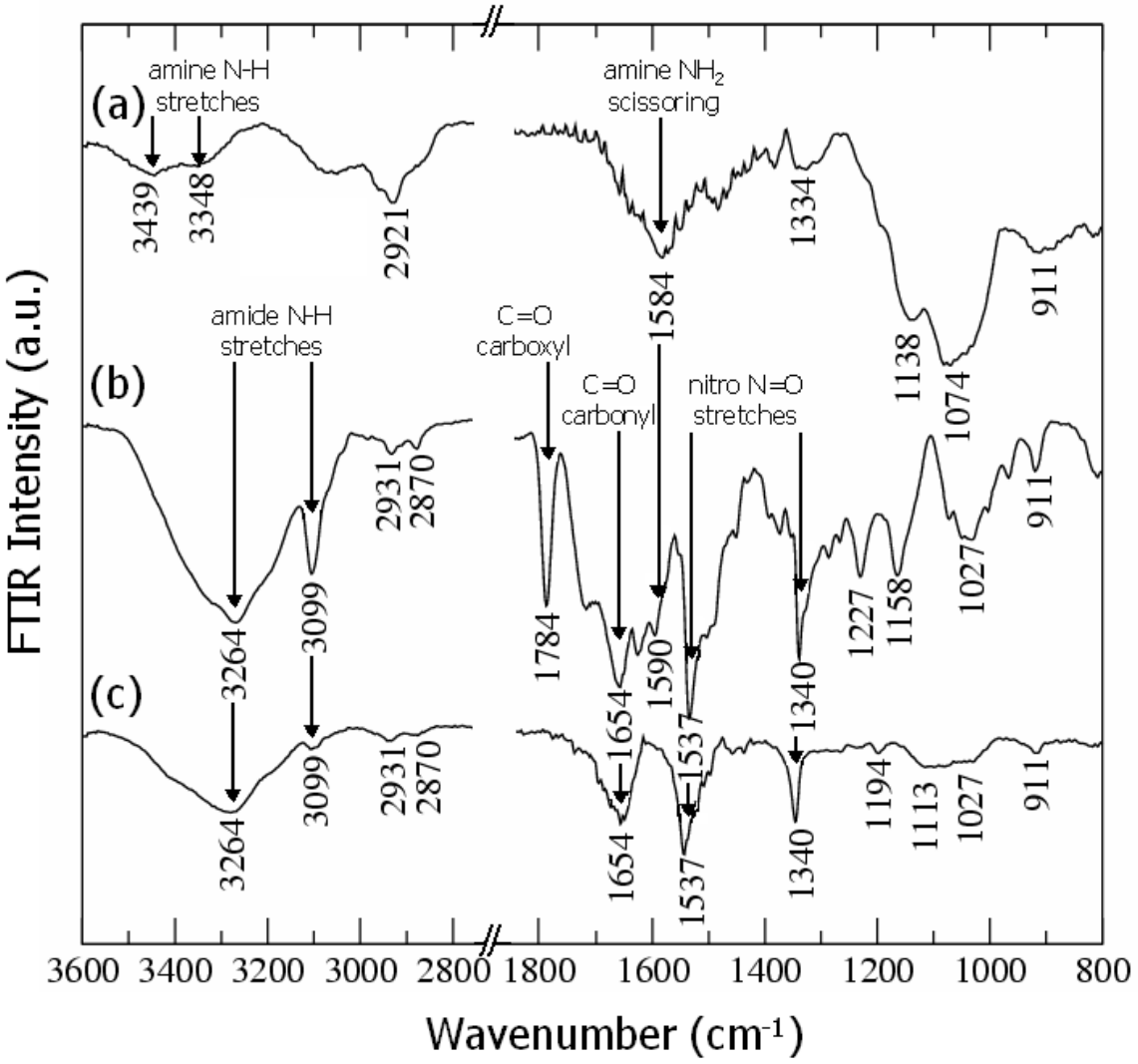

Figure 5.14 Surface FTIR spectra of (a) an γ-aminopropyl functionalized Si(111) surface, (b) *N*-(3,5-dinitrobenzoyl)-phenylglycine reacted with an γ-aminopropyl functionalized surface in the two-stage deposition process and (c) [(3,5-dinitrobenzoyl)amino]-*N*-[3-(triethoxysilyl)propyl]-2-phenylacetamide directly deposited on the Si(111) surface.

Table 5.8 The main surface FTIR bands of (a) an γ-aminopropyl functionalized Si(111) surface, (b) *N*-(3,5-dinitrobenzoyl)-phenylglycine reacted with an γ-aminopropyl functionalized surface in at two-stage deposition process and (c) [(3,5-dinitrobenzoyl)amino]-*N*-[3-(triethoxysilyl)propyl]-2-phenylacetamide directly deposited on the Si(111) surface.

(a) aminopropyl-terminated $\bar{\upsilon}$ (cm^{-1})	(b) two-stage deposited DNB-phenylglycine $\bar{\upsilon}$ (cm^{-1})	(c) directly deposited DNB-phenylglycine $\bar{\upsilon}$ (cm^{-1})	Assignment
3439	-	-	N-H stretch (primary amine)
3348	-	-	N-H stretch (primary amine)
-	3264	3264	N-H asymmetric stretch (amide)
-	3099	3099	N-H symmetric stretch (amide)
2921	2931	2931	C-H stretch (aliphatic)
-	2870	2870	C-H stretch (aliphatic)
-	1750	-	C=O stretch (carboxyl)
-	1654	1654	C=O stretch (amide)
1584	1590	-	NH_2 bend, scissoring
-	1537	1537	N=O asymmetric stretch (nitro)
-	1340	1340	N=O symmetric stretch (nitro)
1334	-	-	CH_2 bend
-	1227	-	C-O stretch (carboxyl)
1138	1158	1113	C-N stretch (amine and amide)
1074	1027	1027	Si-O stretch
911	911	911	Si-O stretch

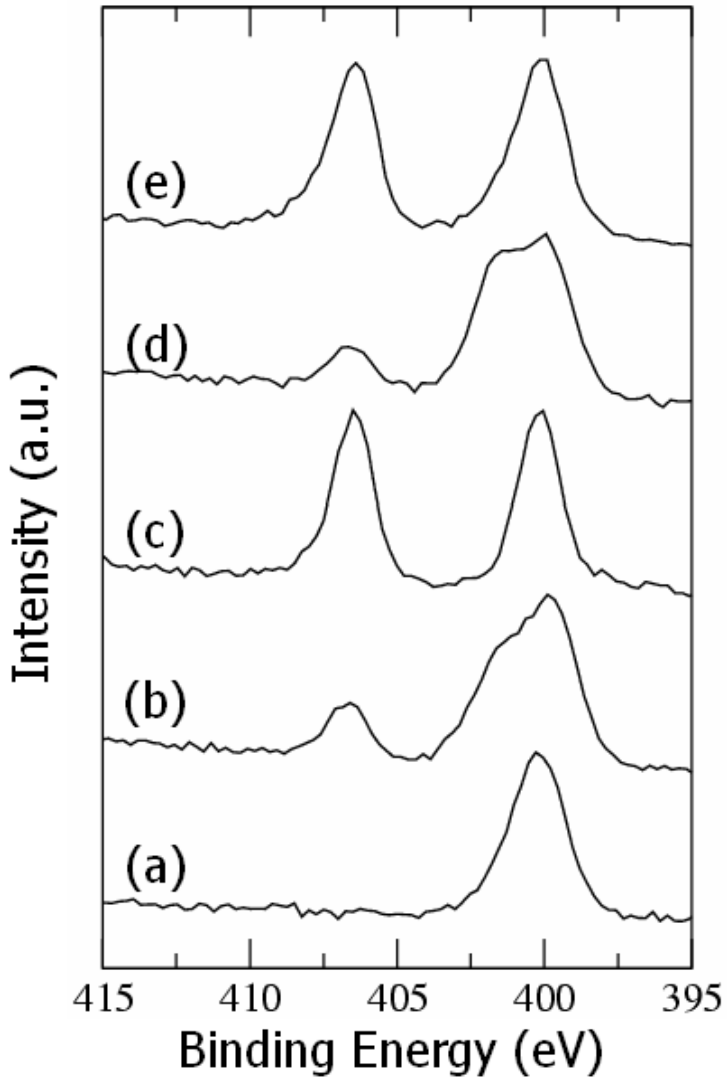

Figure 5.15 N1s XPS spectra of (a) a γ-aminopropyl functionalized Si(111) surface, (b) *R*-*N*-(3,5-dinitrobenzoyl)-phenylglycine reacted with the γ-aminopropyl functionalized Si(111) surface in the two-stage deposition process, (c) *R*-[(3,5-dinitrobenzoyl)amino]-*N*-[3-(triethoxysilyl)propyl]-2-phenylacetamide directly deposited on the Si(111) surface, (d) *R*-DNB-leucine reacted with the γ-aminopropyl functionalized surface in the two-stage deposition process and (e) *R*-[(3,5-dinitrobenzoyl)amino]-*N*-[3-(triethoxysilyl)propyl]-4-methylpentanamide directly deposited on the Si(111) surface.

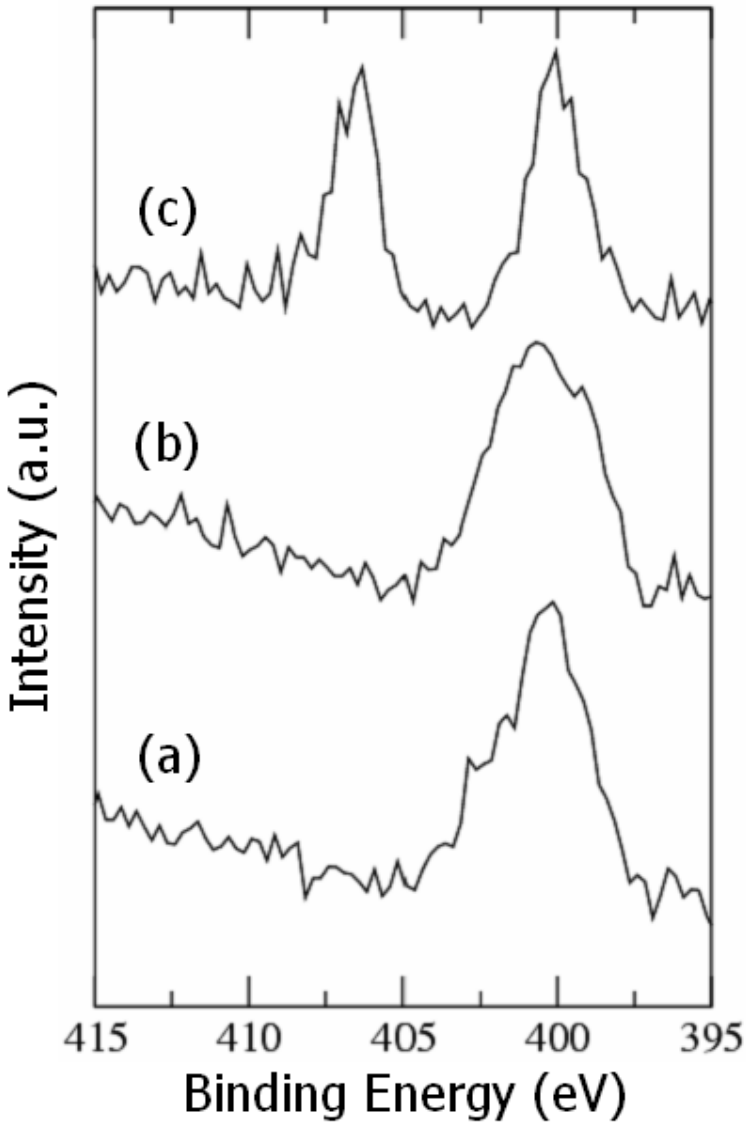

Figure 5.16 N1s XPS spectra of (a) a γ-aminopropyl functionalized AFM tip, (b) *R*-*N*-(3,5-dinitrobenzoyl)-phenylglycine reacted with the γ-aminopropyl functionalized AFM tip in the two-stage deposition process, (c) *R*-[(3,5-dinitrobenzoyl)amino]-*N*-[3-(triethoxysilyl)propyl]-2-phenylacetamide directly deposited on the AFM tip.

Both DNB-phenylglycine and DNB-leucine contain two nitrogen atoms in a nitro environment, and two nitrogen atoms in an amide environment. These are readily distinguished using the XPS, since the N1s signal for nitrogen in amine/amide groups appears at ~400.0 eV and the N1s signal for nitrogen in nitro groups appears at ~407.0 eV. Since each tethered DNB-phenylglycine and DNB-leucine molecule has the same number of nitrogens in amide groups and nitro groups, the two N1s peaks should have identical areas.

The N1s spectrum of an APTES sample is shown in Figure 5.15(a). It displays a single peak at ~400.0 eV for the amine nitrogen, as expected. When this APTES sample was reacted with DNB-phenylglycine and DNB-leucine (two-step surface deposition method), the resulted spectra are shown in Figures 5.15(b) and 5.15(d), respectively. The area ratio for nitro to amine/amide N1s peaks is 0.10:1 – 0.15:1. Evidently, unreacted APTES sites are present in excess on this surface. Furthermore, the peak at 400 eV shows a shoulder to higher binding energy consistent with protonated $–NH_3^+$ species on the surface. When the tethered DNB-phenylglycine and DNB-leucine are directly deposited on the oxidized Si(111) surface, the N1s spectra shown in Figure 4(c) and 4(e) are obtained. The peaks corresponding to nitro and amide/amine nitrogens have the same areas, within experimental error, demonstrating that only tethered DNB-phenylglycine or DNB-leucine are present on the surface. The same XPS analysis was performed on the modified atomic force microscopy tips that were used in the chemical force measurements. Because of the small area of the tips and cantilevers, the XPS signal-to-noise ratio was smaller than that in the previous analysis. The results for tips of tethered

DNB-phenylglycine are shown in Figure 5.16. Tethered DNB-leucine showed similar features. The analysis is much the same as for Figure 5.15, demonstrating that the direct surface deposition method successfully attaches the CSP on the tip surface.

The chemical force spectrometric experiments described below were carried out in 2-propanol and hexane solutions. To determine the stability of these surfaces, a study of the aging effect on the samples prepared using the direct surface deposition method was completed. The samples were exposed to 2-propanol and hexane for times ranging from 2 hours up to 42 hours and the XPS N1s spectrum was analyzed. It was observed that the ratio between the N1s peak areas from nitro groups and amide/amine groups decreased with the increasing exposure time in 2-propanol or hexane. In fresh samples this ratio is 1:1. After a 2 hour exposure to 2-propanol it decreased to about 0.7:1. By 42 hours exposure to 2-propanol it decreased to 0.2:1 (see Figure 5.17). In hexane, this peak ratio decrease with exposure is even more pronounced. After 2 hours exposure to hexane, the peak ratio decreased to about 0.4:1 and continued to decrease in prolonged exposure (0.19:1 after 42 hours). Overall, both peaks diminished in total area after prolonged exposure to both 2-propanol and hexane, suggesting that some compounds were stripped off the surface and dissolved in the solvent. This total peak area decrease is slightly more pronounced in hexane compared to 2-propanol. However, the relative decrease in nitro to amine-type N 1s XPS signal implies that some breaking of the amide linkage takes place, removing the chiral end group. This effect is probably not as predominant in chiral chromatography, as the chiral interface is attached to porous silica. This high surface area material presents many more Si-OH linkages and cross-linking

sites than the flat oxidized Si(111) samples that were used in this study. Since the substrates presented this aging effect, all the chemical force measurements were obtained with freshly prepared samples and tips and the solvent exposure time was limited as much as possible**.**

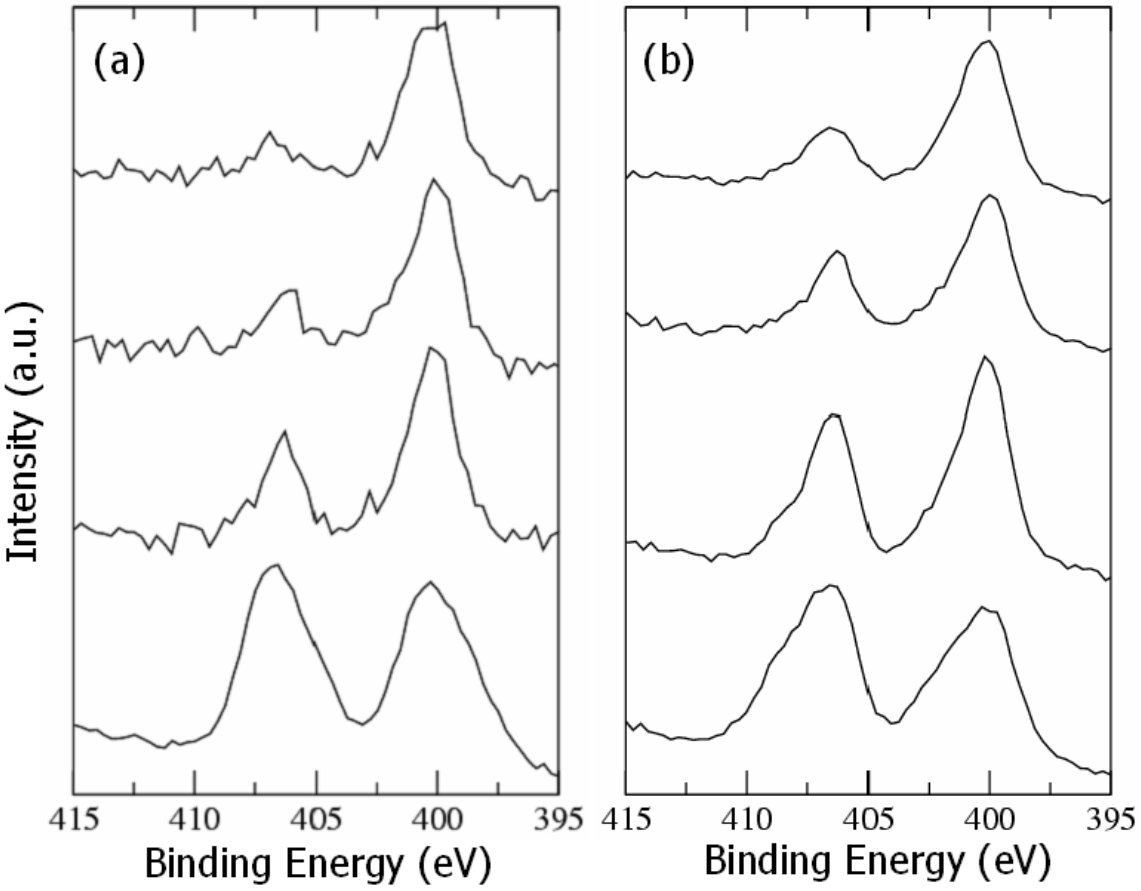

Figure 5.17 XPS spectra of a *R*-[(3,5-dinitrobenzoyl)amino]-*N*-[3-(triethoxysilyl)propyl]--2-phenylacetamide (a) and *R*-[(3,5-dinitrobenzoyl)amino]-*N*-[3-(triethoxysilyl)propyl]--4-methylpentanamide (b) surfaces exposed to 2-propanol for various amounts of time: 0 h, 2 h, 18 h, 42 h (curves from the bottom to the top)

5.3.3 Chemical force spectrometry results

Attempts to probe the chiral selectivity in the samples prepared using the two-step surface deposition method, where the DNB-phenylglycine and DNB-leucine were linked to the APTES-modified surface did not show any evidence of chiral discrimination between different sample-tip chiral combinations. The fact that these chemical force spectrometric measurements do not show a clear chiral discrimination is not surprising as presumably the interactions are dominated by H-bonding to unreacted amine sites on the surface, as demonstrated by the XPS results. This is also similar to the results of Otsuka *et al.*[63] who also had unreacted amine sites on the surface of their samples and did not observe a clear chiral discrimination.

The results of measurements of the adhesion force for DNB-phenylglycine and DNB-leucine modified tips and samples prepared by the direct deposition method are shown in Figure 5.18 and summarized in Table 5.9. The errors reported in Table 5.9 are the standard deviations of the 450-1000 force displacement curves obtained for each interaction. In the DNB-phenylglycine system, a review of the data in Table 5.9 demonstrates that the like (*R*-*R* or *S*-*S*) combination of tip and sample shows a statistically significant larger average adhesion force than the nonlike (*R*-*S* or *S*-*R*) combinations, suggesting that chiral discrimination is indeed observed in this case. The histograms in Figure 5.18 show very similar profiles for the like combinations situated around 12 nN (Figures 5.18(b) and 5.18(d)), a small variation for the *S*-*R* combination around 1.9 nN (Figure 5.18(a)), and a little larger variation for the *R*-*S* combination (Figure 5.18(c)), but still statistically different from the like combinations. As a control

experiment, *S*- and *R*-DNB-phenylglycine tips were used to probe racemic DNB-phenylglycine surfaces. The results show a relatively high force, similar to the adhesive interaction for the like combination (see Table 5.9).

Table 5.9 Adhesive chemical force interactions observed between the DNB-phenylglycine and DNB-leucine-modified tips and samples in 2-propanol.

Tip terminal group	Adhesive interaction (nN) on surface		
	R-DNB-phenylglycine	*S*-DNB-phenylglycine	*Racemic*-DNB-phenylglycine
R-DNB-phenylglycine	12.1 ± 2.7	5.6 ± 2.9	12.9 ± 3.7
S-DNB-phenylglycine	1.9 ± 1.5	12.7 ± 2.4	14.5 ± 1.5
	R-DNB-leucine	*S*-DNB-leucine	*Racemic*-DNB-leucine
R-DNB-leucine	2.9 ± 1.6	1.2 ± 0.3	0.9 ± 0.3
S-DNB-leucine	1.6 ± 0.5	2.7 ± 1.5	0.6 ± 0.2

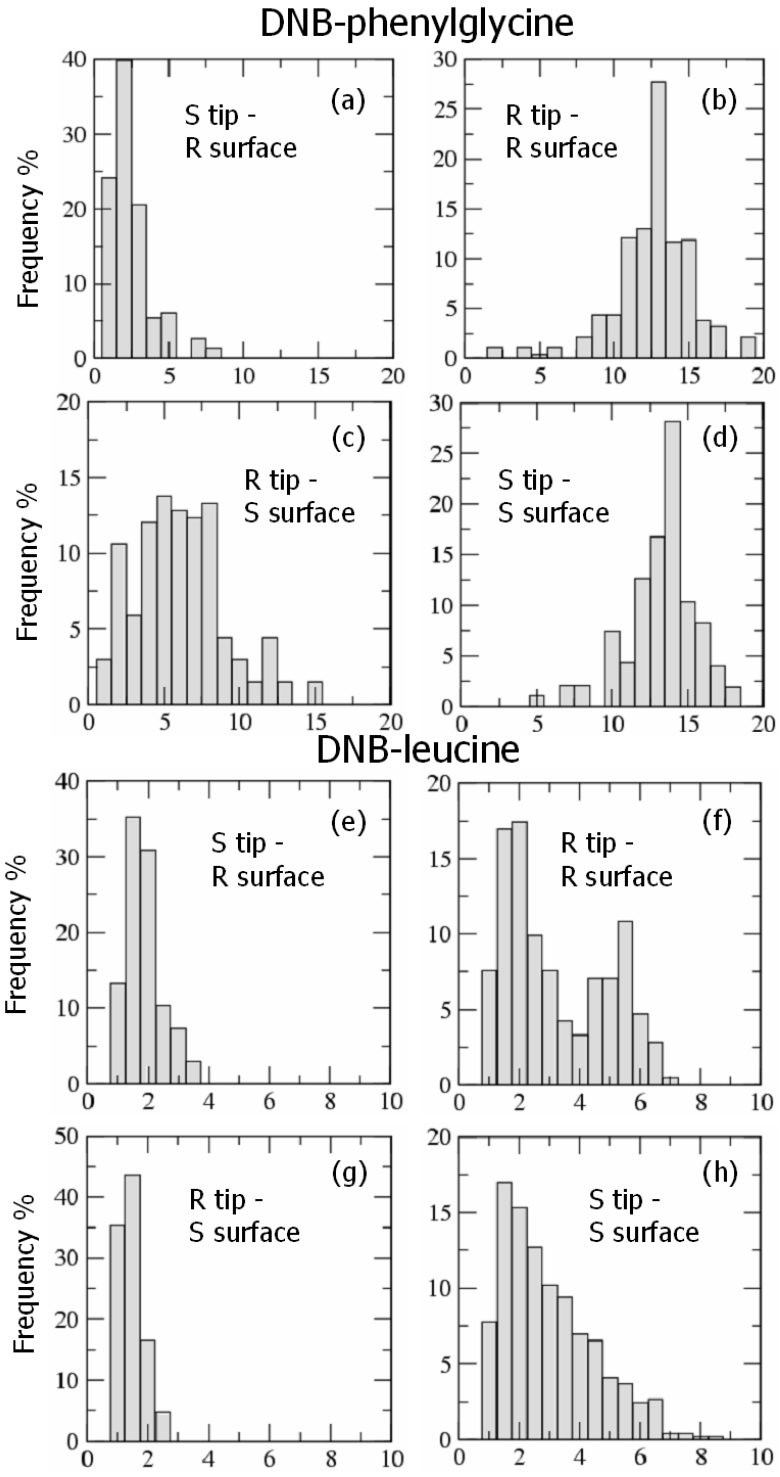

Figure 5.18 Histograms of the adhesion forces in 2-propanol. Panels (a)-(d) show the CFM results between the DNB-phenylglycine-modified tips and samples, and panels (e)-(h) show the CFM results between the DNB-leucine-modified tips and samples.

For *R*- and *S*-DNB-leucine modified tips and samples, the adhesive interactions observed were all considerably smaller than the DNB-phenylglycine case. The average adhesive forces observed for this system are reported in Table 5.9 and show that the like and nonlike tip-sample combinations are not statistically different from one another, and therefore do not show a clear chiral discrimination. The histograms in Figure 5.18 do demonstrate that the distribution of forces observed for the two like or two nonlike tip-sample combinations are relatively close to one another. For the like combinations, there is a shoulder of larger interaction forces up to 6 nN, which leads to a relatively large standard deviation in the average adhesion forces observed. For the two nonlike combinations, the force profile on the histogram is much narrower and centered at 1.2 – 1.6 nN. The relatively small adhesion forces observed therefore appear to mask the chiral discrimination in this system. However, the histograms do suggest limited evidence of discrimination, with a larger interaction for the *R*-*R* or *S*-*S* combination than the *R*-*S*/*S*-*R*.

McKendry *et al*. observed chiral discrimination in a system of DNB-phenylglycine and mandelic acid.[61,62] In their case, the adhesive forces were on the order of 1-2 nN, relatively close to forces observed for the DNB-leucine system, but much smaller than the forces that I have in the DNB-phenylglycine system. The chiral discrimination arises due to the different diastereomeric complexes formed between the chiral molecules on the tip and the sample. The fact that the discrimination is more pronounced in the DNB-phenylglycine system compared to DNB-leucine system is suggestive of the fact that in chiral HPLC, the DNB-phenylglycine CSP is more effective in separating a wide range of compounds, including self-separation.[196,197]

An important difference between the real HPLC systems in use and those reported above is in the solvent mixtures used. Chiral HPLC involving DNB-phenylglycine or DNB-leucine CSPs commonly use hexane and various mixtures of hexane and 2-propanol, as opposed to the pure 2-propanol used here. The attempts to carry out chemical force spectrometric measurements in solutions of high hexane concentration were not successful, as the adhesion forces observed were very small, and the differences between like and nonlike pairs not statistically significant. As the XPS measurements described above indicate, this is probably at least partially due to the rapid degradation of the samples and tips that take place when they are exposed to hexane.

The simulations of DNB-phenylglycine and DNB-leucine interfaces were described in Sections 5.2.7 and 5.2.8. They demonstrated that 2-propanol molecules interact strongly with DNB-phenylglycine and DNB-leucine molecules, even at higher hexane concentrations. Extensive hydrogen bonding between the 2-propanol and DNB-phenylglycine and DNB-leucine molecules has been observed, but the two CSPs have different behaviours. In pure 2-propanol, DNB-phenylglycine molecules have an 18.1 % and 50.5 % hydrogen bonding probability at the amide oxygens O(26) and O(14), but only a 3.7 % and 4.7 % hydrogen bonding probability at the amide hydrogens H(24) and H(12). By contrast, the simulations showed the DNB-leucine to have 54.6 % and 71.8 % hydrogen bonding probabilities at the amide oxygen O(24) and O(14), and equally high probabilities at the amide hydrogens H(22) and H(12) – 49.7 % and 73.9 %. The much more extensive H-bonding of the propanol solvent with the DNB-leucine surface is consistent with the observation of generally lower forces, and limited evidence

for chiral discrimination, as compared to DNB-phenylglycine in the force spectrometry results described here. The more extensive hydrogen-bonding of the DNB-leucine presumably has the effect of interfering with the formation of the diastereomeric complexes in the chemical force spectrometric experiments.

The molecular dynamics simulations also suggested that in mixtures of high hexane concentration, both DNB-phenylglycine and DNB-leucine tended to orient such that the dinitrophenyl ring lies parallel to the surface, and DNB-leucine has a more open conformation that allows an increased hydrogen bonding capability. As the 2-propanol concentration increases, an orientation such that the dinitrophenyl ring points towards the solvent bulk becomes more predominant in both systems. Since the force spectrometric measurements depend on significant interdigitation of the surface species in order to form diastereomeric complexes, this may also partially account for the lack of chiral discrimination observed in solvent mixtures of higher hexane concentrations.

Chapter 6

Conclusions

In chromatography the choice of solvent is critical for achieving a desired separation. A typical separation employs a binary or ternary solvent. The objective of this thesis was to examine in detail the characteristics of a solvent or a solvent mixture near a complex chiral interface. Specifically, I used a combination of experimental and theoretical methods to describe the solvation of three chiral stationary phases: PEPU, DNB-phenylglycine, and DNB-leucine. These molecules, like many other commonly used to build stationary phases for chiral chromatography, contain aromatic rings and hydrogen bond sites.

For PEPU, MD simulations were used to explore the distribution and orientation of water and alcohol molecules at the interface and to quantify the degree of hydrogen bonding. MD simulations of the solvent-PEPU interface revealed that water forms a highly organized layer near the surface. In particular, water molecules tend to lie flat on the surface while forming rings of hydrogen-bonded molecules. Alcohols like methanol also form dense layers but with considerably less organization within the solvent surface layer. In alcohol/water mixtures (methanol/water, 1-propanol/water or 2-propanol/water) the simulations showed that all the alcohols form domains at the interface with the hydrophobic portions of the molecule tending to orient towards the surface. This effect disrupts the water hydrogen bonding network at the interface and leads to the exclusion of water from the surface region relative to the bulk.

Experimental (chemical force microscopy) measurements were used to explore the adhesive interactions between two PEPU surfaces as a function of solvent composition. These showed that for 1- or 2-propanol, the adhesive interaction is rapidly suppressed with increasing alcohol concentration. This effect is less marked for methanol/water mixtures, consistent with the MD simulations that showed water less strongly excluded from the surface region in this system, as well as increased hydrogen bonding interactions between water and methanol as compared with 1- and 2-propanol. Measurements in which the solvent consisted of methanol/1-propanol mixtures showed only a modest increase in adhesive force with increasing methanol concentration. In pure water, the forces measured for hydrated PEPU surfaces were very large but discrimination cannot be detected given the standard errors. In pure methanol, a less polar solvent compared to water, smaller forces and detectable discrimination was observed. In particular, the homochiral forces were significantly larger than those measured when the PEPU on the surface and tip differ in handedness.

The solvation of leucine- and phenylglycine-based chiral stationary phases is also the focus of this thesis. These CSPs were first synthesized by Pirkle *et al.* in the 1980s. Ensuing experimental studies showed that these two CSPs displayed distinct separation characteristics. The difference between these CSPs is somewhat surprising given that leucine and phenylglycine differ only by the replacement of an isobutyl group by a phenyl. In this study, I began by exploring the stable conformations for DNB-leucine and DNB-phenylglycine. I found that the phenylglycine-based selector has an energetically-accessible local energy minimum 11 kJ/mol higher in energy than the global minimum.

For the leucine-based selector, two nearly isoenergetic minima were identified. Thus, even in the gas phase, these compounds have significant differences in their conformations.

In order to properly represent the flexibility of these selectors, potentials were carefully derived. First, the energy was evaluated at the B3LYP/6-311G** level of theory, as the molecule explores a range of conformations. Comparisons were also made with MP2/6-311G** and HF/6-311G** conformers. Second, the intramolecular potential parameters were obtained by least squares fitting. In particular, torsions were all fitted simultaneously to the *ab initio* results. Finally, the incorporation of non-bonding intramolecular interactions has a crucial impact on the conformations predicted from the potential. The scaling parameters that determine the strength of these interactions were varied systematically and optimized by comparison between the corresponding minimum-energy structures and the *ab initio* structures.

Simulations of the chiral interfaces were performed in 100% *n*-hexane, 90:10 *n*-hexane:2-propanol, 80:20 *n*-hexane:2-propanol, and 100% 2-propanol. I find that the DNB-phenylglycine selectors prefer to orient such that the dinitrophenyl groups are either parallel to the surface or oriented such that one nitro group points towards the surface while the other points into the bulk. As the alcohol concentration increases, the latter conformation increases in importance. For DNB-leucine selectors, the dinitrophenyl rings tends to either lie parallel to the surface or point directly into the fluid. The latter becomes more prevalent with an increased presence of 2-propanol.

For the mixed solvents, the alcohol strongly prefers the interfacial region and can be found directly above the end-caps and around the selectors. For the phenylglycine-based selector, the alcohol is not as likely to be found within 9-10 Å above the underlying Si layer. This occurs because of crowding from the selectors in this separation range. The leucine-based selectors are more extended and this crowding is less severe. As a result, 2-propanol shows less depletion between 9-10 Å.

Extensive hydrogen bonding between the 2-propanol and the selectors has been found. For DNB-leucine both the amide oxygens (O(14) and O(24)), and the amide hydrogens (H(12) and H(22)) participate in H-bonding with the solvent. In 100% 2-propanol, each of these four atoms has a 50-74% probability for H-bonding to the alcohol. In contrast, DNB-phenylglycine in 100% 2-propanol has between 3.7-50.5% probability for H-bonding, with the amide hydrogens only H-bonding infrequently. In other words, DNB-phenylglycine selectors typically do not have H-bonding between the amide hydrogens and solvent. This is not the case for DNB-leucine, where these H-bonding interactions are frequent.

The experimental investigation of DNB-phenylglycine and DNB-leucine model chiral systems was performed using a series of surface characterisation methods. Two different sample preparation methods were employed. In the first preparation method, the surface was first derivatized with APTES, followed by a reaction with DNB-phenylglycine or DNB-leucine. In the direct surface deposition method, the tethered chiral compounds were synthesized prior to deposition on the surface. XPS, AFM, and RAIRS analysis show that the best results were obtained by using the direct

surface deposition method: FTIR showed that only the DNB-phenylglycine and DNB-leucine were present on the surface, AFM confirmed that the surface deposition created a smooth layer of "brush-type" chiral molecules on the surface, and N1s XPS of the samples showed peaks of equal area for amine/amide and nitro groups, and no evidence of unreacted amine sites. However, prolonged exposure to propanol or hexane solvent would degrade the surfaces.

Chemical force spectrometric measurements in 2-propanol demonstrated convincing evidence of chiral self-discrimination in DNB-phenylglycine, but smaller forces and less evidence for chiral self-discrimination for DNB-leucine. CSPs derived from both these compounds have shown a significant self-selectivity in chiral chromatography. These results are in agreement with the simulation results. The small forces observed in DNB-leucine system can be understood by the increased ability of this molecule to form hydrogen bonds with the solvent, thus limiting the observation of chiral discrimination.

There are many future research directions for this work. Many chiral separation mechanisms need to be investigated in order to prepare a rationale for the enantioselectivity of chiral stationary phases. As shown here, a molecular level description can be obtained using *ab initio* calculations and MD simulations. At present, these are limited by computational resources. However, considering the high pace of computer development, reasonable resources should be easily attainable in the future. This should enable a better model development, since higher order basis sets and *ab initio* methods could be employed in calculations. Faster computational resources should also

improve the quality of MD simulations that could be designed to include hundreds or thousands of fully-flexible surface molecules and an even bigger number of fluid molecules.

The experimental investigation of chiral surfaces can also be developed in the future research. As shown in this thesis, the CFM technique has the potential of becoming the technique of choice for the direct measurements of discriminating forces between single molecules. For a greater applicability, libraries of functionalized tips coated with chiral stationary phases could be created. Then, samples could be functionalized with the chiral compound that needs to be separated. By approaching selected tips to this surface, CFM can act as a fast single-molecule screening technology for the identification of the best chiral stationary phase for a particular analyte. The first steps toward this methodology have already been taken.

In conclusion, I can say that a complete description of the mechanism of selectivity for chiral interfaces must include a detailed representation of the surface and of the solvent at the interface. Together, XPS, force measurements and simulations are capable of providing the detailed level of description necessary to fully understand these complex chiral interfaces.

References

[1] Ward, T.J; Hamburg, D.M *Anal. Chem.* **2004,** 76, 4635.

[2] Betschinger, F.; Libman, J.; Shanzer, A. *J. Chromatogr. A* **1996,** 746, 53.

[3] Wainer, I. W. *Trends Anal. Chem*. **1987,** 6, 135.

[4] Welch, C.J *J. Chromatogr.***1994,** 666, 3.

[5] Pirkle, W.H.; House, D.W.; Finn, J.M. *J. Chromatogr.* **1980,** 192, 143.

[6] Pirkle, W.H.;.Welch, C.J. *J. Org. Chem.* **1984,** 49, 138.

[7] Yang, A.; Gehring, A.P.; Li, T. *J. Chromatogr. A* **2000,** 878, 165.

[8] Pirkle, W.H.; Finn, J.M.; Schreiner, J.L.; Hamper, B.C. *J. Am. Chem. Soc.* **1981,** 103, 3964.

[9] Berthod, A.; Jin, H.L.; Stalcup, A.M.; Armstrong, D.W. *Chirality* **1990,** 2, 38.

[10] Capka, M.; Bartlova, M.; Krause, H. W.; Schmidt, U.; Fischer, C.; Oehme, G. *Am. Biotech. Lab.* **1995,** 13, 13.

[11] Dyas, A. M.; Robinson, M. L.; Fell, A. F. *Chromatographia* **1990,** 30, 73.

[12] Aboul-Enein, H.Y.; Ali, I. *Chiral separations by liquid chromatography and related technologies*, Marcel Dekker Inc., 2003

[13] Maier, N.M.; Franco, P.; Lindner, W. *J. Chromatogr. A* **2001,** 906, 3.

[14] Allenmark, S.G. *Chromatographic enantioseparation. Methods and applications*, Ellis Horwood Limited, 1988

[15] Ahuja, S. *Chiral separations by chromatography*, Oxford University Press, 2000

[16] Stinson, S.C. *Chem. Eng. News* **2001,** 79, 45.

[17] Rouhi, A.M. *Chem. Eng. News* **2004,** 84, 47.

[18] Thayer, A.M. *Chem. Eng. News* **2007,** 85, 11.

[19] Pasteur, L. *Ann. Chim. Phys.* **1850,** 28, 56.

[20] Franco, P.; Minguillon, C. *Techniques in preparative chiral separations* in *Chiral separation techniques. A practical approach*, Subramanian,G. (ed.), Wiley, 2001

[21] Stinson, S.C. *Chem. Eng. News* **1999,** 77, 101.

[22] Pirkle, W.H.; Pochapski, T.C. *Chem. Rev*. **1989,** 89, 347.

[23] Dalgleish, C.E. *J. Chem. Soc*. **1952,** 3940.

[24] Gubitz, G.; Schmid, M.G. *Biopharm. Drug Dispos.* **2001,** 22, 291.

[25] Toyo'oka, T. *Biomed. Chromatogr.* **1996,** 10, 265.

[26] Svec, F.; Wulff, D.; Frechet, J.M.J. *Combinatorial approaches to recognition of chirality: preparation and use of materials for the separation of enantiomers* in *Chiral separation techniques. A practical approach*, Subramanian,G. (ed.), Wiley, 2001

[27] Allenmark, S.; Bomgren, B.; Boren, H. *J. Chromatogr.* **1983,** 264, 63.

[28] Domenici, E.; Bertucci, C.; Salvadori, P.; Felix, G.; Cahagne, I.; Montellier, S.; Wainer, I.W. *Chromatographia* **1990,** 29, 170.

[29] Miwa, T.; Hattori, T.; Ichikawa, M. *Chem. Pharm. Bull.* **1987,** 35, 682.

[30] Isaksson, R.; Pettersson, C.; Pettersson, G. *Trends Anal. Chem.* **1994,** 13, 431.

[31] Haginaka, J.; Murashima, T.; Seyama, C. *J. Chromatogr. A* **1994,** 666, 203.

[32] Haginaka, J.; Miyano, Y.; Saizen, Y.; Seyama, C.; Murashima, T. *J. Chromatogr. A* **1995,** 708, 161.

[33] Okamodo, Y.; Hatada, K.; Kawashima M.; Yamamoto, K. *Chem. Lett.* **1984,** 5, 739.

[34] Okamoto, Y.; Hatada, K.; Kawashima, M. *J. Am. Chem. Soc*. **1984,** 106, 5357.

[35] Okamodo, Y.; Aburatani, R.; Hatano, K.; Hatada, K. *J. Liq. Chromatogr*. **1988,** 11, 2147.

[36] Senso, A.; Oliveros, L.; Minguillon, C. *J. Chromatogr. A* **1999,** 839, 15.

[37] Cass, Q.B.; Bassi, A.I.; Matlin, S.A. *Chirality* **1996,** 8, 131.

[38] Felix, G.; Zhang, T. *J. Chromatogr.* **1993,** 639, 141.

[39] Wainer, I.C.; Alembik, M.C. *J. Chromatogr*. **1986,** 358, 85.

[40] Blaschke. G. *J. Liq. Chromatogr*. **1986,** 9, 341.

[41] Okamoto, Y.; Hatada, K. *J. Liq. Chromatogr*. **1986,** 9, 369.

[42] Armstrong, D.W.; Tang, Y.B.; Chen, S.S.; Zhou, Y.W.; Bagwill, C.; Chen, J.R. *Anal. Chem.* **1994,** 66, 1473.

[43] Armstrong, D.W.; Liu, Y.; Ekborg-Ott, K.H. *Chirality* **1995,** 7, 474.

[44] Ekborg-Ott, K.H.; Liu, Y.; Armstrong, D.W. *Chirality* **1998,** 10, 434.

[45] Ekborg-Ott, K.H.; Zientara, G.A.; Schneiderheinze, J.M.; Gahm, K.; Armstrong, D.W. *Electrophoresis* **1999,** 20, 2438.

[46] Sogah, G.D.Y.; Cram, D.J. *J. Am. Chem. Soc*. **1979,** 101, 3055.

[47] Armstrong, D.W.; DeMond, W. *J. Chromatogr. Sci*. **1984,** 22, 411.

[48] Davankov, V.A.; Rogozhin, S.V. *J. Chromatogr*. **1971,** 60, 280.

[49] Czerwenka, C.; Lindner, W. *Anal. Bioanal. Chem.* **2005,** 382, 599.

[50] Welch, C.J.; Szczerba, T.; Perrin, S.R. *J. Chromatogr. A* **1997,** 758, 93.

[51] Lin, C.E.; Lin, C.H.; Li, F.K. *J. Chromatogr. A* **1996,** 722, 189.

[52] Machida, Y.; Nishi, H.; Nakamura, K.; Nakai, H.; Sato, T. *J. Chromatogr. A* **1997,** 757, 73

[53] Vaton-Chanvrier, L.; Peullon, V.; Combret, Y.; Combret, J.C. *Chromatographia* **1997,** 46, 613.

[54] Iuliano, A.; Salvatori, P.; Feix, G. *Tetrahedron: Asymmetry* **1999,** 10, 3353.

[55] Messina, A.; Girelli, A.M.; Flieger, M.; Sinibaldi, M.; Sedmera, P.; Cvak, L. *Anal. Chem*. **1999,** 68, 1191.

[56] Lammerhofer, M.; Lindner, W. *J. Chromatogr. A* **1996,** 741, 33.

[57] Lopinski, G. P.; Moffatt, D. J.; Wayner, D. D. M.; Wolkow, R. A. *Nature* **1998,** 392, 909.

[58] Dodero, G.; De Michieli, L.; Cavalleri, O.; Rolandi, R.; Oliveri, L.; Dacca, A.; Parodi, R., *Coll. Surf. A* **2000,** 175, 121.

[59] Xu, Q.; Wan, L.; Wang, C.; Bai, C.; Wang, Z.; Nozawa, T. *Langmuir* **2001,** 17, 6203.

[60] Lorenzo, M. Ortega; Haq, S.; Bertrams, T.; Murray, P.; Raval, R.; Baddeley, C. J., *J. Phys. Chem. B* **1999,** 103, 10661.

[61] McKendry, R.; Theoclitou, M.; Rayment, T.; Abell, C. *Nature* **1998,** 391, 566.

[62] McKendry, R.; Theoclitou, M.; Abell, C.; Rayment, T. *Jpn. J. Appl. Phys*. **1999,** 38, 3901.

[63] Otsuka, H.; Arima, T.; Koga, T.; Takahara, A. *J. Phys. Org. Chem*. **2005,** 18, 957.

[64] Nita, S.; Cann, N.M.; Horton, J.H. *J. Phys. Chem. B* **2004,** 108 3512.

[65] Nita, S.; Cann, N.M.; Horton, J.H. *J. Phys. Chem. B* **2006,** 110, 9511.

[66] Lipkowitz, K.B. *Acc. Chem. Res.* **2000,** 33, 555.

[67] Lipkowitz, K.B. *J. Chromatogr. A* **2001,** 906, 417.

[68] Lipkowitz, K.B.; Pearl, G.; Coner, B.; Peterson, M.A. *J. Am. Chem. Soc.* **1997,** 119, 600.

[69] Altomare, C.; Carotti, A.; Cellamare, S.; Fanelli, F.; Gasparrini, F.; Villani, C.; Carrupt, P.A.; Testa, B. *Chirality* **1993,** 5, 527.

[70] Suzuki, T.; Timofei, S.; Iuoras, B.E.; Uray, G.; Verdino, P.; Fabian, W.M.F. *J. Chromatogr. A* **2001,** 922, 13.

[71] Fabian, W.M.F.; Stampfer, W.; Mazur, M.; Uray, G. *Chirality* **2003,** 15, 271.

[72] Lipkowitz, K.B. *J. Chromatogr. A* **1994,** 666, 493.

[73] Lipkowitz, K.B.; Malik, D.J.; Darden, T. *Tetrahedron Lett.* **1986,** 27, 1759.

[74] Lipkowitz, K.B.; Demeter, D.A.; Zegarra, R.; Larter, R.; Darden, T. *J. Am. Chem. Soc.* **1988,** 110, 3446.

[75] Lipkowitz, K.B.; Baker, B. *Anal. Chem.*, **1990,** 62, 770.

[76] Topiol, S.; Sabio, M.; Moroz, J.; Caldwell, W.B. *J. Am. Chem. Soc.* **1988,** 110, 8367.

[77] Lipkowitz, K.B.; Demeter, D.A.; Landwer, J.M.; Parish, C.A.; Darden, T. *J. Comput. Chem.* **1988,** 9, 63.

[78] Still, M.G.; Rogers, L.B. *J. Comput. Chem.* **1990,** 11, 242.

[79] Norinder, U.; Sundholm, E.G. *J. Liq. Chromatogr.* **1987,** 10, 2825.

[80] Hellriegel, C.; Skogsberg, U.; Albert, K.; Lammerhofer, M.; Maier, N.M.; Linder, W. *J. Am. Chem. Soc*. **2004,** 126, 3809.

[81] Katte, S.J.; Beck, T.L. *J. Phys. Chem.* **1993,** 97, 5727.

[82] Slusher, J.T.; Mountain, R.D. *J. Phys. Chem. B* **1999,** 103, 1354.

[83] Cheng, C.Y.; Chen, T.L.; Wang, B.C. *J. Mol. Struct. (Theochem.)* **2002,** 577, 81.

[84] Zhang, L.; Sun, L.; Siepmann, J.I.; Schure, M.R. *J. Chromatogr. A* **2005,** 127, 1079.

[85] Lipkowitz, K.B.; Raghothama, S.; Yang, J.A. *J. Am. Chem. Soc.* **1992,** 114, 1554.

[86] Zhao, C.; Cann, N.M. *J. Chromatogr. A* **2006,** 1131, 110.

[87] Zhao, C.; Cann, N.M. *J. Chromatogr. A* **2007,** 1149, 197.

[88] Benjamin, I. *Annu. Rev. Phys. Chem*. **1997,** 48, 407.

[89] Benjamin, I. *Chem. Rev.* **1996,** 96, 1449.

[90] Levine, I.N. *Quantum Chemistry, Fifth Edition*, Prentice-Hall Inc., 2000.

[91] Hohenberg,P.; Kohn,W. *Phys. Rev.* **1964,** 136, B864.

[92] Kohn, W.; Sham, L.J. *Phys. Rev*. **1965,** 140, A1133.

[93] Parr, R.G.; Yang, W. *Density-functional theory of atoms and molecules*, Oxford University Press, 1989.

[94] Becke, A.D. *Exchange-correlation approximations in Density-Functional Theory* in *Modern Electronic Structure Theory*, Yarkony, D.R. (ed.), World Scientific, 1995.

[95] Becke, A.D. *J. Phys. Chem.* **1988,** 88, 1053.

[96] Johnson,B.G.; Gill,P.M.W.; Pople,J.A. *J. Chem. Phys.* **1992,** 98, 2155.

[97] Becke, A. D. *J. Chem. Phys.* **1993,** 98, 5648.

[98] Boys, S.F. *Proc. Roy. Soc. (London)* **1950,** A200, 542.

[99] Boyd D.B. *Molecular modeling software in use: publication trends* in *Reviews in computational chemistry, Vol.6*, Boyd D.B.; Lipkowitz, K.B. (ed.), VCH Publishers, 1995.

[100] Gaussian 03, Revision C.02, Frisch, M. J.; Trucks, G. W.; Schlegel, H. B.; Scuseria, G. E.; Robb, M. A.; Cheeseman, J. R.; Montgomery, Jr., J. A.; Vreven, T.; Kudin, K. N.; Burant, J. C.; Millam, J. M.; Iyengar, S. S.; Tomasi, J.; Barone, V.; Mennucci, B.; Cossi, M.; Scalmani, G.; Rega, N.; Petersson, G. A.; Nakatsuji, H.; Hada, M.; Ehara, M.; Toyota, K.; Fukuda, R.; Hasegawa, J.; Ishida, M.; Nakajima, T.; Honda, Y.; Kitao, O.; Nakai, H.; Klene, M.; Li, X.; Knox, J. E.; Hratchian, H. P.; Cross, J. B.; Bakken, V.; Adamo, C.; Jaramillo, J.; Gomperts, R.; Stratmann, R. E.; Yazyev, O.; Austin, A. J.; Cammi, R.; Pomelli, C.; Ochterski, J. W.; Ayala, P. Y.; Morokuma, K.; Voth, G. A.; Salvador, P.; Dannenberg, J. J.; Zakrzewski, V. G.; Dapprich, S.; Daniels, A. D.; Strain, M. C.; Farkas, O.; Malick, D. K.; Rabuck, A. D.; Raghavachari, K.; Foresman, J. B.; Ortiz, J. V.; Cui, Q.; Baboul, A. G.; Clifford, S.; Cioslowski, J.; Stefanov, B. B.; Liu, G.; Liashenko, A.; Piskorz, P.; Komaromi, I.; Martin, R. L.; Fox, D. J.; Keith, T.; Al-Laham, M. A.; Peng, C. Y.; Nanayakkara, A.; Challacombe, M.; Gill, P. M. W.; Johnson, B.; Chen, W.; Wong, M. W.; Gonzalez, C.; and Pople, J. A.; Gaussian, Inc., Wallingford CT, 2004.

[101] Weiner, S.J.; Kollman, P.A.; Nguyen, D.T.; Case, D.A.. *J. Comput. Chem.* **1986,** 7, 230.

[102] Brooks, B.R.; Bruccoleri, R.E.; Olafson, B.D.; States, D.J.; Swarninathan, S.; Karplus, M. *J. Comput. Chem.* **1983,** 4, 187.

[103] Jorgensen, W.L.; Tirado-Rives, J. *J. Am. Chem. Soc*. **1988,** 110, 1657.

[104] Ryckaert, J.P.; Bellemans A. *Chem. Phys. Lett.* **1975,** 30, 123.

[105] McKeehan, L.W. *Phys. Rev.* **1923,** 21, 503.

[106] Guttman L.; Rahman S. M. *Phys. Rev. B* **1988,** 37, 2657.

[107] Foresman, J. B.; Keith, T. A.; Wiberg, K. B.; Snoonian, J.; Frisch, M. J. *J. Phys. Chem.* **1996,** 100, 16098.

[108] McLean A.D.; Chandler, G.S. *J. Chem. Phys.* **1980,** 72, 5639.

[109] Frenkel,D.; Smit, B. *Understanding Molecular Simulation*, Academic Press, 1996.

[110] Allen,M.P.; Tildesley,D.J. *Computer simulation of liquids*, Oxford University Press, 1994.

[111] Metropolis,N.; Rosenbluth, A.W.; Rosenbluth, N.M.; Teller, A.N.; Teller, E. *J. Chem. Phys.* **1953,** 21, 1087.

[112] Eastwood, J.W.; Hockney, R.W.; Lawrence, D. *Comput. Phys. Commun.* **1980,** 19, 215.

[113] Onsager, L. *J. Am. Chem. Soc.* **1936,** 58, 1486.

[114] Ewald P.P. *Ann. Phys.* **1921,** 64, 253.

[115] Smith, E. R. *Proc. R.. Soc. Lond. A* **1981,** 375, 475.

[116] Yeh, I.C.; Berkowitz, M.L. *J. Chem. Phys*. **1999,** 111, 3155.

[117] Nosé, S. *J. Chem. Phys.* **1984,** 81, 511.

[118] Hoover, W.G. *Phys. Rev. A* **1985,** 31, 1695.

[119] Martyna, G.J.; Tobias, T.J.; Klein, M.L. *J. Chem. Phys.* **1994,** 101, 4177.

[120] Cressman E.; Das B.; Dunford J.; Ghenea R.; Huh Y.; Nita S.; Paci I.; Wang. S.; Zhao C.; Cann, N. M. unpublished.

[121] Lide, D. R. (ed.) *CRC Handbook of Chemistry and Physics*, 85th Ed., CRC Press, Boca Raton, FL 2005.

[122] Levitt, M.; Hirshberg, M.; Sharon, R.; Laidig, K. E.; Daggett, V. *J. Phys. Chem. B* **1997,** 101, 5051.

[123] Armen, R. S.; Daggett, V. *Biochem.* **2005,** 44, 16098.

[124] Esposito, L.; Daggett, V. *Biochem.* **2005,** 44, 3358.

[125] Dougan, L.; Hargreaves, R.; Bates, S. P.; Finney, J. L.; Reat, V.; Soper, A. K.; Crain, C. *J. Chem. Phys.* **2005,** 122, 174514.

[126] Dougan, L.; Hargreaves, R.; Bates, S. P.; Hargreaves, R.; Fox, J. P.; Crain, J.; Finney, J. L.; Reat, V.; Soper, A. K. *J. Chem. Phys.* **2004,** 121, 6456.

[127] Allison, S. K.; Fox, J. P.; Hargreaves, R.; Bates, S. P. *Phys. Rev. B* **2005,** 71, 024201.

[128] Ju, S. P.; Chang, J. G.; Lin, J. S.; Lin, Y. S. *J. Chem. Phys.* **2005,** 122, 154707.

[129] Ju, S. P. *J. Chem. Phys.* **2005,** 122, 094718.

[130] Wu, Y.; Tepper, H. L.; Voth, G. A. *J. Chem. Phys.* **2006,** 124, 024503.

[131] Beck, D. A. C.; Armen, R. S.; Daggett, V. *Biochem.* **2005,** 44, 609.

[132] Chen, B.; Potoff, J. J.; Siepmann, J. I. *J. Phys. Chem. B* **2001,** 105, 3093.

[133] Wick, C. D.; Siepmann, J. I.; Schure, M. R. *Anal. Chem.* **2004,** 76, 2886.

[134] Chen, B.; Siepmann, J. I.; Klein, M. L. *J. Am. Chem. Soc.* **2003,** 125, 3113.

[135] Shelley, J. C.; Patey, G. N. *Mol. Phys*. **1996,** 88, 385.

[136] Wasburn, E. W. (ed.) *International Critical Tables of Numerical Data, Physics, Chemistry and Technology*, Knovel, NY 2003.

[137] Pirkle, W.H.; Pochapsky, T.C.; Mahler, G.S.; Field, R.E. *J. Chromatogr.* **1985,** 348, 89.

[138] Szczerba, T.J., Regis Technologies, Inc., Personal communication.

[139] Nawrocki, J. *J. Chromatogr. A* **1997,** 779, 29.

[140] Lopes, P.E.M.; Murashov, V.; Tazi, M.; Demchuk, E.; MacKerell Jr., A.D. *J. Phys. Chem. B* **2006,** 110, 2782.

[141] Stubbs, J.M.; Potoff, J.J.; Siepmann, J.I. *J. Phys. Chem. B* **2004,** 108, 17596.

[142] Andersen, H.C. *J. Comput. Phys.* **1983,** 52, 24.

[143] Morrone, S.R.; Francesconi, A.Z. *J. Chem. Thermodynamics* **1996,** 28, 935.

[144] Moulder, J.F.; Stickle, W.F.; Sobol, P.E.; Bomben, K.D. *Handbook of X-ray Photoelectron Spectroscopy*, Physical Electronics Inc., 1995.

[145] Watts, J.F. *Vacuum* **1994,** 45, 653.

[146] Attard, G.; Barnes, C. *Surfaces*, Oxford University Press Inc., 2001.

[147] Flitsch, R.; Raider, S.I. *J. Vac. Sci. Technol.* **1975,** 12, 305.

[148] Auger, P. *Comptes. Rend.* **1923,** 177, 169.

[149] Linsmeier, C. *Vacuum* **1994,** 45, 673.

[150] Hollins, P. *Vacuum* **1994,** 45, 705.

[151] Binning, G.; Rohrer, H.; Gerber, C.; Weibel, E. *Phys. Rev. Lett.* **1982,** 49, 57.

[152] Binning, G.; Quate, C.F.; Gerber, C. *Phys. Rev. Lett.* **1986,** 56, 930.

[153] Takano, H.; Kenseth, J.R.; Wong, S.S.; O'Brien, J.O.; Porter, M.D. *Chem. Rev.* **1999,** 99, 2945.

[154] Butt, H.J.; Cappella, B.; Kappl, M. *Surf. Sci. Rep.* **2005,** 59, 1.

[155] Veeco Metrology LLC., www.veeco.com (last accessed July 4th, 2008)

[156] Magonov, S.N.; Whangbo, M.H. *Surface analysis with STM and AFM*, VCH, 1996.

[157] Pang, G.K.H.; Baba-Kishi, K.Z.; Patel, A. *Ultramicroscopy* **2000,** 81, 35.

[158] Noy, A.; Vezenov, D.V.; Lieber, C.M. *Annu. Rev. Matter. Sci.* **1997,** 27, 381.

[159] Kato, N.; Suzuki, I.; Kikuta, H.; Iwata, K. *Rev. Sci. Instrum.* **1995,** 66, 5532.

[160] McDermott, M.T.; Green, J.B.D.; Porter, M.D. *Langmuir* **1997,** 13, 2504.

[161] Van der Vegte, E.W.; Hadziioannou, G. *Langmuir* **1997,** 13, 4357.

[162] Thundat, T.; Zheng, X.Y.; Chen, G.Y.; Sharp, S.L.; Warmack, R.J.; Schowalter, L.J. *Appl. Phys. Lett.***1993,** 63, 2150.

[163] Noy, A.; Frisbie, C.D.; Rozsnyai, L.F.; Wrighton, M.S.; Lieber, C.M. *J. Am. Chem. Soc.* **1995,** 117, 7943.

[164] Hutter, J.L.; Bechhoefer, J. *Rev. Sci .Instrum.* **1993,** 64, 1868.

[165] Sader, J. E. *Rev. Sci. Instrum*. **1995,** 66, 4583.

[166] Sader, J. E. *J. Appl. Phys*. **1998,** 84,64.

[167] Sader, J. E.; Chon, J. W. M.; Mulvaney, P. *Rev. Sci. Instrum.* **1999,** 70, 3967.

[168] Green, C. P.; Lioe, H.; Cleveland, J. P.; Proksch, R.; Mulvaney, P.; Sader, J. E. *Rev. Sci. Instrum*. **2004,** 75, 1988.

[169] Price, W. S.; Ide, H.; Arata, Y. *J. Phys. Chem. A* **2003,** 107, 4784.

[170] D'Angelo, M.; Onori, G.; Santucci, A. *J. Chem. Phys.* **1994,** 100, 3107.

[171] Koga, Y.; Nishikawa, K.; Westh, P. *J. Phys. Chem. A* **2004,** 108, 3873.

[172] Dixit, S.; Soper, A. K.; Finney, J. L.; Crain, J. *Europhys. Lett.* **2002,** 59, 377.

[173] Jorgensen, W. L. *J. Phys. Chem*. **1986,** 90, 1276.

[174] Jorgensen, W. L. *J. Am. Chem. Soc*. **1980,** 102, 543.

[175] Noskov, S. I.; Lamoureux, G.; Roux, B. *J. Phys. Chem. B* **2005,** 109, 6705.

[176] Dixit, S.; Poon, W. C. K.; Finney, J. L.; Soper, A. K. *Nature* **2002,** 416, 829.

[177] Fidler, J.; Rodger, P. M. *J. Phys. Chem*. **1999,** 103, 7695.

[178] Laaksonen, A.; Kusalik, P. G.; Svishchev, I. M. *J. Phys. Chem. A* **1997,** 101, 5910.

[179] Lipkowitz, K. B. *J. Chromatogr. A* **1995,** 694, 15.

[180] Booth T. D.; Azzaoui K.; Wainer I. W. *Anal. Chem*. **1997,** 69, 3879.

[181] Wolf R. M.; Francotte E.; Lohmann D. *J. Chem. Soc., Perkin Trans*. **1988,** 2, 893.

[182] Wallwork, M. L.; Smith, D. A.; Zhang, J.; Kirkham, J.; Robinson, C. *Langmuir* **2001,** 17, 1126.

[183] Skulason, H.; Frisbie, C. D. *J. Am. Chem. Soc*. **2002,** 124, 15125.

[184] CHARMM. MacKerell, Jr., A. D.; Bashford, D.; Bellott, M.; Dunbrack Jr., R.L.; Evanseck, J.D.; Field, M.J.; Fischer, S.; Gao, J.; Guo, H.; Ha, S.; Joseph-McCarthy, D.; Kuchnir, L.; Kuczera, K.; Lau, F.T.K.; Mattos, C.; Michnick, S.; Ngo, T.; Nguyen, D.T.; Prodhom, B.; Reiher, III, W.E.; Roux, B.; Schlenkrich, M.; Smith, J.C.; Stote, R.; Straub, J.; Watanabe, M.; Wiorkiewicz-Kuczera, J.; Yin, D.; Karplus, M.; *J. Phys. Chem. B* **1998,** 102, 3586.

[185] De Loof, H.; Nilsson, L.; Rigler, R. *J. Am. Chem. Soc.* **1992,** 114, 4028.

[186] Luzar, A; Chandler, D. *Phys. Rev. Lett.* **1996,** 76, 928.

[187] Hines, M.A., *Int. Rev. Phys. Chem.* **2001,** 20, 645.

[188] Chaudhury, M.K.; Whitesides, G.M. *Langmuir* **1991,** 7, 1013.

[189] Osterholtz, E.D.; Pohl, E.R. *Silane and Other Coupling Agents*, ed. Mittal, K.I., VSP International Science Publishers, Zeist, Netherlands, 1992.

[190] Sinniah, S.K.; Steel, A.B.; Miller, C.J.; Reutt-Robey, J.E. *J. Am. Chem. Soc.* **1996,** 118, 8925.

[191] Magora, A.; Abu-Lafi, S.; Levin, S. *J. Chromatogr. A* **2000,** 866, 183.

[192] Regis Technologies Inc., www.registech.com (last accessed July 4th, 2008)

[193] Pirkle, W.H.; Welch, C.J.; Zych, A.J. *J. Chromatogr.* **1993,** 648, 101.

[194] Pirkle, W.H., McCune, J.E. *J. Chromatogr.* **1989,** 469, 67.

[195] Wainer, I.W.; Doyle, T.D. *J. Chromatogr.* **1984,** 284, 117.

[196] Hyun, M.H.; Kim, Y.D.; Han, S.C.; Lee, J.B. *J. High Resol.Chromatogr.* **1998,** 21, 464.

[197] Forjan, D.M.; Vinkovic, V.; Kontrec, D. *Acta Chromatogr.* **2006,** 17, 97.

[198] Still, M.G.; Rogers, L.B. *Talanta* **1990,** 37, 599.

[199] Gallagher, J.F.; Kenny, P.T.M.; O'Donohoe M. *Acta Crys.* **2000,** C56, e157.

[200] Lipkowitz, K.B.; Demeter, D.A.; Parish, C.A.; Landwer, J.M. *J. Comput. Chem.* **1987,** 8, 753.

[201] Chin, W.; Piuzzi, F.; Dimicoli, I.; Mons, M. *Phys. Chem. Chem. Phys.* **2006,** 8, 1033.

[202] Ryckaert, J.P.; Bellemans, A. *Far. Disc. Chem. Soc.* **1978,** 66, 95.

[203] Jorgensen, W.L.; Madura, J.D.; Swenson, C.J. *J. Am. Chem. Soc.* **1984,** 106, 6638.

[204] Briggs, J.M.; Jorgensen, W.L. *J. Comput. Chem.* **1990,** 11 958.

[205] E04USF*, The NAG Fortran Library, Mark 21,* Numerical Algorithms Group, Oxford, UK, 2005

[206] Gung, B.W.; MacKay, J.A.; Zou, D. *J. Org. Chem.* **1999,** 64, 700.

[207] Price, M.L.P.; Ostrovsky, D.; Jorgensen, W.L. *J. Comput. Chem.* **2001,** 22, 1340.

[208] Duffy, E.M.; Kowalczyk, P.J.; Jorgensen, W.L. *J. Am. Chem. Soc.* **1993,** 115, 9271.

[209] Lorentz, H.A. *Annalen Phys.* **1981,** 12, 127.

[210] Berthelot, D.C. (r) *Hebd. Séanc. Acad. Sci., Paris* **1988,** 126, 1703.

[211] Breneman, C.M.; Wiberg, K.B. *J. Comp. Chem.* **1990,** 11, 361.

[212] Kony, D.; Damm, W.; Stoll, S.; Van Gunsteren, W.F. *J. Comput. Chem*. **2002,** 23, 1416.

[213] De Oliveira, O.V.; Freitas, L.C. *J. Mol. Struct*. **2005,** 728,179.

[214] Berardi, R.; Carnelli, G.; Galletti, P.; Giacomini, D.; Gualandi, A., Muccidi, L.; Zannoni, C. *J. Am. Chem. Soc*. **2005,** 127, 699.

[215] Jorgensen, W.L.; Madura, J.D.; Swenson, C.J. *J. Am. Chem. Soc.* **1984,** 106, 6638.

[216] Levitt, M.; Sharon, R. *Proc. Natl. Acad. Sci.* **1988,** 85, 7557.

[217] Pirkle, W.H.; Pochapsky, T.C. *J. Am. Chem. Soc.* **1987,** 109, 5975.